The neuroimaging signature of cognitive automaticity and the role of the cerebellum

A thesis submitted in fulfillment of the requirements for the degree of Doctor of Philosophy

Joshua Bradley Chan Tan

Faculty of Medicine and Health

The University of Sydney

2025

The research reported in this thesis was supported by the award of a Research Training Program Scholarship and Fee Offset to the PhD Candidate

Acknowledgements

This thesis was made possible due to the support from numerous people, including family, friends, colleagues and experts in the field. I'm extremely grateful to all the researchers who shared their data and the participants of those studies, of which made this research possible.

I would like to first show my utmost appreciation to my supervisor, Mac. Thank you for always having my back. Your unending support gave me certainty that there are no problems without answers – or at least a sensible answer. Thank you for welcoming me to your team, for creating an environment where we learn from each other and help each other grow. Thank you for your mentorship and guidance. Being around you has helped me become a better communicator and stay true to myself in my science. I will forever remember our chaotic meetings, the side tangents that lead us down rabbit-holes, and us, talking science.

To Claire, you were the one who introduced me to the academic world, and I would have it no other way. Thank you for showing me that science, is driven by curiosity and passion for our own work. Your ability to always find a positive spin is infectious, and I am grateful to have been in your lab.

Special thanks to Eli and Brandon. Eli, you encouraged me to embrace complex approaches and own them, and Brandon, thanks for being with me in that park. You both have influenced how I want to do research and have made my experience feel truly unique. To my favourite crew: Bella, Tash, Gabe, Chris, and Annie. I am extremely honoured to have shared my journey with all of you and have been inspired by each and every one of you in many ways. Bella, your perseverance and adaptability. Tash, your honesty and love for pure science. Gabe, your carefree attitude. Chris, your confidence in your identity as a scientist. Annie, your ability to tell a visually, captivating story. I look forward to where our science takes us and working together in the future.

I am also grateful to Giulia, Jayson and Chet. In the short timeframe that we've worked together, you have all given me insightful advice that have led me to explore outside my comfort zone. Thank you Vicente, for your guidance on academic careers. And to Jungwoo, your presence itself changed my future and opened up options I did not think were possible.

Many thanks to Kim, Aaron, Elise, and the staff at Kim Warwick Tennis Academy. Our interactions and discussions have shaped the research questions that interest me.

Thanks to my friends. Angus, Calvin, James, Jin, Robert, William, Winston, and Yves. Our adventures are my highlights each year. Together, we have seen the world, and I hope that even after we go our separate ways, we find time for another adventure.

Lastly, I'd like to thank my family who have been supporting me from the start. To my brothers, Daniel and Matthew. You two are the best brothers ever. Daniel, you have been my role model from the very beginning, whether it be your decisiveness to do what you want, or even eating left-handed. Matthew, your achievements consistently amaze me and make me proud to be your older brother. To my parents, I find it awkward to say thanks for what you have done for me, because once I start, I would be thanking you till the end of days. Thanks for your sacrifices, for giving me opportunities, and for making me the person I am today.

Table of Contents

Statement of Originality

This is to certify that to the best of my knowledge, the content of this thesis is my own work. This thesis has not been submitted for any degree or other purposes. I certify that the intellectual content of this thesis is the product of my own work and that all the assistance received in preparing this thesis and sources have been acknowledged. No content produced by generative AI tools has been used in the preparation of this thesis. I understand if awarded a higher degree by The University of Sydney following examination of this thesis that it will be lodged with the University Librarian and made available for immediate use in accordance with The University of Sydney Degree by Research Rule.

Due to amendments made during the thesis submission phase, some empirical chapters may slightly differ in content compared to the online published versions.

Joshua Bradley Chan Tan

Date 24/07/2025

As supervisor for the candidature upon which this thesis is based, I hereby certify that this thesis is sufficiently well presented to be examined and that it does not exceed the prescribed word limit.

James M. Shine

Date 24/07/2025

Authorship attribution statement

Chapter 2 of this thesis is published as: Tan, J. B. C., Orlando, I. F., Whyte, C., Bryant, A. G., Munn, B. R., Baracchini, G., King, M., O'Callaghan, C., Müller E. J., & Shine, J. M. (2025). Cerebellar and Subcortical Contributions to Working Memory Manipulation. *Communications Biology*, 8(1028). https://doi.org/10.1101/2025.02.20.639399

- Joshua Tan conceptualised the design, preprocessed and analysed the data, and wrote the manuscript
- Assisted by Isabella Orlando (analysis advice), Christopher Whyte, Annie Bryant (analysis advice), Brandon Munn (analysis advice), Giulia Baracchini, Maedbh King (data acquisition), Claire O'Callaghan (analysis advice, supervision), Eli Müller (analysis advice, supervision), and James M. Shine (study conceptualisation, analysis advice, supervision). All co-authors contributed to the final manuscript.

Chapter 3 of this thesis is published as: Tan, J. B., Müller, E., Zahorodnii, A., & Shine, J. M. (2024). The engagement of the cerebellum and basal ganglia enhances expertise in a sensorimotor adaptation task. *Imaging Neuroscience*, *2*, 1–20. https://doi.org/10.1162/imag_a_00271.

- Joshua Tan conceptualised the design, preprocessed and analysed the data, and wrote the manuscript
- Assisted by Eli Müller (study conceptualisation, analysis advice, supervision), Andrii Zahorodnii (analysis), and James M. Shine (study conceptualisation, analysis advice, supervision). All co-authors contributed to the final manuscript.

Chapter 4 of this thesis is in preparation with the assistance of Isabella F. Orlando, Jungwoo Kim, Jayson Jeganathan, Giulia Baracchini, Rebekah Wong, Eli J. Müller, Claire O'Callaghan, James M. Shine.

- Joshua Tan conceptualised the design, preprocessed and analysed the data, and wrote the manuscript

- Assisted by Isabella Orlando (analysis advice), Jungwoo Kim (analysis advice), Jayson Jeganathan (analysis advice), Giulia Baracchini (analysis advice), Rebekah Wong, Eli Müller (study conceptualisation, analysis advice, supervision), Claire O'Callaghan (study conceptualisation, analysis advice, supervision), and James M. Shine (study conceptualisation, analysis advice, supervision). All co-authors contributed to the final manuscript.

In addition to the statements above, in cases where I am not the corresponding author of a published item, permission to include the published material has been granted by the corresponding author.

Joshua Bradley Chan Tan

Date 24/07/2025

As supervisor for the candidature upon which this thesis is based, I can confirm that the authorship attribution statements above are correct.

James M. Shine

Date 24/07/2025

First authored publications associated with this thesis

Chapter 2 of this thesis is published as: Tan, J. B. C., Orlando, I. F., Whyte, C., Bryant, A. G., Munn, B. R., Baracchini, G., King, M., O'Callaghan, C., Müller E. J., & Shine, J. M. (2025). Cerebellar and Subcortical Contributions to Working Memory Manipulation. *Communications Biology*, 8(1028). https://doi.org/10.1101/2025.02.20.639399

Chapter 3 of this thesis is published as: Tan, J. B., Müller, E., Zahorodnii, A., & Shine, J. M. (2024). The engagement of the cerebellum and basal ganglia enhances expertise in a sensorimotor adaptation task. *Imaging Neuroscience*, *2*, 1–20. https://doi.org/10.1162/imag_a_00271.

Appendix V of this thesis is published as: Tan, J. B., Müller, E. J., Orlando, I. F., Taylor, N. L., Margulies, D. S., Szeto, J., Lewis, S. J. G., Shine, J. M., & O'Callaghan, C. (2023). Abnormal higher-order network interactions in Parkinson's disease visual hallucinations. *Brain*. https://doi.org/10.1093/brain/awad305

Co-authored publications arising from candidature

Müller, E. J., Palesi, F., Hou, K. Y., **Tan, J.**, Close, T., Gandini Wheeler-Kingschott, C. A. M., D'Angelo, E., Calamante, F., & Shine, J. M. (2023). Parallel processing relies on a distributed, low-dimensional cortico-cerebellar architecture. Network Neuroscience, 1–20. https://doi.org/10.1162/netn_a_00308

Noble, C., Taylor, N. L., Milton, F., Fulford, J., **Tan, J. B.**, O'Callaghan, C., Zeman, A., & Shine, J. M. (2025). Seeing through the Static: Reduced Imagery Vividness in Aphantasia is Associated with Impaired Temporal Lobe Signal Complexity. https://doi.org/10.1101/2025.05.25.655911

Orlando, I. F., O'Callaghan, C., Lam, A., McKinnon, A. C., **Tan, J. B. C.**, Michaelian, J. C., Kong, S. D. X., D'Rozario, A. L., & Naismith, S. L. (2023). Sleep spindle architecture associated with distinct clinical phenotypes in older adults at risk for dementia. Molecular Psychiatry. https://doi.org/10.1038/s41380-023-02335-1

Orlando, I. F., **Tan, J. B.**, Taylor, N. L., Medel, V., Wainstein, G., Lewis, S. J. G., Shine, J. M., & O'Callaghan, C. (2025). Dopamine alters functional gradients in Parkinson's disease. Imaging Neuroscience, 3, imag_a_00564. https://doi.org/10.1162/imag_a_00564

Abstract

Delegation of behaviours to automaticity is an evolutionary advantage, allowing for parallel processing and adaptive behaviour. In primates and humans, both motor and cognitive behaviours are automatised allowing for increasingly complex behaviours. Across these species, the cortico-cerebellar circuit has become exceedingly prominent, however the contributions of the cortico-cerebellar circuit to cognitive automaticity remains largely unknown. In this thesis, we attempt to characterise the role of the cortico-cerebellar circuit in cognitive automaticity and adaptation. Specifically, this thesis highlights distinct contributions from the cerebellum that facilitate adaptive behaviours. We reveal that the cerebellum serves unique contributions to cognitive automaticity during a mental rotation task. We demonstrate that expertise during sensorimotor adaptation is driven by increased dependence on the cerebellum and decreased dependence on the cerebral cortex. Then, we explore features of compositional cognition that facilitate adaptive behaviour. We breakdown compositional cognition into two systems: specialised components (i.e., existing behaviours) that mainly feature specialised cerebral regions, and recombination, a generalised process supported by the cortico-cerebellar circuitry. Lastly, we combine insights from complementary dimensionality reduction approaches to understand resting-state brain patterns in Parkinson's disease patients with and without visual hallucinations. Together, this thesis illustrates the cortico-cerebellar circuitry as pivotal to cognitive automaticity, driving the development of adaptive, complex behaviours.

Chapter 1: Introduction

1.1 Automaticity

The ways in which the brain and body work in tandem while interacting with the environment varies widely from person to person. This is a prominent observation when watching elite athletes. For example, Roger Federer can effortlessly hit a tennis ball with great power and precision, whereas a novice tennis player struggles to hit a ball with their racquet. Between the two, there are clear differences in how their brain and body coordinate. For experts like Federer, hitting a tennis ball is like riding a bike, an action that is well-committed to memory through automaticity, which refers to the ability to perform behaviours with minimal conscious effort (Bloom, 1986). The extent to which novices differ from Federer is dependent on how actions are automatised in the brain and how they implement them. However, our understanding of how automaticity arises in the brain is under-developed, ignoring what makes experts like Federer unique. For one, automaticity typically refers to motor behaviours (i.e., swinging a tennis racquet), disregarding automatised cognitive behaviours (i.e., mathematical operations) (Ding et al., 2017). Automaticity is ingrained in repetitive training, encouraging rigidity and an inability to adapt to changing conditions. However, experts are able to flexibly adapt automatic behaviours to environmental conditions. Furthermore, automatic behaviours serve as building blocks that are recombined to produce spontaneous, novel behaviours. In the following thesis, we will address these gaps, combining neuroimaging techniques and behavioural paradigms to put forward a whole-brain perspective of how the brain operationalises automaticity.

1.2 Characteristics of flexible automaticity

Both motor and cognitive behaviours can be automatised, suggesting that they share a common neural circuitry. Motor learning is a well-established field in cognitive neuroscience, with variant studies across species (Areshenkoff et al., 2022; Gallego et al., 2018), task complexity (Churchland et al., 2012; Standage et al., 2023), and imaging modalities (Berlot et al., 2020a; Gallego et al., 2020). In motor learning studies, automaticity is characterised by an initial increased performance followed by an asymptote in behavioural performance (Krakauer, 2009; Kübler et al., 2006). Cognitive behaviours can also be trained to automaticity. Similar to motor learning, cognitive learning also demonstrates practice effects with an eventual asymptote in

behaviour (Kübler et al., 2006). Furthermore, the range of complexity in cognitive behaviours surpasses the complexity of motor behaviours that we can measure in a scanner. The main difference between motor and cognitive automaticity is found at in sensorimotor areas or brain regions that directly output actions or receive input from the environment e.g. the primary visual and motor areas. For any information processing that occurs up/downstream possibly relies on a shared neural circuitry (Ramnani, 2014).

The brain can be functionally segmented, with areas biased towards motor actions and others to more cognitive behaviours (Margulies et al., 2016; Yeo et al., 2011). Practicing a task to automaticity can both increase and decrease activation in task-related regions further differentiating between motor and cognitive behaviours (Kelly & Garavan, 2005; Kübler et al., 2006). Decreased brain activity in task-related areas may suggest increased neural efficiency and lower effort (Poldrack, 2005). In contrast, increased activity has two distinct interpretations (Kelly & Garavan, 2005). During initial learning, increased activity is seen in task-related areas, indicating development of task-related areas (i.e., increased plasticity). After extended practice, increased activity is observed in new brain areas combined with decreased activity in task-related areas, indicating a transition from conscious control to automatised behaviour (Bassett et al., 2015; Debarnot et al., 2014). These brain areas that specifically increase with automatization may share commonalities between motor and cognitive behaviours. Therefore, combining insights from both motor and cognitive automaticity can point towards the underlying principles of automaticity in the brain.

But how do we know the signs of automaticity in behaviour? For behaviour, there are distinct hallmarks of automaticity including, response time and accuracy reaching an asymptote in performance, a speed up in processing and reduced variability in performance, or being able to multi-task i.e., perform a primary task with little to no interference by a demanding secondary task (Balsters & Ramnani, 2011; Kübler et al., 2006; Toner et al., 2015). Other methods commonly used to test for automaticity or minimal learning, is to compare performance across sessions or days, where no significant difference in performance also suggests behavioural automaticity. It is also unclear what is the distinction between automaticity and habitual behaviours, especially when both terms have been used interchangeably (Du et al., 2022). Both automaticity and habitual behaviours involve repetitive actions that require minimal cognitive effort. However, where habitual behaviours focuses on recalling specific stimulus-response associations, automaticity focuses on the intermediate processes that make up the behaviour

(Du et al., 2022). To this end, this thesis attempts to bridge our understanding of automaticity both in behaviour and neuroimaging modalities.

Experts, those who excel in their respective fields, flexibly adapt automatic behaviours, making small adjustments depending on the current context. This depends on balancing two systems – automatic processing *versus* controlled, conscious processing (Ramnani, 2014). Automatic processing allows for faster and consistent responses under the same conditions, and most importantly is not disrupted by multi-tasking. However, total dependence on this system can be detrimental to performance. It is heavily reliant on the context which behaviours are learned, and often times does not transfer outside of the learned context (Toner et al., 2015). Fully automatic processing is uncontrollable and unable to adapt to sudden changes. Controlled processing is slower and deliberate, using ongoing feedback to adjust ongoing behaviour (Ramnani, 2014). It relies on conscious effort and cannot be completed in parallel with other tasks. To flexibly adapt automatised behaviours, experts balance automatic processing with controlled processing achieving the best of both worlds.

How can behaviours both be automatic and adaptable? One answer to this apparent dilemma can be attributed to differential learning. Differential learning is an approach framed around exposure to variation (or noise) during learning, resulting in multiple variations of the same automatised action (Schöllhorn et al., 2006). Each variation produces the same outcome with minor adjustments, depending on the context. For example, imagine navigating from location A to location B. A sensible strategy could be to memorise the most direct route from A to B. Alternatively, you could memorise two alternative routes that go from A to B, but with a minor detour in the middle. By having multiple routes to traverse from A to B, you are better prepared for when your direct route from A to B has heavy traffic conditions. Differential learning is the behavioural analogue of the latter strategy – by learning multiple ways to execute a particular skill, an athlete can become proficient at executing the skill across a range of different noise conditions. In this way, differential learning develops practical automatised behaviours that can flexibly adapt to the environment.

The standard approach to investigating automatised behaviours is through adaptation paradigms (Israely et al., 2025; Krakauer & Mazzoni, 2011; Standage et al., 2023). The typical structure of these paradigms involves three phases: learning a specific motor movement (e.g., reaching towards a target), followed by a perturbation phase (e.g., rotating control input to reach 45º clockwise to the original), ending with a washout phase where the original conditions

are reintroduced. Adaptation can be measured by how quickly participants adapt to perturbations and described by the common neural signatures found across perturbation and washout phases. This approach is useful for identifying how neural signatures have changed between the phases but does not tap into specific training approaches to develop flexible automatised behaviours.

To understand how training facilitates flexible adaptation in the brain, we can integrate differential learning approaches with adaptation paradigms. Differential learning can be applied to adaptation paradigms in several ways. The first involves forcefully introducing movement variation during the learning phase and measuring adaptation performance compared to groups that trained without variation. This approach has been successfully applied using neural networks which serve as mathematical models built to do brain-like behaviours (Abdi, 1994). In these studies, models trained on multiple tasks develop an abstract understanding that facilitates learning novel behaviours (Driscoll et al., 2024; Hocker et al., 2025; Johnston & Fusi, 2023; G. R. Yang et al., 2019). Alternatively, we can manipulate brain circuitries either in animals (Israely et al., 2025) or through model simulations (Pemberton et al., 2024), gaining insights into how different brain areas contribute to the adaptation process. The final approach is to investigate whether variation in neural signatures relates to task performance. Typically in neuroimaging studies, variation is treated as 'noise' that should be removed from the data (De Blasi et al., 2020), however some studies suggest that variation can also be brain-related (Grady et al., 2023). In adaptation paradigms, variation in neural signatures may signify a participant's attempt at varied actions and be associated with learning flexible behaviours. Therefore, integrating differential learning with adaptation paradigms can provide insights into neural signatures of flexible adaptation.

Complete mastery of a skill is demonstrated through combining various automatised behaviours to compose novel actions (Dreyfus & Dreyfus, 1980; Samuels & Flor, 1997). Individuals with the highest skill in their fields are able to transcend usual high-level performances, defying our understanding (Bloom, 1986). For example, Roger Federer can hit an unbelievable shot between the legs to lob the ball over his opponent. While most players will have already lost the point, Federer is able to pull together his various tools and utilise them in an unprecedented way in order to win the point. This ability to generate novelty by mixing previously automatised behaviours is referred to as 'compositionality' (Lande, 2024).

Through various neuroimaging studies, it is well understood that extensively training can result in automaticity, however it is unclear how automatised behaviours are compositionally recombined in the brain. A possible theory is through understanding functional specificity of neural populations. At the neural population level, neural populations can be functionally specific – respond to a specific event but not to others (i.e., neurons that fire when vertical lines are presented but not horizonal lines). They can also show mixed specificity (Fusi et al., 2016). This dichotomy between specialised and mixed populations is analogous to balancing automatic and controlled processing. During compositional cognition, specialised neural populations – like automatic processing – are highly responsive to single events, however, neural populations with mixed specificity are required to interact with specialised neural populations in order to demonstrate higher cognitive behaviours e.g., problem-solving adaptation, and generalisation (Bernardi et al., 2020; Fusi et al., 2016). Similarly, at the macro-scale, brain regions can be separated by their functional specificity. Sensory and unimodal regions demonstrate functional specificity while higher-order multimodal regions serve abstract and general functions (Margulies et al., 2016). However, it is unclear whether compositional interpretations at the neural population level translate to findings at the macro-scale. By translating neural population frameworks of compositionality to the macro-scale, we can understand whole-brain interactions that enable recombination of automatised behaviours.

1.3 Evolution of cognition and the brain

How does automaticity arise from neural interactions in the brain? To answer this question, it is important to consider evolutionary changes. From one perspective, cognition and behaviour are processes that arise from adapting primal behaviours such as sensory and motor mechanisms to changes in the environment (Cisek, 2021, 2022). This concept of 'embodied cognition' emphasises that behaviours are shaped by the environment and adapt from preexisting behaviours (Cisek, 2019). This can be applied when comparing evolutionary changes across species (Cisek, 2019). Hence, while the complexity of our behaviours outstrips other species, automaticity itself is not unique to humans.

Humans and primates have a vast variety of affordances and complex behaviours in both motor and cognitive actions compared to other species. Specifically, humans have the ability to flexibly utilise a multitude of tools, as well as mentally juggle multi-step planning. A common opinion is that the development and expansion of the cerebral cortex (neocortex) supported the development of complex behaviours and overall higher cognitive functions, notably described as 'the crowning achievement of evolution and the biological substrate of human mental prowess' (Rakic, 2009). However, this perspective has since been refuted. While the neocortex expansion serves as a significant stage in evolution, the size of the brain, specifically the cerebral cortex is more so related to body size of the species (Barton, 2012). For example, sperm whales have larger brains than humans which are also neocortically dominated (~87% of the brain is the neocortex) (Barton, 2012), but arguably human behaviour is still more complex. Therefore, evolutionary history suggests that behavioural complexity evolves alongside changes in the whole-brain and not solely the cerebral cortex.

Another brain structure that underwent considerable expansion in primates – even more than the neocortex – is the cerebellum (Barton & Venditti, 2014; Figure 1a). The cerebellum, which is Latin for 'little brain' and sometimes considered merely the 'pillow of the brain', is thought to have emerged roughly 500 million years ago in sharks and fish (Cisek, 2022; Montgomery & Bodznick, 2016). Consisting of more than half the neurons in the mammalian brain (Kawato et al., 2021), the cerebellum expanded over time most notably in apes (Barton & Venditti, 2014). Unlike the neocortex, cerebellum size does not scale with body size, suggesting that the expansion of the cerebellum is non-trivial and serves an important role in distinguishing behaviour between primates and other species (Barton, 2012). In recent years, appreciation for

the cerebellum has grown with the cerebellum now implicated in numerous neural circuitries and behaviours both motor and cognitive (Kang et al., 2021; Prati et al., 2024; B. Wang, 2025).

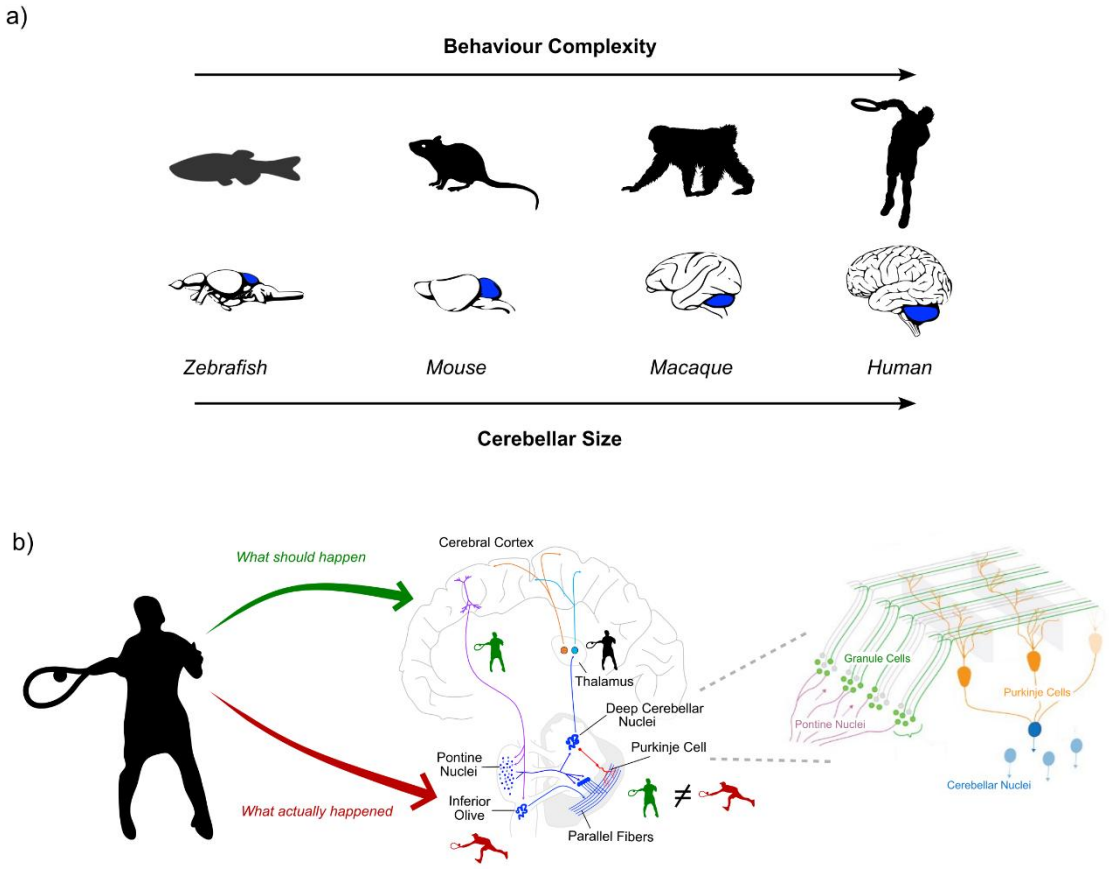

Figure 1. Integrating theories from evolution, automaticity, and neurobiology. a) Linking evolution of behaviour complexity with cerebellar size. b) Mapping action refinement to the cortico-cerebellar circuitry. Adapted from Shine (2021) and Eli Müller. Middle: An efference copy of actions travels from the cerebral cortex to the cerebellum via the pontine nuclei. Action feedback travels from the spinal cord to the cerebellum via the inferior olive. Both the efference copy and action feedback are compared, and adjustments are made. Right: Cerebellar cortical microstructure is modular and features numerous synapses.

1.4 Cerebellar structure and function

The cerebellum can be divided into a cortex (outer area) and the deep area where the cerebellar nuclei reside (Guell & Schmahmann, 2020). The cerebellar cortex can be further subdivided into three layers: the granular layer (contains granule cells), a thin layer containing Purkinje cells, and the molecular layer (Albus, 1971). Within the cerebellar cortex there are various cells such as basket cells and golgi cells (Kawato et al., 2021), however for simplification we will

focus on granule cells (including their parallel fibres), Purkinje cells, and climbing fibres as the main cells and features of the cerebellar cortex.

The cerebellum is interconnected both with the cerebral cortex and the rest of the brain. Overall, the main input to the cerebellar cortex is through a cortico-pontine-cerebellar pathway and from the inferior olive (Kang et al., 2021; Figure 1b). The cortico-pontine-cerebellar pathway is the main method of communication between the cerebral cortex and cerebellum and conveys copies of actions enacted by the cerebral cortex (Wolpert et al., 1998). Meanwhile, climbing fibres from the inferior olive receives inputs from the peripheral system (via the spinal cord) and red nucleus (De Zeeuw et al., 1998; Figure 1b). The spinal cord conveys information related to the body – i.e., the location of your arm at a specific moment in time – and while historically the red nucleus was associated with limb control, it remains unclear how the red nucleus function specifically the parvocellular part has evolved in animal models and humans (Basile et al., 2021). By combining both inputs from the cerebral cortex and the inferior olive, the cerebellar cortex can refine actions (Wolpert et al., 1998; Wolpert & Flanagan, 2001). The main output pathway of the cerebellum is from the cerebellar nuclei to the cerebral cortex via the thalamus. Through this pathway, the cerebellum conveys refined behaviours back to the cerebral cortex to be enacted (Wolpert et al., 1998; Wolpert & Kawato, 1998).

The cerebellum has a vast capacity for information processing. The high neuronal count and its connections with both the cerebral cortex and inferior olive suggest that the cerebellum serves an integral function in controlling the body. In brief, information from the cerebral cortex passes through the pontine nuclei of the brainstem to reach the granule cells via mossy fibres (Albus, 1971; Figure 1b). Signals are then passed from granule cells along parallel fibres, which contact dendrites of several Purkinje cells. Climbing fibres from the inferior olive also contact Purkinje cells here. From here, signals pass from Purkinje cells to the cerebellar nuclei which then feeds out to the cerebral cortex via the thalamus. From this circuit, it is important to consider the connection types and number of neurons involved at each stage. For example, it has previously been reported that, in the human cerebellum, there are approximately 50 billion granule cells (Kawato et al., 2021). Considering that there are approximately 250 million mossy fibres, studies estimate close to 200 billion synapses occur between mossy fibres and granule cells (Kawato et al., 2021). Even with these connections, the majority of energy consumption occurs at the Purkinje cells. Parallel fibres from granule cells contact multiple Purkinje cells each. With estimations of up to 15 million Purkinje cells, there is approximately 10,000 billion synapses between parallel fibres and Purkinje cells (Kawato et al., 2021). In context with the

rest of the brain, there are 50 times more synapses between parallel fibres and Purkinje cells compared to the number of synapses across the whole brain (Kawato et al., 2021). The sheer number of cells and synapses combined with the fact that the cerebellum significantly expanded due to evolution, points to the cerebellum serving critical functions in the human brain.

Due to these characteristics, the initial role of the cerebellum was embedded in motor learning (M. Ito, 2002). Specifically, during a motor action, cerebral inputs to the cerebellum via pontine nuclei were considered as 'the possible actions available', and inputs from the spinal cord to the cerebellum consisted of 'what actually happened' (Wolpert & Kawato, 1998). Combining with indirect pathways to the basal ganglia – a key area for reward and goal-orientated information (Bostan & Strick, 2018; Yin & Knowlton, 2006) – the brain can predict the outcomes of actions and learn how to modify these actions for a specific goal. Building from this foundation, studies continued to find evidence for cerebellar involvement in motor learning, eventually expanding cerebellar function to encompass motor prediction and coordination (Balsters & Ramnani, 2008, 2011; Wolpert & Flanagan, 2001).

The defining feature of motor automaticity is the transition from a clumsy, awkward action to a ballistic, automated movement. The cerebellum is well-situated to facilitate motor automaticity by refining and perfecting movements sent by the cerebral cortex (Gao et al., 2018; Koziol et al., 2014; Wolpert et al., 2011). Furthermore, the cerebellum may become the main driver of automatised behaviours after learning. Studies have shown that after a movement has been automatised, activity continues to be recorded from the cerebellum (Imamizu et al., 2000a, 2003). By delegating the cerebellum to drive automatised behaviours, the cerebral cortex is freed up to process other information – a key step in multi-tasking and parallel processing (Müller et al., 2023; Shine & Shine, 2014). Therefore, the cerebellum serves an important role both during motor learning and after behaviours have been automatised.

Is cerebellar function limited to motor learning? From an evolutionary perspective, the cerebellum significantly expanded in size alongside evolutions in the repertoire and complexity of cognitive behaviours (Barton, 2012). Insights from cerebellar anatomy suggests an expanded role beyond motor learning. Alongside motor inputs, the cerebellum also shares connections with higher-order areas such as the prefrontal cortex, parietal and temporal areas (Balsters et al., 2010; D'Angelo & Casali, 2013; Kang et al., 2021; R. M. Kelly & Strick, 2003). Perhaps most relevant to evolution is the homogenous structure of the cerebellum that can handle both motor and cognitive inputs in a similar manner (M. Ito, 2008; Leiner et al., 1986), serving as

direct evidence of a sensorimotor circuitry that has evolved to include cognitive behaviours. Therefore, cerebellar functions are now believed to underlie both motor and cognitive automaticity (M. King et al., 2019; Magielse et al., 2024).

1.5 Cortico-cerebellar circuitry underlying flexible automaticity

Understanding cortico-cerebellar circuitry may provide key insights into cognitive automaticity, flexible adaptation, and compositional cognition. In neuroimaging studies, cognitive automaticity has been tested through cognitive learning paradigms such as mental rotation and n-back tasks (M. S. Cohen et al., 1996; Ganis & Kievit, 2015; Hautzel et al., 2009; M. King et al., 2019). However, many of these studies ignore cerebellar contributions, even when cerebellar activity is task-evoked. The cerebellar structure and connectivity with the rest of the brain suggests a unified role of the cerebellum for both motor and cognitive automaticity (Ramnani & Miall, 2004). In both cases, the cerebellum refines actions and behaviours using information from both the cerebral cortex and inferior olive, resulting in automaticity. This explanation is consistent with evolutionary changes in behaviour and biology, proposing the cerebellum as integral to both motor and cognitive learning.

Cortico-cerebellar circuitry plays a pivotal role in learning flexible behaviours during adaptation. The compression of input (cerebral cortex to pontine nuclei) followed by expansion (pontine nuclei to granule cells) is a common feature among biological species serving as an efficient biological architecture for flexible computation (Muscinelli et al., 2023). Importantly, manipulations of cortico-cerebellar circuitry (i.e., lesioning, blocking cerebellar output), results in impaired adaptation (Israely et al., 2025; Sendhilnathan et al., 2024). Furthermore, individuals with impaired cerebellar functions are unable to learn to adapt previously automatised behaviours to novel situations (Morton & Bastian, 2006; Tzvi et al., 2022). From computational modelling, simulations with neural networks trained on adaptation paradigms can provide insights into cortico-cerebellar contributions. Networks without cerebellar-like modules eventually demonstrated high-level performance in adaptation paradigms, however required extensive retraining for after perturbation was applied (Pemberton et al., 2024). Whereas, networks with cerebellar-like modules demonstrated rapid adaptation to perturbations with minimal retraining (Pemberton et al., 2024). Therefore, evidence from clinical, neuroimaging and model simulations provide support that the cortico-cerebellar circuitry drives flexibility across automatised behaviours.

Cortico-cerebellar interactions may also underpin our ability to compositionally recombine automatised behaviours. Cerebellar activity persists even after behaviours have been automatised suggesting that the cerebellum is needed when recalling learned behaviours (Imamizu et al., 2000a, 2003). But do cerebellar contributions extend beyond behaviour recall, enabling recombination? The recombination process is also a skill. Similar to cerebellar predictive functions during motor and cognitive learning, the cerebellum possibly facilitates recombination by optimising combinations of different automatised behaviours. Current studies of compositional cognition have focused on the cerebral cortex (Cocuzza et al., 2020; T. Ito, Yang, et al., 2022) and the hippocampus (Bakermans et al., 2025; Schwartenbeck et al., 2023), but see (Mill & Cole, 2025). Extending compositional frameworks to consider cerebellar contributions can provide insights into how the brain flexible recombines automatised behaviours.

1.6 Understanding the brain at the macro-scale

So far, we have outlined our framework for cognitive automaticity and the role of the cerebellum. To test how cerebellar contributions to complex, cognitive behaviours in the context of whole-brain interactions, a useful modality is functional magnetic resonance imaging (fMRI). fMRI is a technique that non-invasively measures changes in haemodynamic responses in the brain (Logothetis, 2003). Haemodynamic responses can be linked to neural activity as brain areas that increase in activity demonstrate increases in blood flow to the surrounding area (Logothetis et al., 2001). fMRI is especially useful in cognitive neuroscience due to its non-invasive nature. This makes it safe to scan humans, allowing for the testing of a variety of behaviours with the simultaneous measurement of blood flow changes from the whole-brain (including cerebellum and subcortical structures). Since fMRI was first introduced, it has now become a staple of neuroimaging, being especially useful in both clinical and non-clinical applications.

Even though fMRI is capable of capturing cerebellar signals, the cerebellum is consistently overlooked. Previously, an understanding of the cerebellar anatomy and function was overlooked, with misconceptions that the cerebellum was ‘inert’ and could be treated as a reference area in neuroimaging (Pickut, 1999). This was further exemplified in fMRI due to the lower signal-to-noise ratio of the cerebellum compared to the cerebral cortex, as well as data preprocessing pipelines that were optimised specifically for the cerebral cortex (Esteban

et al., 2019; Glasser et al., 2013; B. Wang, 2025). For example, scanning sequences were optimised to capture the cerebral cortex, even if the cerebellum was not fully captured in the field of view, as well as processing pipelines included steps to 'remove' the cerebellum. Fortunately, appreciation for the cerebellum has been growing. With improvements in spatial and temporal resolution of imaging techniques (Mackinnon et al., 2025; Mandino et al., 2020) and the introduction of standardised cerebellar atlases (Buckner et al., 2011; Diedrichsen, 2006; Nettekoven et al., 2024; Zhi et al., 2025), more and more studies are including the cerebellum.

Neuroimaging data is inherently complex with hundreds if not thousands of variables to interpret. An approach to simplify interpretations of neuroimaging data is through dimensionality reduction techniques. Dimensionality reduction involves extracting latent components of the data while preserving relationships of the original data and discarding idiosyncratic features (Cunningham & Yu, 2014; Nguyen & Holmes, 2019). In this way, information specific to behaviour (Churchland et al., 2012; Krishnan et al., 2011), or underlying functional relationships can be explored (Margulies et al., 2016). A pitfall of dimensionality techniques (and statistical techniques in general) is that each have their own assumptions and biases. By simplifying relationships in the original data, other more nuanced relationship may be ignored. This can be done intentionally – using supervised techniques (Krishnan et al., 2011; Müller et al., 2021) to focus on specific behavioural relationship, or, if done unintentionally – through unsupervised techniques (de la Porte et al., 2008; Margulies et al., 2016), can be combined with alternative techniques that have different biases. Combining insights from multiple techniques may converge onto plausible interpretations of the data. Therefore, dimensionality reduction is a useful tool to simplify interpretations and find connections between behaviour and the brain.

With advancements in computational approaches, it is now possible to simulate realistic patterns of brain activity. By combining computational modelling and neurobiological understanding of the cerebellum, we can test predictions and hypotheses about the benefits and function of cerebellar-like modules. As previously mentioned, cerebellar function is well-grounded in feedforward processing and prediction. An example of implementing this structure into computational models is by comparing performance of a neural network with and without a separate feedforward network that is representative of the cerebellum (Pemberton et al., 2024). In this study, the feedforward cerebellar network receives a copy neural activity from the main neural network, before sending predictions back to the main neural network for learning (Pemberton et al., 2024). All networks with and without the feedforward network were able to

learn the initial task, but only networks with the extra feedforward network were able to flexibly switch and generalise between different task contexts (Pemberton et al., 2024). Alternatively, we can test whether the proposed anatomical structure of the cerebellum is appropriate for feedforward processing. By building neural networks specifically with a 'bottle-neck' structure i.e., compression and expansion structure, Muscinelli demonstrates conditions in which networks with distributed connectivity (similar to motor cortex outputs to pontine nuclei) learn an optimal compression and maximise performance in different tasks (Muscinelli et al., 2023). Using computational modelling to complement findings from *in vivo* can push the boundaries of theories, providing insight into the underlying principles of cerebellar function.

1.7 Thesis Overview

Despite robust evidence for training to automaticity, there remains considerable gaps in our understanding of how our brain flexibly applies cognitive automatised behaviours. By exploring neural signatures beyond the cerebral cortex, we can gain a comprehensive understanding of how cognitive automatised behaviours are implemented. In this thesis, we propose that the cortico-cerebellar circuitry serves a crucial role in developing cognitive automatised behaviours and flexible adaptation. The remainder of this thesis is structured as follows.

Chapter 2 explores the unique contributions of the cerebellum to cognitive automaticity in the form of a mental rotation task while undergoing fMRI scanning. Chapter 3 uses the differential learning framework to demonstrate that performance in an adaptation paradigm is driven by the cerebellum and not the cerebral cortex. Chapter 4 continues on to understand how the cortico-cerebellar circuitry promotes adaptation through compositional cognition. Finally, Chapter 5 summarises the main findings and contextualises them in our framework of cognitive automaticity, followed by a discussion of the implications and future directions. Note that each chapter consists of journal articles that are either published (Chapters 2 and 3), or in preparation (Chapter 4).

Chapter 2
Cerebellar and Subcortical Contributions to Working Memory Manipulation

Joshua B. Tan[1,2], Isabella F. Orlando[1], Christopher Whyte[1,2], Annie G. Bryant[1,2,3], Brandon R. Munn[1,2], Giulia Baracchini[1,2], Maedbh King[4], Claire O'Callaghan[1], Eli J. Müller[1,2], James M. Shine*[1,2]

Author Affiliations:

[1]Brain and Mind Centre, School of Medical Sciences, Faculty of Medicine and Health, University of Sydney, Sydney, Australia

[2]Centre for Complex Systems, The University of Sydney, Sydney, Australia

[3]School of Physics, The University of Sydney, Sydney, Australia

[4]Department of Psychology, University of California, Berkeley, CA, USA.

DISCLAIMER: Due to amendments made during the thesis submission phase, some empirical chapters may slightly differ in content compared to the online published versions.

Chapter 2 of this thesis is published as: Tan, J. B. C., Orlando, I. F., Whyte, C., Bryant, A. G., Munn, B. R., Baracchini, G., King, M., O'Callaghan, C., Müller E. J., & Shine, J. M. (2025). Cerebellar and Subcortical Contributions to Working Memory Manipulation. *Communications Biology*, 8(1028). https://doi.org/10.1101/2025.02.20.639399.

Abstract

Working memory is critical for manipulating and temporarily storing information during cognitive tasks such as problem-solving. Most models focus primarily on cortical-cortical interactions, neglecting subcortical and cerebellar contributions. Given the extensive connectivity between the cerebellum, subcortex, and cortex, we hypothesize that they contribute distinct, yet complementary, functions during working memory manipulation. To test this, we used functional Magnetic Resonance Imaging (fMRI) to measure blood oxygen-level dependent (BOLD) activity while participants performed a mental rotation task. Our results revealed a distributed network spanning the cortex, subcortex, and cerebellum that differentiates rotated from non-rotated stimuli and correct from incorrect responses. Notably, delayed responses in premotor, subcortical, and cerebellar regions during incorrect trials, suggest that their precise recruitment is crucial for successful working memory manipulation. These findings expand current models of working memory manipulation, revealing the collaborative role of subcortical and cerebellar regions in coordinating higher cognitive functions.

Introduction

Working memory refers to the ability to store information over a short period of time, such as remembering song lyrics or items from a grocery list (Baddeley & Hitch, 1974; Camina & Güell, 2017). This capacity is thought to involve a distributed network of frontoparietal brain regions that store the information in either local resonant circuits or in short-term plastic inter-synapses changes (Christophel et al., 2017; Constantinidis & Wang, 2004). Despite its ubiquity, our understanding of the neural processes governing our capacity to manipulate the information stored in working memory over time remains incomplete (Nyberg & Eriksson, 2016). For one, working memory manipulation is a dynamic and highly variable process that involves mentally manipulating and transforming information, clearly distinct from merely storing information (Chen et al., 2023; Davis et al., 2018; D'Esposito et al., 1999; Masse et al., 2019; Nyberg & Eriksson, 2016). It is also less clear how a network of neurons typically associated with unsupervised learning – such as the cerebral cortex – can selectively instantiate the context-dependent, multi-system interactive processes required under the many varied ways in which we manipulate the contents of working memory in our day-to-day lives (Doya, 2000). Furthermore, it has previously been shown that subcortical structures can provide complementary functions for cognitive processing (Doya, 2000; Pemberton et al., 2024; Shine, 2021). Here, we advocate for new approaches and perspectives that consider the functional architecture of the whole brain in the mediation of working memory manipulation.

Current popular frameworks characterize working memory as arising from a central system – consisting of brain regions in the prefrontal cortex, parietal lobe and anterior cingulate – that stores and controls information (working memory storage) with accompanying arms that can process and manipulate the information (i.e., a phonological loop in Broca's and Wernicke's area and a visuo-spatial sketch-pad in the occipital lobe) (Baddeley & Hitch, 1974; Camina & Güell, 2017; Nyberg & Eriksson, 2016). While these frameworks provide a foundation for understanding working memory, there is a lack of consensus regarding how information is stored and manipulated (Nozari & Martin, 2024; Nyberg & Eriksson, 2016; Wager & Smith, 2003). This is due in part to the complexity of working memory manipulation. Neural signatures underlying working memory manipulation can vary depending on the modality of the information (i.e., visual, verbal, spatial) and the specific manipulation being applied (i.e., continuously updating information as is done when creating a list, or discrete manipulation by mentally transforming information as is done during mental rotation) (Nyberg & Eriksson,

2016; Wager & Smith, 2003). Furthermore, many of these frameworks are cortico-centric, with only a few frameworks including subcortical brain regions, such as the substantia nigra and thalamus (Bolkan et al., 2017; Nozari & Martin, 2024; Nyberg & Eriksson, 2016; O'Reilly & Frank, 2006). This has resulted in a lack of discussion and investigation into other regions of the brain, such as the cerebellum, which are consistently recruited in working memory studies but have yet to find a place within these frameworks (Ben-Yehudah et al., 2007; Brissenden & Somers, 2019; Deverett et al., 2019; Hautzel et al., 2009; Hayter et al., 2007; M. King et al., 2019; Luis et al., 2015; McDougle et al., 2022; Ravizza et al., 2006; Tomlinson et al., 2014; Vandervert et al., 2007). By continuing to advance analyses and frameworks to be inclusive of regions from the whole brain, a more comprehensive understanding of how the brain processes information can be attained.

There is now strong cross-species evidence that the cerebellum plays a crucial role in working memory (Deverett et al., 2019). With one of the highest neuronal counts in the adult human brain, the cerebellum has a remarkable capacity for information processing (Wagner et al., 2019). Its modular circuitry(Albus, 1971; Apps et al., 2018; Diedrichsen et al., 2019; Koziol et al., 2014) is linked to distinct cognitive functions, including pattern separation and anticipation (Cayco Gajic & Silver, 2019; Imamizu & Kawato, 2009; Ramnani, 2014; Stein, 2021; Wolpert et al., 1998), as well as skill execution and adaptation (Doyon et al., 2003; Krakauer et al., 2004; Tan et al., 2024; Wolpert et al., 1998). While a common misconception is that the cerebellum's main functions are limited to motor coordination and prediction, evidence indicates that the cerebellum both receives input and sends output back to association areas of the cerebral cortex, such as the prefrontal cortex and parietal lobe (R. M. Kelly & Strick, 2003; Ramnani, 2012). Through these connections, the role of the cerebellum extends beyond motor actions to cognitive and multi-domain functions like parallel processing (Müller et al., 2023).

Building on this broader role, the cerebellum's computational properties make it well-suited for working memory manipulation. Specifically, the cerebellum has been implicated in the formation of internal models that predict how objects will behave under different conditions (Imamizu & Kawato, 2009; M. Ito, 2008; Wolpert et al., 1998). This capacity can then be extended to purely mental scenarios – e.g., in a similar way that the cerebellum helps predict the many possible ways to reach for a cup, it can also predict the possible reconfigurations of mentally rotating an object (M. Ito, 2008; Leiner et al., 1986). In this way, the cerebellum may contribute to more abstract concepts, such as action planning and the prediction of outcomes (Gao et al., 2018; Koziol et al., 2014; Vandervert et al., 2007; Zhu et al., 2023), which holds

consistent across species (Christophel et al., 2017; Gao et al., 2018; Magielse et al., 2023). Furthermore, in studies with impaired cerebellar function (i.e., lesioning, degeneration, optogenetic perturbation), working memory performance is degraded (Deverett et al., 2019; McDougle et al., 2022; Ravizza et al., 2006). In a case where impairments were alleviated through pharmacotherapy, there were changes in the cerebellum that significantly related to improved performance (Manktelow et al., 2017). Hence, we predict that through the cortico-cerebellar circuitry, the cerebellum contributes significantly to a model of working memory manipulation.

Along with the cerebellum, other subcortical structures – notably, the basal ganglia – serve important roles in working memory manipulation (O'Reilly & Frank, 2006). Currently, the focus on subcortical contributions to working memory is limited to the cortico-basal ganglia circuitry, particularly on the role of dopaminergic signalling in learning (Nozari & Martin, 2024; Nyberg & Eriksson, 2016; Vijayraghavan et al., 2007). The basal ganglia play an important role in habituation and goal-directed learning, both important facets for learned skills (Yin & Knowlton, 2006). Furthermore, the basal ganglia are disynaptically connected with the cerebellum (Bostan & Strick, 2018; Caligiore et al., 2019), suggesting a degree of functional integration that could underpin emergent higher-order functions. Through these connections, the basal ganglia can guide the cerebellum on what to learn (Bostan & Strick, 2018; Caligiore et al., 2019) and thus update the brain's internal model in a way that has the capacity to augment adaptive behaviour (Shine, 2021; Shine & Shine, 2014). Therefore, a systems-level perspective that incorporates interactions between the cerebellum, basal ganglia, and cerebral cortical regions, can provide a more comprehensive understanding of how the brain manipulates working memory.

In the current study, we analysed BOLD fMRI patterns within the cerebral cortex, cerebellum, basal ganglia, and thalamus during a mental rotation task, an example of how the brain manipulates working memory. The purpose of this study was to extend previous investigations of working memory manipulation to incorporate spatial-temporal signatures from the whole brain. We hypothesized that successful mental rotation recruits a distributed network of regions that would involve regions from the whole brain. Furthermore, we predicted that the cerebellum and other subcortical regions provide unique contributions to performing the mental rotation task that is not found in the cerebral cortex.

Methods

Experimental Design

The following dataset was originally published by King and colleagues (M. King et al., 2019) and is openly available for download on OpenNeuro (accession number ds002105). All participants gave informed consent under an experimental protocol approved by the institutional review board at Western University, Canada. All ethical regulations relevant to human research participants were followed. A total of 26 participants participated in this study, with two participants excluded from analyses as they failed to complete all scanning runs. The final sample consisted of 24 healthy individuals (16 women, 8 men; mean age = 23.8 years, s.d. = 2.6) with no self-reported history of neurological or psychiatric illness. All participants self-reported as right-handed (Edinburgh Handedness Inventory > 40).

The original study contained two sets of tasks (set A and B) of which we only analysed data from set B. In set B, a total of 17 tasks that covered both motor and cognitive domains were performed during each imaging run, with each task lasting 35 s. Of these 17 tasks, our analyses focused on the mental rotation task which is an example of how the brain manipulates information in working memory (Wager & Smith, 2003).

The mental rotation task consisted of stimuli obtained from Ganis and Kievit (Ganis & Kievit, 2015) and were made to follow the traditional Shepard and Metzler three-dimensional stimulus design. The stimuli consisted of a pair of three-dimensional objects: the original object on the left, and a target object on the right. During the task, participants were asked to mentally rotate the target object to determine whether it could be brought to alignment with the original object by only rotating (no flipping/mirroring). There were two types of stimuli: the first being when the two objects could be aligned meaning that they were the "same" object, and the second for when they could not be aligned, in which case they were "different" (Figure 1a). For each stimulus there were three possible angles of rotation around the vertical axis with differing levels of difficulty: 0º (no rotation, easy), 50º rotation (medium), 150º (hard). These angles of rotation were chosen to reflect most of the behavioural range typically used in mental rotation studies without causing significant self-occlusion at any of the orientations. For more details regarding the presentation and creation of the stimuli refer to Ganis and Kievit (Ganis & Kievit, 2015).

The mental rotation task was performed across a 35 s block. Within the 35 s, the first 5 s was the instruction period, where the task name ('mental rotation'), the response effector ('use your RIGHT hand') and the button-to-response assignment ('1 = same, 2 = different') were displayed. Following the instruction period, 9 trials of the mental rotation task were presented during the remaining 30 s (duration = 3 s; ITI = 300 ms per trial). The 9 trials included 3 trials per difficulty, with the order of difficulty randomized between scans but the order kept consistent across participants. Participants responded using a four-key button box and pressing the buttons with their right index and middle fingers. Feedback was provided in the form of a red X for incorrect or a green tick for correct under the given stimulus. Cross-session reliability of activation within a task had previously been reported by King and colleagues (M. King et al., 2019).

Behavioural Training

For tasks in set B, participants completed 3 days of training before the first scanning session. The three training sessions took place over 4-7 days (mean spread of days = 4.4, s.d. = 1.8). During the first day, participants focused on a single task at a time, completing multiple task blocks consecutively. The timing was self-paced, and participants were instructed to read the instructions with the 35 s task block only beginning when they were ready. During this training, online feedback was provided and an overall accuracy score for the task was provided at the end of the practice.

On the second day of training, switching between tasks was introduced. Participants were given six runs of training, wherein each run consisted of a single task block from 11 different tasks. For the first four runs, the timing was self-paced, like the first day of training. For the final two runs, the instruction period was restricted to 5 s to replicate the timing when in the scanner. On the third day of training, participants practiced 17 tasks in four 10-minute runs (35 s per task), emulating the protocol to be used in the scanner sessions.

This training program ensured that participants were familiar with the requirements for each task and had considerable experience in switching between tasks. By introducing training before the scanning, learning during the scanning sessions was minimized. On the third training day, performance was asymptotic, with participants responding correctly to at least 85% of the trials for all the tasks (M. King et al., 2019).

Scanning Sessions

Participants completed two days of scanning for the tasks in set B. The first day of scanning was conducted within 2-3 days following the final training session (mean = 2.2 days following final training session, s.d. = 1.7 days), and the second day of scanning was completed no more than 7 days after the first day of scanning (mean = 2.7 days following final training session, s.d. = 2.3 days). Each day of scanning consisted of eight imaging runs (10 min per run) with each of the 17 tasks presented once for 35 s per imaging run (Figure 1b). In total there were 16 independent measurements of the mental rotation task per participant. The task order was randomized across runs and to reduce order effects, no two tasks were presented in the same order in two different runs. The order of the runs and the order of the tasks within the run were kept consistent across participants and novel stimuli were used when possible, to reduce the recall of specific stimulus-response associations.

Imaging Acquisition

All fMRI data were acquired on a 3T Siemens Prisma at the Centre for Functional and Metabolic Mapping at Western University. Whole brain functional images were acquired using an echo-planar imaging sequence with multi-band acceleration (factor 3, interleaved) and in-plane acceleration (factor 2), developed at the Centre for Magnetic Resonance Research at the University of Minnesota. Imaging parameters were as follows: repetition time = 1 s; field-of-view = 20.8 cm; phase encoding direction P to A; 48 slices; 3 mm thickness; in-plane resolution 2.5 ×2.5 mm^2. Online physiological recordings of both heart and respiration were acquired during each functional run. For anatomical localization and normalization, a 5 min high-resolution scan of the whole brain was acquired (magnetization-prepared rapid acquisition gradient echo; field-of-view =15.6×24×24 cm^3, at 1×1×1 mm^3 voxel size).

Pre-processing

Neuroimaging data was organized in BIDS format and pre-processed with fMRIprep version 23.1.4 (https://fmriprep.org/en/stable/#), a standard pipeline that incorporates toolboxes from the gold-standard preprocessing software in the field (Esteban et al., 2020). fMRIPrep involves the basic pre-processing steps (co-registration, normalization, unwarping, noise component extraction, segmentation, skull-stripping etc.) and produces a report for quality checking at

each step. See Supplementary Material 1 for a full description of each step. Regression of twelve head motion artifacts, and the average combined white matter, CSF signal was conducted using custom python scripts, with a high-pass filter set at 0.01. Mean BOLD time series were extracted from 400 Schaefer cortical regions (Schaefer et al., 2018), 28 cerebellar regions (SUIT atlas) (Diedrichsen, 2006), and 54 subcortical regions (Tian et al., 2020) using custom python scripts. The following atlases were chosen as robust and popular parcellations that reveal meaningful neurobiological features (Diedrichsen, 2006; Schaefer et al., 2018; Tian et al., 2020).

Behavioural Analysis

To check whether changes in difficulty affected performance, generalized linear mixed models were constructed using participants' response time (RT) in seconds, and their accuracy (%) across trials within a scan. Only trials that were correctly answered were used for the model of RT. Correct responses were selected as they were likely to be task related, whereas incorrect responses could be due to several reasons i.e., making a mistake in the trial, getting distracted, struggling to handle equipment. Linear mixed models were constructed to find the relationship between RT or accuracy with the level of difficulty (easy, medium, hard) and the specific day of which the scanning took place (Day 1 or 2) while controlling for repeated measurements from the same scan and subject.

Finite Impulse Response Model (FIR) - The Relationship Between Task Difficulty and BOLD Activity

Rather than using a single estimate which captures the estimated average amplitude of the response during the task, the finite impulse response (FIR) model allows the estimation of the response at specific time-points of the task. Furthermore, the FIR model is not biased towards a particular shape, such as the hemodynamic response function which is typically used in task-based functional MRI analyses.

A 3 s box-car regressor was convolved with the hemodynamic response function in order to estimate a window length of response related to a single trial (Figure 2a). From this plot, the convolved curve first dips below zero 14 s after the start of a trial (i.e., 15 frames). Therefore, a window length of 15 s starting at the beginning of the trial and ending 14 s after the start of

a trial (15 regressors; 1 per second) was used in the FIR models to estimate the BOLD activity during a trial.

To estimate the relationship between the BOLD response and task difficulty, trials were grouped by difficulty and the FIR model for each trial was fit to each region's BOLD time series. Only trials with correct responses were included in this model. The final design matrix had 15 regressors (1 per time point) per difficulty (15 x 3), a regressor defining which day the scanning took place, and which scan on the day. Participant-level BOLD activity was estimated by concatenating the BOLD time series for all scans of a participant together and fitting a generalized linear mixed model per participant. In the model, task difficulty (15 x 3 timepoints) and day regressors were modelled as fixed while the specific scan was controlled for as a random effect. From this model, beta coefficients per timepoint within the 15 s window for each difficulty were obtained. By concatenating trials within each difficulty, temporal blurring between adjacent trials was minimized and the common effects across similar trials was emphasized.

Estimating BOLD activity for Hard and Incorrect Responses

A similar pipeline was followed to model Incorrect responses during Hard trials. For this comparison the final design matrix for the FIR model consisted of 15 regressors (15 timepoints for Incorrect responses during Hard trials), a regressor for the day of the scan and a regressor for the specific scan on that day (total 32 regressors). Only Hard-Incorrect responses were modelled as not all participants made errors during Easy and Medium trials.

Linear Discriminant Analysis

For each subject, the FIR time series were z-scored across regions at each timepoint. The z-scored time series underwent Principal Component Analysis (PCA), producing vectors that capture independent axes of variation. The original data were then projected onto these axes of variation and passed through a Linear Discriminant Analysis (LDA) classifier to separate out specific conditions. The initial PCA step minimizes redundant information and enforces independence between variables, improving classification accuracy and robustness (Müller et al., 2021).

There were two LDAs trained on the data: one separating Easy-Correct from Hard-Correct, and a second separating Hard-Correct from Hard-Incorrect. To have a comprehensive understanding of the classification performance, we trained the LDA across two parameter sweeps: the first across each timepoint (t = 1-15), and the second across differing number of principal components (max PCs = 40). For each of these classifiers, we evaluated performance using 5-fold nested cross-validation where folds were constrained to either contain or exclude all measurements of specific participants, as well as balanced accuracy – which is calculated as the average between specificity and sensitivity. To decide which timepoint had the best classification performance, we observed which timepoint had the highest performance (ties included) across varying number of PCs. The timepoints that had the best performance for each separation were timepoint 6 (Easy-Correct vs. Hard-Correct) and timepoint 15 (Hard-Correct vs. Hard-Incorrect). The minimum number of PCs to reach the best performance was 9 and 12 respectively. We chose up to the first 13 PCs, accounting for the minimum number of PCs required for both models to reach best performance as well as following common standard guidelines for using dimensionality reduction methods in which case we choose up to the first PC which has an added explained variance < 1% (Nguyen & Holmes, 2019). The first 13 PCs explained a total of ~44% variance. For a summary of the performance and evaluation of these models refer to Supplementary Materials 2 and 3.

The resulting two LDA separation axes were trained independently of one another, meaning that these two axes might have shared information. To enforce independence between the two LDA axes, we first normalized each LDA and then orthogonalized the axes following Gram-Schmidt procedures. By definition, as these two axes are now orthogonal, they also describe unique pieces of information from one another. To verify that this transformation has produced axes still related to the original LDA separations, we correlated these new axes (LDA_n) to the original LDA axes.

From these two LDA_n separations, we projected the original data onto these axes to see two perspectives: first the contributions of each brain region to the desired separation (spatial), and second how does this separation vary across time and conditions. To check whether these results were consistent across scales, these analyses were also reproduced in a finer parcellation, which consists of 1,000 Schaefer cortical regions, 28 cerebellar regions, and 54 subcortical regions.

Selecting Regions Important for Task Performance

From visual observation, the contributions of each brain region to each separation have clear similarities and differences (Figure 2). Through this process, the two modified maps now define distinct axes for task difficulty and Hard-Correct vs. Hard-Incorrect responses. Each brain region was plotted based off their loadings on the two LDA_n axes (Figure 3a, 3b). From this plot, we divided the regions into four quadrants: regions recruited when completing the task correctly and during harder trials (quadrant 1: top right), completing the task correctly and during easier trials (quadrant 2: bottom right), completing the task incorrectly and during easier trials (quadrant 3: bottom left), and completing the task incorrectly during harder trials (quadrant 4: top left) (Figure 3a). All future analyses only involved regions important for completing the task correctly during harder trials (quadrant 1: top right).

Estimating the Effect of Task Difficulty on BOLD Signal

Using the regions from quadrant 1 (identified previously), we can observe changes in their FIR time series across conditions. To estimate the amplitude of the BOLD signal per region, for each region, we calculated the cumulative area between the time series (curve) and $y = 0$ across all timepoints, where directionality (positive/negative) does matter. In this case, as positive and negative recruitment will cancel each other out, the total BOLD amplitude of a region from $y = 0$ across the 15 seconds is the net BOLD amplitude. Generalized linear mixed models were then fit to the data, estimating the effects of task difficulty on the net BOLD amplitude per region, controlling for repeated participants. The resulting estimates were then corrected for multiple comparisons using the False Discovery Rate (FDR) and significant regions were visualized on the brain.

Estimating Phasic Changes in BOLD Activity Through Cross-correlation

When comparing the FIR time series for Hard-Correct and Hard-Incorrect, visually there was no difference between the amplitude of the BOLD signal. To assess whether there were changes in timing of regional activity, we calculated the cross-correlation of a region's FIR time series between the two conditions. The resulting measurements describe the correlation of a region's activity between both conditions with different delays (lags) in the time series.

Brain-state Displacement and the Energy Landscape

As previously mentioned, a benefit to using the FIR model design over a traditional box-car is that we can analyse recruitment of a region at specific timepoints of a trial. Building from this idea, we can evaluate the probability of that a region is recruited (via increases in BOLD activity) using an approach introduced by Munn and colleagues (Munn et al., 2021) (code for this analysis is available at https://github.com/ShineLabUSYD/Brainstem_DTI_Attractor_Paper). The energy landscape analysis estimates the probability that a given brain state will take place. This is done by estimating the probability distribution of BOLD activity at each timepoint and inverting this value to estimate the energy required to change from one brain state to another.

In our study, we calculated the energy landscape across the participant-level estimates from the FIR model. The specific conditions we compared were activity during Hard-Correct trials, and Hard-Incorrect trials. The following steps were replicated for these two conditions. For each timepoint, the absolute value of BOLD activity across regions from quadrant 1 were isolated. We then estimated the probability distribution of BOLD activity, $P(BOLD_t)$, between 0 and 1.8 within the given window using a non-linear Kernel density estimation:

$$P(BOLD_t) = \frac{1}{0.1n}\sum_{i=1}^{n} K\left(\frac{BOLD_{t,i}}{0.1}\right)$$

Where *K* is the Gaussian kernel summed over *n* samples. This probability distribution was then converted to energy, *E*, by taking the negative natural logarithm.

$$E = -ln\big(P(BOLD_t)\big)$$

From this approach, we can describe the likelihood of time-resolved BOLD activity through the intuition of energy requirements. Highly probable BOLD activity corresponds to a low energy requirement (i.e., small E), and an unlikely BOLD activity has higher energy requirements (i.e., large E) (Munn et al., 2021).

Statistics and Reproducibility

Statistics were assessed using a combination of linear mixed models and linear discriminant classifiers. False Discovery Rate (FDR) correction was applied wherever it was appropriate. Classifiers were trained and assessed using 5-fold nested cross-validation. Behaviour and

cross-session reliability of activation within a task had previously been reported by King and colleagues (M. King et al., 2019). The final sample consisted of 24 healthy individuals (16 women, 8 men; mean age = 23.8 years, s.d. = 2.6). Participants complete two days of scanning. Each day of scanning consisted of eight imaging runs (10 min per run) with each of the 17 tasks presented once for 35 s per imaging run. In total there were 16 independent measurements of the mental rotation task per participant.

Data Availability

All imaging and behavioural data are publicly available in an OpenNeuro repository (accession number ds002105).

Code Availability

Analysis of both the behavioural and functional MRI data were conducted in MATLAB v2022b. Code required to reproduce the statistical analyses and figures are publicly available at https://github.com/ShineLabUSYD/WM_Manipulation.

Results

Behavioural Performance

Twenty-four participants (16 women, 8 men; mean age = 23.8 years, standard deviation (s.d.) = 2.6 years) completed a mental rotation task while undergoing 3T fMRI scanning (data were analysed as a sub-sample of a larger battery of tasks) (M. King et al., 2019). The stimuli consisted of a pair of three-dimensional objects, with the original object on the left and a target object on the right (Figure 1a). For each stimulus, there were three possible angles of rotation around the vertical axis that corresponded to differing levels of difficulty: 0º (no rotation, Easy), 50º rotation (Medium), 150º (Hard). Participants were tested across 2 days of scanning, with 8 scans per day (Figure 1b). Each scan consisted of a 35 s mental rotation block including 5 s instruction, 3 s per trial (total 9 trials; 3 per difficulty), and 0.33 s inter-trial interval (ITI). Order of trial difficulty was randomized between scans, with this trial order held consistent across participants. Participants underwent 3 days of training before entering the scanner and were trained on 17 different tasks (refer to King and colleagues (M. King et al., 2019) for a full list of the tasks). The training program increased in difficulty each day from focusing on single tasks (day 1) to switching between tasks (day 2), and finally a complete set of the 17 tasks to emulate the protocol used during the scanning sessions. For more details regarding the task paradigm, refer to the Methods. Behavioural performance was measured by accuracy and response time (RT) and only correct trials for these measurements were analysed. The relationship between accuracy and RT generally followed the speed-accuracy trade-off (Figure 1c).

We first investigated whether there was an effect of task difficulty on performance. We used generalized linear mixed models to estimate the relationship between task difficulty and testing day with response time and accuracy. When comparing accuracy and task difficulty, we observed a significant effect of task difficulty on accuracy (Figure 1d). Specifically, for each increase in level of task difficulty, there was a 9% decrease in accuracy ($t_{1,149}$ = -12.89, $p < 0.001$, CI = -0.12, -0.08). There was no significant relationship between the day of testing and accuracy ($p = 0.55$). When modelling the relationship between response time and task difficulty, a significant relationship was found (Figure 1e). Specifically, for each increase in level of task difficulty, the response time increased (i.e., responses slowed) by 0.26 seconds ($t_{2,906}$ = 29.27, $p < 0.001$, CI = 0.25, 0.28). There was no significant relationship found between the day of testing and response time ($p = 0.12$). From these results, there were differences in

behavioural performance across difficulties that were not related to learning across days, hence the analysis below was collapsed across both days.

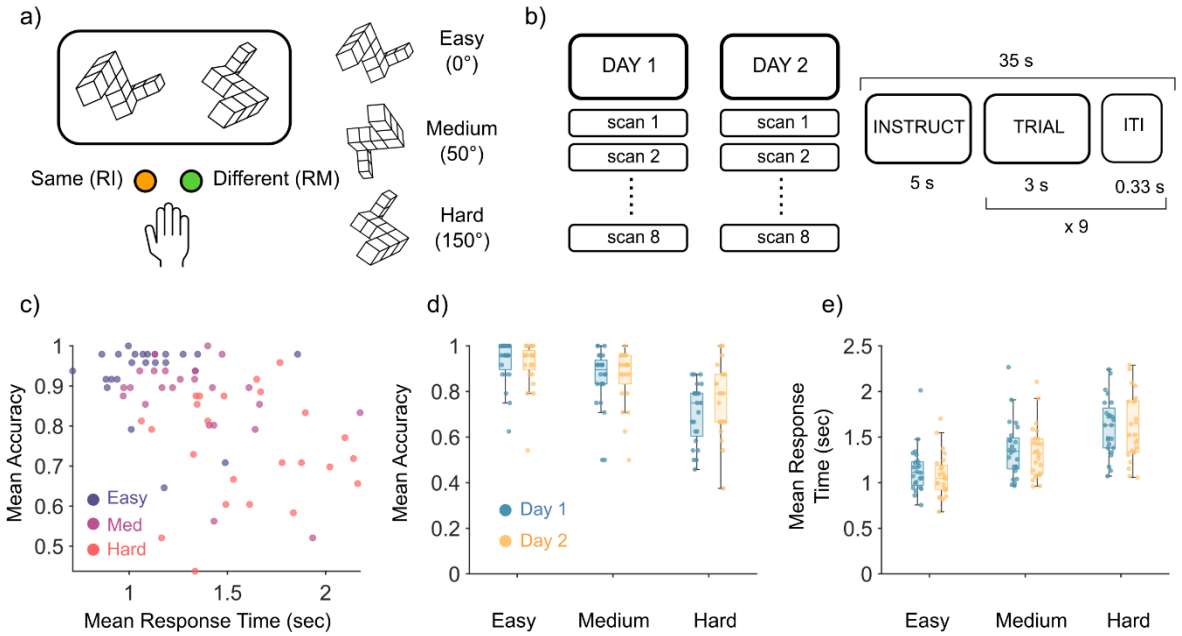

Figure 1. Mental Rotation Task and Behavioural Results. a) Mental Rotation stimuli example. Participants respond with two fingers: right middle (RM), right index (RI). Three levels of difficulty based on angles of rotation applied to the stimulus. **b)** Scanning summary with timing of trial. Each participant underwent 2 days of scanning with 8 scans per day. During each scan, the task was performed for 35 s, consisting of 9 trials as laid out. **c)** Scatter plot of mean response time plotted against mean accuracy across all difficulties. Each data point is the mean response time across all trials of that difficulty for a participant. **d)** Mean accuracy across difficulties between each day. Each data point (n = 24) is the mean accuracy of a participant. Centre line, median, box limits, upper and lower quartiles. Whiskers, 1.5x interquartile range. **e)** Mean response time across difficulties between days. Each data point (n = 24) is the mean response time of a participant.

Optimal Separation Across Trial Types Occurs at Distinct Timepoints

The fMRI BOLD data were preprocessed and parcellated into 482 regions that covered the cerebral cortex, the cerebellum and a range of subcortical structures (Diedrichsen, 2006; Schaefer et al., 2018; Tian et al., 2020). We fit a finite impulse response (FIR) model to estimate BOLD activity during a 15 second window per condition (Figure 2a), allowing us to identify signatures in the BOLD time series related to working memory manipulation. The resulting FIR time series were z-scored before undergoing principal component analysis (PCA; Figure 2b), which provides the principal components (PCs, axes) that capture the most variance of the data, as well as PC loadings which refers to the original data projected into the PCA space

(Figure 2b). We then trained linear discriminant analysis (LDA) classifiers on the PC loadings to separate out pairs of conditions (LDA_1: Easy-Correct vs. Hard-Correct; LDA_2: Hard-Correct vs. Hard-Incorrect) at each timepoint. We examined a range of PCs for each timepoint (1-40 PCs), finding that timepoint 6 (with 9 PCs) yielded the best classification for LDA_1 and timepoint 15 (with 12 PCs) yielded optimal classification for LDA_2. For the final LDA classifiers, we used the first 13 PCs (all PCs > 1% explained variance) which explained a total of ~44% variance of the data (Figure 2c). By transforming the PC loadings and the PC spatial maps into the LDA space, we can analyse and interpret how the groups were separated, both spatially and temporally. To enforce independence, the LDA axes were normalized and orthogonalized using the Gram-Schmidt procedure. The orthogonalized LDA axes (LDA_n) and the original LDA axes (LDA_1: Easy-Correct vs. Hard-Correct; LDA_2: Hard-Correct vs. Hard-Incorrect) showed a strong linear correlation (LDA_1 $|r| = 0.71$, $p = 0.0063$; LDA_2 $|r| = 0.70$, $p = 0.0072$). For details on the performance and evaluation of these models, refer to Supplementary Figure S1. Similar results were replicated using a finer parcellation including 1000 Schaefer cortical regions, 28 cerebellar regions, and 54 subcortical regions (Supplementary Figure S2).

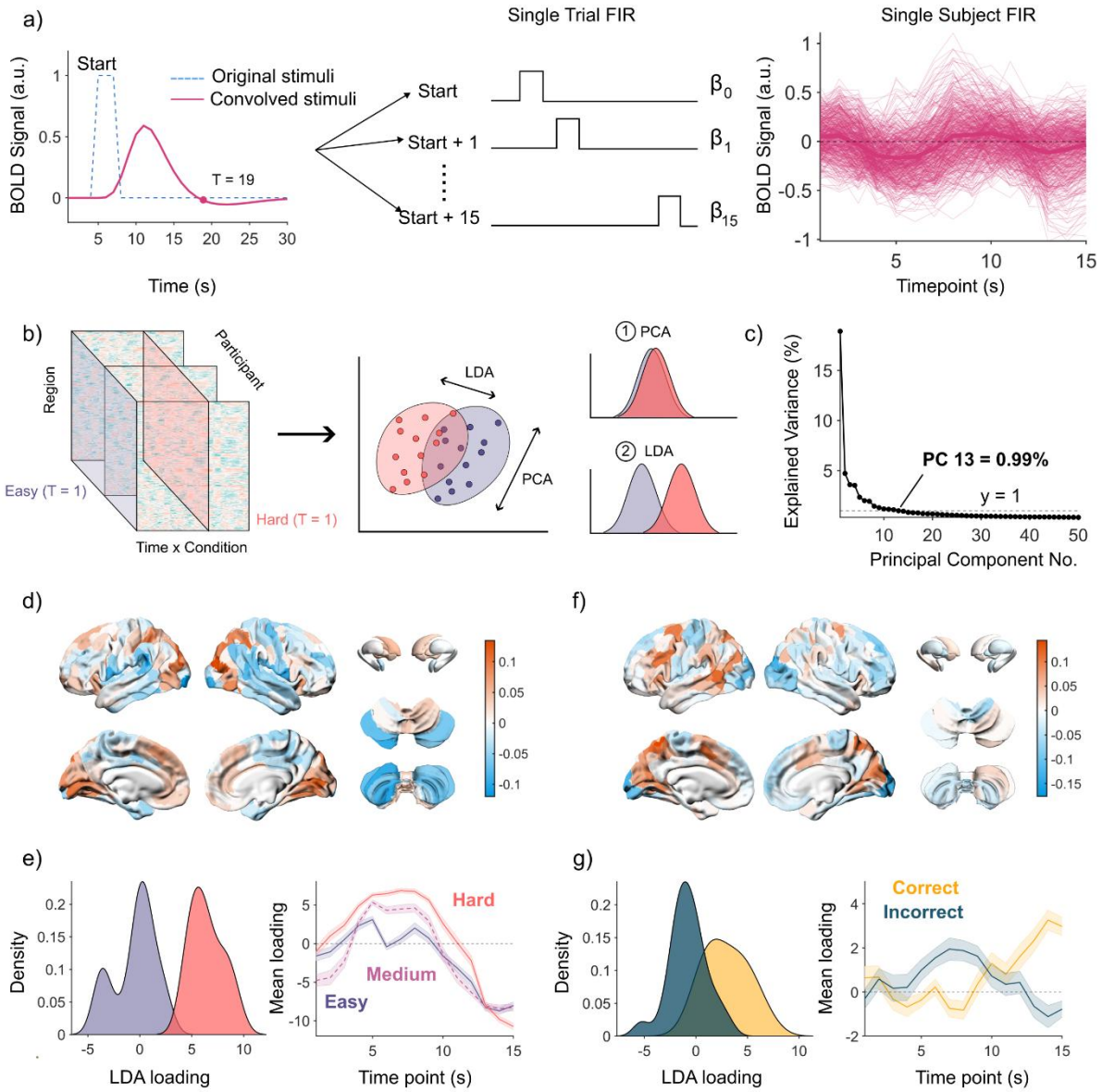

Figure 2. Neuroimaging Analysis Pipeline. a) Timing of trial (dotted blue line), and estimated timing after convolving with the hemodynamic response function from SPM12 (pink line). Example design matrix, modelling 15 timepoints per condition. Example of the beta coefficients from a single participant using the FIR design matrix, mean BOLD signal coloured by a bold line, thinner lines are individual regions (n = 482). **b)** Overview of dimensionality reduction pipeline. First the data were z-scored and underwent principal component analysis (PCA). Then the data at each timepoint in PCA space was fed into the LDA classifier with a varying number of principal components. **c)** For the final model, we used the first 13 PCs explaining a total of ~44% variance. **d)** Regions valued by their ability to separate easy vs. hard trials (orange = useful for Hard, blue = useful for Easy). **e)** Left: Distribution of Easy and Hard LDA loadings. Right: Loadings of each difficulty across the duration of a trial. Note - data were not trained on Medium trials. Mean and standard error are plotted (n = 24). **f)** Regions valued by their ability to separate Hard-Correct vs. Hard-Incorrect (orange = biased to Hard-Correct, blue = biased to Hard-Incorrect). **g)** Left: Distribution of Hard-Correct and Hard-Incorrect LDA loadings. Right: Loadings of each response across the duration of a trial. Mean and standard error are plotted (n = 24).

Distinct distributed networks of regions distinguished the Difficulty level in Correct trials (LDA_1: Figure 2d, 2e) and Performance on Hard trials (LDA_2: Figure 2f, 2g) – for a detailed list of the specific atlas labels for these regions, refer to Supplementary data 1 and 2. Importantly, LDA_1 and LDA_2 cleanly delineated these axes with an orthogonal basis set. Specifically, LDA_1 separated Easy-Correct (purple) from Hard-Correct (pink) trials (Figure 2e; right panel) in a way that showed characteristic changes over time. Specifically, during timepoints 5-10, Hard trials were easily classifiable, whereas Easy trials were uncertain (i.e., around chance performance). Importantly, even though we did not train the classifiers on data from the Medium condition, the Medium condition trials sat between Easy and Hard trials in the LDA space, underscoring the ability of the LDA classifier to distinguish task difficulty levels (Figure 2e; right panel). In contrast to LDA_1, LDA_2 clearly separated Hard-Correct (yellow) and Hard-Incorrect (blue) trials (Figure 2g; left panel). When looking at the classification across timepoints, the confidence for Hard-Correct increases from t = 10 onwards and peaks at t = 14, whereas confidence in Hard-Incorrect peaks around t = 7 before decreasing (Figure 2g; right panel). These plots demonstrate that the separation between conditions is dynamic and is dependent on specific timepoints.

Identifying Overlapping Regions Between Task Difficulty and Performance

To further explore the dynamics of Difficulty (LDA_1) and Performance (LDA_2), we mapped individual regions into LDA space (x-axis: LDA_1; y-axis: LDA_2; Figure 3a). We then separated regions into four quadrants to identify the regions that were selectively associated with Hard trials and Correct Performance, as we reasoned that this reflected the completion of the task when most challenging, while avoiding non-specific aspects of performance difficulty. In total, we observed a collection of 108 overlapping regions that best differentiated Hard trials that were also performed Correctly (Figure 3a, orange). Consistent with our original hypothesis, these regions were distributed across the whole brain, including the premotor cortex (bilateral), superior parietal lobe (bilateral), ventral- and orbitofrontal cortex (bilateral), caudate (bilateral), dorso- and ventro-anterior putamen (bilateral), hippocampus (bilateral), nucleus accumbens, and the vermis and lobule VI (bilateral) of the cerebellum (Figure 3b). For a detailed list of specific atlas labels refer to Supplementary data 3. Lateralization in these regions was present, with more regions from the left cerebral cortex compared to the right (Figure 3b). In contrast, regions more classically associated with cognitive control (such as the canonical frontoparietal

'cognitive control network') were found in the quadrant that differentiated Hard from Easy trials, but only when the trials were performed Incorrectly (Supplementary Figure S3).

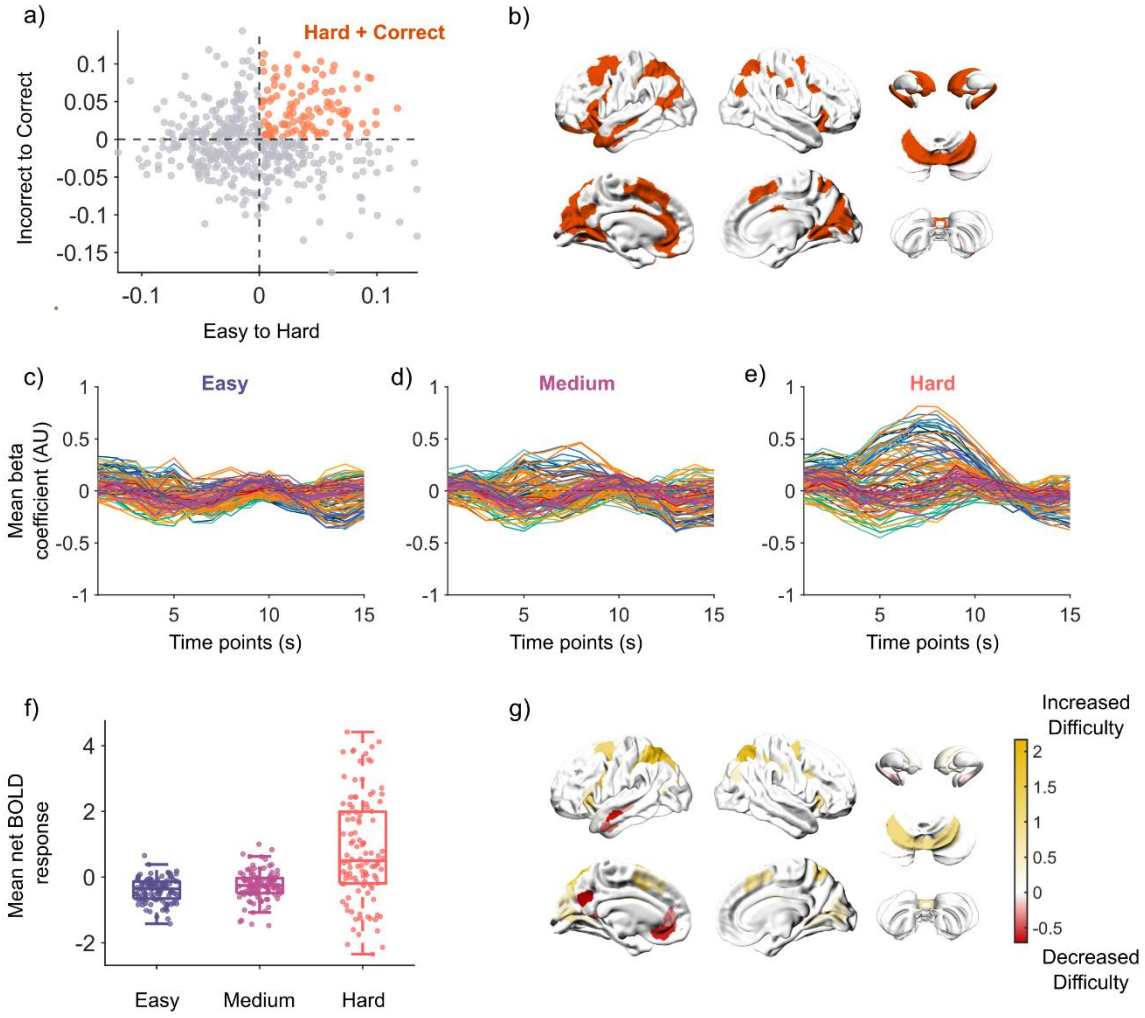

Figure 3. Effect of Task Difficulty on Regional BOLD dynamics. a) Plotting regions by their loadings on both LDA vectors (n = 482). **b)** Visualizing regions important that separate Hard from Easy, and Hard-Correct from Hard-Incorrect – detailed atlas labels for these regions are in Supplementary data 3 (n = 108). For brain visualizations of the other quadrants, refer to Supplementary Figure S4. **c-e)** Group average beta coefficients for **c)** Easy, **d)** Medium, and **e)** Hard trials. Each line is a single region, lines are coloured by the 7-Yeo resting-state networks for cerebral regions(Yeo et al., 2011), then the cerebellum, thalamus, hippocampus, basal ganglia, and other subcortical regions as separate groups. **f)** Group average net BOLD response per difficulty. Each dot is a region's net BOLD response (n = 108). Net BOLD response is calculated by measuring the area between the curve and y = 0, where direction does matter (positive and negative values cancel out). Centre line, median; box limits, upper and lower quartiles; whiskers, 1.5x interquartile range. **g)** Estimated linear relationship between net BOLD and task difficulty as measured from generalized linear mixed models after correcting for multiple comparisons (n = 108; false discovery rate $Q < 0.05$).

We employed a finite impulse response (FIR) model to obtain a time-resolved estimation of BOLD activity, which in turn allowed us to observe the effect of task difficulty within the overlapping regions across time (Figure 3c-f). Using this approach, we observed a clear increase in BOLD activity around t = 6-10 seconds as task difficulty increased, although we also noticed decreased BOLD activity in some regions preceding this window. To quantify these effects, for each overlapping region (per participant) we calculated the area between the curve and the y-axis (y = 0), which we refer to as the net BOLD response (Figure 3f). By fitting generalized linear mixed models comparing each region's net BOLD response to increases in task difficulty, we identified regions that increased or decreased in mean net BOLD response due to increasing task difficulty (Figure 3g; $p_{FDR} < 0.05$). Regions from the premotor, superior parietal lobe, medial extrastriate cortex, vermis and lobule VI of the cerebellum demonstrated increased net BOLD activity as task difficulty increased, whereas regions from the left temporal lobe, left anterior cingulate, and left inferior parietal lobe decreased in net BOLD activity as task difficulty increased.

Delayed Patterns of Activity Differentiate Between Correct and Incorrect Responses

The LDA approach also allowed us to directly compare BOLD dynamics in different trial types, which in turn facilitated unique insights. For instance, comparing the FIR time series between the Hard-Correct and Hard-Incorrect conditions, the amount of BOLD activity did not clearly differentiate the two conditions (Figure 4a, 4b). In fact, the BOLD activity during Hard-Correct appears to vary in a specific time window, whereas BOLD activity during Hard-Incorrect varies throughout the whole 15 second period. To check for changes in variation, we calculated the cross-correlation between corresponding regions of two conditions. When comparing Hard-Correct and Hard-Incorrect trials for the overlapping regions, we found that the BOLD activity of select regions were delayed during the Hard-Incorrect trials (Figure 4c; n = 68). We next asked whether these differences were unique to performance or also impacted by task difficulty. To this end, we calculated the cross-correlation between Easy and Hard (Figure 4d) and Medium and Hard (Supplementary Figure S4) trials. Based on this logic, any increases in the amount of rotation required would result in temporal variation in BOLD activity across larger windows of time. However, there was no delay effect in this comparison with all regions showing similar timing of BOLD activity (Figure 4d). The regions that were delayed in Hard-Incorrect trials included the premotor, extrastriate cortex (bilateral), left temporal lobe, left

anterior cingulate, left caudate, putamen (bilateral), hippocampus (bilateral), vermis and lobule VI (bilateral) of the cerebellum (Figure 4e). These results suggest that there were temporal changes driving participants to complete the task successfully, independent of changes due to task difficulty.

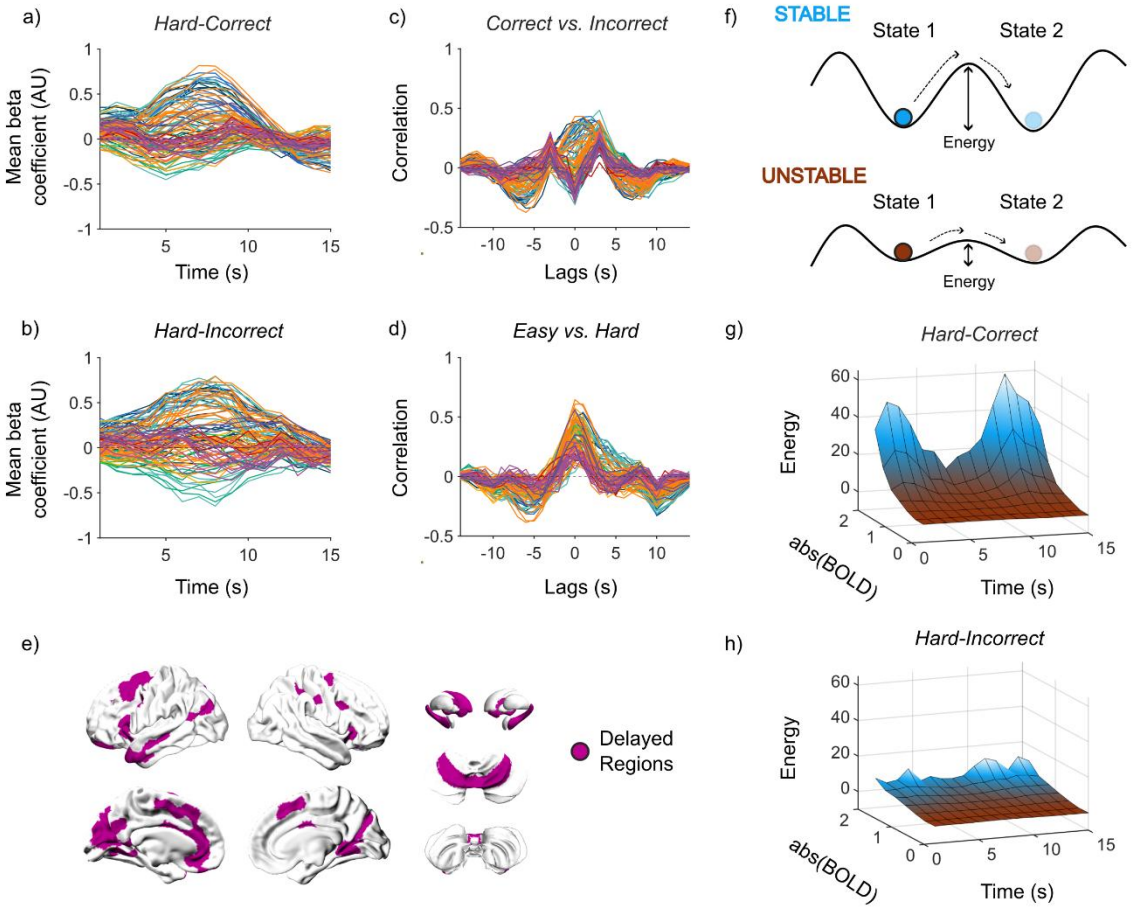

Figure 4. Cross-correlation of Corresponding Regions Between Hard-Correct and Hard-Incorrect. a) Group average beta coefficients for Hard-Correct trials (n = 108). **b)** Group average Beta coefficients for Hard-Incorrect trials (n = 108). **c)** Cross-correlation of corresponding regions between Hard-Correct and Hard-Incorrect. **d)** Cross-correlation of corresponding regions between Easy and Hard trials. **a-d)** Each line represents a single region and is colored by the 7-Yeo resting-state networks for cerebral regions, then cerebellum, thalamus, hippocampus, basal ganglia, and other subcortical regions as separate groups. **e)** Regions (n = 68) that were delayed by 3 s as seen from **c)**. **f)** Schematic describing the intuition behind the attractor landscape analysis. The analysis estimates the probability that an event will occur (i.e. a specific brain state), and this value is then transformed into the energy requirement for the state to occur - greater energy requirements incur a lower probability, while lower energy requirements incur a higher probability. **g)** Attractor landscape for the delayed regions in Hard-Correct trials (n = 68). **h)** Attractor landscape for delayed regions in Hard-Incorrect trials (n = 68).

Another perspective of temporal changes in BOLD activity is attained by observing variance in the BOLD signal, specifically high variance has been linked to cognition, socioemotional measures, and aging(Garrett et al., 2011; Grady et al., 2023; Grady & Garrett, 2014). One way of measuring variance is through the lens of the energy landscape analysis (refer to Methods for details on this analysis) (Munn et al., 2021). This approach reframes neural time series according to the overall 'state-space' of potential changes that can occur in the data. Through this analysis, we can quantify how much energy (where energy is inferred via the relationship between probability and energy in statistical physics) is associated with a specific brain state (Figure 4f). By observing the probability of different brain states (high and low BOLD activity), we gain insights into how variable the BOLD signal was across time. To this end, we investigated the probability that a region is recruited or suppressed at each timepoint – measured by the absolute value of BOLD activity. During Hard-Correct trials, between t = 5-10 there is decreased energy requirements (increased probability) for large amounts of BOLD activity to occur (Figure 4g). Outside of this window, there is a high energy requirement (low probability) of BOLD activity to occur. This contrasts with Hard-Incorrect trials, in which lower energy was required for greater BOLD activity across all timepoints (Figure 4h). While there was still a slight increase in energy requirements outside of the t = 5-10 window, it was lower compared to Hard-Correct trials (Figure 4h). These results suggest that successful completion of the task is dependent on increasing variance of BOLD activity at specific moments in time.

Discussion

In the current study, a mental rotation task was used to probe how the brain manipulates working memory. Through a combination of a finite impulse response (FIR) model and linear discriminant analysis (LDA), we identified a distributed set of regions spanning the cerebral cortex, cerebellum, and basal ganglia that were important for completing the task correctly during trials of higher difficulty. By probing the temporal dynamics expressed within these regions, we identified unique spatial and temporal characteristics for each condition. Separation between the conditions (Easy vs. Hard, Correct vs. Incorrect) was sensitive to specific timepoints during a trial. Increasing the angle of rotation (increased difficulty) was associated with an overall increase in the BOLD response for regions in the premotor cortex, parietal lobe, and cerebellum, accompanied by decreased BOLD response in the anterior and posterior

cingulate cortices and the hippocampus. Hard-Correct and Hard-Incorrect trials showed temporal differences in BOLD response; namely, there was a delayed response in Hard-Incorrect trials compared to Hard-Correct trials in regions from the premotor, medial extrastriate, anterior cingulate, cerebellum, and basal ganglia. Furthermore, the BOLD activity during Hard-Correct trials was more precise – that is, large amplitudes of BOLD activity at specific timepoints, compared to the less constrained BOLD activity during Hard-Incorrect trials. Overall, these results confirm that the manipulation of working memory involves precise recruitment of a distributed network (spanning across the cerebral cortex, basal ganglia, and cerebellum), and advances our understanding of temporal changes in BOLD recruitment during working memory manipulation.

The notion that manipulation of working memory extends beyond the cerebral cortex has been slowly gaining traction (Bolkan et al., 2017; Christophel et al., 2017; Gao et al., 2018; Nyberg & Eriksson, 2016; O'Reilly & Frank, 2006; Stein, 2021). However, understanding the specific contributions of each element in such a distributed network is difficult. In this study, by analysing fMRI BOLD measurements of working memory manipulation, we identified regions beyond the cerebral cortex such as the vermis, lobule VI of the cerebellum, caudate, putamen, nucleus accumbens, and hippocampus. These regions have been implicated across working memory studies (Borders et al., 2022; Tomlinson et al., 2014) but have not been featured in current working memory frameworks (Christophel et al., 2017; Nozari & Martin, 2024; Nyberg & Eriksson, 2016). For example, the vermis and lobule VI of the cerebellum have previously been associated with a range of motor and cognitive functions such as visual working memory, motor planning, and tasks requiring the active maintenance of information (Koziol et al., 2014; Stein, 2021). These functions are possible due to connections from frontal and posterior parietal areas (R. M. Kelly & Strick, 2003; Ramnani, 2012), both of which have previously been implicated in non-motor functions such as working memory (Diwadkar et al., 2000) as well as regions important for task execution such as the premotor and motor cortices (R. M. Kelly & Strick, 2003). Furthermore, with the significant role of the cerebellum in learning skills and automaticity (Caligiore et al., 2019; Doyon et al., 2003; Shine & Shine, 2014), it is possible that after extensive training in mental rotation (as is the case in the current study), the cerebellum aids in developing a comprehensive model of how to mentally rotate objects (Leiner et al., 1986; Stein, 2021; Tomlinson et al., 2014). Hence, proficient working memory manipulation may be achieved through cortico-cerebellar interactions.

Similar to the cerebellum, the basal ganglia are underappreciated in existing working memory manipulation frameworks. The basal ganglia have previously been associated with habituation, reward, and learning processes (Caligiore et al., 2019; Yin & Knowlton, 2006), however much of the discussion around the basal ganglia has focused exclusively on the circuitry involving the thalamus, and cerebral cortex (Y. Wang et al., 2021). The basal ganglia – specifically, the putamen and caudate (striatum) are also disynaptically connected with the deep cerebellar nuclei (Bostan & Strick, 2018). These connections may guide the cerebellum toward specific goals and outcomes (Bostan & Strick, 2018; Caligiore et al., 2019). Previously, the striatum has been associated with the cortico-cerebellar network during motor planning (Doyon et al., 2003). The evidence in the present study suggests that not only does cerebellar function generalize for all action planning (both motor and non-motor), the involvement of the basal ganglia also serves an important role in general action planning. Our results complement and expand on previous findings (Ben-Yehudah et al., 2007; Brissenden & Somers, 2019; Deverett et al., 2019; Hautzel et al., 2009; Hayter et al., 2007; Luis et al., 2015; McDougle et al., 2022; Ravizza et al., 2006; Tomlinson et al., 2014; Vandervert et al., 2007) by linking cerebellar and subcortical activity to behaviour, highlighting that recruitment of these regions is important for both task difficulty and correct responses. Therefore, working memory manipulation requires a distributed network that spans beyond the cerebral cortex, involving regions from the cerebellum and basal ganglia.

Expanding current frameworks to include cerebellar and subcortical contributions may have broader implications for treating cognitive function deficits. Mental rotation and working memory manipulation are required for various cognitive functions which are impaired across diseases and disorders (Deverett et al., 2019; Lewis et al., 2003; McDougle et al., 2022; S. Park, 1992). In some cases, deficits in either the striatum and cerebellum were associated with decreased performance in working memory manipulation (Deverett et al., 2019; Lewis et al., 2003; McDougle et al., 2022). The current study focused on healthy, young adults. It is likely that there are both similarities and differences in cognitive deficits caused by Parkinson's disease and cerebellar degeneration, and cognitive deficits in a healthy cohort. Therefore, while the results in this study complements working memory literature, future studies should apply similar techniques to investigate neural changes in diseases with working memory deficits.

Execution of working memory manipulation involves both activation and deactivation of specific brain regions. Typically, in task fMRI studies, the focus is on regions that are recruited or increase in BOLD activity during the task condition. However, suppression or inhibition of

specific brain regions is also important for task execution (Constantinidis et al., 2002; Nashef et al., 2022). In our study, along with the increased recruitment of the regions discussed above, there was a decrease in BOLD activity for regions typically associated with the default mode network, and the hippocampus. BOLD activity in the default mode network typically increases during resting-state and has been linked to self-reflection, autobiographical memory, and memory (Raichle, 2015; Spreng & Grady, 2010). In working memory, the default mode network and hippocampus have both been associated with maintaining information (Borders et al., 2022; Čeko et al., 2015). In contrast to the manipulation of working memory, maintenance is a repetitive process that involves holding information over a period with minimal changes to the information (D'Esposito et al., 1999; Nyberg & Eriksson, 2016). The decreased BOLD activity in the default mode network and hippocampus could be related to the general suppression of these task-negative regions; however, in the context of working memory, these results also point to a difference in neuronal processes between working memory manipulation and working memory maintenance. This would add extra insights into the discussion about maintenance versus manipulation of working memory which is currently focused on differences in frontal and prefrontal regions (Davis et al., 2018; D'Esposito et al., 1999). Hence, suppression of regions from the default mode network and hippocampus is important for task execution and may distinguish between maintenance and manipulation of working memory processes.

The FIR model teases apart temporal differences in BOLD response, providing a unique perspective on fMRI data. The results from the FIR model and accompanying temporal analyses revealed a temporal precision in regional BOLD time series which was present only when completing the task correctly. Specifically, there was a distributed network of regions that were delayed in recruitment during hard and incorrect trials. These results demonstrate that the difference between completing the task correctly and incorrectly was driven by timepoint-specific changes, rather than whether a region was recruited or not. In the context of this study, participants were highly trained on the task, such that incorrect responses were more likely to be caused by an unsuccessful completion of the task rather than confusion. This questions the validity of including temporal basis functions in fMRI analyses, and whether recent, more complex models with temporal functions could perhaps tease apart unique temporal changes in the data (Brunton et al., 2016). Therefore, the use of temporal basis functions in fMRI analysis may provide unique insights into temporal dynamics of BOLD activity and future

studies could perhaps explore the nuances behind adding different temporal basis functions, finding a balance between minimal constraints and over-fitting parameters to the data.

Proficient working memory manipulation is dependent on the precise recruitment of brain regions. Psychological descriptions of how our brain processes information suggest a continuous relationship between how much an object is rotated and how much rotation our brain processes (Ganis & Kievit, 2015). For example, for a visual rotation if the brain is mentally rotating the stimuli (as the task name suggests) to match each other, then the larger the rotation required, the more rotation the brain needs to process. However, from our study, using a basic measure of correlation, between Medium and Hard trials there were no changes in temporal patterns. Furthermore, when comparing Hard-Correct and Hard-Incorrect trials, recruitment of specific regions was delayed. A possible explanation is that contrary to intuition, the brain is solving the task by loading a model of mental rotation (M. Ito, 2008; Leiner et al., 1986; Wolpert et al., 1998). Therefore, under well practiced conditions, rather than visually rotating the stimuli, participants already know the possible reconfigurations based on previous experience. This coincides with the current results, as the regions presented have previously been associated with action planning and memory (Koziol et al., 2014; Stein, 2021). Hence, there would be no relationship between angles of rotation and temporal changes as the approach of this network remains constant regardless of the angle of rotation. Overall, these results expand on previous findings suggesting temporal changes that may influence mental rotation performance.

One key limitation of the current study is the temporal resolution of fMRI. The scanning paradigm used in this study sampled the BOLD signal every second (TR = 1), which may not be sufficient to capture the fast timescale at which mental rotation processes could occur. If mental rotation operates on a sub-second scale, future research employing techniques with higher temporal resolution, such as EEG, could provide valuable insights. The task requires several cognitive steps: stimulus recognition, information processing (mental rotation), and decision-making. Given that participants were well-trained, it is likely that the information processing stage was automated, with response time delays primarily reflecting decision-making (Shine & Shine, 2014). While prior work suggests that increased mental rotation is associated with a positive relationship between response time and task difficulty (Wager & Smith, 2003), one limitation of the present work is that we cannot differentiate between the various stages of processing. Future studies could improve this design by incorporating a more nuanced task that isolates these processing stages, allowing for a clearer distinction between

automated and controlled cognitive processes while still maintaining some resemblance to the real-world. Other considerations include how the results can generalize across different cohorts (older adults, patient cohorts) and different strategies of working memory manipulation (e.g. reordering or updating information). Working memory deficits in older adults and patient cohorts may be different to deficits observed in a young, healthy cohort like the one in our study. Specifically, it is possible that deficits in older adults and patients may be due to an inability to recruit brain areas that contribute to working memory manipulation (Deverett et al., 2019; Ravizza et al., 2006). Furthermore, neural signatures underlying working memory manipulation can vary depending on the modality (spatial, verbal) and cognitive processes required (manipulating, updating, storage and retrieval) (Wager & Smith, 2003). Overall, questions remain regarding how well the current results generalize across cohorts and working memory processes which can be addressed with complementary methods and improvements in task design and data collection.

In summary, our results demonstrate that mental rotation as an example of working memory manipulation involves a distributed network consisting of regions beyond the cerebral cortex such as the cerebellum and subcortex. Current frameworks of working memory manipulation can be biased to the cerebral cortex with minimal discussion about the possible roles of the cerebellum and subcortex. However, these regions are underappreciated and are associated with working memory manipulation. Using time-resolved model estimations of BOLD activity of regions both from and beyond the cerebral cortex, we found that regions from the cerebellum and subcortex contribute both in terms of the amount of BOLD activity, as well as the temporal patterns during a mental rotation task. These findings suggest an alternative approach to how our brain processes information and underscore the broader role of the cerebellum and subcortex in higher cognitive functions.

Acknowledgements

The authors acknowledge the University of Sydney HPC service at The University of Sydney for providing HPC resources that have contributed to the processing of the data contained within this data collection. JBT and AGB were funded by the Research Training Program Stipend (SC3227, SC3229). JMS was funded by the Australian Research Council (DP240101295) and the National Health and Medical Research Council (GNT1193857). CO was funded by the Australian National Health and Medical Research Council Fellowship (2016866) and the University of Sydney Robinson Fellowship. EJM was funded by the Discovery Early Career Researcher Ward (DE250100540). GB was funded by the Canadian Institutes of Health Research (MFE193920).

Author Contributions

Conceptualization: JBT, JMS

Methodology: JBT, IFO, AGB, BRM, CO, EJM, JMS

Investigation: MK

Formal Analysis: JBT

Visualization: JBT

Writing—original draft: JBT, JMS

Writing—review & editing: JBT, IFO, CW, AGB, BRM, GB, MK, CO, EJM, JMS

All roles and responsibilities of the co-authors were agreed on.

Competing interests:

Authors declare that they have no competing interests.

Chapter 2 Summary

In Chapter 2, we explored the underlying macroscale pattern for working memory manipulation through a mental rotation task. We showed that mental rotation was driven by a distributed network involving cerebral, subcortical and cerebellar regions. Specifically, a network involving premotor and temporal cerebral regions, the caudate and hippocampus, and lobule VI of the cerebellum had a delayed response during incorrect trials compared to correct trials.

This first empirical chapter serves as the foundation for showing cerebellar involvement in cognitive automaticity. Mentally rotating objects is an automatised skill that we use throughout our lives. Not only did we show that the cerebellum relates to cognitive load of mental rotation, but it also distinguishes between correct and incorrect responses alongside a distributed network of brain regions. The specific cerebellar lobule involved (lobule VI), is typically associated with motor planning functions (M. King et al., 2019), but we show that lobule VI also serves an important role in mental rotation, extending its associated functions to overall action planning.

In Chapter 3, we move to a sensorimotor adaptation task to understand how automatised behaviours can be developed to be flexible or inflexible. Our questions in this chapter are focused on adaptation, which we believe similarly to action planning generalises across both motor and cognitive domains. Specifically, we ask what brain network facilitates adaptive performance, and how do different learning approaches result in different learning outcomes.

Chapter 3

The Engagement of the Cerebellum and Basal Ganglia Enhances Expertise in a Sensorimotor Adaptation Task

Joshua B. Tan[1], Eli Müller[1,2], Andrii Zahorodnii[3], James M. Shine[1,2]

Author affiliations:

1 Brain and Mind Centre, School of Medical Sciences, Faculty of Medicine and Health, University of Sydney, Sydney, Australia

2 Centre for Complex Systems, School of Physics, University of Sydney, Sydney, Australia

3 Massachusetts Institute of Technology, Boston, MA, USA

DISCLAIMER: Due to amendments made during the thesis submission phase, some empirical chapters may slightly differ in content compared to the online published versions.

Chapter 3 of this thesis is published as: Tan, J. B., Müller, E., Zahorodnii, A., & Shine, J. M. (2024). The engagement of the cerebellum and basal ganglia enhances expertise in a sensorimotor adaptation task. *Imaging Neuroscience*, *2*, 1–20. https://doi.org/10.1162/imag_a_00271.

Abstract

The ability to adapt to changes in the environment is essential for skilled performance, especially in competitive sports and events, where experts consistently perform at the highest level, rapidly adapting to unpredictable conditions. Current studies have identified cortical-cortical interactions between the premotor and primary motor cortex during expert performance, however while these interactions are important for planning and execution, our understanding of the mechanisms underlying learning, feedback and adaptation remain unclear. Subcortical structures, such as the cerebellum, have dense connections with the cerebral cortex through which they provide precise topological constraints that could putatively play a crucial role in fast, accurate task execution. To test this hypothesis, we tracked cortical, subcortical, and cerebellar BOLD activity during a visuomotor rotation task in which participants executed a visual cue-driven, ballistic motor task across three conditions: at baseline; following a 45^{o} clockwise motor rotational perturbation; and then within a follow-up (washout) condition. We observed increased recruitment of primary visual, basal ganglia, and cerebellar regions that robustly covaried with fast, accurate performance across all conditions (baseline, rotation, and washout). Tracking individualised performance across participants, we observed three distinct groups: experts (consistently fast and accurate), adapters (initially poor with improvement to expert-level), and non-adapters (initially good but ultimately poor performance). The experts and adapter groups demonstrated performances that were robust to changes in conditions and were more variable in their neural signatures between trials, whereas the performance of non-adapters decreased with changes in conditions and were characterised by less variable neural signatures. These results aligned with the tenets of differential learning theory. To establish the validity of our interpretation of these whole-brain signatures and behavioural patterns, the neuroimaging results were reproduced by training recurrent neural networks representing each group and analysing their resultant activity patterns. Together, these results provide evidence for cerebellar and basal ganglia contributions to expertise in adaptation and suggest a possible connection between variable brain patterns and robust performance.

Introduction

A defining characteristic of expertise is the ability to adapt – to perform at high levels across multiple scenarios including surprising and novel situations (Bransford & Schwartz, 1999; Cheung & Kulasegaram, 2022). At high levels of sports (e.g., tennis), adaptation is crucial. For instance, an athlete (such as a tennis player) has to adjust to perturbations caused by environmental factors (e.g., effects of wind and temperature on ball trajectories) or from the opposing player (e.g., different types of spins on the ball). Similarly, adaptation is important in cognitive tasks, including tasks that require translating skills from one situation to another (e.g., playing a game of chess after losing a Queen). However, between individuals, there can be differences in how fast one adapts to changes as well as what strategies are used to adapt (I. Schollhorn, 2012; McDougle et al., 2016; Taylor & Ivry, 2011). Hence adaptation is a complex skill applicable in both physical and mental activities, and understanding how to optimally adapt would lead to improved performance and expertise.

Understanding the neural correlates of actions both physical and cognitive is inherently difficult. Within a single action, multiple processes are undertaken – both sequentially and in parallel – however to isolate specific sub-components of actions, experimental tasks are often designed in order to isolate a specific event. Furthermore, with limitations in signal strength during standard neural recordings, experimental tasks can range from being so simple that the specific function that is isolated bears no resemblance of the desired action; to so complex that the new task requires the execution of an entirely new movement. Motor adaptation tasks offer a work-around, in that they accurately simplify natural behaviours through tasks that anyone can perform, while still modifying a participant's performance by altering specific task rules without changing the difficulty of the task (Krakauer, 2009; Tsay et al., 2022). There are numerous versions of motor adaptation tasks that evoke different sensory adaptations, such as visuomotor rotations (Areshenkoff et al., 2022; Krakauer, 2009; Perich et al., 2018) and force-field perturbations (Perich et al., 2018; Perich & Miller, 2017). Importantly, these tasks have been performed during simultaneous functional neuroimaging (Areshenkoff et al., 2022; Perich et al., 2018; Perich & Miller, 2017), and can also be decoded using neural networks (Pemberton et al., 2022). By consolidating findings across modalities and techniques, an understanding of how the brain adapts to changes in the environment can be attained. Thus begs the questions, how might the brain reconfigure its activity to mediate effective adaptation?

In the past decade, both technological and methodological advances have improved our understanding of adaptation in the brain, however a comprehensive understanding of how the brain as a whole learns to adapt to perturbations remains unclear. The current motor learning literature has a strong focus towards the cerebral cortex and cortical-cortical interactions, with the consensus approach highlighting how primary motor regions change with learning and with different inputs (Churchland et al., 2006, 2012; Gallego et al., 2020; Perich et al., 2018). As the relationship between primary motor regions and movement dynamics remain unchanged during adaptive behaviour (Perich & Miller, 2017), connections between primary motor regions and other cerebral cortical regions (such as the premotor cortex) may serve an important role in adaptive learning. However, these cortical-cortical interactions are unable to capture the complete scope of motor learning, such as how the brain as a whole processes error feedback (O. Cohen et al., 2017; Prut et al., 2001) and the decrease in cortical regions over the duration of a task (Bassett et al., 2015; Berlot et al., 2020b). Furthermore, premotor and motor regions share connections with numerous other subcortical structures of the brain such as the basal ganglia, thalamus, and cerebellum (R. M. Kelly & Strick, 2003; Middleton & Strick, 1994; Shine, 2021). Perhaps most damning for cortico-centric hypotheses is that much of the motor cortex can be surgically removed in expert mice, without an observable decline in performance (Kawai et al., 2015; Wolff et al., 2022). Hence, a cerebral cortico-centric focus on motor learning and adaptation does not justify the complexity of the anatomical connections within the brain nor explain the wide variations in behaviour.

Although the basal ganglia has long been associated with the execution of habitual behaviours (Graybiel & Grafton, 2015; Yin & Knowlton, 2006), there are other subcortical structures – such as the cerebellum (Gilbert & Thach, 1977; Rotondo et al., 2022) – that are well-suited to facilitate adaptive behaviour, but have not received sufficient theoretical attention. Consisting of more than 50% of the total neurons in the whole brain (Wagner et al., 2019; Zagon et al., 1977), the cerebellum has a repeated, modular structure that integrates the cerebellar cortex with the cerebral cortex, both via inputs (via the cortico-pontine-cerebellar system) and outputs (via the cerebello-thalamo-cortical circuits) (Albus, 1971; Koziol et al., 2014; Nashef et al., 2018), as well as with the spinal cord (Albus, 1971; O. Cohen et al., 2017; Zinger et al., 2013). The modular structure of the cerebellum allows for compartmentalisation of unique inputs (Hayter et al., 2007; Kostadinov & Häusser, 2022), the learning and execution of complex, nested sequences of input-output patterns (Khilkevich et al., 2018), as well as more complex, multi-domain functions like parallel processing (Müller et al., 2023). Furthermore, the

cerebellum has also been linked to pattern separation and feed-forward predictions, akin to a forward model for effective motor control (Bastian, 2006; Imamizu & Kawato, 2009; Ramnani, 2014; Stein, 2021; Wolpert et al., 1998). These functions play pivotal roles in adaptation and learning, as pattern separation allows the brain to disentangle similar actions from each other, and feed-forward mechanisms facilitate rapid learning, however to date, few studies have investigated this systems-level perspective in adaptation tasks. Feed-forward mechanisms or the anticipation of movement outcomes has previously been linked with learning an internal model of the task – where the internal model refers to encoding the task in the brain (e.g. understanding how a tennis racquet would move when your arm moves) (Imamizu et al., 2000b; Wolpert et al., 1998). In adaptation paradigms, the cerebellum has been suggested to serve a role in developing and storing internal models through implicit learning and error feedback (Doyon et al., 2003; Doyon & Benali, 2005; Hikosaka et al., 2002; Imamizu et al., 2000b; Mazzoni & Krakauer, 2006; Tseng et al., 2007). Importantly, both lesioning of the cerebellum (Sendhilnathan et al., 2024) and patients with cerebellar ataxia (Morton & Bastian, 2006) resulted in impaired adaptation specifically learning in-between trials (Tzvi et al., 2022). Hence, the cerebellum facilitates learning in adaptation by contributing important functions such as pattern separation and feed-forward predictions.

Another key subcortical structure involved in adaptation and learning are the basal ganglia (Foerde & Shohamy, 2011; Lanciego et al., 2012) which are a small group of nuclei with internal inhibitory connectivity and a modulatory (GABAergic) role controlling thalamic firing (Nambu, 2008; Wilson, 2013). The basal ganglia are also disynaptically connected with the cerebellum (Bostan & Strick, 2018; Todorov et al., 2019), though the precise interplay between these two structures remains somewhat enigmatic. Therefore, approaching expertise and adaptation from a systems-level perspective that involves interactions between the cerebellum, basal ganglia and cortical regions would enable better adjustments to perturbations and increase the speed of learning.

Here, we analyse BOLD fMRI patterns within the cerebral cortex, cerebellum, and basal ganglia during a sensorimotor adaptation task to determine the relationship between these structures following a perturbation to the sensorimotor contingencies inherent within the task (i.e., a 45° rotation to cursor movements). We hypothesised that increased performance in the adaptation task would be associated with an increased response within the cerebellum and basal ganglia. To tackle the inter-individual differences during learning, we compared differences between trials using a data-driven clustering approach. Based on differential learning theory

(Frank et al., 2008), we predicted that variation in strategies during learning would drive inter-individual differences, with individuals that had more variation during learning adapting faster to perturbations. Finally, we created a simple recurrent neural network model to test the validity of this predicted mechanism. Overall, our results provide important evidence to support distributed cortico-cerebellar circuits in sensorimotor adaptation.

Methods

Participant demographics

Forty right-handed individuals between the ages of 18 and 35 (mean = 22.5, SD = 4.51; 13 males) participated in the study and received financial compensation for their time. Data from eight participants were excluded due to either head motion in the MRI scanner (N = 4; motion greater than 2 mm or 2º rotation within a single scan) or their inability to learn the rotation task (N = 4). The final dataset consisted of 32 participants. Right-handedness was assessed with the Edinburgh handedness questionnaire (Oldfield, 1971). Participants' written, informed consent was obtained before commencement of the experimental protocol. The Queen's University Research Ethics Board approved the study, and it was conducted in accordance with the principles outlined in the Canadian Tri-Council Policy Statement on Ethical Conduct for Research Involving Humans and the principles of the Declaration of Helsinki ("World Medical Association Declaration of Helsinki," 2013). Data was obtained from a previous study (Standage et al., 2023) and is available on the *OpenNeuro* repository (accession number ds004021).

Study Design

Participants performed hand movements directed toward a target by applying a directional force onto an MRI-compatible force sensor (ATI technologies) using their right index finger and thumb. Once directional force was applied, there was no ability to adjust directions until the next trial began. The target and cursor stimuli were rear-projected with an LCD projector (NEC LT265 DLP projector, 1024 × 768 resolution, 60 Hz refresh rate) onto a screen mounted behind the participant. The stimuli on the screen were viewed through a mirror fixed to the MRI coil directly above participants' eyes, thus preventing participants from being able to see their hand. The force sensor and associated cursor movement were sampled at 500 Hz.

This experiment used a well-established VMR task (Krakauer, 2009) to probe sensorimotor adaptation. To start each trial, the cursor (20-pixel radius) appeared in a central start position (25-pixel radius). A white target circle (30-pixel radius) appeared at one of eight locations (0°, 45°, 90°, 135°, 180°, 225°, 270°, 315°) on an invisible ring around the central position (300-pixel radius) and filled in (white) following a 200 ms delay. Participants then applied a directional force on the sensor resulting in the cursor being launched towards the input direction. Once launched, the cursor would travel the 300-pixel distance to the invisible ring over a 750 ms period (with a bell-shaped velocity profile) before becoming stationary at the ring to provide participants with end-point error feedback. End-point error feedback is provided by the target white circle changing colours. If the cursor overlapped with the target to any extent, the target would become green, signifying a target 'hit', and if there was no overlap the target would remain white. Each trial was separated by 4 s and within this period, participants had 2.6 s from target presentation to complete the trial (including the 200 ms target delay, participants' own reaction time, and the 750 ms cursor movement; any remaining time was allotted to providing the end-point error feedback) (Figure 1A). At 2.6 s the trial was ended, the screen was blanked, the data saved, and participants would briefly wait for the next trial to begin. Reaction times were not stressed in this experimental procedure. On trials in which the reaction time exceeded 2.6 s, the trial would end, and the participant would wait for the next trial to begin.

Data collection occurred across two days in order to observe both the initial learning (first day) and learning retention (second day). For each day, 120 baseline trials (15 sets of eight trials) were completed without a rotation of the cursor. Following these trials, 320 learning trials (40 sets of eight trials) were completed, wherein a 45° clockwise rotation of the cursor was applied. The baseline and learning trials were completed during one continuous fMRI scan. Following this scan, conditions were restored to baseline (i.e., no rotation of cursor) in a separate scan and participants performed 120 washout trials allowing participants to de-adapt before relearning on the second day. Within each set of eight trials, the white target circle can appear in one of eight locations without replacement. In addition to these VMR-related task components, there were also three 6 min resting-state fMRI scans interspersed prior to, between, and following VMR learning and washout. During these resting-state scans, participants were instructed to rest with their eyes open, while fixating a central cross location presented on the screen. The total testing time was 75 min on each testing day (including setup time) with the baseline and rotation scan taking ~30 min, and the washout scan lasting ~9 min (see Supplementary

Materials for breakdown of this timing). For our analyses, we only focused on the first day of testing as we were concerned with the initial learning and adaptation.

Behavioural processing

The absolute angle error between the target and final cursor position (RE), and the time taken to make a response (RT) were measured for each trial (Fig 1B). The angle error was measured as the angle between the initiated direction and the optimal path to the target where positive values mean that the initiated direction was clockwise to the optimal path, and negative values mean that the initiated direction was anticlockwise to the optimal path. To ignore the direction of the error and only consider the amplitude of the error, we took the absolute value of the angle error. Based on the distribution of RT, response times greater than 2 s and less than 0.3 s were removed (the latter was removed due to not being reproducible - could be due to anticipation) (Figure 1B). RE greater than 100 were removed and could be due to participants sending the cursor in the wrong direction (Figure 1B). Corresponding fMRI data related to the removed trials were also excluded. For each participant, their RT was plotted against RE to visually demonstrate learning.

The RT and RE of each trial were z-scored and combined by addition to create a Balanced Integration Score (BIS) (Liesefeld et al., 2015; Liesefeld & Janczyk, 2019) (Figure 1C). Compared to the original BIS score, which measures the number of correct responses, our dataset tracked the angle error (distance of cursor from centre of the target). Therefore, rather than subtracting RE from RT, we have added them together. Note that the BIS score was flipped (multiplied by -1) to make interpretation more intuitive, wherein higher scores are indicative of better performance in the task (and *v.v.* for lower scores). The BIS score was calculated across all trials and conditions to retain between-condition effects. If BIS was calculated per condition, each condition would have the same mean value of 0 therefore eliminating any significant effects between conditions (Liesefeld & Janczyk, 2019). In our study, the participants learned at different rates and reached different levels of "expertise" in the task. To control for this variation, we only included participants that reached a final performance above a certain threshold ($BIS \geq 0$), where the final performance was defined as the average BIS score across the final set of eight trials during the washout scan (Figure 1C). Performance during washout was used to control for participants that learned during the rotation condition but were unable to de-adapt when the task rules were reset. To make sure that the thresholding captured

participants that adapted to both the rotation and washout conditions, the BIS scores across trials for each subject was visualised. For the rest of this article, we've separated the trials by their condition e.g. Baseline condition has no rotation on the cursor, Rotation includes trials with the 45º rotation, and Washout includes trials with no rotation after the learning (Rotation) trials.

To compare differences between early and late performance within each condition, the mean BIS score was calculated for the first (early) and last (late) sets of each condition (Baseline: Sets 1 & 15; Rotation: Sets 16 & 55; Washout: Sets 56 & 70) for each participant. For each condition, a paired sample t-test was used to compare participants' early performance against their performance in the last set of trials (Set 1 vs. Set 15; Set 16 vs. Set 55; Set 56 vs. Set 70). While we are using an adaptation task, it is still important to check that task difficulty is similar across conditions, otherwise we would be unable to rule out differences due to cognitive load. To compare task difficulty, a one-way ANOVA was used to compare final performance across the three conditions (Set 15 vs. Set 55 vs. Set 70).

Imaging Acquisition

Participants were scanned using a 3T Siemens TIM MAGNETOM Trio MRI scanner located at the Centre for Neuroscience Studies, Queen's University (Kingston, Ontario, Canada). For each participant on each day, a T1-weighted ADNI MPRAGE anatomical (TR = 1760 ms, TE = 2.98 ms, field of view = 192 mm × 240 mm × 256 mm, matrix size = 192 × 240 × 256, flip angle = 9°, 1 mm isotropic voxels) was collected. fMRI volumes were acquired using a 32-channel head coil and a T2*-weighted single shot gradient-echo echo-planar imaging acquisition sequence (TR = 2000 ms, slice thickness = 4 mm, in-plane resolution = 3 mm × 3 mm, TE = 30 ms, field of view = 240 mm × 240 mm, matrix size = 80 × 80, flip angle = 90°), and acceleration factor (integrated parallel acquisition technologies) = 2 with generalized auto-calibrating partially parallel acquisitions reconstruction. Each volume comprised 34 contiguous (no gap) oblique slices acquired at a 30° caudal tilt with respect to the plane of the anterior and posterior commissure, providing whole-brain coverage of the cerebrum and cerebellum. For each resting-state scan, 180 imaging volumes were collected. For the baseline and learning epochs, we collected a single, continuous scan of 896 imaging volumes. For the washout scan, we collected one scan of 256 imaging volumes. Each scan included an additional eight imaging

volumes at both the beginning and the end. All imaging and behavioral data are publicly available in an OpenNeuro repository (Standage et al., 2023, accession number ds004021).

Pre-processing

Neuroimaging data was in BIDS format and was pre-processed with fMRIprep version 21.0.2 (https://fmriprep.org/en/stable/#), a standard pipeline that incorporates toolboxes from the gold-standard preprocessing software in the field. *fMRIPrep* involves the basic pre-processing steps (co-registration, normalisation, unwarping, noise component extraction, segmentation, skull-stripping etc.) and produces a report for quality checking at each step. See Supplementary Material for a full description of each step. Regression of twelve head motion artifacts, and the average combined whiter matter, CSF signal was conducted using custom python scripts, with a high-pass filter set at 0.01. Mean BOLD signal time-series data were extracted from the fMRI data for 400 Schaefer cortical regions (Schaefer et al., 2018), 28 cerebellar regions (SUIT atlas; Diedrichsen, 2006), and 26 basal ganglia regions (Tian et al., 2020) using custom python scripts. The following atlases were chosen as robust parcellations that reveal meaningful neurobiological features, with parcels that cover regions from the cerebral cortex, subcortex and cerebellum which we believe to be involved in expertise and adaptation (de Reus & van den Heuvel, 2013; Diedrichsen, 2006; Khilkevich et al., 2018; Schaefer et al., 2018; Tian et al., 2020). All code is available on https://github.com/ShineLabUSYD.

General Linear Model Design

Due to the thresholding of behavioural data in Methods 2.3 (0.3 s < RT < 2 s; RE < 100), we only considered BOLD data with corresponding behavioural data that passed this thresholding. If the behavioural data did not pass these criteria, then the BOLD data of the trial was removed. Due to this thresholding, there was an unequal number of trials per participant.

For each of the remaining trials, we have the timing for when the trial begins (onset time). Following event-related fMRI designs, the onset time for each trial was convolved with the hemodynamic response function (HRF) to approximate the blood flow during a trial (Chee et al., 2003; Friston et al., 1999). In the original dataset, there was no jittering of onset time (consistent trial timing) and the amount of time between trials was less than 10 s, hence there was a consistent overlap of convolved onset times between adjacent trials resulting in temporal

blurring of the BOLD activity. In order to guarantee that the BOLD information of each trial was independent of each other trial, we adopted a finite impulse response (FIR) model to select non-overlapping estimates of trial-by-trial BOLD response (Bai et al., 2007; Glover, 1999). Specifically, by taking advantage of the fact that for each trial the behavioural data was thresholded to 2 s (see Methods 2.3 for rationale) and that the imaging sequencing captured BOLD data every 2 s (TR = 2 s), we can select a single imaging volume from the time-series that captured BOLD activity during the task response. Aligning the BOLD time-series to the convolved onset time allowed for the selection of a single imaging volume per trial that contained independent task-related information and took into consideration the delay in activity response as estimated by the HRF (imaging volume at the peak of the convolved onset time) (Figure 1D).

This collapsed time-series data consisting of peak BOLD measurement was used for the rest of the analyses. Due to the previous removal of trials, the number of remaining trials per participant were unequal. To normalise the number of trials per participant, from each set of eight trials, four trials that met the criteria above were randomly sampled without replacement resulting in a total of 280 trials per participant across baseline, rotation, and washout. To account for variation in results due to random sampling we conducted 100 iterations of the random sampling. The mean and standard deviation for cortical, basal ganglia, cerebellar time-series, and BIS were plotted to check for large differences between iterations. The first iteration was chosen as the sample dataset for future analyses.

A general linear model (GLM) was fitted with BIS score as the explanatory variable, and the peak BOLD time-series as the outcome variable. This GLM was fitted for each ROI time-series (400 cortical, 28 cerebellar regions) of each participant as a 1st level analysis. For group-level analysis (2nd level), significance testing for each region was calculated via a one-sample t-test. Group-level results were calculated for the BIS score and visualised on the brain.

$$ROI\ timeseries \sim BIS$$

A similar GLM was constructed using RT and RE instead of BIS for the explanatory variables. Group-level analysis results were generated via a one-sample t-test and visualised on the brain. Participant-level beta coefficients for RT and RE were averaged and correlated against the group average BIS beta coefficients. To check whether the relationships between BIS and brain

regions changed between conditions, a GLM was fitted with BIS divided per condition and the associated peak BOLD time-series. The group average beta coefficients across conditions were correlated against one another. To see whether the BIS brain map was driven by individual participants, the dataset was split roughly in half (n = 12, n = 11). Following a hold-out approaches (Dear et al., 2024), by splitting the initial data into smaller sub-datasets (groups) we can evaluate the robustness of the results by seeing how similar the results are across the two groups. Each group had the BIS beta coefficients generated by fitting a GLM with BIS against the peak BOLD time-series (as done above), and the group-level significant testing for each region conducted via a one-sample t-test. The similarity of the thresholded brain map for each group was compared against one another using Pearson's correlation. To check whether these results are consistent across scales, these analyses were also reproduced in a finer parcellation which consists of the 1000 Schaefer cortical regions, 28 cerebellar regions, and 26 basal ganglia regions. All comparisons were calculated using Pearson's correlation and significance of all correlations were evaluated through spin-permutation testing for cerebral cortical regions.

$$ROI\ timeseries \sim RT + RE$$

Comparison with Neurosynth database

The initial GLM results were surprising as we did not expect primary motor regions to decrease in BOLD activity with performance. As an exploratory analysis and to check whether the BIS brain map was similar to what has been reported in the literature, we compared the BIS brain map against probabilistic fMRI atlases from the neurosynth database version 7 (https://github.com/neurosynth/neurosynth-data). Neurosynth is a meta-analytic tool that synthesises results from more than 15,000 published fMRI studies and generates brain maps where for each voxel, there is an estimated probability that a given cognitive process is associated with activation at that voxel across the studies. The Neuroimaging Meta-Analysis Research Environment (NiMARE; Salo et al., 2022) was accessed and probabilistic whole-brain probabilistic maps for 400 neurosynth topics containing terms clustered via a latent Dirichlet allocation (LDA) topic model were downloaded and extracted using custom python scripts. The Pearson's correlation was used to measure the similarity of the BIS brain map with each of the 400 neurosynth topics. Each topic was then ranked based off how similar or

dissimilar they were to the BIS brain map. It is important to note that while the neurosynth database can reproduce robust meta-analytical maps, the selection criteria of studies using topics/terms results in a broad collection of studies which may or may not be comparable with the specific task analysed in this study.

K-means Clustering and Inter-trial Correlations

Individual performance and learning were heterogenous across participants. K-means clustering – a non-supervised clustering algorithm (Hartigan & Wong, 1979) – was used to cluster the participants into distinct sub-groups based off their BIS scores across all conditions. Using BIS scores across all conditions allowed us to group participants by overall trends in performance and not be driven by standout performance in a specific condition. We ran *k*-means clustering from $k = 2–22$ for 100 iterations per level, *k*. To check for cluster similarity across iterations, the adjusted mutual information (AMI; (Vinh et al., 2009, 2010; Vinh & Epps, 2009) was calculated at each *k*. The smallest number of clusters that had the highest AMI across iterations was used for further analyses ($k = 3$).

From differential learning literature, participants that attempt different strategies during learning demonstrate better performance (I. Schollhorn, 2012). In our dataset, for each trial we have a static snapshot of the peak BOLD response in the brain for each trial. Using these data, the average BOLD response was calculated for each cluster. To check whether participants were repeating the same action or trying different strategies, we correlated the average BOLD response for each individual trial with every other trial for the baseline and rotation conditions. To compare strategies between clusters, a two-sample Kolmogorov-Smirnov test was used to determine whether the distribution of correlation values between the clusters came from the same sample.

Brain-state Displacement and the Energy Landscape

In order to evaluate inter-trial changes in BOLD activity, we utilised an approach introduced in Munn et al., 2021 (code for this analysis available https://github.com/ShineLabUSYD/Brainstem_DTI_Attractor_Paper). The energy landscape analysis estimates the likelihood that a given brain state will change to another distinct brain state within a given time window. Changes between brain states are calculated using the mean-

squared displacement (MSD; the mean squared difference between 2 periods of time), with greater differences between brain states resulting in a higher MSD value. We then estimate the probability distribution of MSD values and invert this value to estimate the energy required to change from one brain state to another.

In our study, we calculated the energy landscape during the rotation condition for each group cluster separately. For each cluster, we calculated the energy landscape during the first half of the rotation trials and the second half of the rotation trials. The squared displacement of BOLD activity was calculated across all regions between all trials (t_0 to t_0+t) within a given window (first half, second half). We then averaged across regions resulting in a single MSD value per trial in the window, $< >_r$ is the mean across regions. To control for bias towards specific trials, we calculate the MSD of BOLD activity at one trial against all other trials within the window. As our dataset involves learning, to control for temporal structure and learning effects we randomly shuffle the order of trials within a window 100 times (100 permutations) and combine the MSD calculations for all permutations together.

$$MSD_{t,t_0} = \langle \left| x_{t_0+t} - x_{t_0} \right|^2 \rangle_r$$

We then estimated the probability distribution of MSD values, $P(MSD_t)$, between 0 and 10 within the given window using a Gaussian kernel density estimation.

$$P(MSD_t) = \frac{1}{0.1n} \sum_{i=1}^{n} K\left(\frac{MSD_{t,t_0(i)}}{0.1}\right)$$

This probability distribution was then converted to energy, *E*, by taking the negative natural logarithm.

$$E = -ln(P(MSD_t))$$

From this approach, we can describe the likelihood of changes in BOLD activity through the intuition of energy requirements. Highly probably relative changes in BOLD (calculated by MSD) corresponds to a low energy requirement (i.e., small E), and an unlikely change in BOLD has higher energy requirements (i.e., large E) (Munn et al., 2021).

Recurrent Neural Network Modelling

The RNN was trained on two conditions: a no rotation context where the network reproduces the input direction, and a rotation context, where the network reproduces the input direction + 90°. For training, only the output of the network during the last 100 timesteps (when the go cue comes on) is used in the loss function.

For the first 10 timesteps of the task (corresponding to 100 ms), the direction-selective input neurons are active, providing the network with information of the start direction. Throughout the first 10 timesteps, and also the subsequent 60-timestep delay period, a "task context" input is either active (equal to 1) or inactive (equal to 0), signalling to the network that the context is to rotate or not rotate the input, respectively. After the first 70 timesteps, all inputs turn off, and instead a "go cue" input turns on (equals to 1), signalling to the network that it's time to output the direction. This go cue period persists for 100 timesteps, after which the trial is finished.

The dynamics of simulated neurons for the recurrent neural network were governed by the standard continuous-time RNN equation and discretised using the Euler method.

$$\tau \frac{dx}{dt} = -x + W^{rec} f(x) + W^{in} I + b$$

Where tau was set at 100 ms. The firing rate of each neuron, f(x), was related to its total input x through a rectified *tanh* nonlinearity, f(x) = max(0, tanh(x)). All RNNs in this paper contained 100 recurrent units, with the results being largely insensitive to network size. Each of the 100 neurons in the RNN received input from all other neurons through the recurrent weight matrix W^{rec} and also received external input, I(t), through the weight matrix W^{in}. Firing rates were linearly combined to produce the output y(t) according to $y = W^{out} * f(x)$. The task input and distractor (Figure 6) were modelled with 100 direction-selective neurons, as described by Teich and Qian (2003); the outputs were modelled with sin and cos functions. During training, all directions (0-360º) were used for the input and distractor.

With the following architecture, three networks were trained with backpropagation initialised from a random initialization and optimized for 3,000 training steps with Adam in Pytorch, with a learning rate of 0.0001. Networks were trained with square loss.

$$W^{in} = \frac{N(0,1)}{\sqrt{N_{neurons}}}, W^{rec} = \frac{N(0,1)}{\sqrt{N_{neurons}}}, W^{out} = 0$$

Two of the networks were trained either on a baseline condition (no rotation) or rotated condition (90º rotation). The third network was trained equally on both the baseline and rotation conditions, with the designated condition randomly sorted during training. Task condition was controlled by the "task context".

The energy landscape was calculated from the outputs of the networks, considering all timesteps leading to the go cue (first 70 timesteps of the task – direction input and first delay). The output signal was two-dimensional (sin and cos). MSD was calculated at adjacent timesteps. The MSD of all trials in a given task condition were concatenated to obtain the final probability mass function. This probability was converted to energy by taking the natural logarithm of the inverse probability.

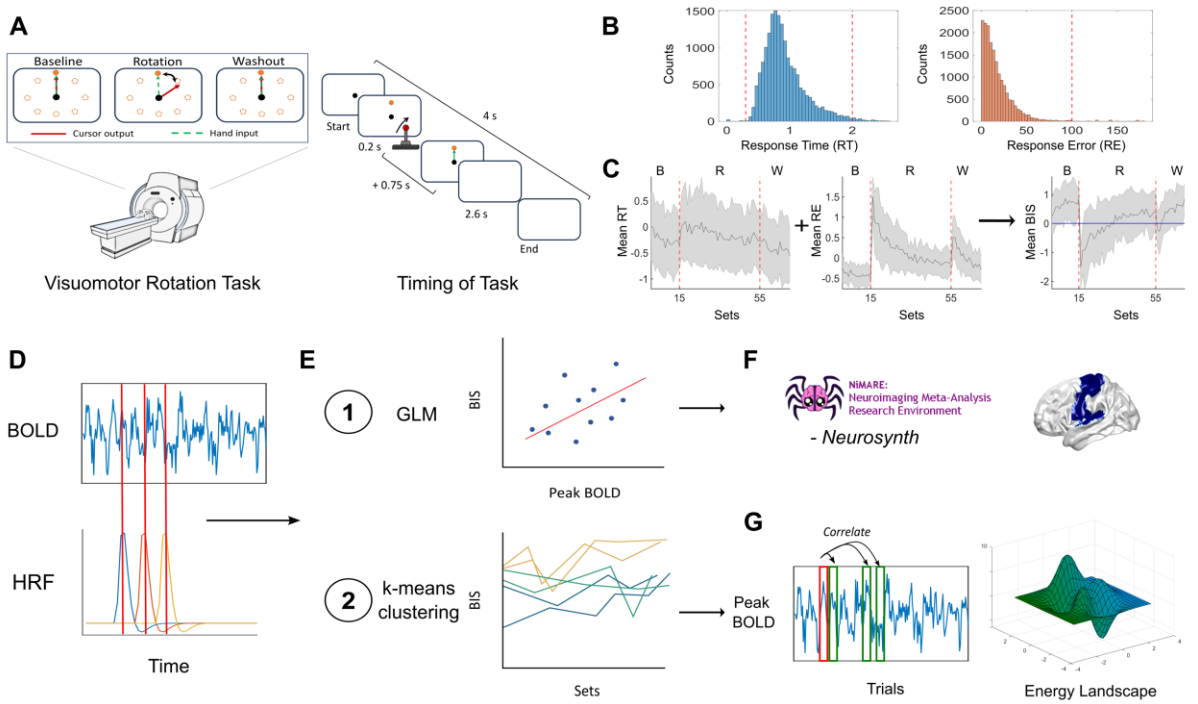

Figure 1 Summary of methods. A. Task design including the three conditions, timing of stimuli and response. B. Thresholding of behaviour measurements. C. Calculation of balanced integration score (BIS), and selection of individuals that completed the task competently. D. Matching the trial onset time convolved by the hemodynamic response function (HRF) with the BOLD timeseries (peak BOLD). E. General linear model (GLM) fitting BIS to peak BOLD timeseries for each participant. K-means clustering was applied using the BIS scores. F. Comparing the generated brain map from the GLM with topics from the neurosynth database. G. Analysing variance and inter-trial changes in brain responses using correlation and energy landscape analyses.

Results

Behavioural Data

To check whether the thresholding of our cohort appropriately selected participants that improved during the task, we compared performance both within and across the three task conditions (baseline, rotation, and washout). There was no significant difference between final performance across conditions from the one-way ANOVA ($F = 2.39$; $p = 0.099$; Figure 2B). Using paired sample t-tests, we then compared changes in performance from the first and last set of each condition (Baseline = Set 1 vs. Set 15; Rotation = Set 16 vs. Set 55; Washout = Set 56 vs. Set 70). During all conditions, the participants demonstrated significant improvement in performance. In baseline, there was an average increase of 0.755 in BIS score ($t = -4.366$; $p = 0.002$; Figure 2C). During the rotation condition, participants demonstrated the most improvement with an average increase of 2.147 in BIS score ($t = -10.956$; $p < 0.001$; Figure 2D), and during washout there was a significant increase of 0.963 in BIS score ($t = -6.342$; $p < 0.001$; Figure 2E). These results demonstrate that any differences in neural correlates related to performance were due to learning and not differences in task difficulty.

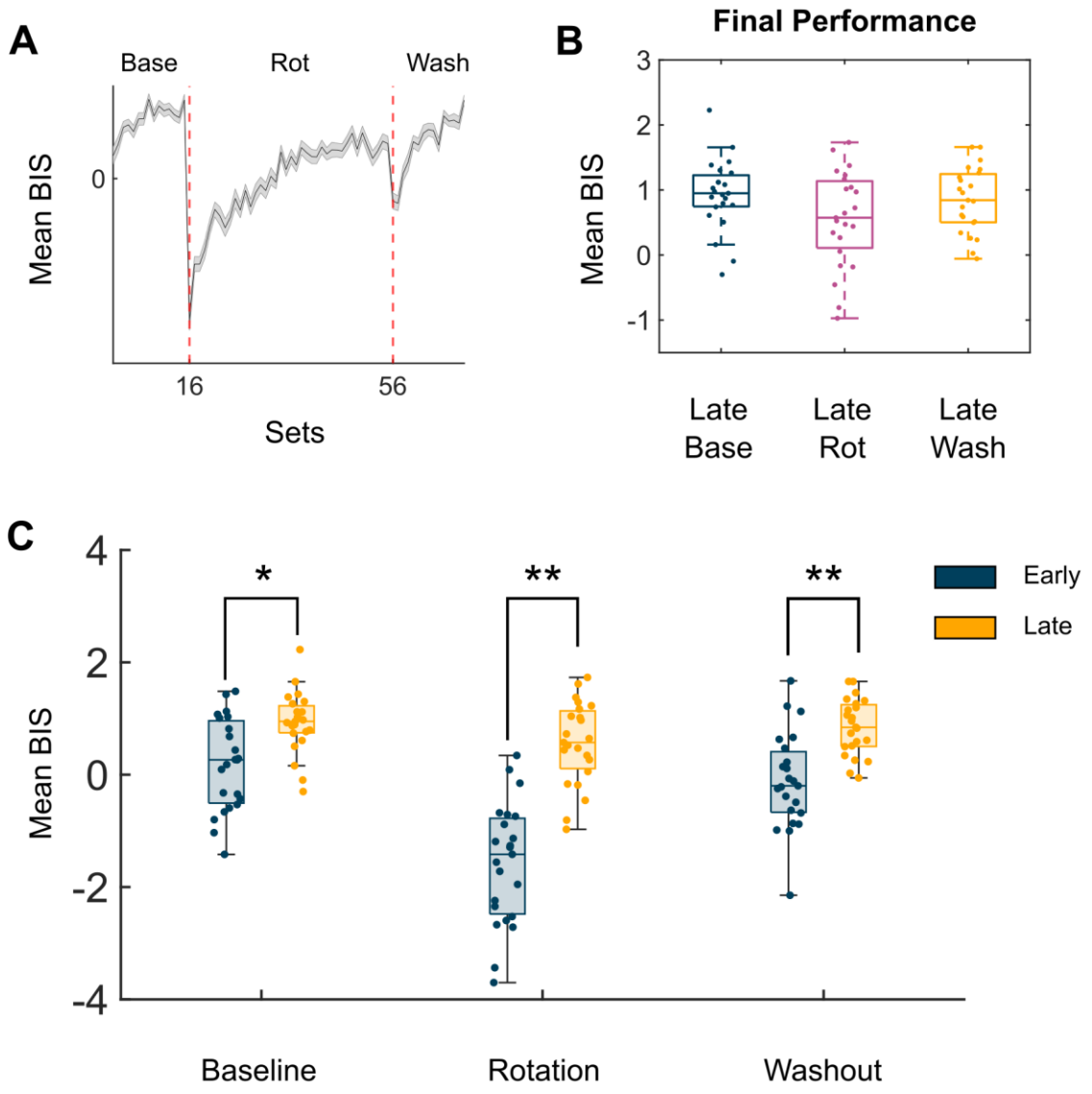

Figure 2 Comparison of behavioural scores within and across conditions. A. Mean balanced integration score (BIS) across 100 random samples of the data. Standard deviation is plotted as the shaded error bar. Dotted red lines indicate the start of a new condition (16 = rotation, 56 = washout). Base = Baseline, Rot = Rotation, Wash = Washout. B. Boxplots of BIS scores for participants during the final set of trials (n = 4) for each condition. C. Boxplots of BIS scores for participants during the first and final set of trials for each condition. Blue boxplots are for the first set, and orange boxplots are the final set. * notes a significant different $p < 0.05$, ** notes a significant difference $p < 0.01$.

Improved Performance is Associated with Recruitment of Cerebellar and Basal Ganglia Regions

A group average was calculated from the peak BOLD response for all participants (n = 23) across all trials (n = 280) and visualised on a 3D surface (Figure 3A). During the task, regions

that produced a positive BOLD response included sensory areas such as the primary motor, somatosensory, and extrastriate cortices. Control regions such as the medial frontal lobe, temporoparietal junction, inferior temporal lobe, and posterior cingulate cortices, as well as regions from the right Crus I and II, and left semilunar lobule from the cerebellum (Figure 3). Regions that had a negative BOLD response included sensory regions from the primary visual, lateral motor, and lateral somatosensory cortices. Other regions that produced a negative BOLD response included the inferior frontal lobe and medial prefrontal cortex. There was also a negative BOLD response in lobules I-V of the cerebellum, as well as the head of the caudate nuclei and nucleus accumbens in the basal ganglia.

After fitting the peak BOLD response to BIS in a general linear model (GLM), a one-sample t-test was used to create a thresholded group map (Figure 3B bottom panel; $p < 0.05$). Regions that increased in BOLD with improved performance included the primary visual cortex, right Crus I of the cerebellum, and the right putamen. Regions that were associated with worse performance included regions from premotor, primary motor and somatosensory cortices, the superior parietal lobe, ventrolateral prefrontal cortex, head of the caudate nuclei, and lobule V on the right hemisphere of the cerebellum. The following results suggest that better performance was mainly driven by increased BOLD in basal ganglia and cerebellar regions, accompanied by a decreased dependence on primary motor and somatosensory regions. Refer to Table 1 in the Supplementary Materials for a detailed breakdown of the significant regions and their coefficient estimates from the GLM model.

Balanced Integration Score Retains Features of Both Response Time and Response Error

The BIS group map was compared to group maps fitted with RT and RE in the GLM. From these maps, the regions that were associated with worse performance in the BIS map were due to participants taking longer to respond (Figure 3B, top panel), and regions that were associated with better performance were mainly driven by participants becoming more accurate with the task (Figure 3B, middle panel). Furthermore, calculating the correlation between beta coefficients for RT and RE against BIS, there were strong anticorrelations between the beta coefficients (Figure 3C; $r = -0.78$, $p < 10^{-10}$; $r = -0.74$, $p < 10^{-10}$, respectively). These results demonstrate that the BIS score successfully captured the key aspects from RT and RE and is a useful measure of expertise. The BIS scores and BOLD responses were divided into four conditions (baseline, early rotation, late rotation, and washout). Each condition was fit to the

peak BOLD response in a GLM. The beta coefficients for each condition were then correlated against the other conditions. All conditions were strongly correlated to each other, with the correlation between baseline and late rotation having the strongest correlation (Figure 3D; $r = 0.7$, $p < 10^{-10}$). All brain map correlations underwent spin-permutation testing for the cortical regions and all comparisons were significantly different ($p_{spin} < 2 \times 10^{-5}$).

Expertise Brain Maps are Robust to Individuals and Parcellation Effects

After dividing the dataset in half and fitting each group to their expertise scores in two separate GLMs, the average beta coefficients were compared between the two groups. The beta coefficients of the two groups were strongly correlated (Figure 3E; $r = 0.67$, $p < 10^{-10}$), providing evidence that these results were not driven by individual participants. To control for parcellation effects (Arslan et al., 2018), we reproduced the above analyses using a finer parcellation that consisted of 1000 Schaefer cortical nodes, 28 SUIT cerebellar regions, and 26 basal ganglia regions. From these analyses, the results were similar to the current results. For more details on these analyses refer to the Supplementary Materials.

Expertise Brain Maps are Anticorrelated with Motor Maps Derived from Meta-analyses

We generated an expertise (i.e., BIS) brain map from performance in a visuomotor rotation task and compared this brain map against 400 topics from the *Neurosynth* database (Salo et al., 2022; Yarkoni et al., 2011). From these comparisons, the top 5 strongest correlated topics were the *"substantia nigra"* (218), *"loss/gain"* (151), *"scenes/places"* (68), *"temporal"* (293), and *"voices/vocal"* (301). While these topics were the strongest positive correlations, they were relatively weakly correlated ($r < 0.2$; Figure 3F, top panel). The top 5 anti-correlated topics were *"finger tapping"* (140), *"hands/foot"* (232), *"movement/motor"* (176), *"motor cortex/sensorimotor"* (116), and *"tool/objects"* (168). In contrast to the positive weights, these topics were strongly anti-correlated ($r > 0.5$; Figure 3F, bottom panel). Overall, the *Neurosynth* comparisons suggest that the BIS map generated is not similar to regions mentioned in the literature and is in fact opposite to regions described in the majority of motor task studies.

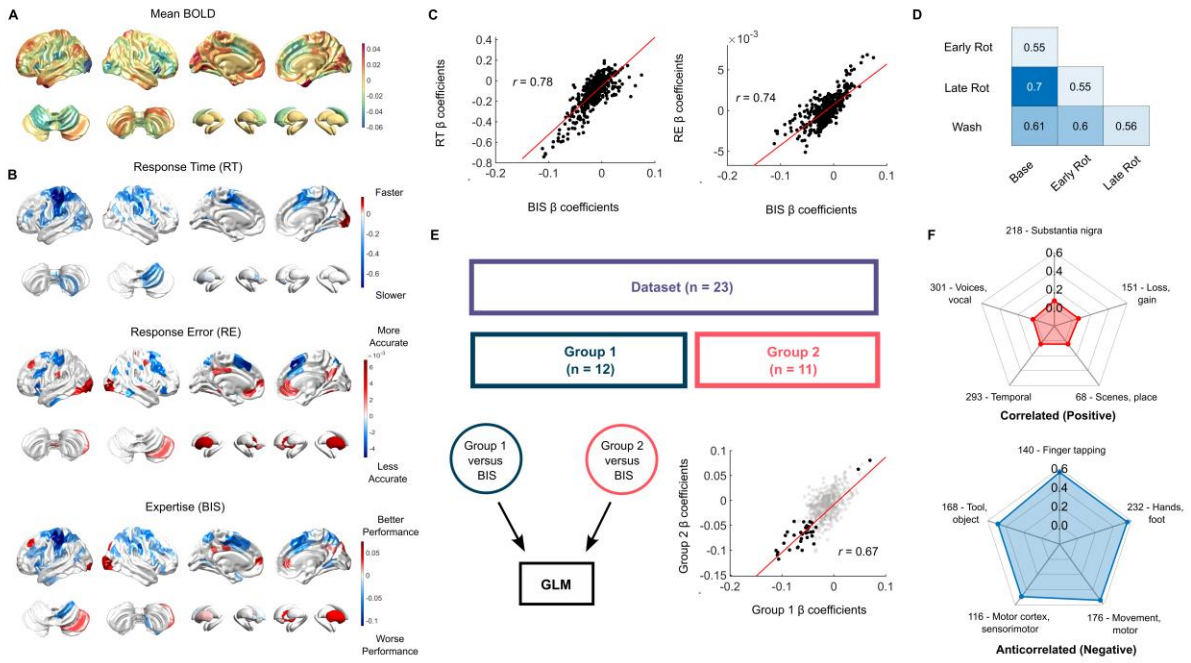

Figure 3 Summary of findings and validation of brain maps from general linear modelling. A. Average BOLD activity across all participants. B. Thresholded 2nd level group beta maps from general linear models for response time (RT), responses error (RE), and the balanced integration score (BIS). C. Pearson's correlation comparing the beta coefficients of BIS against RT and RE separately. D. Pearson's correlation of BIS beta coefficients across conditions, where rotation has been separated in half into two sub-conditions (baseline, early rotation, late rotation, washout). E. Validation of individual bias by splitting the dataset into two groups and correlating the beta coefficients for BIS of each group. F. Top 5 positive and negative correlations of the BIS brain map with the *Neurosynth* LDA-400 topics.

K-means Clustering on Performance Reveals Three Distinct Performance Groups

As an overview for how performance as a whole changed throughout the task, we correlated the group average BIS scores across sets (Figure 4A). From these correlations, it was apparent that performance in baseline could predict performance during rotation, however, did not predict performance during washout. To better understand these results, we applied k-means clustering on the BIS scores to check for any distinct sub-groups and calculated the adjusted mutual information (AMI) to select an appropriate number of clusters. From checking the AMI between iterations for each cluster size, $k = 3$ (Figure 4B) was the smallest number of clusters that were robust across iterations. Our dataset can then be characterised by three clusters (Figure 4C): a major cluster (experts; n = 16) characterised by high performance across all conditions and two minor clusters; one consisting of participants who had worse performance with each change in task condition (non-adapters; n = 3), and one consisting of participants

who started out the worst but improved and demonstrated similar performance to the expert cluster during washout (adapters; n = 4). While there were a small number of participants in the two minor clusters, the number of clusters (k = 3) has been chosen after generating 100 iterations for values of from k = 2 to k = 22 and finding the cluster size with the highest similarity across iterations (AMI). These results suggest that the two minor clusters drive the anticorrelated performance between trials for baseline and washout, as these two groups demonstrated opposite trajectories in performance across task conditions.

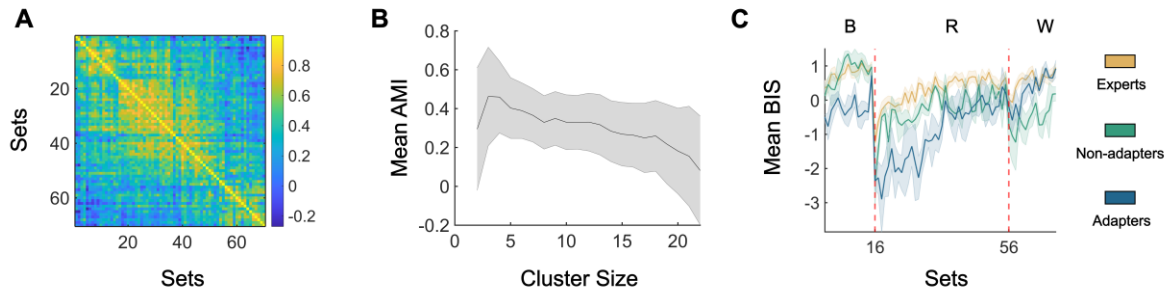

Figure 4 K-means clustering generated three distinct groups. A. Correlation of the group average balanced integration score (BIS) between sets. B. Mean and standard deviation (shaded error bar), of the adjusted mutual information (AMI) cluster sizes 2-22 across 100 iterations. C. Cluster average BIS scores across sets. The yellow line denotes individuals that always performed well (experts), green line for individuals' performance that worsened across conditions (non-adapters), and blue line for individuals that improved across conditions (adapters).

Expert Adaptation is Driven by Variation in BOLD Activity

A possible explanation for the experts and adapters performing well during washout, i.e., returning to non-rotated/baseline trials, is that their understanding of the task is comprehensive and robust to small perturbations. For experts, they come into the task with high understanding and are already robust to small perturbations, whereas adapters have an alternate approach. For adapters to achieve this performance, we suggest that during task learning this groups attempt various distinct actions. This variation would then result in a more flexible, comprehensive understanding of the task. To test this idea, we calculated the correlation between brain patterns across trials during the first and second half of rotation trials (Figure 5A/B). During the first half, the distribution of correlations for the expert had a higher peak at the zero-correlation, meaning that they produced more unique brain patterns for each trial compared to the other two groups (D_{1v2} = 0.0494, p_{1v2} = 0.0009; D_{1v3} = 0.0484; p_{1v3} = 0.0001, respectively). When

comparing the distributions of adapters and non-adapters, there was no significant difference in their distributions across the first half of rotation trials ($D = 0.0247$; $p = 0.287$). During the second half, the distribution of inter-trial brain map correlations had a higher peak at the zero-lag correlation, similar to the experts ($D = 0.0285$; $p = 0.151$), and the distribution of the adapters was also significantly different from the non-adapters ($D = 0.0636$; $p < 0.0001$).

Another perspective on flexibility of brain states is attained through energy landscape analysis. In this framework, we ask how much energy is required (inverse of likelihood) for an event to occur. For this study, we calculate how much energy is required to make changes in brain states for each cluster separately. During the first half of rotation trials, all groups demonstrated low energy requirements across brain state changes (Figure 5C). During the second half, the experts and adapters stayed with this flexible mindset with low energy requirements for both small and large brain state changes (Figure 5D). However, the non-adapters had large energy requirements for large changes in brains states – they were less likely to make large changes between trials, suggesting a more rigid performance (Figure 5D). To account for possible temporal and learning biases and the small number of participants in the minor clusters, 100 iterations of the data was generated by randomly shuffling the trials 100 times. Together these results suggest that expert adaptation is attained by having greater diversity in actions and a willingness to change during learning.

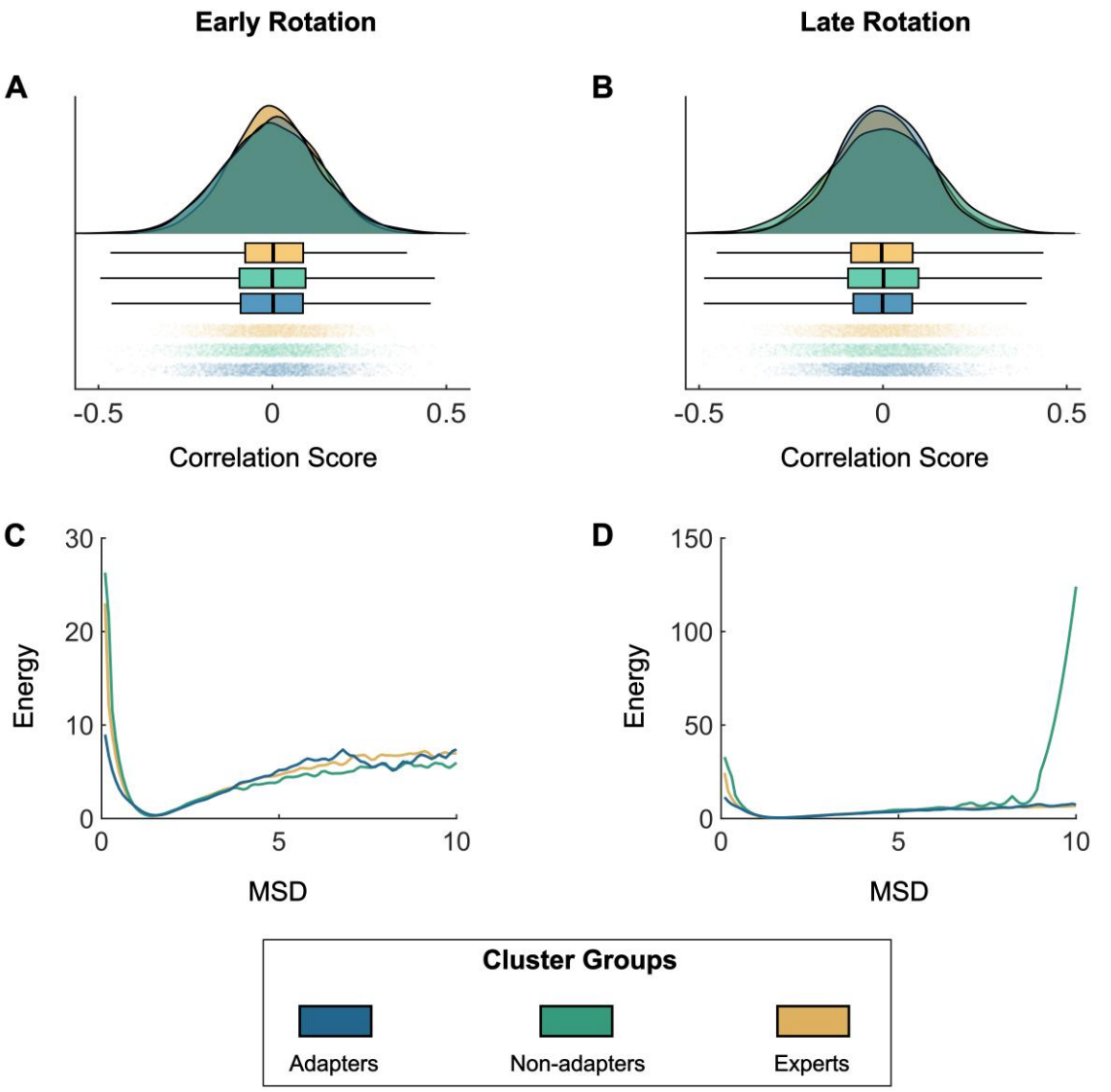

Figure 5 Inter-trial variability analyses for early and late rotation trials. Top panel (A and B) are raincloud plots of inter-trial correlations within the early and late rotation conditions for each group cluster. Each data point is the correlation of cluster average BOLD activity between different trials. Bottom panel (C and D) are plots of the energy landscape analyses for each group cluster. Mean-squared displacement (MSD) is calculated between all trials within a condition (early or late rotation). The MSD is converted to Energy by taking the natural logarithm of the inverse probability distribution of MSD.

Neural Networks Trained Under Multiple Conditions Develop Generalised Task Performance

Recurrent neural networks (RNN) offer a unique means to explore computational strategies employed by an organism to solve a given behavioural task. Whereby, the complete space of algorithmic solutions can be constrained by the investigator to assess biological validity of implementation within a particular organism, but also the versatility of solutions as a function of environmental variables. Here, we exploit this degrees-of-freedom control to demonstrate potential computation strategies being employed in a RNN trained on a simplified rotation paradigm analogous to the visuomotor rotation task. We train three separate RNNs under unique conditions, compare their performance as a function of changes to input/environmental variables to determine each solutions flexibility, and demonstrate network features comparable to those seen in the imaging data during the visuomotor rotation task.

Two of the networks were trained on only one task condition (baseline or rotation) and developed a rigid solution to the task, specific to only those task conditions seen during training (Figure 6A, 6B). The first network was trained similar to the baseline condition, outputting the input angle for all angles of rotation (0º-90º). The second network trained only on the rotation condition, output the 90º rotated input for all angles of rotation. Next, a third network was trained on both the baseline and rotation conditions. This network developed a more flexible and generalised solution to the task, performing accurately across all angles of rotation between 0º-90º (Figure 6C). That is, despite only learning on two environmental conditions, namely – non-rotated and 90º rotated conditions, the network learned a more general solution capable of handling any specified rotation angle between 0º-90º which included environmental conditions the network has not seen.

Finally, we calculated the attractor landscape for each of the networks and, thus, the likelihood of their corresponding activity changes. The third, flexible, network was more likely to change in activity across all MSD values. The energy required to change was lower across all MSD values for the flexible network compared to the rigid networks, which matched with the networks' variable outputs (Figure 6D).

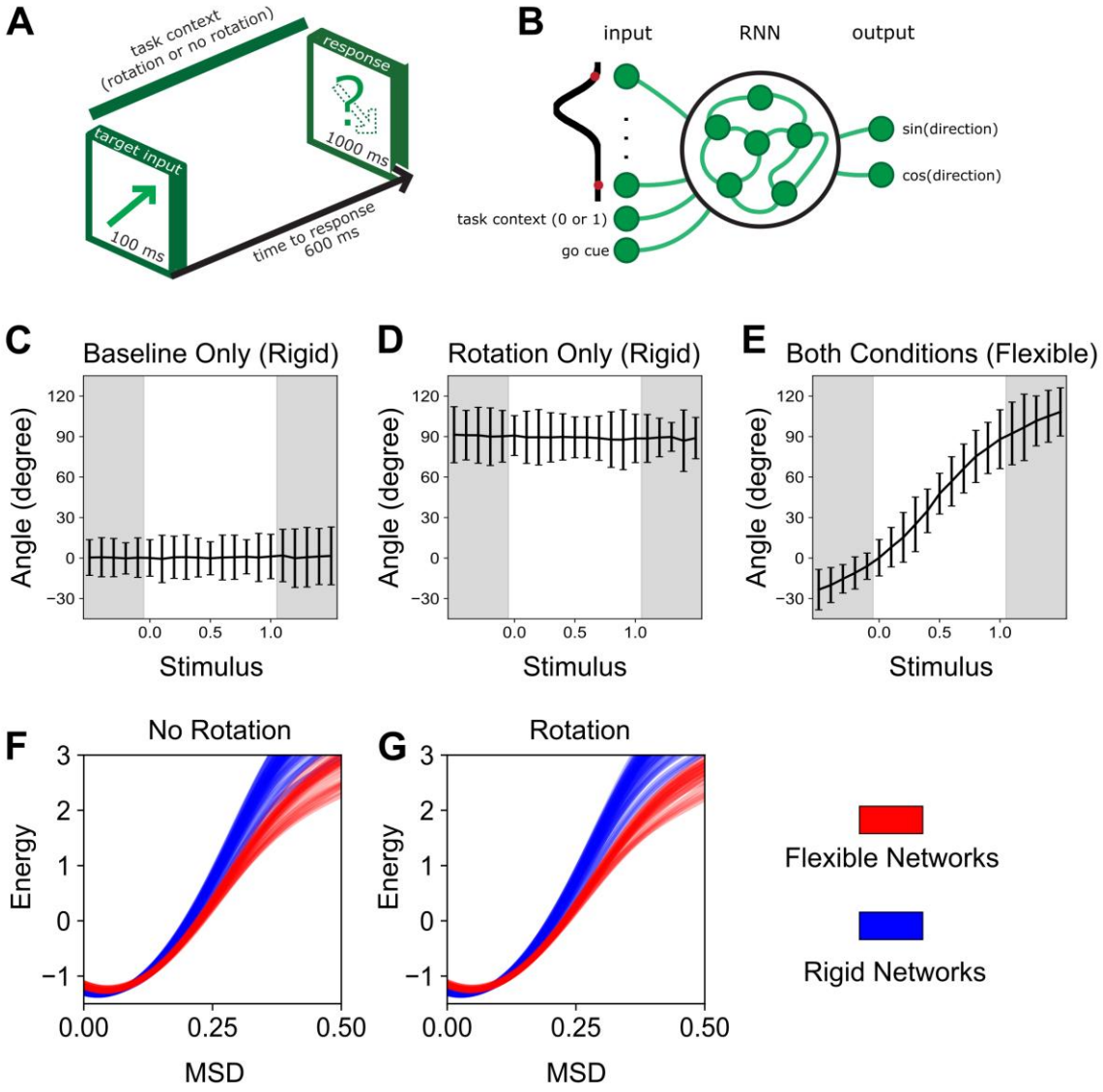

Figure 6 A recurrent neural network model of sensorimotor adaptation. A. Continuous time recurrent neural networks (RNN) were trained to output either the same direction as the input (context = 0) or a 90º rotation of the input (context = 1). B. Architecture of the RNN. C-E. Following training, the networks were tested across a range of task contexts (0 to 1) which varied the amount of rotation applied on the input. C-D. The two networks that were trained only on baseline (0) or a 90º rotation (1) only generated the trained output (rigid networks). E. The network trained on both baseline and rotation performed well under both conditions as well as for all angles of rotation between 0 and 90º (flexible network). F-G. For each of the three original networks, twenty additional networks were trained under the same conditions with random seeds. After training, for each network the MSD was calculated across adjacent trials and the probability distribution was estimated and converted into energy. For both the No Rotation and Rotation conditions, the networks trained on both conditions (flexible networks) had lower energy requirements than the networks only trained on one condition (rigid networks) across higher MSD values.

Discussion

In this study, we used a unique measurement of skill expertise to determine the neural signatures of experts in a sensorimotor adaptation task. We demonstrate a novel application of the balanced integration score (BIS) for fMRI studies, providing an alternative perspective on neural signatures of expertise. Expertise in adaptation was associated with decreased recruitment of the primary motor cortex, and increased dependence on cerebellar and subcortical regions. Furthermore, by exploring sub-groups within the dataset we found evidence that flexibility in the BOLD response was key for rapid adaptation and robustness to perturbations. During the rotation task, participants that learned to adapt were more likely to have large inter-trial differences in brain maps, consistent with behaviour observed in expert individuals. These results contrasted with participants who failed to adapt and were not as robust to perturbations. To complement the fMRI analyses, we trained RNNs to perform a similar task and demonstrated that a network only trained on the baseline condition was unable to adapt to rotation perturbation, however a network trained on both the baseline and a 90º rotation was competent across all angles of rotation between 0º and 90º. Overall, these results suggest that expertise in adaptation is facilitated by flexible brain patterns that are also dependent on increased BOLD responses from subcortical and cerebellar regions.

The balanced integration score (i.e., BIS) captures the key aspects of both speed and accuracy, serving as an operationalisation for expertise in the sensorimotor adaptation task. There is a well-known trade-off between speed and accuracy, wherein accuracy is improved by being careful and taking more time, whereas working quickly results in more reckless and inaccurate responses (Heitz, 2014). Importantly, we define expertise as having the capability to customise the speed-accuracy trade-off, resulting in performances which are both fast and accurate (Debarnot et al., 2014). While the BIS has previously been applied in mental rotation tasks (Liesefeld et al., 2015), typically neuroimaging studies would either analyse speed and accuracy separately, or estimate a speed-accuracy trade-off function (Heitz, 2014). A key difference between the BIS and the typical speed-accuracy curve estimates, is that the BIS retains the raw values whereas speed-accuracy estimates fit a curve to summarise the data, potentially applying a smoothing effect (Heitz, 2014; Liesefeld & Janczyk, 2019). In this study, combining the BIS with fMRI BOLD measurements successfully summarised speed and accuracy with a comprehensive brain map in a sensorimotor adaptation task. Furthermore, these results matched findings from analysing speed and accuracy separately. The

comprehensive brain map generated from the BIS scores was also anticorrelated to meta-analytical motor brain maps, supporting studies that suggest expertise in a task is different to the general brain activity required to complete a task (Bassett et al., 2015; J. Yang, 2015). Therefore, our study provides evidence for the utility of the BIS in neuroimaging studies, generating novel insights of expertise.

Expert performance during adaptation is dependent on the recruitment of subcortical regions, such as the cerebellum and basal ganglia, which is a conclusion that has been underappreciated in existing task-based imaging studies. There are numerous reasons for this, ranging from statistical constraints (e.g., induced head motion while completing a task), to hardware choices (e.g., designing coils that augment signal-to-noise ratios near the cortical surface) and even scanning procedures themselves (e.g., the harrowing choice in many prior studies to completely remove large portions of the cerebellum from the field-of-view. These studies inherently limit their scope to the cerebral cortex, ignoring the extensive brain-wide connections between the cortex, subcortex and cerebellum (R. M. Kelly & Strick, 2003; Middleton & Strick, 1994; Shine, 2021, 2022). Our study builds upon this literature by trying to understand how interactions between the cortex, subcortex, and cerebellum facilitate skilled performance in a task. Adapting to the final position of the target and not focusing on the trajectory taken has previously been associated with driving learning in visuomotor adaptation paradigms (Anguera et al., 2007). Our results agree with this notion, as better performance was driven by minimising error in the task and this minimisation involved cortical and cerebellar regions. Furthermore, our results found that motor regions in the cerebral cortex and cerebellum were associated with slower responses, providing evidence that decreased dependence on cortical regions is related to higher efficiency in the task (Bassett et al., 2015). By constraining behaviour by both the task and performance, our study demonstrated that expertise in adaptation, was driven by both an increased recruitment of subcortical and cerebellar regions and a decreased dependence on motor cortical regions.

The involvement of the cerebellum in adaptation learning aligns with previous ideas suggesting that the cerebellum provides functions for feed-forward processing (Ramnani & Miall, 2004; Wolpert & Flanagan, 2001) and pattern separation (Cayco Gajic & Silver, 2019). These functions could help disentangle the different interactions between inputs and outputs to the motor cortex, developing an internal model that provides a basis set of principles of possible ways to complete an action (Doyon & Benali, 2005; Egger et al., 2019; Imamizu et al., 2000b; Wolpert et al., 1998). These actions would account for changes in the environment, allowing

individuals to rapidly adapt to any changes in the task, a key aspect of expert behaviour (Debarnot et al., 2014; Imamizu et al., 2000b). An important aspect is the specificity of the task design and how this specificity influences the current results. For example, the current visuomotor paradigm is biased towards visual sensory processes and right-hand activation. Our results reflect this task specificity with lateralisation of cerebellar activity in the right cerebellar hemisphere and recruitment of regions from the visual cortex. The involvement of right cerebellar activity aligns with the general notion that cerebellar regions map contralateral with the cerebrum (Xue et al., 2021). In this case, right hand actions map to the left cerebral hemisphere which maps to the right cerebellar hemisphere. Primary visual regions are typically recruited during visuomotor tasks (Anguera et al., 2007; Sendhilnathan et al., 2024; Tzvi et al., 2022), however are usually not associated with learning (Striemer et al., 2019). In fact, the reliance on visual feedback and explicit strategies has been deemed less efficient compared to implicit learning processes (Mazzoni & Krakauer, 2006). While there are very few visual inputs directly from the primary visual cortex to the cerebellum (Glickstein, 2000; Glickstein et al., 1980; Glickstein & Doron, 2008), it is possible that primary visual activity can interact with cerebellar activity via the pontine nuclei or higher order visual regions (Glickstein, 2000; Tzvi et al., 2020). Finally, the association between the right putamen and higher performance in visuomotor adaptation is possibly related to functional lateralisation in the basal ganglia (Scholz et al., 2000; Viñas-Guasch & Wu, 2017). While it is more common to think about dividing the putamen functionally into anterior and posterior zones (Milardi et al., 2019; Oberhuber et al., 2013), it has been suggested that lateralisation is also a key feature of the putamen with the right putamen serving a role in visual and orthographic processing and the left putamen serving a role in language processing (Viñas-Guasch & Wu, 2017). While the micro-details behind cortical, cerebellar, and subcortical interactions are still not clear, these results highlight the importance of the cerebellum and subcortex in expertise and adaptation.

Adaptation is facilitated by a flexible mindset and a willingness to explore the boundaries of the task (Frank et al., 2008; Henz & Schöllhorn, 2016; Santos et al., 2018). Traditional training plans that focus on repeating the same action “10,000 times” overfit learning to the context of the action, resulting in diminished ability to adapt to changes in the environment. For example, a tennis player that practices serving close to the mid-line (as you do in singles) may struggle to translate this skill to serving in doubles, where they are required to stand closer towards the sidelines. A framework of learning that potentially overcomes this overfitting and facilitates adaptation is differential learning (I. Schollhorn, 2012). Studies that have trained athletes using

differential learning, demonstrated increased performance in various sports compared to athletes who follow more traditional training regimes (Beckmann & Schöllhorn, 2003; Coutinho et al., 2018; Henz & Schöllhorn, 2016). We suggest that differential learning improves final performance by allowing individuals to explore the boundaries of the action and perform at a high level independent of the context. In our study, while the participants were not instructed specifically on learning strategies, we found that participants that had more variable brain patterns performed better in the final condition. We suggest that variation in brain patterns across trials is due to participants attempting different actions/strategies allowing them to develop a comprehensive understanding of the task. While steps have been taken to account for the low number of participants in the sub-groups, replication of these results in larger sample sizes could further cement the relationship between variation during learning and generalisation across tasks. In addition, when training recurrent neural networks on the same task, the network that learned both the baseline and rotation conditions was able to adapt to intermediate amplitudes of rotation that lie between the baseline and rotation conditions, suggesting a generalisation of skill between the boundaries of the task. Therefore, variation in strategies and actions develops flexible learning of a task and generalises performance across different scenarios.

The current study focused on expertise in sensorimotor adaptation, specifically visuomotor rotations and how cortico-cerebellar circuits change throughout learning. However, cortico-cerebellar interactions also exist outside motor regions, specifically connections with granular regions in the frontal lobes of the cerebral cortex (R. M. Kelly & Strick, 2003; Ramnani, 2012; Ramnani et al., 2006). With the relatively homogenous cytoarchitecture of the cerebellum (Diedrichsen et al., 2019; Schmahmann & Pandya, 1997) and connections with non-motor regions (R. M. Kelly & Strick, 2003; Ramnani, 2012; Ramnani et al., 2006), we anticipate that the cerebellum will undoubtedly play an important role in pattern separation during cognitive tasks. As it stands, apart from motor learning and coordination, cerebellar activity has been found to be integral to a number of higher order functions such as working memory (Baier et al., 2014; Brissenden & Somers, 2019; D'Esposito et al., 1999) and parallel processing (Müller et al., 2023). Future research is required to understand cerebellar contributions to these various behaviours and could provide a parsimonious view on expertise and skilled performance across both motor and cognitive aspects.

This study revealed cortico-cerebellar patterns related to expertise in a sensorimotor adaptation task. Dependence on subcortical and cerebellar regions increased with performance and was

accompanied by decreased recruitment of primary motor regions suggesting a subcortical-cerebellar drive on expertise in adaptation. We also found that variable brain patterns and the willingness to change strategies between trials during learning resulted in improved performance in the final task. By focusing analyses on whole-brain interactions that include subcortical and cerebellar regions, a comprehensive understanding of adaptation across tasks and modalities can be attained.

Data and code availability

All imaging and behavioural data are publicly available in an OpenNeuro repository (Standage et al., 2023, accession number ds004021). Analysis of both the behavioural and functional MRI data was conducted in MATLAB. Code required to reproduce the statistical analyses and figures are publicly available https://github.com/ShineLabUSYD/VM_Adaptation. The recurrent neural network analysis was conducted in python and is available at https://github.com/azaho/adaptation_rnn.

Author contributions

The authors confirm contribution to the paper as follows:

- Study conception and design: Joshua B. Tan, Eli Müller, James M. Shine
- Data collection: Open source data - OpenNeuro repository (Standage et al., 2023, accession number ds004021)
- Analysis and interpretation of results: Joshua B. Tan, Eli Müller, Andrii Zahorodnii, James M. Shine
- Draft manuscript preparation: Joshua B. Tan, Eli Müller, Andrii Zahorodnii, James M. Shine
- All authors reviewed the results and approved the final version of the manuscript

Funding

JBT was supported by a Research Training Program Stipend (Full Time) (SC3227)

JMS was supported by a National Health and Medical Research Council Emerging Leader Fellowship (GNT1193857) and a Viertel/Bellberry Senior Principle Research Fellowship.

Competing Interests

The authors report no competing interests.

Chapter 3 Summary

In Chapter 3, we used a sensorimotor adaptation task to understand what brain network and features facilitate flexible and inflexible adaptive performance. We found that expertise in adaptation was facilitated by decreased BOLD activity in primary motor cortices – possibly a sign of increased neural efficiency, and increased BOLD activity in premotor, subcortical and cerebellar regions. These results suggest that increased performance in adaptation was associated with increased dependence on premotor regions, the subcortex and cerebellum.

Sensorimotor adaptation is not a cognitive action, however similar to Chapter 2 where action planning serves as a general function for both motor and cognitive planning, we believe that adaptation serves a similar role for both motor and cognitive adaptation. The results from this study further support this by highlighting Crus I of the cerebellum as important for adaptive performance. Crus I is typically associated with cognitive processing, attention, and memory (M. King et al., 2019), and as a posterior cerebellar region, experienced significant evolutionary expansion across species (Barton & Venditti, 2014). Together with our findings in Chapter 2, this possibly suggests that Crus I serves a general role for both motor and cognitive adaptation. These results follow along with literature that proposes the homogenous structure of the cerebellum handling both motor and cognitive inputs in a similar manner (M. Ito, 2008; Leiner et al., 1986), with Chapter 2 showing "motor" cerebellar regions involved in a cognitive task, and Chapter 3 showing "cognitive" cerebellar regions being involved in a motor task. Therefore, Chapter 2 and 3 together showcase the cerebellum's involvement in cognitive automaticity through overlapping circuits for motor and cognitive actions in action planning and adaptation.

In Chapter 4, we shift our focus towards how automatised actions can be recombined to develop novel behaviours. Our questions in this chapter, relate to distinguishing between automatised behaviours and recombination, and what features of recombination drive flexible, generalisable performance.

Chapter 4
Compositional Recombination Relies on a Distributed Cortico-Cerebellar Network

Joshua B. Tan[1], Isabella Orlando[1], Jungwoo Kim[3], Jayson Jeganathan[1,2], Giulia Baracchini[1,2], Rebekah Wong[1], Eli J. Müller[1,2], Claire O'Callaghan[1*], James M. Shine[1,2*]

Author Affiliations

1 Brain and Mind Centre, School of Medical Sciences, Faculty of Medicine and Health, University of Sydney, Australia

2 Centre for Complex Systems, School of Physics, University of Sydney, Australia

3 Centre for Neuroscience Imaging Research, Institute for Basic Science, Suwon, South Korea

*These authors contributed equally to this work

DISCLAIMER: Due to amendments made during the thesis submission phase, some empirical chapters may slightly differ in content compared to the online published versions.

Chapter 4 of this thesis is in preparation with the assistance of Isabella F. Orlando, Jungwoo Kim, Jayson Jeganathan, Giulia Baracchini, Rebekah Wong, Eli J. Müller, Claire O'Callaghan, James M. Shine.

Abstract

The ability to flexibly recombine prior knowledge underpins many aspects of human cognition, particularly the processes underlying compositionality, which is thought to rely on key regions of the cerebral cortex, including the dorsolateral prefrontal cortex and hippocampus. Importantly, subcortical regions – most notably, the cerebellum – have been separately implicated in a wide range of cognitive processes, but are often neglected in explanations of compositional cognition. To determine whether these distributed systems are involved in compositional cognition, we analysed whole-brain blood-oxygen-level-dependent (BOLD) activity with functional MRI while participants performed the Concrete Permuted Rules of Operation (C-PRO) task. Using dimensionality reduction techniques and a dynamic approach to task modelling, we dissociated neural processes responsible for two key underlying processes involved in compositional cognition: the specialist cortical regions tracking task Components; and a distributed, low-dimensional and generalisable cortico-cerebellar system that tracked with the Recombination process. Between-network connectivity for these two processes was dependent on the task context, and the Recombination network was found to be low-dimensional, integrated, generalisable and associated with effective task performance. These findings revise existing models of compositional cognition by highlighting cortico-cerebellar interactions as a mechanism for flexible generalisation.

Introduction

Adaptive behaviour is driven by our ability to indefinitely recombine and apply existing knowledge and behaviour to novel situations or in new ways (Duncan et al., 2017; Wu et al., 2024) – a capacity known as compositional cognition (Cole, Laurent, et al., 2013; Lande, 2024; Reverberi et al., 2012; Schwartenbeck et al., 2023). Compositional cognition is integral in both our daily lives (e.g., coming up with a new route to drive when your familiar one is blocked by road works), and for highly specialised behaviours (e.g., switching strategies in a tennis match to target your opponent's weakness). Previous work in human functional MRI (fMRI) has typically focused on compositionality as a cerebral cortical process (Reverberi, Görgen and Haynes, 2012; Cole *et al.*, 2013; Ito *et al.*, 2017; Cocuzza *et al.*, 2020; but see Mill and Cole, 2025), with a growing body of animal work highlighting the role of the prefrontal cortex and hippocampus in compositional processes (Bakermans et al., 2025; Bernardi et al., 2020; El-Gaby et al., 2024). How these cortical mechanisms interact with the subcortex and cerebellum to implement compositional cognition remains incompletely understood.

There are two key processes underlying compositional cognition: the capacity to categorise, store and recall specific *Components* (i.e., existing knowledge or behaviours), and the *Recombination* process that flexibly combines components to be applied across different contexts (Rigotti *et al.*, 2013; Fusi, Miller and Rigotti, 2016; Cole, 2024; Lande, 2024; Figure 1a). During compositional cognition, the two processes work in tandem: Components ensure functional specialisation within specific contexts, whereas Recombination is a flexible process that generalises across contexts (Bernardi et al., 2020; Čeko et al., 2022; El-Gaby et al., 2024; Lande, 2024; Reverberi et al., 2012; Tye et al., 2024). Importantly, both Components and Recombination are essential for compositional cognition – without the Components, behaviour will lack nuance or complexity, and without Recombination, behaviour becomes non-generalisable and yoked to each specific scenario. Here, we distinguish between the capacity to store and retrieve Components – that is, those features to which a compositional process is applied – versus the Recombination process that is typically synonymous with compositionality (Kurth-Nelson et al., 2023; Schwartenbeck et al., 2023). Differentiating the brain networks responsible for these distinct aspects of compositional cognition is crucial for advancing our understanding of the process.

Like many cognitive capacities in neuroscience, the current leading explanations for how the human brain supports compositional cognition are predominantly cortico-centric (Cole *et al.*,

2013; Ito *et al.*, 2017; Cocuzza *et al.*, 2020; Fu *et al.*, 2022; Schwartenbeck *et al.*, 2023; Kikumoto *et al.*, 2024; Tafazoli *et al.*, 2024; Park, Holmes and Snyder, 2025; though see Mill and Cole; 2025). Importantly, there is now overwhelming evidence that cognitive processes are not localised to the cerebral cortex, but rather are subserved by interactions between distributed networks that span cortical and subcortical systems (Mesulam, 1998; Nau et al., 2024; Shine, 2021; Shine et al., 2019). Viewing compositional cognition through a whole-brain perspective may help reconcile how compositional cognition arises in the brain.

Among a host of important subcortical structures, a particularly important system for cognitive processes is the cerebellum (Prati et al., 2024; B. Wang, 2025). Boasting one of the highest neuronal counts in the adult human brain, the cerebellum has previously been linked to distinct cognitive functions, such as pattern separation, skill execution, and adaptation (Cayco Gajic & Silver, 2019; Doyon et al., 2003; Imamizu & Kawato, 2009; Israely et al., 2025; Ramnani, 2014) all of which rely on a balance of Component separation and Recombination. The cerebellum both receives and sends information to the rest of the brain (Kang et al., 2021), including the prefrontal cortex (R. M. Kelly & Strick, 2003), a key area of interest identified in compositional studies (Bernardi et al., 2020; Cocuzza et al., 2020; Cole, Reynolds, et al., 2013; J. Park et al., 2025; Reverberi et al., 2012; Tafazoli et al., 2024). With growing evidence that cerebellar functions contribute to both cognitive and motor processes (Prati et al., 2024), it is possible that the cerebellum also serves a role in compositional cognition.

Linking behaviour to neural activity is possible through dimensionality reduction approaches. Prominent examples in animal literature include joint Principal Component Analysis (Churchland et al., 2012), Targeted Dimensionality Reduction (Mante et al., 2013) and demixed Principal Component Analysis (Kobak et al., 2016). An alternative approach that has been well-established in functional MRI (fMRI) literature is Partial Least Squares (PLS) analysis (Krishnan et al., 2011; McIntosh et al., 2004; McIntosh & Lobaugh, 2004). PLS defines a low-dimensional space that captures the covariance between neural activity and the task design, allowing for the separation of different conditions and task variables. Through PLS, it is possible to identify distinct patterns relating to Component and Recombination processes.

To achieve these aims, we used fMRI to analyse time-resolved BOLD responses across the cerebral cortex, subcortex, and cerebellum during performance of the Concrete Permuted Rules of Operation (C-PRO) paradigm, which has previously been used to investigate compositional cognition (Cocuzza et al., 2020; T. Ito et al., 2017; T. Ito, Yang, et al., 2022). Our primary aims

were to extend current compositional cognition frameworks to: 1) decompose compositional cognition into Component processes and the Recombination process; 2) to test the hypothesis that compositional Recombination involves distributed computations across subcortical and cerebellar structures; and 3) to identify any inter-regional dynamics that may be crucial for compositionality. We hypothesised that: 1) Recombination is consistent and generalisable across varied rule contexts, while Components are specifically recruited for each rule; 2) that Components would involve specialist regions, whereas Recombination would recruit a distributed network across cortical and cerebellar regions; and 3) that networks underlying Components and Recombination should work together dynamically in order for effective compositional cognition to occur. We found robust evidence for each of our hypotheses, which we detail in the remainder of the manuscript.

Methods

Experimental Design

Ninety-five healthy adults (mean age = 22.23 years, s.d. = 3.93; female:male = 54:41; right-handed) were recruited from Rutgers University and the surrounding Newark, New Jersey community. All participants completed the C-PRO paradigm while undergoing fMRI scanning.

The C-PRO paradigm was designed to test rapid instructed task learning and adaptive behaviour by recombining various task rules (Cole, Laurent, et al., 2013; T. Ito et al., 2017). We used the modified version introduced by (T. Ito et al., 2017). This version utilised 12 task rules that were categorised under three domains: four logic rules (BOTH, NOT BOTH, EITHER, NEITHER), four sensory rules (RED, VERTICAL orientation, HIGH PITCH sound, CONSTANT tone), and four motor rules (LEFT INDEX, LEFT MIDDLE, RIGHT INDEX, and RIGHT MIDDLE finger). During a trial, a single rule from each domain is combined (e.g., BOTH, RED, LEFT INDEX). By matching every rule with every other rule across all domains a total of 64 unique permutations were created.

During the task, participants completed three trials in a row for each of the 64 unique permutations which we called a “mini-block”. Each mini-block lasted a total of 28,260 ms (36 TRs) and consisted of an instruction period of 3925 ms (5 TRs), followed by a jittered delay between 1570 – 6280 ms (2 – 8 TRs) sampled from uniform distribution, then three trials, where each trial is 2355 ms (3 TRs) with an inter-trial interval of 1570 ms (2 TRs), followed

by another jittered delay between 7850 – 12,560 ms (10 – 16 TRs, randomised) before the start of the next mini-block. For each trial, participants were presented two sets of simultaneous audiovisual stimuli (Figure 1c). The audio stimulus was either a high pitch sound or constant tone, and the visual stimulus was a bar either in vertical or horizontal orientation, and either blue or red coloured. Response time and accuracy for each trial was measured. The paradigm was presented using E-Prime software version 2.0.10.535 (Schneider et al., 2007).

Participants completed all 64 mini-blocks twice spread across eight runs (16 per run). Within the first four runs, participants completed all 64 unique mini-blocks before completing all mini-blocks for a second time in the last four runs. Order of mini-blocks was randomised between participants and runs. Alongside the eight task scanning runs, each participant also completed a resting-state scan however for the purpose of this study, only the task runs were analysed. Before entering the scanner, participants trained on four of the possible 64 mini-blocks. The four training mini-blocks were chosen such that all 12 rules were equally practiced.

Imaging Acquisition

Data were collected at the Rutgers University Brain Imaging Center (RUBIC). Whole-brain multiband echo-planar imaging (EPI) acquisitions were collected with a 32-channel head coil on a 3T Siemens Trio MRI scanner with TR = 785 ms, TE = 34.8 ms, flip angle = 55º, Bandwidth 1924/Hz/Px, in-plane FoV read = 208 mm, 72 slices, 2.0 mm isotropic voxels, with a multiband acceleration factor of 8. Whole-brain high-resolution T1-weighted and T2-weighted anatomical scans were also collected with 0.8 mm isotropic voxels. Spin echo field maps were collected in both the anterior to posterior direction and the posterior to anterior direction in accordance with the Human Connectome Project preprocessing pipeline (Glasser et al., 2013). A resting-state scan was collected for 14 mins (1070 TRs), prior to the task scans. Eight task scans (runs) were subsequently collected, each spanning 7 min and 36 s (581 TRs). Each of the eight task runs (in addition to all other MRI data) were collected consecutively with short breaks in between (participants did not leave the scanner).

Pre-processing

Neuroimaging data was organized in BIDS format and pre-processed with fMRIprep version 23.1.4 (https://fmriprep.org/en/stable/#), a standard pipeline that incorporates toolboxes from

the gold-standard preprocessing software in the field (Esteban et al., 2020). fMRIPrep involves the basic pre-processing steps (co-registration, normalization, unwarping, noise component extraction, segmentation, skull-stripping etc.) and produces a report for quality checking at each step. See Supplementary Material for a full description of each step. Regression of twelve head motion artifacts, and the average combined white matter, CSF signal was conducted using custom python scripts, with a high-pass filter set at 0.01. Mean BOLD time series were extracted from 400 Schaefer cortical regions (Schaefer et al., 2018), 28 cerebellar regions (SUIT atlas) (Diedrichsen, 2006), and 54 subcortical regions (Tian et al., 2020) using custom python scripts. The following atlases were chosen as robust and popular parcellations that reveal meaningful neurobiological features (Diedrichsen, 2006; Schaefer et al., 2018; Tian et al., 2020; Yeo et al., 2011).

Behavioural Analysis

Accuracy was calculated as the percentage of correct responses within a mini-block. We then thresholded performance by the number of mini-blocks participants got 100% (3/3) correct. Participants that performed at 100% accuracy across more than 64 mini-blocks were kept for further analyses, leaving 87 participants in the final dataset.

Behavioural data was fit using a generalised linear mixed model, comparing the effects of different rules and learning over time against accuracy in a mini-block. Fixed effects were measured for each domain (logic, sensory, motor) separately, accuracy across runs, and whether it was the first or second time completing the mini-block in the scanner (instance) (Equation 1). Each domain was treated as a categorical variable (rules 1 – 4). Random effects included repeated measures per run and participant.

$$Accuracy \sim 1 + logic\ rule + sensory\ rule + motor\ rule + run\ id + instance + (1 \mid participant\ id : run\ id) \quad (1)$$

Finite Impulse Response Model (FIR)

The finite impulse response (FIR) model estimates changes in BOLD activity at multiple time points and is not biased towards a particular shape, such as the hemodynamic response function which is typically used in task-based functional MRI analyses (Friston et al., 1995).

To choose an appropriate window of time, we measured the maximum number of time points available across all mini-blocks. Due to some mini-blocks occurring towards the end of the scan (less time points available), we chose 23 time points or TRs (~18 seconds), starting from trial onset. Each mini-block (n = 64) was modelled separately in the FIR model, resulting in 23 estimates per mini-block. Random effects for the run number and instance were included, allowing intercepts to account for repeated measures. The final design matrix had 23 regressors per mini-block (fixed effects), and regressors for which run and which instance (random effects; Equation 2). The FIR models were fit at the participant-level using generalised linear mixed models to compare the changes in the design matrix variables with a participant's BOLD time series concatenated across runs (Equation 2). By concatenating time points within each mini-block, temporal blurring between adjacent trials was minimised and common effects across similar mini-blocks were emphasized.

$$Concatenated\ BOLD\ time\ series \sim time\ points * number\ of\ mini\ blocks + (1 \mid run\ id) + (1 \mid instance) \quad (2)$$

Partial Least Squares Analysis

Partial Least Squares (PLS) analysis is a supervised multivariate approach that finds the relationship between brain activity and behaviour. The two main components of PLS are the X matrix that consists of brain activity, and the Y matrix which consists of behavioural data. The following PLS method follows from mean-centred task PLS correlation as described by Krishnan *et al.* (2011). For the X matrix, we used the beta estimates from the FIR model. The beta estimates were concatenated across participants resulting in number of rows equal to number of participants (87) x number of mini-blocks (64), and number of columns equal to number of time points (23) x number of regions (482). For the Y matrix, we dummy coded in task contrasts specifying labels for each rule separately. This resulted in a matrix where rows equals the number of participants (87) x number of mini-blocks (64), and the number columns equals the number of rules (12).

To compare the X and Y matrices, we calculated the covariance matrix M (Equation 3).

$$M = diag\{1^T Y_{dummy\ coding}\}^{-1} Y_{dummy\ coding}^T X \quad (3)$$

$\{1^T Y_{dummy\ coding}\}$ is the sum of each column in the Y matrix. Diag{} is the diagonal values from the matrix. Y^T is the transpose (swap rows and columns) of the Y matrix.

The covariance matrix M was then mean-centred through demeaning. Demeaning was calculated for each column by subtracting the mean of the column from all values within the column. To find the latent variables of this matrix, the demeaned covariance matrix $M_{mean\text{-}centreed}$ underwent singular value decomposition (SVD). This resulted in three matrices: U, which is a left singular vector (latent variables) that characterises axes of behaviour in PLS space; S, singular values (diagonal matrix); and V, the right singular vector (latent variables) characterising axes of brain activity in PLS space. This approach optimally separates each task rule, and shares similarities with discriminant analysis approaches (Abdi & Williams, 2010; Williams et al., 2010)

To decide how many latent variables to include we calculate the explained variance (Equation 4), and cumulative explained variance using the singular values from S.

$$Explained\ variance = 100 * \left[\frac{diag(S)^2}{sum(diag(S)^2)}\right] \quad (4)$$

By plotting explained variance using a scree plot, we can observe how many latent variables were included before added explained variance asymptotes (elbow) (Nguyen & Holmes, 2019). From looking at explained variance, and the cumulative explained variance, the first 3 latent variables were used to characterise the PLS space. In this PLS space, each latent variable forms an axes that contrasts different groups of task rules.

To verify the latent variables, we used permutation testing (McIntosh et al., 2004; McIntosh & Lobaugh, 2004). Rows of the X matrix were randomly shuffled 1000 times, with Y matrix remaining unchanged. The same steps applied for each shuffled X matrix, such as calculating the covariance matrix of $X_{shuffled}$ and Y, followed by SVD. The singular values from S were used to create a null distribution for each latent variable. The original singular values were then compared against the null distribution.

To validate that the patterns we found from PLS were stable across both task execution and preparation phases, we applied the PLS analysis to time points during the instruction phase. To compare between the trial and instruction phases, we calculated the Pearson's correlation for the corresponding top 3 latent variables of matrix V.

Identifying Component and Recombination Regions

Characterising regions as rule dependent Components was dependent on a region's bias to particular rules (measured using Euclidean distance) in the PLS space. Identifying regions involved in Recombination was based on the following criteria: i) they should be engaged across many different trials of the task; ii) they should not be selectively associated with one particular task Component; and iii) they should show correlated activity with task-specific dimensions on relevant task trials.

Using regional loadings in the first 3 latent variables from PLS from matrix V, we created a 3-dimensional co-ordinate space for regions across time, where extreme values suggest bias towards rules, and values closer to the origin (0,0) suggest no bias. To measure regional rule bias across time, we calculated the Euclidean distance of a region from the origin at each time point. For each region, we calculated the total sum of their rule bias across time and normalised the data by z-scoring. Regions that had Euclidean distance z-score values > 1 were categorised as integral for Component (rule dependent) processes. For the remaining regions, we calculated the group average FIR time series using estimates from the FIR model. This average estimate was then normalised by z-scoring. Regions with z-scored values > 1 were categorised as rule independent. Component regions were assigned to specific domains (Motor, Logic, Sensory) depending on which PLS axes the region had the most extreme value on (e.g., regions with large positive/negative loadings on LV_1 were assigned to the motor domain). These labels were used for the functional connectivity analyses.

Functional Connectivity Between Components and Rule independent Regions

Functional connectivity matrices were generated by calculating the Pearson's correlation between rule independent and rule dependent Component regions' time series during the trial period. Average functional connectivity matrices were calculated for each contrast as identified from the PLS analysis (left hand, right hand, positive, negative, visual, auditory rules). These matrices were vectorized and pairwise pattern similarity was estimated using Pearson's correlation between all possible pairs.

Delta matrices between contrast pairs (left hand – right hand, positive – negative, visual – auditory) were calculated by comparing functional connectivity matrices for each contrast (Supplementary Figure S2). Rule dependent Component regions (columns) were rearranged

into their assigned domains from the PLS analyses. We next ran a set of 2-sample t-tests comparing different axes of each Component process ($p < 0.05$) and then constructed a conjunction analysis by identifying Recombination regions that showed significantly different regional functional connectivity across all three comparisons.

Characteristics of Recombination Regions

To measure the extent of which regional activity generalised across contexts we relied on two measures: activity similarity across mini-blocks, and dimensionality of regional time series (Fusi et al., 2016; Israely et al., 2025; Muscinelli et al., 2023; Posani et al., 2025).

Similarity across mini-blocks was measured by taking the group average FIR time series and comparing how similar (Pearson's correlation) were time series of a given mini-block (e.g. mini-block 1) and every other mini-block. This was done for both rule independent and rule dependent regions at the participant level. To compare whether rule independent regions generalised across task contexts more than rule dependent regions, we averaged across similarity comparisons for both groups of regions at the participant level. Then we used a generalised linear mixed model to compare the average similarity value between the two groups (Equation 5).

$$Mini\ block\ similarity \sim 1 + group\ id + (1 \mid participant\ id) \quad (5)$$

To measure the dimensionality of regions, for every mini-block, we take the group averaged FIR time series for rule independent and rule dependent regions and calculate principal component analysis (PCA) on each group separately. We chose PCA as it is intuitive, interpretable and widely used amongst the neuroscience community. We then compared the explained variance of the top 3 principal components between the two groups using paired t-tests.

To measure the extent a region was integrated with the rest of the brain, we followed standard pipelines from the Brain Connectivity Toolbox (Rubinov & Sporns, 2010). We calculated a population average functional connectivity matrix from trial period time series. Then, we identified modules using the Louvain algorithm. We performed a sweep across gamma values 0.5 to 2 with increments of 0.1. At each step we ran 100 iterations and calculated the adjusted mutual information (Vinh et al., 2009, 2010; Vinh & Epps, 2009). Stability was assessed by

measuring the standard deviation of modularity (Q) at each gamma value. There was low variability across all gamma values with gamma = 1 having the highest adjusted mutual information. Participation coefficient was calculated for Recombination and Component regions using the module assignment from gamma = 1. A two-sample t-test was used to compare participation coefficient between Recombination and Component regions.

Results

The Concrete Permuted Rules of Operations Task

Ninety-five participants completed the C-PRO paradigm, as part of an openly available dataset (OpenNeuro, accession number ds003701) that has been previously published (Cocuzza et al., 2020; T. Ito et al., 2017; T. Ito, Yang, et al., 2022). The C-PRO paradigm operationalises compositional cognition by introducing rules as Components from distinct domains that are recombined during the task (Figure 1a). By varying the specific combination of rules, the C-PRO creates different task contexts. Therefore, each trial contains information that is specific to the context (the Motor, Logic and Sensory-specific *Component* processes) and information that generalises across contexts (the *Recombination* process; Figure 1b).

Participants were presented with 3 rules, with 1 per task domain (Motor, Logic and Sensory). After a short delay, two stimuli were presented sequentially and participants then made a response (e.g., if the instructions were “BOTH”, “VERTICAL”, and “LEFT INDEX”, participants would press a button with their LEFT INDEX finger if BOTH bars were VERTICAL; Figure 1c). With four possible rules per domain, there were a total of 64 unique permutations of rules (i.e., 64 task contexts, which were presented in “mini-blocks” of three of the same rule combination in a row). Participants who scored 100% on more than 64 mini-blocks were kept in the final dataset, resulting in eighty-seven participants. For more details regarding the task paradigm refer to the *Methods*.

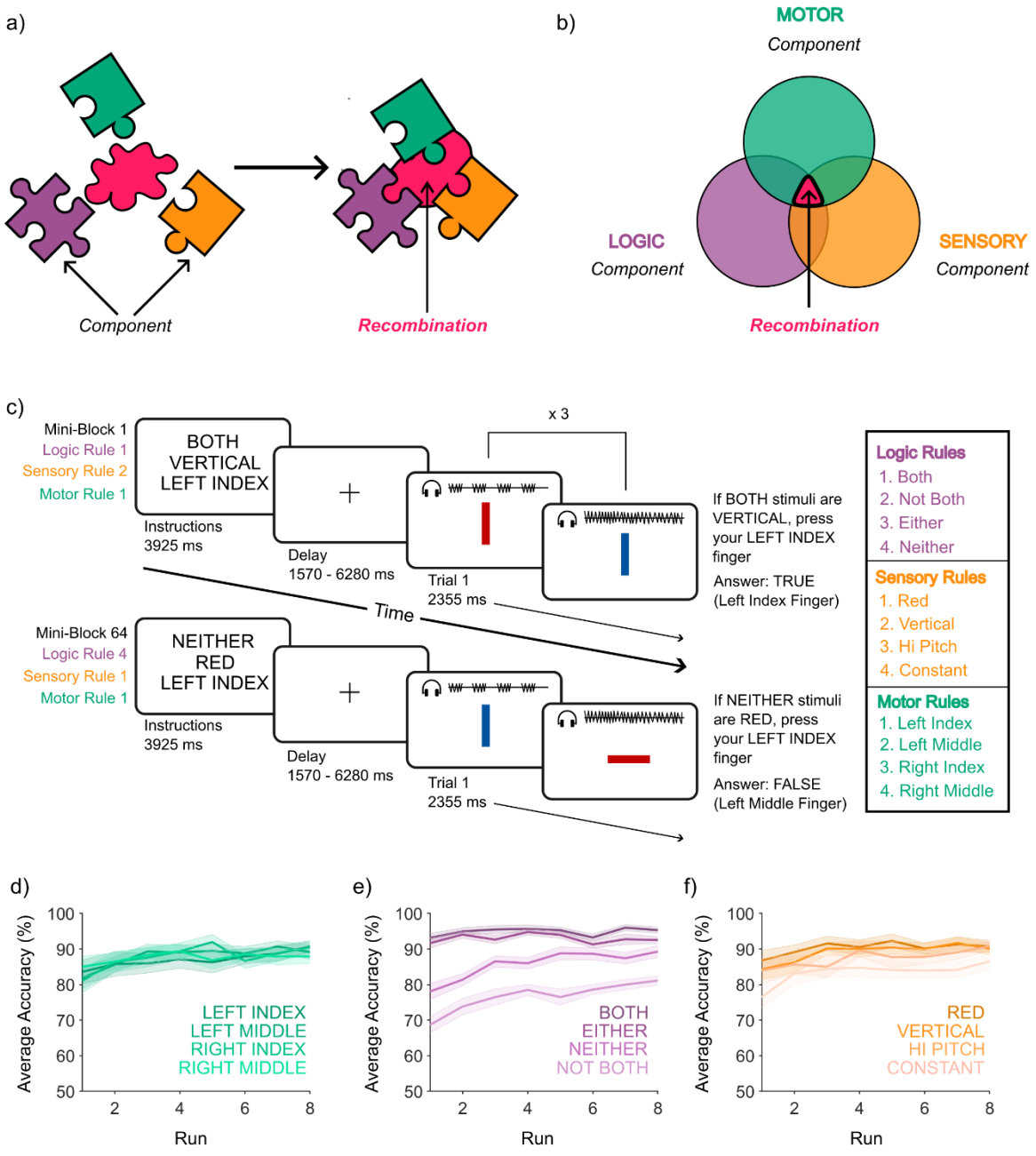

Figure 1. Compositional Cognition and Task Behaviour. a) A schematic of compositional processes, in which the puzzle pieces symbolise Component concepts (different colours represent different rule domains) that can be combined by a flexible Recombination process in the centre that adapts its shape to each puzzle piece. b) the compositional process is comprised of the Recombination of different Component process – each wing of the Venn diagram represents one of the context-dependent Component dimensions (Motor, Logic or Sensory), whereas the centre of the Venn diagram represents the Recombination process, which is flexible and relatively context-independent. c) the Concrete Permuted Rules Operation (C-PRO) task, wherein each trial requires the flexible Recombination of three Component domains (Motor, Logic and Sensory), adapted from (T. Ito et al., 2017). d-f) Group accuracy across runs for each rule per domain d) Motor e) Logic f) Sensory. Note that mean performance was relatively stable across runs. d-f) was inspired by (T. Ito, Klinger, et al., 2022).

To measure differences in accuracy between rules and across time, we fit a generalised linear mixed model that compared accuracy between rules across runs and whether there was a difference in performance between the first and second exposure to a specific mini-block, while controlling for repeated measures across runs and participants. From the model, we observed a significant difference in accuracy depending on which Logic and Sensory rules were applied ($p < 0.05$; Figure 1d-f). For the Logic rules, accuracy was significantly higher for the rule "BOTH" compared to all others (BOTH vs. NOT BOTH: $t_{11,124} = -28.87$, 95% CI [-0.19 -0.17], $p < 1e\text{-}16$; BOTH vs. EITHER: $t_{11,124} = -3.15$, 95% CI [-0.03 -0.01], $p = 0.0016$; BOTH vs. NEITHER: $t_{11,124} = -14.47$, 95% CI [-0.10 -0.08], $p < 1e\text{-}16$; Figure 1d). For the Sensory rules, accuracy was significantly higher for the rule "RED" compared to the auditory rules "HI PITCH" and "CONSTANT" (RED vs. HI PITCH: $t_{11,124} = -4.27$, 95% CI [-0.04 -0.01], $p = 1.98e\text{-}05$; RED vs. CONSTANT: $t_{11,124} = -11.03$, 95% CI [-0.08 -0.06], $p < 1e\text{-}16$; Figure 1e). Accuracy increased by 1% across runs ($t_{11,124} = 3.61$, 95% CI [0.01 0.02], $p = 3.08e\text{-}04$). There were no significant differences in accuracy across the different Motor rules, or whether it was the first or second exposure to the mini-block ($p > 0.05$). In summary, different Logic and Sensory rules influenced overall accuracy during the task with participants slightly improving in accuracy across runs.

The Compositional Component Processes

To detect time-resolved task-related brain activity associated with each of the Component constructs within the C-PRO task, we subjected pre-processed functional MRI data from 482 regions that covered the cerebral cortex, cerebellum, and a range of subcortical structures (Diedrichsen, 2006; Schaefer et al., 2018; Tian et al., 2020) to a finite impulse response (FIR) model (constructed across a time window of 23 TRs for each mini-block starting from trial onset). The time window was specified using the maximum number of time points consistent across all mini-blocks, allowing us to identify signatures in the BOLD time series of compositional cognition (see *Methods*). An inherent design feature of the C-PRO paradigm made our task challenging: specifically, every trial of the task contained a blend of rules from all 3 domains, meaning that there is no simple means for isolating the brain patterns for each task domain. To circumvent this issue, we applied a mean-centred, task-based Partial Least Squares (PLS) analysis (Figure 2a; Krishnan *et al.*, 2011). This allowed us to identify a low-dimensional orthogonal basis set associated with the task (the top 3 latent variables explained

88.7% of the variance; Figure 2b). To further confirm whether the first 3 latent variables were significant or occurred by chance, we created a null distribution of singular values by permuting regional brain activity 1,000 times while holding the design matrix static. Importantly, all 3 latent variables were significant after permutation testing ($p = 0.001$), which allowed us to conclude that the first 3 latent variables were sufficient to explain the data. Hence, all further analyses were conducted in a PLS space constructed using these 3 latent variables.

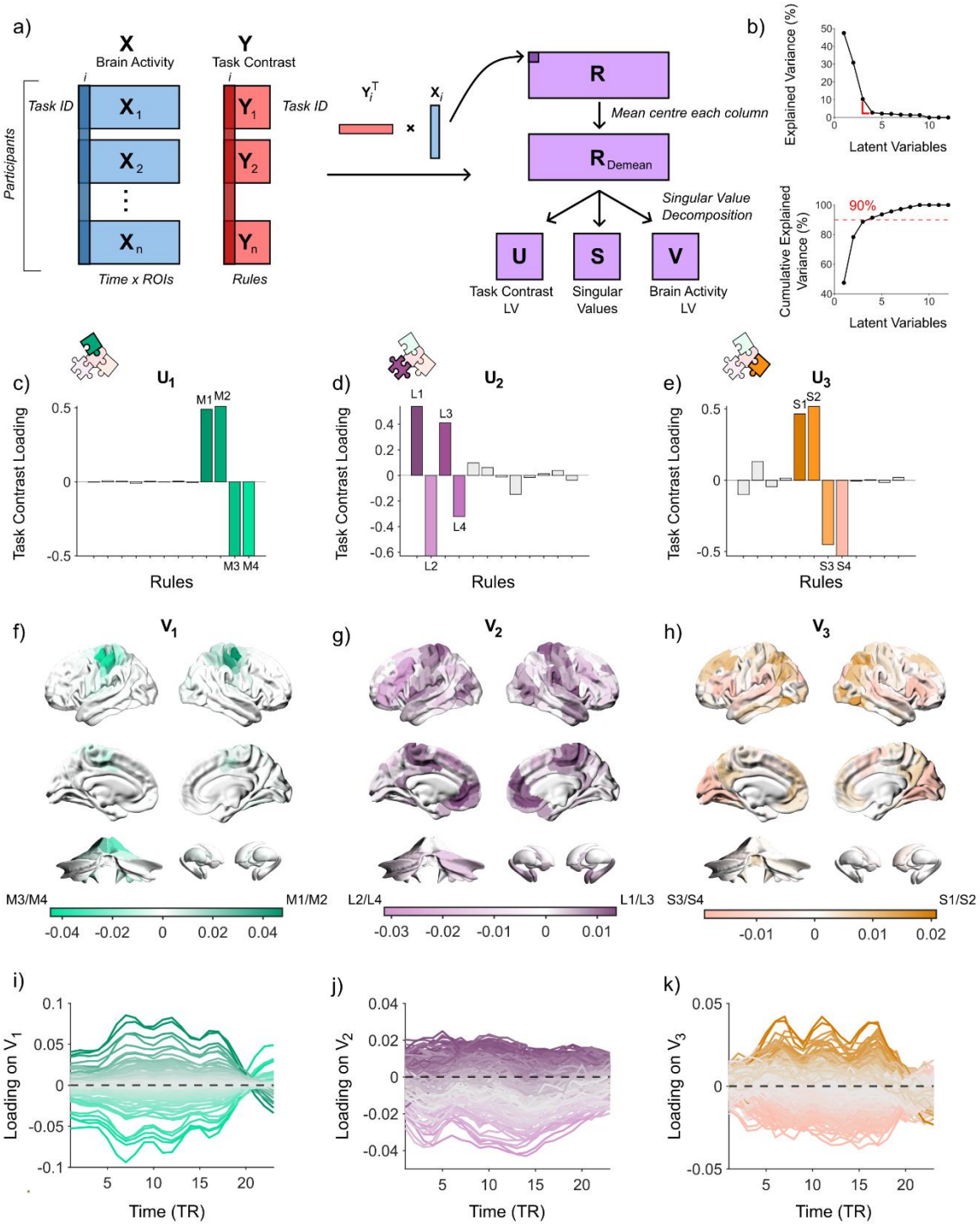

Figure 2. Segregated Subnetworks Are Required for Compositional Component Processes. a) Schematic of steps to run PLS analyses. Brain activity refers to the FIR time series. Task Contrast refers to a design matrix where each rule is dummy coded (12 regressors, 1 per rule). Covariance of brain activity and task contrast is calculated and demeaned. The demeaned matrix undergoes singular value decomposition (SVD). b) Diagnostics for deciding how many latent variables to keep. Top: Scree plot of explained variance per latent variable. Elbow (red) occurs from LV_3 to LV_4. Bottom: Cumulative explained variance plot. Cumulative explained variance crosses 90% between LV_3 and LV_4. c-e) Bar plot of the first 3 LVs of Task Contrast scores in PLS space. f-h)

Brain visualisation of first 3 LVs of average brain activity in PLS space. i-k) Loadings of brain activity across time in PLS space. The three 'peaks' in i) and k) relate to the three trials completed per mini-block. Each line denotes an individual region's dynamics across time.

To interpret the latent variables, we sought convergence across two distinct approaches: we mapped each C-PRO rule to the three latent PLS variables (Figure 2c-e) and interrogated the brain loadings onto each latent variable (Figure 2f-k). Both approaches offered clearly congruent interpretations. LV_1 was dominated by *Motor* rules (left hand *vs.* right hand; Figure 2c) and separated the left and right motor regions of the cerebral and cerebellar cortex (Figure 2f); LV_2 was mainly driven by *Logic* rules (positive *vs.* negative; Figure 2d) and separated higher cognitive areas from unimodal and memory-associated areas (Figure 2g); and LV_3 was driven by *Sensory* rules (visual *vs.* auditory; Figure 2e) and separated attentional processing and higher order visual processing from primary auditory and primary visual regions (Figure 2h). We thus concluded that the task-based PLS was able to effectively identify the three main Component processes that comprised the C-PRO task.

To track how brain region dynamics evolved in the PLS space, we plotted the region's time-resolved loadings (Figure 2i-k). For LV_1 and LV_3 we observed trial related dynamics denoted by three peaks (1 per trial), whereas LV_2 was more consistently associated with task-based negative deflections. Note that the interpretation of PLS loadings is invariant to sign, such that the negative deflections can be interpreted either as a negative loading on the positive (purple) regions of LV_2, or as a positive loading on the negative (pink) regions of LV_2. In this case, interrogation of the PLS loadings was consistent with the latter interpretation.

Task-related neural signatures can appear during preparation phases (Churchland & Shenoy, 2024), however it is unclear to what extent neural signatures between preparation and task execution are similar. To verify whether this decomposition was unique to the trial period or was consistent for all aspects of compositional processing, we generated a PLS space from time series related to the Instruction period. The first 3 LVs of the Instruction period separated the rules per domain in the same manner as the decomposition of the trial period (Supplementary Figure S1). The brain patterns for the first 3 latent variables for the Instruction period were similar to the brain patterns generated from the trial period ($|r_1| = 0.99$; $|r_2| = 0.98$, $|r_3| = 0.96$, respectively; Supplementary Figure S1). A key difference between the decomposition was that the regional dynamics in the PLS space for the trial period showed peaks and troughs related to each individual trial, whereas the regional dynamics of the Instruction period showed block activation dynamics (Supplementary Figure S1). In conclusion, our analysis demonstrated that

PLS was able to successfully separate out brain patterns and dynamics specific to each domain and these patterns were consistent across compositional processing as a whole and not specific to task execution.

The Compositional Recombination Process

Having identified a set of axes associated with the Component processes of the C-PRO task, we next designed an approach to identify regions associated with the Recombination process. In order for regions to be involved in Recombination, we reasoned that: i) they should be engaged across many different trials of the task; ii) they should not be selectively associated with one particular task Component; and iii) they should show correlated activity with task-specific dimensions on relevant task trials.

We began our approach by further interrogating the orthogonal state-space defined by the first three dimensions of the PLS analysis (Figure 3a), which clearly separated out brain patterns by each Component process (Figure 2). The absolute value of the loading on each PLS dimension is interpretable as the extent to which a particular region was associated with a specific task dimension. In our case, regions that loaded towards the extremity (positive or negative) were biased towards specific rules (i.e., rule dependent Component processes), whereas regions closer to the origin (0,0) showed consistent patterns across all rules (were rule independent). We quantified each region's rule-specificity by calculating the Euclidean distance of each region in the PLS state-space from the origin at every time point of the task. To find the total bias of a given region, we calculated the area under the curve for a region's distance from the origin. We then normalised this measurement and identified rule dependent Component regions if the normalised area under the curve was > 1 (i.e., greater than 1 *s.d.* from the mean). Using this criterion, 54/482 regions were identified as 'rule dependent' (Figure 3b, 3f; silver). These regions were assigned labels denoting which PLS dimension they were most biased towards. From the remaining regions 65/482 regions were identified as 'rule independent' (Figure 3b; pink), in that their normalised score was > 1 *s.d.* from the mean FIR estimate – i.e., they were not biased towards any specific rule – but were still strongly recruited during the task. These analyses thus identified 65 regions that fulfilled criteria *i)* and *ii)* outlined above.

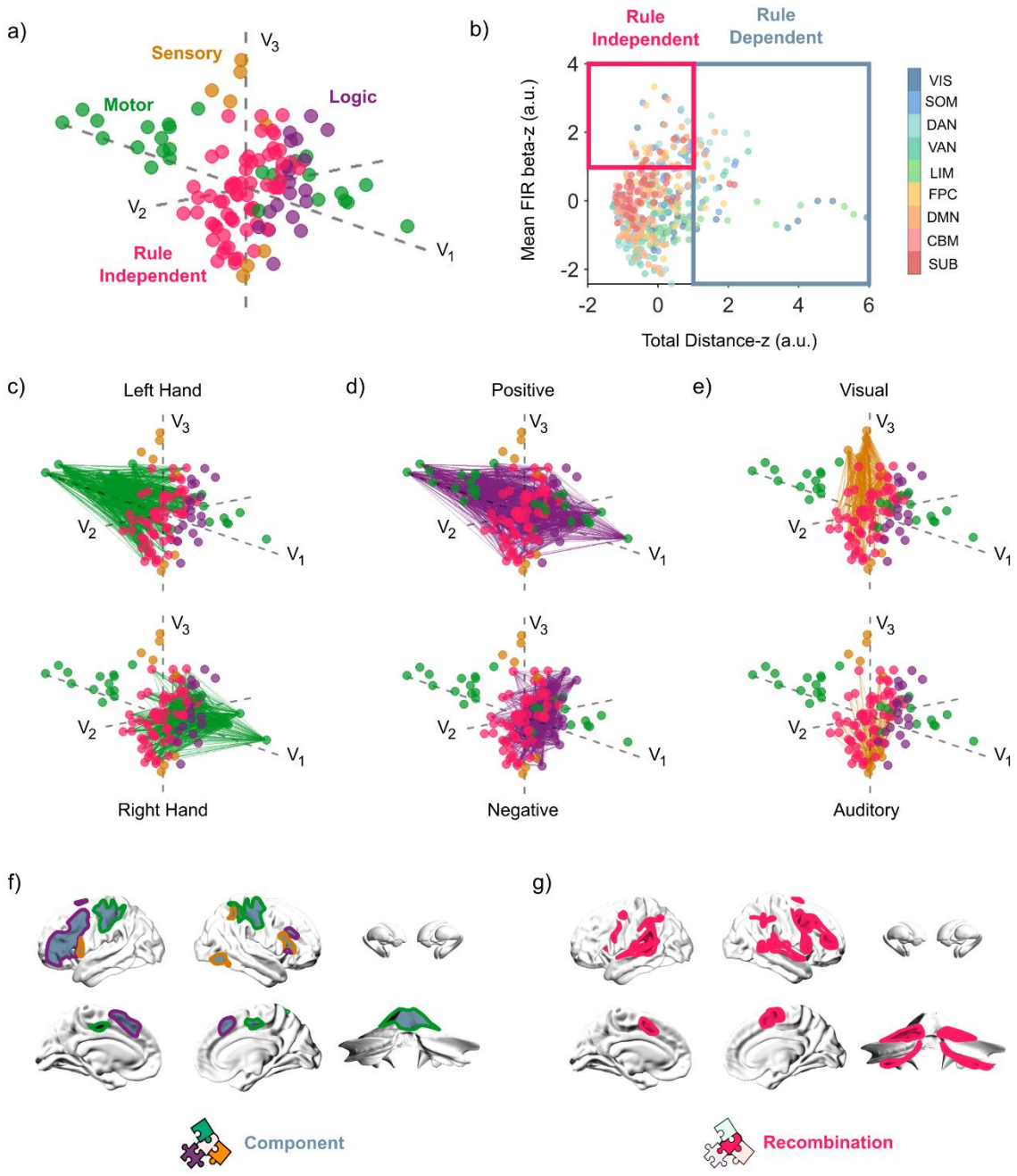

Figure 3. Identifying Regions Involved in Compositional Recombination. a) 3D visualisation of rule dependent and rule independent brain region at t = 7 using the first 3 latent variables. Rule independent regions were coloured in pink. Rule dependent regions (green, purple, orange) were coloured by the rule domain (Motor, Logic, Sensory) that they were most biased towards. Euclidean distance was calculated for each region to the origin (0,0). b) Plotting regions by distance from the origin and average FIR estimate. Both measures were z-scored and boundaries were drawn at x = 1 (separated rule dependent regions) and y = 1 (separated rule independent regions). Regions were coloured by the Yeo 7-networks (Yeo *et al.*, 2011), cerebellum, and subcortex. c-e) Significant functional connectivity between rule independent and rule dependent regions for each rule domain. c) Regions for Left Hand (top) and Right Hand (bottom) rules. d) Regions for Positive logic (top) and Negative logic (bottom) rules. e) Regions for Visual (top) and Auditory (bottom) rules. f) Brain visualisation of

Component regions with outlines coloured by specific rule domains. g) Brain visualisation of Recombination regions with outline.

To test whether the rule independent regions identified from the PLS analysis were selectively correlated with specific Components (criteria *iii*), we calculated functional connectivity matrices using Pearson's correlation of time series during the trial period. We compared the strength of functional connectivity patterns between rules in each domain (left hand – right hand; positive – negative; visual – auditory). Functional connectivity differences were consistent across rule independent regions for motor and sensory domains. Specifically, rule independent regions showed higher functional connectivity to rule dependent regions that were biased towards the specific rule – i.e., 64/65 regions showed significantly higher functional connectivity to left hand regions in left hand contexts ($p < 0.05$; Figure 3c), 56/65 regions showed significantly higher functional connectivity to positive Logic regions in positive Logic contexts ($p < 0.05$; Figure 3d), and 60/65 regions showed significantly higher functional connectivity to visual regions in visual rule contexts ($p < 0.05$; Figure 3e). Note that bias towards positive Logic or negative Logic was driven by whether the participant responded, in which case there were significantly more incorrect responses during negative Logic contexts. A conjunction analysis across these three contexts identified 51/65 regions that were significant across all three Component trial types (Figure 3g). Importantly, the 51 regions we identified were distributed across both the frontoparietal cerebral cortex and the cerebellum thus providing robust evidence in support of our original hypothesis. From these sets of analyses, we have identified a set of regions serving rule dependent Component processes and a set of regions that fit our criteria for Recombination. For detailed atlas labels of Component and Recombination regions refer to Supplementary Material Tables 1 and 2.

The Recombination Network is Low-dimensional, Generalises Across Task Contexts, and is Integrated

The extent to which neural activity generalises has been related to the dimensionality of the neuronal time series – i.e., time series of generalisable neurons were low-dimensional with low separability across contexts, whereas non-generalisable neurons were more complex, high-dimensional and were separable across contexts (Fusi et al., 2016; Israely et al., 2025). To apply this framework at the macro-scale, for every participant we measured the dimensionality of Recombination and Component regions separately, using principal component analysis (PCA)

on participant-level FIR time series concatenated across mini-blocks. We then compared the difference in variance explained by the first principal component (PC_1) between Recombination and Component regions using paired t-tests. Across participants, PC_1 of Recombination regions explained on average 8.33% more variance than PC_1 of Component regions (t_{86} = 15.34, s.d. = 5.06, p < 1e-16, 95% CI [7.25 9.41]). Furthermore, when comparing the variance explained across the top 3 principal components for each group, we observed that the explained variance was more 'front-loaded' for Recombination regions (PC_1 dominated the explained variance), whereas the explained variance was more distributed among the top principal components for Component regions (Figure 4a). Specifically, PC_2 and PC_3 explained 6.26% and 1.46% more variance for Component regions compared to Recombination regions (PC_2: t_{86} = 20.72, s.d. = 2.82, p < 1e-16, 95% CI [5.66 6.86]; PC_3: t_{86} = 5.89, s.d. = 2.31, p = 7.24e-08, 95% CI [0.97 1.95]), respectively. These results demonstrate that Recombination regions were low-dimensional compared to Component regions, suggesting that recruitment of Recombination regions had low separability across mini-blocks, whereas recruitment of Component regions had higher separability across mini-blocks.

Both Component and Recombination regions are important for compositional cognition, however the differential contributions of these regions to the task are hard to dissociate using traditional analyses. We hypothesised that the coupling of a given region's activation to the task context would differentiate the two groups. Using this feature, we predicted that Recombination regions would be non-specific – e.g., no matter whether the mini-block uses right or left hand, the region will have the same response (Figure 4b; pink), whereas Component regions will be more specific to the context – e.g., regions that are specific to right hand rules will have different patterns during mini-blocks with left hand rules (Figure 4b; silver).

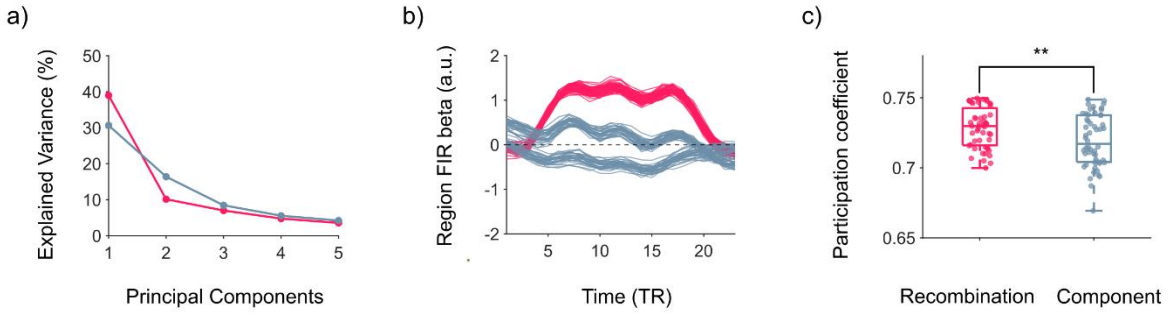

Figure 4. Characteristics of Recombination regions. a) Group average beta estimates across time for an example region from Recombination (pink) and Component (silver) regions. Each line is the FIR estimate for a different mini-block. b) Mean explained variance for the top 5 principal components (PCs) of Recombination (pink) and Component (silver) regions. c) Boxplot of participation coefficient scores for Recombination (pink) and Component (silver) regions. Each dot is a region. Centre line, median, box limits, upper and lower quartiles. Whiskers, 1.5x interquartile range. ** denotes significant difference $p < 0.01$.

To test this hypothesis, for every participant, we correlated each region's FIR time series within each mini-block to every other mini-block. We compared the similarity of FIR estimates between Recombination and Component regions using a generalised linear mixed model, while controlling for repeated measures across participants. Consistent with our prediction, Recombination regions were more correlated than Component regions across mini-blocks ($t_{9,913}$ = 42.58, p < 1e-16, 95% CI [0.11 0.12]). Therefore, recruitment of Recombination regions was non-specific and generalised across all mini-blocks, while recruitment of Component regions was specific to the rules being implemented.

A key feature of Recombination regions is their ability to flexibly interact with the rest of the brain. To measure the extent of communication between distinct brain regions, we used a measure of integration (Rubinov & Sporns, 2010). We calculated participation coefficients for Recombination and Component regions using a population averaged functional connectivity matrix (refer to *Methods*). From these analyses, Recombination regions were more integrated with the rest of the brain compared to Component regions (t_{103} = 2.93, s.d. = 0.02, p = 0.004, 95% CI [0.003 0.016]; Figure 4c). Overall, Recombination regions were low-dimensional, generalised across task contexts, and integrated with the rest of the brain.

Discussion

Compositional cognition can be characterised by two related yet separable processes: the specialised Components that are recruited to achieve the task demands, and the more generalised process of Recombination that allows these components to be applied in novel situations. Here, we used dimensionality reduction, time-varying modelling and functional connectivity to interrogate functional MRI measurements collected during a compositional task (C-PRO) in an effort to dissociate these processes. We found clear evidence that the two processes differed. First, Components were embedded in specific contexts and rules, whereas Recombination was a feature that generalised across all contexts. Second, regions related to

Recombination were low-dimensional and distributed across cortical and subcortical (predominantly cerebellar) regions, whereas task components were high-dimensional and predominantly identifiable in cortical specialist regions. Finally, we demonstrated that compositional cognition required specific, dynamic interactions and differentiation between these two processes, and that the Recombination network was low-dimensional, integrated, and generalised across task contexts. Overall, these results provide evidence that whole-brain interactions underpin two distinct processes forming compositional cognition.

During compositional cognition, generalisation is important for flexibility and applying similar behaviours across many different contexts, whereas specialisation is important for distinguishing between behaviours and adding complexity and nuance (Fusi et al., 2016; Tye et al., 2024). In human neuroimaging studies, brain networks have been described using specialised or generalised functions. For example, task fMRI studies have described a range of brain networks from specialised sensory functions (i.e., motor network; Livne *et al.*, 2022) to generalised higher cognitive functions (i.e., cognitive control; Spreng and Grady, 2010). However, typically these networks encompass the whole task – e.g., generalised networks are recruited during tasks that recruit higher cognitive functions, such as the n-back task. Our study expands on these frameworks, applying measurements from neural population studies (Muscinelli et al., 2023; Posani et al., 2025) to demonstrate that both specialised and generalised brain networks exist during compositional cognition. Our results identified two distinct task-related networks consisting of Component and Recombination regions. Component regions were tightly coupled to specific rules and contexts – e.g., regions recruited for right-hand movements were not recruited during left-hand movements, whereas Recombination regions were recruited regardless of the context and rule. By characterising macro-scale signatures of task fMRI through neural population measures, we offer a more nuanced explanation of how specialised and generalised networks give rise to compositional cognition.

Recombination recruits a distributed cortico-cerebellar network that is not associated with specific rules of the paradigm. Recombination is typically associated with specific areas of the brain, such as the frontoparietal control network (Cocuzza et al., 2020; Cole, Reynolds, et al., 2013) and hippocampus (Bakermans et al., 2025; Schwartenbeck et al., 2023). Our results expand on this framework by taking a whole-brain perspective, identifying a distributed cortico-cerebellar network important for recombination (Figure 3g). Crucially, while some rule independent regions overlap with frontoparietal areas, we also find evidence for regions from

the superior temporal cortex and cerebellum to serve a role in Recombination. The superior temporal cortex is related to several functions such as language, memory, and emotion (Baylis et al., 1987; Karnath, 2001). We found bilateral recruitment of superior temporal regions, contrasting with previous studies that show lateralised functionality for language and spatial processing in the temporal lobe (Baylis et al., 1987; Bonelli et al., 2012). Smaller subdivisions of the superior temporal cortex can be found using high-resolution imaging techniques (Carr et al., 2010), with rostral temporal areas serving as integrative hubs for visual information (Karnath, 2001). Therefore, alongside the hippocampus, rostral temporal regions also contribute to compositional cognition.

There is growing evidence that the cerebellum which is typically associated with motor movements and coordination is also important for cognitive processes such as pattern separation and prediction (Cayco Gajic & Silver, 2019; Koziol et al., 2014; Prati et al., 2024). From our results, we dissociated between anterior cerebellar lobules (I-V) and more posterior lobules (VI, VIIb, and VIIIa), where the anterior lobules were related to Components and rule specialisation and the posterior lobules were related to Recombination and generalisation. This dissociation follows with overall cerebellar functional patterns that dissociate between motor regions (anterior) and higher order executive functions (posterior) (Guell et al., 2018). Lobules VI, VIIb, and VIIIa have specifically been associated with motor planning (M. King et al., 2019), and the multi-demand network (Duncan et al., 2020), including functions such as updating, shifting, and inhibition (Nettekoven et al., 2024; Zhi et al., 2025).

During recombination, depending on how components are recombined, there will be different behavioural outcomes. Due to the cerebellum's role in pattern separation (Cayco Gajic & Silver, 2019), the cerebellum can aid in developing internal models that control how components are recombined during compositional cognition (Imamizu & Kawato, 2009; Wolpert et al., 1998, 2003). Through these models, the cerebellum contributes to refining the recombination of task-components. In cats and monkeys, the cerebellum shares anatomical connections with the temporal cortex (Heath & Harper, 1974), therefore it is possible that these connections were also preserved in the human brain therefore forming a cortico-cerebellar circuitry specifically recruited for recombination. To gain a more concrete understanding of this cortico-cerebellar circuitry future studies can try manipulating outputs from the cerebellum (Israely et al., 2025) while recording from the temporal cortex. Hence, contributions from the cerebellum to the temporal cortex may facilitate recombination and generalisation of actions across contexts.

Task networks dynamically interact depending on the task context. In compositional cognition and generally across task fMRI studies, understanding the influence of task design and changing contexts on neural signatures is underdeveloped (Poldrack, 2012; Smith, 2012), where connectivity approaches typically analyse the whole task, identifying a consensus task network – through averaging and thresholding, that is "on" during the task and "off" in other stages. These approaches lack the nuance to identify networks that underlie the cognitive function and networks that result from the task design. For example, motor responses are useful in signalling whether a participant completes the task, however this can result in motor networks appearing in task fMRI results including higher cognitive functions (Bennett & Miller, 2013). To account for influences of task design on BOLD signatures, studies have explored modelling (Friston et al., 1998) and regressing out task responses and timing (Cole et al., 2019). While regressing out task responses accounts for task design biases, it can also remove context specific dynamics between brain networks. In this study, we followed an alternative approach by first separating out networks related to the cognitive function and networks related to task design. Using this approach, we revealed that a generalised recombination network flexibly interacts with a specialised component network, increasing connectivity to regions depending on the task context. These results demonstrate that both networks are important for compositional cognition and dynamically interact through the task. A limitation of this study is the inability to compare novel recombination i.e., generalisation to a new context, versus generalisation to a previously seen context (repeated recombination). It is possible that repeated recombination is comparable to automatic (over-learned) behaviours and no longer requires the recombination network. Future studies can include multiple repeats of a specific recombination context to test how learning impacts recombination. Therefore, understanding interactions between component and recombination networks provides a dynamic perspective on how brain networks meet task demands.

Developing a paradigm that can elicit compositional cognition in combination with human fMRI is non-trivial. Compositional task designs require task components that are easily learned but are combinable into complex paradigms with enough variation to induce novelty throughout the task. Among the paradigms that have achieved this balance (T. Ito et al., 2017; Reverberi et al., 2012; Schwartenbeck et al., 2023), the C-PRO paradigm stands out as a well-established example (Cocuzza et al., 2020; T. Ito et al., 2017; T. Ito, Yang, et al., 2022), with recent updates to the C-PRO paradigm further improving the ecological validity of the task stimuli (Mill & Cole, 2025). However, one aspect that is still lacking in the C-PRO paradigm

is the range of task variability. During the C-PRO paradigm, task variations occur on the scale of 1-3 rules. While this is optimal for adaptation across explicitly similar skills (e.g., adapting tennis skills to pickle ball), adaptation can also occur between skills that overlap at an abstract level (e.g., adapting tennis skills to chess; Taatgen, 2013). Currently, adaptation at the abstract level has been explored in neural networks (Driscoll et al., 2024; G. R. Yang et al., 2019) but is yet to be explored in human fMRI. Future studies could explore compositional cognition at the abstract level by having individuals perform a multitude of tasks that overlap at an abstract level.

Compositional cognition is facilitated by two distinct processes: Component engagement and Recombination. Recombination recruited a cortico-cerebellar circuitry that generalised across task contexts, whereas task components were only recruited for the specific rules that they were strongly related to. Functional connectivity between these two processes were context dependent. Together, these findings demonstrate that compositional cognition is facilitated by dynamic whole-brain interactions.

Acknowledgements

The authors acknowledge the University of Sydney HPC service at The University of Sydney for providing HPC resources that have contributed to the processing of the data contained within this data collection. All final writing and interpretations are the authors' own.

Funding

Australian National Health and Medical Research Council Fellowship 2016866 (CO)

Australian Research Council DP240101295 (JMS)

Australian Research Council DP250102186 (JMS, CO, EJM)

Canadian Institutes of Health Research MFE193920 (GB)

Discovery Early Career Researcher Award DE250100540 (EJM)

National Health and Medical Research Council GNT1193857 (JMS)

Research Training Program Stipend SC3227 (JBT)

University of Sydney Robinson Fellowship (CO)

Author Contributions

Conceptualization: JBT, JMS, EM, CO

Methodology: JBT, IO, RW, JK, JJ, GB, EM, JMS, CO

Formal Analysis: JBT

Visualization: JBT

Writing—original draft: JBT, JMS, CO

Writing—review & editing: JBT, IO, RW, JK, JJ, GB, EM, JMS, CO

All roles and responsibilities of the co-authors were agreed on.

Competing Interests:

Authors declare that they have no competing interests.

Data and Code Availability

All imaging and behavioural data are publicly available in an OpenNeuro repository (accession number ds003701). Analysis of both the behavioural and functional MRI data was conducted in MATLAB v2022b. Code required to reproduce the statistical analyses and figures are publicly available at https://github.com/ShineLabUSYD/Compositionality_C-PRO.

Chapter 4 Summary

In Chapter 4, we explored how automatised behaviours are recombined to produce novel behaviours, also known as compositional cognition. We dissociated between two processes that facilitate compositional cognition: Components which relates to networks that were embedded in automatised, specialised behaviours (e.g. button pressing, processing visual or auditory stimuli) and Recombination, a cortico-cerebellar network that recombines specialised behaviours for generalised performance. The cortico-cerebellar network underlying Recombination demonstrated characteristics related to generalisation such as low-dimensional embedding, integration with the rest of the brain, and generalisable responses across different task contexts. Furthermore, these characteristics were also found in multi-tasking recurrent neural networks, demonstrating that these characteristics are underlying features that separate Recombination and Component processes during compositional cognition, irrespective of the specific implementation-level details of each system.

In this final empirical chapter, we explored features underlying compositional cognition to understand how the brain implements flexible, generalisable behaviours. A pitfall of automatised behaviours is that they can be inflexible and non-generalisable. Compositional recombination overcomes this limitation allowing for flexible application of automatised behaviours across contexts even extending to novel situations. In this study, we dissociated Components that relate to automatised behaviours, and Recombination, the process that generalises automatised behaviours across contexts. Between the two, we also dissociated between cerebellar lobules. Specifically, lobules I-V which serve functions such as finger tapping and motor actions was associated with Component processes, whereas lobule VI (same as Chapter 2), VIIb, and VIIIa were associated with Recombination. Together these results dissociate between motor regions (anterior) and higher order executive functions (posterior) (Guell et al., 2018).

In empirical Chapter 2, 3, and 4, we have shown examples of cerebellar involvement in cognitive automaticity, overlapping circuitry between motor and cognitive actions in the cerebellum, and finally how a cortico-cerebellar network recombines automatised behaviours. In the next chapter, we will summarise our findings and discuss limitations and future directions for cerebellar and automaticity neuroimaging.

Chapter 5: Conclusion

In this thesis, we have argued that a distributed cortico-cerebellar network underlies cognitive automaticity by facilitating flexible application and adaptation of a range of cognitive capacities. In Chapter 2, we demonstrated that a distributed network that includes the cerebellum provided unique contributions to a mental rotation task which serves as an example of working memory manipulation and cognitive automaticity. In Chapter 3, we showed that expertise in sensorimotor adaptation was achieved through delegation of the task to the cerebellum, and that adaptive learning was driven by variable neural activity during initial learning periods. In Chapter 4, we identified a cortico-cerebellar network that facilitates compositional recombination of behaviours and described key features that promote flexible adaptation. Together, these findings highlight cortico-cerebellar interactions during cognitive automaticity, placing this circuitry at the forefront for developing expertise.

5.1 Summary of key findings

In Chapter 2, we investigated whether the cortico-cerebellar network was important for cognitive automaticity by observing performance during a mental rotation task. In this study, participants achieved consistent performance across two separate scanning sessions (indication for achieving automaticity) while judging whether two images were the same or mirrored. To judge whether the two images were the same or mirrored, requires the ability to mentally rotate the images and predict the shape of the image with different orientations. By investigating the fMRI BOLD signal during these sessions, we found that the cortico-cerebellar network was associated with task difficulty, with greater recruitment observed with increasing requirement for mental rotation. Notably, differences between correct and incorrect performance were decided by recruitment of distributed network including cerebellar and subcortical regions.

A key finding from this study showed that increasing the angular rotation of the stimuli resulted in increased BOLD recruitment but had no effects on the length of the BOLD response. Supposedly, if participants were mentally rotating the stimuli, then an increased angular rotation should result in more mental rotation and a longer period of neural activity response. Our results did not reflect this hypothesis which can be attributed to several reasons. First, the temporal resolution of the data was on the scale of seconds (TR = 1 second), whereas mental

rotation occurs on the sub-second timescale. Therefore, the data may not be able to capture temporal differences between task difficulties. Alternatively, the innate temporal resolution of the BOLD signal may not be appropriate for capturing these effects (Bolt et al., 2025), even if the temporal resolution was decreased to sub-second timescale. If these results hold true even at finer temporal resolutions, then the results suggest that cognitive automaticity is perhaps stored similar to a look-up table, where distinct features of the stimuli are associated with specific responses i.e., each feature has a separate associated response that can be recruited as a shortcut to complete the mental rotation task (Logan, 1988). Future studies can corroborate these ideas by using neural recordings in animals completing a similar task or replicating this study in humans but with sub-second temporal resolution.

In Chapter 3, we explored the relationship between BOLD activity and expertise in a sensorimotor adaptation paradigm. Previous studies noted that increased proficiency in a task resulted in decreased activity in the output regions – decreased activity in motor areas for a motor task (Bassett et al., 2015). These changes were explained through ideas such as neurons becoming more efficient (Bassett et al., 2015) and brain areas delegating task-associated resources to subcortical and cerebellar areas (Shine & Shine, 2014). In line with the second hypothesis, we demonstrated that higher expertise in sensorimotor adaptation related to a shift in BOLD recruitment from primary motor regions to a distributed network that includes the cerebellum. These findings do not discount that expertise could result in increased neural efficiency in output areas, specifically learning-induced changes on neural plasticity (Doyon & Benali, 2005). However, this would require direct measurements of neural activity which is unavailable through fMRI methods. By using spatial specificity obtained from fMRI studies, direct neural measurements from electrodes implanted in these areas may provide a comprehensive perspective on expertise-related changes in neural activity.

Variability in BOLD data has only recently been acknowledged as an informative measure as opposed to disregarded as “noise”. The BOLD signal was plagued by various confounds, such as head motion and scanner sounds (Power et al., 2014). These putative artifacts introduce variability in the BOLD signal, and were often identified as non-neural related signals that would be removed during signal cleaning (Aquino et al., 2020). Due to these confounds, any variability in the signal including individual variation, was typically attributed to non-neural sources and weakened by only observing changes at the population level. However, there is now growing appreciation for understanding variability and what it means for the BOLD signal to be variable (Baracchini et al., 2021; Grady et al., 2023; Grady & Garrett, 2014). We explored

how variability in BOLD data related to variability in actions (Garrett et al., 2011) and learning. We found that greater variability in the BOLD signal during early learning, resulted in better performance and greater improvement by the end of the task. This contrasted with individuals who performed well at the beginning, but progressively performed worse as the task progressed. Furthermore, by explaining variability through the lens of the attractor landscape (Munn et al., 2021) and combining the results with trained recurrent neural networks, we were able to make inferences about the relationship between neural variability and different learning strategies. By showing matching results in both the fMRI data and neural networks, we provide cross-modality evidence for variability in brain activity (direct and indirect) as insightful for behaviour. Explaining learning strategies through the attractor landscape and the possible affordances during learning is an important step to understanding individual variability during learning (Chang et al., 2024). Therefore, our findings suggest that BOLD variability and possibly neural variability is important for developing expertise, providing insights into how different learning strategies impact behavioural flexibility.

In Chapter 4, we focused on how a distributed cortico-cerebellar facilitated the flexible recombination of automatised behaviours to generate complex, novel behaviours. Complex behaviours can be broken down into separate components. For example, in order to hit a tennis ball, you need to know how to swing the racquet, how to position your body correctly, and the correct timing to hit the ball. Then, each time you hit a tennis ball, these components are recombined in various forms depending on what is needed. To investigate how the brain flexibly recombines these components we analysed BOLD activity during the Concrete Permuted Rules of Operations (C-PRO) paradigm (T. Ito et al., 2017). Through partial least squares analysis, we separated out component-related brain patterns, and brain patterns related to recombination. We found that recombination was dependent on a distributed cortico-cerebellar network. BOLD patterns of recombination regions generalised across all task variations, whereas component-related patterns were only recruited for specific rule components. Previous work has suggested that neuronal populations can differ in selectivity, with some neuron populations showing high selectivity to specific stimuli, and other populations showing mixed selectivity (Fusi et al., 2016; Tye et al., 2024). We showed that this framework can also be used to describe brain activity at the macro-scale with whole-brain patterns that showed high selectivity for specific rule components, and a cortico-cerebellar circuit that showed mixed selectivity. Therefore, cortico-cerebellar interactions facilitate behavioural flexibility by compositionally recombining automatised behaviours.

5.2 Future Directions

The work presented in this thesis contributes greatly to understanding the role of the cortico-cerebellar circuitry in cognitive automaticity. Open questions remain around important and pertinent topics addressed in this thesis, for instance: how to interpret the BOLD signal in the cerebellar cortex? What is next for cerebellar neuroimaging? How to further push dimensionality reduction approaches to understand automaticity and skill expertise? In the following section, we will discuss these topics, with a focus on the inherent limitations within each study as well as how future studies can address these questions and limitations.

Interpreting BOLD signal in cerebellar cortex

Other than the aforementioned points about lower signal-to-noise ratio and difficulties in cerebellar functional imaging, a recent discussion about the relationship between neuronal activity in the cerebellar cortex and the BOLD signal has emerged (Shahshahani et al., 2024). Electrical stimulation of mossy fibres (Gagliano et al., 2022; Mapelli et al., 2017) and parallel fibres (Attwell & Iadecola, 2002; Iadecola et al., 1996; Mathiesen et al., 1998) in the rat cerebellum demonstrated robust increases in cerebellar blood flow, whereas the effect of Purkinje cell firing on blood flow was less clear. For example, excitation of Purkinje cells in the rat cerebellar cortex seemed to have minimal effects on oxygen changes in the cerebellar cortex (Thomsen et al., 2009). Based on these pieces of evidence, it was suggested that BOLD dynamics in the cerebellar cortex were mainly driven by mossy fibre inputs to granule cells. How does this understanding challenge the interpretations of cerebellar cortical BOLD dynamics? From the current evidence, it would suggest that BOLD changes in the cerebellar cortex were mainly driven by cerebral cortical input rather than cerebellar cortical processing and output. Therefore, rather than gaining insights into cerebellar function, the BOLD signal in the cerebellar cortex captures how the cerebral cortex communicates with the cerebellum.

The main criticism of the ability for these experiments to inform human studies is that they were all done in rats, and it is known that the size and anatomy of the cerebellum has evolved greatly in humans by comparison (Barton, 2012; Barton & Venditti, 2014). Furthermore, if BOLD dynamics in the cerebellar cortex were solely due to mossy fibre input, then we would expect cerebellar BOLD dynamics to co-fluctuate directly with cerebral cortical changes,

which was not the case (as seen from the work in this thesis). Neurobiologically, it is still unclear whether cerebellar BOLD dynamics are mainly driven by mossy fibre to granule cell inputs, by Purkinje cell outputs, or by a complex intersection of different physiological states in the cerebellum (e.g., simple vs. complex spikes; Streng et al., 2018). With recent developments in neuroimaging technology (Gozzi et al., 2025; Mackinnon et al., 2025), such as the recent cerebellar imaging using a 9.4 T scanner (Van Der Zwaag et al., 2025) and the capacity for targeted optogenetic control via specific mouse Cre lines, these questions will likely be answered in the coming years. Another point from this thesis is that the current work was completed using the SUIT cerebellar anatomical atlas. As outlined in the Introduction, depending on whether you use a structural (anatomical) or functional atlas (Nettekoven et al., 2024) can change the spatial patterns of the results. By comparing results across both structural and functional atlases we can gain a better understanding to how cerebellar contributions may be similar or different to the rest of the brain.

The future of cerebellar imaging

With growing appreciation for cerebellar contributions to both cognitive and motor functions and an increased understanding of how the cerebellum connects with the rest of the brain (Kang et al., 2021; Prati et al., 2024), what lies next for cerebellar imaging? Recent studies have used knowledge of the cortico-cerebellar circuitry to directly manipulate inputs and outputs resulting in perturbations to behaviour (Gao et al., 2018; Israely et al., 2025; Zhu et al., 2023). These studies lay out an exciting future for cerebellar imaging, demonstrating the benefits and applications from manipulating cortico-cerebellar interactions within a controlled environment. Combining insights from these experiments with reduced cortico-cerebellar models (Boven et al., 2023; Pemberton et al., 2024) will enable us to test hypotheses and gain a deeper understanding of how the cerebellum contributes to behaviour.

Another avenue for cerebellar imaging is to follow in the steps of cerebral cortical studies by diving into structural and functional patterns (Margulies et al., 2016; Pang et al., 2023). Already, underlying patterns (Guell, 2021) and structure-function coupling (L. King et al., 2025) in the cerebellum differs to the cerebral cortex. Perhaps most practical for cerebellar imaging is that neuroimaging pipelines and analyses will be updated to be appropriate for all brain structures and not just the cerebral cortex (Magielse et al., 2024). A challenge along these lines is that the cerebellar cortex is far more convoluted than the cerebral cortex in humans,

which makes the accurate unfolding of the structure challenging. There is also previous work that demonstrated the presence of multiple repeated "body maps" in the cerebellum (Boillat et al., 2020), and it is unclear how this non-Euclidean representation of body space might be effectively mapped to the cerebellar cortical surface in a manner similar to that achieved for the cerebral cortex. Thus, cerebellar imaging is stepping into the spotlight with an abundance of interesting directions to follow.

Tracking the nuanced complexity of expertise with concomitant neuroimaging

Tracking neural signatures of expertise and complex behaviours is non-trivial. When individuals interact with their surrounding environment, there is a vast number of affordances available. So many that you would not expect two individuals to make the same actions or even the same individual to make the same action in two separate instances. To keep actions consistent across time and individuals, neuroimaging experiments create simplified psychological paradigms that capture foundation blocks of behaviour. By enforcing strict control over the behaviour and possible actions, the investigators can constrain behaviour to be consistent. However, while this enhances the reproducibility and statistical robustness of findings, it lacks the ecological validity to connect with naturalistic behaviours and trivialises expertise – i.e., rather than a goal to work towards, expertise is easily achieved. Furthermore, some paradigms are so 'simple' and repetitive, that participating individuals become bored and apathetic, requiring explicit monetary rewards to incentivise participation.

An alternative that is more ecologically valid than psychological paradigms but still provides a controlled set of actions within an environment is using video games. Video games are engineered intuitive real-world environments that are enjoyable and intrinsically motivating, minimalising problems of individual's disengaging with the task. Through video games, it is possible to investigate neural correlates underlying complex behaviours and add nuance to research questions (e.g., understanding individual strategic differences; (Allen et al., 2023; Tomov et al., 2023). The main barrier for combining video games and research is that video games have in-built elements that are unrelated to the behaviour, meaning that the structure and design of video games can be a strong confounder for the results. This can be alleviated in a couple ways: modifying or creating a personalised game that controls for these confounds or combining existing psychological paradigms as the control and baseline of the behaviour being

tested in the video game. With improvements in analysis techniques and modelling, it is only a matter of time before video games are more integrated into neuroimaging experiments.

Characterising expertise using dimensionality reduction

Dimensionality reduction techniques are a powerful tool for simplifying interpretations of neuroimaging data as seen in this thesis. However, caution with these approaches must be emphasised as they always produce an output and can result in results that do not relate to the research question. Most importantly, dimensionality reduction techniques are limited by the data. For example, some latent components in the BOLD signal are strongly related to physiology rather than neural activity (Bolt et al., 2022; Shinn et al., 2023). To focus on neural related latent components, it is important to relate any outputs to behaviour (Churchland et al., 2012), task design (Krishnan et al., 2011), pre-established patterns (Margulies et al., 2016; Markello et al., 2022) or even meta-analyses (Magielse et al., 2024; Salo et al., 2022).

With the advent of computational modelling, and more recently artificial intelligence, models built to conduct 'brain-like' operations are becoming more prevalent. A key limitation of neural networks and AI-like generative models is that they can be characterised as "black box" – they can learn to mimic almost any task given to them, but we remain ignorant of how these models have solved the task (Sussillo & Barak, 2013). This can be an issue as while models can be pushed to learn almost anything, it is less meaningful if the method of solving the problem is nothing like our brains. In such scenarios, dimensionality reduction techniques bridge the gap between *in vivo* and *in silico*, where latent components with similar features suggest common inner workings between the two (Sussillo & Barak, 2013). These approaches have developed to an extent that they now characterise behaviours through state-space analysis. Through dimensionality reduction, a state-space is created via the latent components that can be interpreted using geometric measurements (Chang et al., 2024; Gallego et al., 2017, 2018). In these state-spaces, it is possible to infer different brain-states while completing an action, as well as infer how different stimuli presentation and learning can change the structure of these state-spaces (Chang et al., 2024; Meirhaeghe et al., 2023). Using dimensionality reduction to construct state-spaces of expertise and skilled movements serves as a powerful lens to understand how our brains dynamically engage with the environment. A consideration regarding dimensionality reduction approaches is that the interpretations can vary depending on what spatial or cognitive scale they are measured e.g., the prefrontal cortex has been

described as both low and high dimensional (Badre et al., 2021). It is important that interpretations of dimensionality are compared across both spatial and cognitive scales to standardise interpretations and definitions across the literature. Overall, these approaches are a staple for neuroimaging analyses and will be essential for integrating neuroimaging, model simulations, and behaviour.

Translating cerebellar insights from the bench to the bedside

Our understanding of the cortico-cerebellar circuitry can be applied to patient populations. Cerebellar dysfunction and degeneration has been linked to a range of motor diseases such as Parkinson's disease (O'Callaghan et al., 2016), dystonia and ataxia among others (Bastian et al., 1996; Gellersen et al., 2017; Manto, 2008; Reeber et al., 2013). Based on both human and animal studies, dysfunctional Purkinje cells are the main drivers of these diseases (Manto et al., 2022; Reeber et al., 2013). To confirm the role of Purkinje cells in diseases, genetic models of dystonia in mice and rodents have demonstrated that Purkinje cells lose their regular firing patterns, emitting irregular burst-like patterns instead (Reeber et al., 2013). These symptoms were then alleviated with the removal and degeneration of Purkinje cells (Reeber et al., 2013). By applying our understanding of the cortico-cerebellar circuitry to animal models of diseases, a deeper understanding of symptoms and treatment is attained.

The cerebellum's role in diseases goes beyond motor dysfunction possibly contributing to cognitive impairment and a wider range of symptoms (Streng, 2023; Streng et al., 2024). Among higher order cognitive deficits, the cerebellum has been linked to impaired emotional and language processing in developmental disorders and Autism Spectrum Disorders (Manto et al., 2022; Prati et al., 2024). One way to understand the role of cerebellar dysfunction in these disorders is by framing Autism Spectrum Disorder as a disorder of prediction (Sinha et al., 2014). In this framework, the rigidity and anxiety present in individuals with autism arises from a necessity of repetitive behaviours and an inability to make accurate predictions of their surroundings (Sinha et al., 2014). Previously in this thesis we have argued for the cerebellum's role in prediction and pattern separation. Therefore, cerebellar dysfunction possibly serves to compromise prediction capabilities, inducing anxiety in individuals with autism. As prediction serves as the backbone of sensory functions, it is possible that cerebellar dysfunction also plays a common role amongst sensory dysfunctions (e.g. visual hallucinations; Bar, 2004). With the cerebellum sharing direct and indirect connections to many other parts of the brain (Kang et

al., 2021; Prati et al., 2024), it is important to reassess the role of the cerebellum across neurodegenerative and neurodevelopmental diseases and disorders.

5.3 Concluding Remarks

In this thesis, we have demonstrated that the cortico-cerebellar circuitry serves an important role in cognitive automaticity and expertise. In addition, we have shown that the cerebellum provides unique insights into automaticity, distinct from the cerebral cortex. Future studies can further explore these contributions by causally manipulating the cortico-cerebellar circuitry and observing changes in behaviour. Furthermore, with ongoing technological improvements such as high-resolution scanning of the cerebellum combined with more complex 'brain-like' models, understanding cerebellar function is inevitable. By broadening our perspective to include the whole brain, we can understand how the whole brain works together to develop automaticity and expertise.

References

Please note, the reference list below corresponds to the references for all chapters of this thesis.

Abdi, H. (1994). A neural network primer. *Journal of Biological Systems*, *2*(3), 247–281.

Abdi, H., & Williams, L. (2010). Barycentric Discriminant Analysis. In *The SAGE Encyclopedia of Research Design*. Sage.

Albus, J. S. (1971). A theory of cerebellar function. *Mathematical Biosciences*, *10*(1–2), 25–61. https://doi.org/10.1016/0025-5564(71)90051-4

Allen, K. R., Brändle, F., Botvinick, M. M., Fan, J., Gershman, S. J., Gopnik, A., Griffiths, T. L., Hartshorne, J. K., Hauser, T. U., Ho, M. K., De Leeuw, J. R., Ma, W. J., Murayama, K., Nelson, J. D., Van Opheusden, B., Pouncy, H. T., Rafner, J., Rahwan, I., Rutledge, R., … Schulz, E. (2023). *Using Games to Understand the Mind* [Preprint]. PsyArXiv. https://doi.org/10.31234/osf.io/hbsvj

Anguera, J. A., Russell, C. A., Noll, D. C., & Seidler, R. D. (2007). Neural correlates associated with intermanual transfer of sensorimotor adaptation. *Brain Research*, *1185*, 136–151. https://doi.org/10.1016/j.brainres.2007.09.088

Apps, R., Hawkes, R., Aoki, S., Bengtsson, F., Brown, A. M., Chen, G., Ebner, T. J., Isope, P., Jörntell, H., Lackey, E. P., Lawrenson, C., Lumb, B., Schonewille, M., Sillitoe, R. V., Spaeth, L., Sugihara, I., Valera, A., Voogd, J., Wylie, D. R., & Ruigrok, T. J. H. (2018). Cerebellar Modules and Their Role as Operational Cerebellar Processing Units. *The Cerebellum*, *17*(5), 654–682. https://doi.org/10.1007/s12311-018-0952-3

Aquino, K. M., Fulcher, B. D., Parkes, L., Sabaroedin, K., & Fornito, A. (2020). Identifying and removing widespread signal deflections from fMRI data: Rethinking the global signal regression problem. *NeuroImage*, *212*, 116614. https://doi.org/10.1016/j.neuroimage.2020.116614

Areshenkoff, C., Gale, D. J., Standage, D., Nashed, J. Y., Flanagan, J. R., & Gallivan, J. P. (2022). Neural excursions from manifold structure explain patterns of learning during human sensorimotor adaptation. *eLife*, *11*, e74591. https://doi.org/10.7554/eLife.74591

Arslan, S., Ktena, S. I., Makropoulos, A., Robinson, E. C., Rueckert, D., & Parisot, S. (2018). Human brain mapping: A systematic comparison of parcellation methods for the human cerebral cortex. *NeuroImage*, *170*, 5–30. https://doi.org/10.1016/j.neuroimage.2017.04.014

Attwell, D., & Iadecola, C. (2002). The neural basis of functional brain imaging signals. *Trends in Neurosciences*, *25*(12), 621–625. https://doi.org/10.1016/S0166-2236(02)02264-6

Baddeley, A., & Hitch, G. (1974). Working Memory. *Psychology of Learning and Motivation*, *8*, 47–89. https://doi.org/10.1016/S0079-7421(08)60452-1

Badre, D., Bhandari, A., Keglovits, H., & Kikumoto, A. (2021). The dimensionality of neural representations for control. *Current Opinion in Behavioral Sciences*, *38*, 20–28. https://doi.org/10.1016/j.cobeha.2020.07.002

Bai, B., Kantor, P., & Shokoufandeh, A. (2007). Effectiveness of the Finite Impulse Response Model in Content-Based fMRI Image Retrieval. In N. Ayache, S. Ourselin, & A. Maeder (Eds.), *Medical Image Computing and Computer-Assisted Intervention – MICCAI 2007* (Vol. 4792, pp. 742–750). Springer Berlin Heidelberg. https://doi.org/10.1007/978-3-540-75759-7_90

Baier, B., Müller, N. G., & Dieterich, M. (2014). What part of the cerebellum contributes to a visuospatial working memory task? *Annals of Neurology*, *76*(5), 754–757. https://doi.org/10.1002/ana.24272

Bakermans, J. J. W., Warren, J., Whittington, J. C. R., & Behrens, T. E. J. (2025). Constructing future behavior in the hippocampal formation through composition and replay. *Nature Neuroscience*. https://doi.org/10.1038/s41593-025-01908-3

Balsters, J. H., Cussans, E., Diedrichsen, J., Phillips, K. A., Preuss, T. M., Rilling, J. K., & Ramnani, N. (2010). Evolution of the cerebellar cortex: The selective expansion of prefrontal-projecting cerebellar lobules. *NeuroImage*, *49*(3), 2045–2052. https://doi.org/10.1016/j.neuroimage.2009.10.045

Balsters, J. H., & Ramnani, N. (2008). Symbolic representations of action in the human cerebellum. *NeuroImage*, *43*(2), 388–398. https://doi.org/10.1016/j.neuroimage.2008.07.010

Balsters, J. H., & Ramnani, N. (2011). Cerebellar Plasticity and the Automation of First-Order Rules. *Journal of Neuroscience*, *31*(6), 2305–2312. https://doi.org/10.1523/JNEUROSCI.4358-10.2011

Bar, M. (2004). Visual objects in context. *Nature Reviews Neuroscience*, *5*(8), 617–629. https://doi.org/10.1038/nrn1476

Baracchini, G., Mišić, B., Setton, R., Mwilambwe-Tshilobo, L., Girn, M., Nomi, J. S., Uddin, L. Q., Turner, G. R., & Spreng, R. N. (2021). Inter-regional BOLD signal variability is an organizational feature of functional brain networks. *NeuroImage*, *237*, 118149. https://doi.org/10.1016/j.neuroimage.2021.118149

Barton, R. A. (2012). Embodied cognitive evolution and the cerebellum. *Philosophical Transactions of the Royal Society B: Biological Sciences*, *367*(1599), 2097–2107. https://doi.org/10.1098/rstb.2012.0112

Barton, R. A., & Venditti, C. (2014). Rapid Evolution of the Cerebellum in Humans and Other Great Apes. *Current Biology*, *24*(20), 2440–2444. https://doi.org/10.1016/j.cub.2014.08.056

Basile, G. A., Quartu, M., Bertino, S., Serra, M. P., Boi, M., Bramanti, A., Anastasi, G. P., Milardi, D., & Cacciola, A. (2021). Red nucleus structure and function: From anatomy to clinical neurosciences. *Brain Structure and Function*, *226*(1), 69–91. https://doi.org/10.1007/s00429-020-02171-x

Bassett, D. S., Yang, M., Wymbs, N. F., & Grafton, S. T. (2015). Learning-induced autonomy of sensorimotor systems. *Nature Neuroscience*, *18*(5), 744–751. https://doi.org/10.1038/nn.3993

Bastian, A. J. (2006). Learning to predict the future: The cerebellum adapts feedforward movement control. *Current Opinion in Neurobiology*, *16*(6), 645–649. https://doi.org/10.1016/j.conb.2006.08.016

Bastian, A. J., Martin, T. A., Keating, J. G., & Thach, W. T. (1996). Cerebellar ataxia: Abnormal control of interaction torques across multiple joints. *Journal of Neurophysiology*, *76*(1), 492–509. https://doi.org/10.1152/jn.1996.76.1.492

Baylis, G., Rolls, E., & Leonard, C. (1987). Functional subdivisions of the temporal lobe neocortex. *The Journal of Neuroscience*, *7*(2), 330–342. https://doi.org/10.1523/JNEUROSCI.07-02-00330.1987

Beckmann, H., & Schöllhorn, W. I. (2003). *Differencial learning in shot put*. European Workshop on Movement Science, Köln, Germany.

Bennett, C. M., & Miller, M. B. (2013). fMRI reliability: Influences of task and experimental design. *Cognitive, Affective, & Behavioral Neuroscience*, *13*(4), 690–702. https://doi.org/10.3758/s13415-013-0195-1

Ben-Yehudah, G., Guediche, S., & Fiez, J. A. (2007). Cerebellar contributions to verbal working memory: Beyond cognitive theory. *The Cerebellum*, *6*(3), 193. https://doi.org/10.1080/14734220701286195

Berlot, E., Popp, N. J., & Diedrichsen, J. (2020a). A critical re-evaluation of fMRI signatures of motor sequence learning. *eLife*, *9*, e55241. https://doi.org/10.7554/eLife.55241

Berlot, E., Popp, N. J., & Diedrichsen, J. (2020b). A critical re-evaluation of fMRI signatures of motor sequence learning. *eLife*, *9*, e55241. https://doi.org/10.7554/eLife.55241

Bernardi, S., Benna, M. K., Rigotti, M., Munuera, J., Fusi, S., & Salzman, C. D. (2020). The Geometry of Abstraction in the Hippocampus and Prefrontal Cortex. *Cell*, *183*(4), 954-967.e21. https://doi.org/10.1016/j.cell.2020.09.031

Bloom, B. S. (1986). Automaticity: "The Hands and Feet of Genius." *Educational Leadership*, *43*, 70–77.

Boillat, Y., Bazin, P.-L., & Van Der Zwaag, W. (2020). Whole-body somatotopic maps in the cerebellum revealed with 7T fMRI. *NeuroImage*, *211*, 116624. https://doi.org/10.1016/j.neuroimage.2020.116624

Bolkan, S. S., Stujenske, J. M., Parnaudeau, S., Spellman, T. J., Rauffenbart, C., Abbas, A. I., Harris, A. Z., Gordon, J. A., & Kellendonk, C. (2017). Thalamic projections sustain prefrontal activity during working memory maintenance. *Nature Neuroscience*, *20*(7), 987–996. https://doi.org/10.1038/nn.4568

Bolt, T., Nomi, J. S., Bzdok, D., Salas, J. A., Chang, C., Thomas Yeo, B. T., Uddin, L. Q., & Keilholz, S. D. (2022). A parsimonious description of global functional brain organization in three spatiotemporal patterns. *Nature Neuroscience*, *25*(8), 1093–1103. https://doi.org/10.1038/s41593-022-01118-1

Bolt, T., Wang, S., Nomi, J. S., Setton, R., Gold, B. P., deB.Frederick, B., Yeo, B. T. T., Chen, J. J., Picchioni, D., Duyn, J. H., Spreng, R. N., Keilholz, S. D., Uddin, L. Q., & Chang, C. (2025). Autonomic physiological coupling of the global fMRI signal. *Nature Neuroscience*, *28*(6), 1327–1335. https://doi.org/10.1038/s41593-025-01945-y

Bonelli, S. B., Thompson, P. J., Yogarajah, M., Vollmar, C., Powell, R. H. W., Symms, M. R., McEvoy, A. W., Micallef, C., Koepp, M. J., & Duncan, J. S. (2012). Imaging language networks before and after anterior temporal lobe resection: Results of a longitudinal fMRI study. *Epilepsia*, *53*(4), 639–650. https://doi.org/10.1111/j.1528-1167.2012.03433.x

Borders, A., Ranganath, C., & Yonelinas, A. (2022). The hippocampus supports high-precision binding in visual working memory. *Hippocampus*, *32*, 217–230.

Bostan, A. C., & Strick, P. L. (2018). The basal ganglia and the cerebellum: Nodes in an integrated network. *Nature Reviews Neuroscience*, *19*(6), 338–350. https://doi.org/10.1038/s41583-018-0002-7

Boven, E., Pemberton, J., Chadderton, P., Apps, R., & Costa, R. P. (2023). Cerebro-cerebellar networks facilitate learning through feedback decoupling. *Nature Communications*, *14*(1), 51. https://doi.org/10.1038/s41467-022-35658-8

Bransford, J. D., & Schwartz, D. L. (1999). Rethinking Transfer: A Simple Proposal with Multiple Implications. *Review of Research in Education*, *24*, 61. https://doi.org/10.2307/1167267

Brissenden, J. A., & Somers, D. C. (2019). Cortico-Cerebellar Networks for Visual Attention and Working Memory. *Current Opinion in Psychology*, *29*, 239–247. https://doi.org/10.1016/j.copsyc.2019.05.003

Brunton, S. L., Proctor, J. L., & Kutz, J. N. (2016). Discovering governing equations from data by sparse identification of nonlinear dynamical systems. *Proceedings of the National Academy of Sciences*, *113*(15), 3932–3937. https://doi.org/10.1073/pnas.1517384113

Buckner, R. L., Krienen, F. M., Castellanos, A., Diaz, J. C., & Yeo, B. T. T. (2011). The organization of the human cerebellum estimated by intrinsic functional connectivity. *Journal of Neurophysiology*, *106*(5), 2322–2345. https://doi.org/10.1152/jn.00339.2011

Caligiore, D., Arbib, M. A., Miall, R. C., & Baldassarre, G. (2019). The super-learning hypothesis: Integrating learning processes across cortex, cerebellum and basal ganglia. *Neuroscience & Biobehavioral Reviews*, *100*, 19–34. https://doi.org/10.1016/j.neubiorev.2019.02.008

Camina, E., & Güell, F. (2017). The Neuroanatomical, Neurophysiological and Psychological Basis of Memory: Current Models and Their Origins. *Frontiers in Pharmacology*, *8*, 438. https://doi.org/10.3389/fphar.2017.00438

Carr, V. A., Rissman, J., & Wagner, A. D. (2010). Imaging the Human Medial Temporal Lobe with High-Resolution fMRI. *Neuron*, *65*(3), 298–308. https://doi.org/10.1016/j.neuron.2009.12.022

Cayco Gajic, N. A., & Silver, R. A. (2019). Re-evaluating circuit mechanisms underlying pattern separation. *Neuron*, *101*(4), 584–602. https://doi.org/10.1016/j.neuron.2019.01.044

Čeko, M., Gracely, J. L., Fitzcharles, M.-A., Seminowicz, D. A., Schweinhardt, P., & Bushnell, M. C. (2015). Is a Responsive Default Mode Network Required for Successful Working Memory Task Performance? *The Journal of Neuroscience*, *35*(33), 11595–11605. https://doi.org/10.1523/JNEUROSCI.0264-15.2015

Čeko, M., Kragel, P. A., Woo, C.-W., López-Solà, M., & Wager, T. D. (2022). Common and stimulus-type-specific brain representations of negative affect. *Nature Neuroscience*, *25*(6), 760–770. https://doi.org/10.1038/s41593-022-01082-w

Chang, J. C., Perich, M. G., Miller, L. E., Gallego, J. A., & Clopath, C. (2024). De novo motor learning creates structure in neural activity that shapes adaptation. *Nature Communications*, *15*(1), 4084. https://doi.org/10.1038/s41467-024-48008-7

Chee, M., Venkatraman, V., Westphal, C., & Chun Siong, S. (2003). Comparison of Block and Event-Related fMRI Designs in Evaluating the Word-Frequency Effect. *Human Brain Mapping*.

Chen, Z., Sun, Q., & Li, X. (2023). Differences of resource allocation to active and passive states in visual working memory. *Psychological Research*, *87*(6), 1761–1767. https://doi.org/10.1007/s00426-022-01772-x

Cheung, J. J. H., & Kulasegaram, K. M. (2022). Beyond the tensions within transfer theories: Implications for adaptive expertise in the health professions. *Advances in Health Sciences Education*, *27*(5), 1293–1315. https://doi.org/10.1007/s10459-022-10174-y

Christophel, T. B., Klink, P. C., Spitzer, B., Roelfsema, P. R., & Haynes, J.-D. (2017). The Distributed Nature of Working Memory. *Trends in Cognitive Sciences*, *21*(2), 111–124. https://doi.org/10.1016/j.tics.2016.12.007

Churchland, M. M., Cunningham, J. P., Kaufman, M. T., Foster, J. D., Nuyujukian, P., Ryu, S. I., & Shenoy, K. V. (2012). Neural population dynamics during reaching. *Nature*, *487*(7405), 51–56. https://doi.org/10.1038/nature11129

Churchland, M. M., Santhanam, G., & Shenoy, K. V. (2006). Preparatory Activity in Premotor and Motor Cortex Reflects the Speed of the Upcoming Reach. *Journal of Neurophysiology*, *96*(6), 3130–3146. https://doi.org/10.1152/jn.00307.2006

Churchland, M. M., & Shenoy, K. V. (2024). Preparatory activity and the expansive null-space. *Nature Reviews Neuroscience*. https://doi.org/10.1038/s41583-024-00796-z

Cisek, P. (2019). Resynthesizing behavior through phylogenetic refinement. *Attention, Perception, & Psychophysics*, *81*(7), 2265–2287. https://doi.org/10.3758/s13414-019-01760-1

Cisek, P. (2021). An Evolutionary Perspective on Embodiment. In M. D. Robinson & L. E. Thomas (Eds.), *Handbook of Embodied Psychology* (pp. 547–571). Springer International Publishing. https://doi.org/10.1007/978-3-030-78471-3_24

Cisek, P. (2022). Evolution of behavioural control from chordates to primates. *Philosophical Transactions of the Royal Society B: Biological Sciences*, *377*(1844), 20200522. https://doi.org/10.1098/rstb.2020.0522

Cocuzza, C. V., Ito, T., Schultz, D., Bassett, D. S., & Cole, M. W. (2020). Flexible Coordinator and Switcher Hubs for Adaptive Task Control. *The Journal of Neuroscience*, *40*(36), 6949–6968. https://doi.org/10.1523/JNEUROSCI.2559-19.2020

Cohen, M. S., Kosslyn, S. M., Breiter, H. C., DiGirolamo, G. J., Thompson, W. L., Anderson, A. K., Bookheimer, S. Y., Rosen, B. R., & Belliveau, J. W. (1996). Changes in cortical activity

during mental rotation A mapping study using functional MRI. *Brain*, *119*(1), 89–100. https://doi.org/10.1093/brain/119.1.89

Cohen, O., Harel, R., Aumann, T. D., Israel, Z., & Prut, Y. (2017). Parallel processing of internal and external feedback in the spinocerebellar system of primates. *Journal of Neurophysiology*, *118*(1), 254–266. https://doi.org/10.1152/jn.00825.2016

Cole, M. W. (2024). Cognitive flexibility as the shifting of brain network flows by flexible neural representations. *Current Opinion in Behavioral Sciences*, *57*, 101384. https://doi.org/10.1016/j.cobeha.2024.101384

Cole, M. W., Ito, T., Schultz, D., Mill, R., Chen, R., & Cocuzza, C. (2019). Task activations produce spurious but systematic inflation of task functional connectivity estimates. *NeuroImage*, *189*, 1–18. https://doi.org/10.1016/j.neuroimage.2018.12.054

Cole, M. W., Laurent, P., & Stocco, A. (2013). Rapid instructed task learning: A new window into the human brain's unique capacity for flexible cognitive control. *Cognitive, Affective, & Behavioral Neuroscience*, *13*(1), 1–22. https://doi.org/10.3758/s13415-012-0125-7

Cole, M. W., Reynolds, J. R., Power, J. D., Repovs, G., Anticevic, A., & Braver, T. S. (2013). Multi-task connectivity reveals flexible hubs for adaptive task control. *Nature Neuroscience*, *16*(9), 1348–1355. https://doi.org/10.1038/nn.3470

Constantinidis, C., & Wang, X.-J. (2004). A Neural Circuit Basis for Spatial Working Memory. *The Neuroscientist*, *10*(6), 553–565. https://doi.org/10.1177/1073858404268742

Constantinidis, C., Williams, G. V., & Goldman-Rakic, P. S. (2002). A role for inhibition in shaping the temporal flow of information in prefrontal cortex. *Nature Neuroscience*, *5*(2), 175–180. https://doi.org/10.1038/nn799

Coutinho, D., Santos, S., Gonçalves, B., Travassos, B., Wong, D. P., Schöllhorn, W., & Sampaio, J. (2018). The effects of an enrichment training program for youth football attackers. *PLOS ONE*, *13*(6), e0199008. https://doi.org/10.1371/journal.pone.0199008

Cunningham, J. P., & Yu, B. M. (2014). Dimensionality reduction for large-scale neural recordings. *Nature Neuroscience*, *17*(11), 1500–1509. https://doi.org/10.1038/nn.3776

D'Angelo, E., & Casali, S. (2013). Seeking a unified framework for cerebellar function and dysfunction: From circuit operations to cognition. *Frontiers in Neural Circuits*, *6*. https://doi.org/10.3389/fncir.2012.00116

Davis, S. W., Crowell, C. A., Beynel, L., Deng, L., Lakhlani, D., Hilbig, S. A., Lim, W., Nguyen, D., Peterchev, A. V., Luber, B. M., Lisanby, S. H., Appelbaum, L. G., & Cabeza, R. (2018). Complementary topology of maintenance and manipulation brain networks in working memory. *Scientific Reports*, *8*(1), 17827. https://doi.org/10.1038/s41598-018-35887-2

De Blasi, B., Caciagli, L., Storti, S. F., Galovic, M., Koepp, M., Menegaz, G., Barnes, A., & Galazzo, I. B. (2020). Noise removal in resting-state and task fMRI: Functional connectivity and activation maps. *Journal of Neural Engineering*, *17*(4), 046040. https://doi.org/10.1088/1741-2552/aba5cc

de la Porte, J., Herbst, B. M., Hereman, W., & van der Walt, S. J. (2008). *An Introduction to Diffusion Maps*. https://inside.mines.edu/~whereman/talks/delaPorte-Herbst-Hereman-vanderWalt-DiffusionMaps-PRASA2008.pdf

de Reus, M. A., & van den Heuvel, M. P. (2013). The parcellation-based connectome: Limitations and extensions. *NeuroImage*, *80*, 397–404. https://doi.org/10.1016/j.neuroimage.2013.03.053

De Zeeuw, C. I., Hoogenraad, C. C., Koekkoek, S. K. E., Ruigrok, T. J. H., Galjart, N., & Simpson, J. I. (1998). Microcircuitry and function of the inferior olive. *Trends in Neurosciences*, *21*(9), 391–400. https://doi.org/10.1016/S0166-2236(98)01310-1

Dear, R., Wagstyl, K., Seidlitz, J., Markello, R. D., Arnatkevičiūtė, A., Anderson, K. M., Bethlehem, R. A. I., Lifespan Brain Chart Consortium, Raznahan, A., Bullmore, E. T., & Vértes, P. E. (2024). Cortical gene expression architecture links healthy neurodevelopment to the imaging, transcriptomics and genetics of autism and schizophrenia. *Nature Neuroscience*. https://doi.org/10.1038/s41593-024-01624-4

Debarnot, U., Sperduti, M., Di Rienzo, F., & Guillot, A. (2014). Experts bodies, experts minds: How physical and mental training shape the brain. *Frontiers in Human Neuroscience*, *8*, 280. https://doi.org/10.3389/fnhum.2014.00280

D'Esposito, M., Postle, B. R., Ballard, D., & Lease, J. (1999). Maintenance versus Manipulation of Information Held in Working Memory: An Event-Related fMRI Study. *Brain and Cognition*, *41*(1), 66–86. https://doi.org/10.1006/brcg.1999.1096

Deverett, B., Kislin, M., Tank, D. W., & Wang, S. S.-H. (2019). Cerebellar disruption impairs working memory during evidence accumulation. *Nature Communications*, *10*(1), 3128. https://doi.org/10.1038/s41467-019-11050-x

Diedrichsen, J. (2006). A spatially unbiased atlas template of the human cerebellum. *NeuroImage*, *33*(1), 127–138. https://doi.org/10.1016/j.neuroimage.2006.05.056

Diedrichsen, J., King, M., Hernandez-Castillo, C., Sereno, M., & Ivry, R. B. (2019). Universal Transform or Multiple Functionality? Understanding the Contribution of the Human Cerebellum across Task Domains. *Neuron*, *102*(5), 918–928. https://doi.org/10.1016/j.neuron.2019.04.021

Ding, Y., Liu, R.-D., Xu, L., Wang, J., & Zhang, D. (2017). Working memory load and automaticity in relation to mental multiplication. *The Journal of Educational Research*, *110*(5), 554–564. https://doi.org/10.1080/00220671.2016.1149794

Diwadkar, V. A., Carpenter, P. A., & Just, M. A. (2000). Collaborative Activity between Parietal and Dorso-Lateral Prefrontal Cortex in Dynamic Spatial Working Memory Revealed by fMRI. *NeuroImage*, *12*(1), 85–99. https://doi.org/10.1006/nimg.2000.0586

Doya, K. (2000). Complementary roles of basal ganglia and cerebellum in learning and motor control. *Current Opinion in Neurobiology*, *10*(6), 732–739. https://doi.org/10.1016/S0959-4388(00)00153-7

Doyon, J., & Benali, H. (2005). Reorganization and plasticity in the adult brain during learning of motor skills. *Current Opinion in Neurobiology*, *15*(2), 161–167. https://doi.org/10.1016/j.conb.2005.03.004

Doyon, J., Penhune, V., & Ungerleider, L. G. (2003). Distinct contribution of the cortico-striatal and cortico-cerebellar systems to motor skill learning. *Neuropsychologia*, *41*(3), 252–262. https://doi.org/10.1016/S0028-3932(02)00158-6

Dreyfus, S., & Dreyfus, H. (1980). *A five-stage model of the mental activities involved in directed skill acquisition*. https://apps.dtic.mil/sti/pdfs/ADA084551.pdf

Driscoll, L. N., Shenoy, K., & Sussillo, D. (2024). Flexible multitask computation in recurrent networks utilizes shared dynamical motifs. *Nature Neuroscience*, *27*(7), 1349–1363. https://doi.org/10.1038/s41593-024-01668-6

Du, Y., Krakauer, J. W., & Haith, A. M. (2022). The relationship between habits and motor skills in humans. *Trends in Cognitive Sciences*, S1364661322000389. https://doi.org/10.1016/j.tics.2022.02.002

Duncan, J., Assem, M., & Shashidhara, S. (2020). Integrated Intelligence from Distributed Brain Activity. *Trends in Cognitive Sciences*, *24*(10), 838–852. https://doi.org/10.1016/j.tics.2020.06.012

Duncan, J., Chylinski, D., Mitchell, D. J., & Bhandari, A. (2017). Complexity and compositionality in fluid intelligence. *Proceedings of the National Academy of Sciences*, *114*(20), 5295–5299. https://doi.org/10.1073/pnas.1621147114

Egger, S. W., Remington, E. D., Chang, C.-J., & Jazayeri, M. (2019). Internal models of sensorimotor integration regulate cortical dynamics. *Nature Neuroscience*, *22*(11), 1871–1882. https://doi.org/10.1038/s41593-019-0500-6

El-Gaby, M., Harris, A. L., Whittington, J. C. R., Dorrell, W., Bhomick, A., Walton, M. E., Akam, T., & Behrens, T. E. J. (2024). A cellular basis for mapping behavioural structure. *Nature*. https://doi.org/10.1038/s41586-024-08145-x

Esteban, O., Ciric, R., Finc, K., Blair, R. W., Markiewicz, C. J., Moodie, C. A., Kent, J. D., Goncalves, M., DuPre, E., Gomez, D. E. P., Ye, Z., Salo, T., Valabregue, R., Amlien, I. K., Liem, F., Jacoby, N., Stojić, H., Cieslak, M., Urchs, S., … Gorgolewski, K. J. (2020). Analysis of task-based functional MRI data preprocessed with fMRIPrep. *Nature Protocols*, *15*(7), 2186–2202. https://doi.org/10.1038/s41596-020-0327-3

Esteban, O., Markiewicz, C. J., Blair, R. W., Moodie, C. A., Isik, A. I., Erramuzpe, A., Kent, J. D., Goncalves, M., DuPre, E., Snyder, M., Oya, H., Ghosh, S. S., Wright, J., Durnez, J., Poldrack,

R. A., & Gorgolewski, K. J. (2019). fMRIPrep: A robust preprocessing pipeline for functional MRI. *Nature Methods*, *16*(1), 111–116. https://doi.org/10.1038/s41592-018-0235-4

Foerde, K., & Shohamy, D. (2011). The role of the basal ganglia in learning and memory: Insight from Parkinson's disease. *Neurobiology of Learning and Memory*, *96*(4), 624–636. https://doi.org/10.1016/j.nlm.2011.08.006

Frank, T. D., Michelbrink, M., Beckmann, H., & Schöllhorn, W. I. (2008). A quantitative dynamical systems approach to differential learning: Self-organization principle and order parameter equations. *Biological Cybernetics*, *98*(1), 19–31. https://doi.org/10.1007/s00422-007-0193-x

Friston, K. J., Fletcher, P., Josephs, O., Holmes, A., Rugg, M. D., & Turner, R. (1998). Event-Related fMRI: Characterizing Differential Responses. *NeuroImage*, *7*(1), 30–40. https://doi.org/10.1006/nimg.1997.0306

Friston, K. J., Holmes, A. P., Poline, J.-B., Grasby, P. J., Williams, S. C. R., Frackowiak, R. S. J., & Turner, R. (1995). Analysis of fMRI time-series revisited. *Neuroimage*, *2*, 45–53.

Friston, K. J., Zarahn, E., Josephs, O., Henson, R. N. A., & Dale, A. M. (1999). Stochastic Designs in Event-Related fMRI. *NeuroImage*, *10*(5), 607–619. https://doi.org/10.1006/nimg.1999.0498

Fu, Z., Beam, D., Chung, J. M., Reed, C. M., Mamelak, A. N., Adolphs, R., & Rutishauser, U. (2022). The geometry of domain-general performance monitoring in the human medial frontal cortex. *Science*, *376*(6593), eabm9922. https://doi.org/10.1126/science.abm9922

Fusi, S., Miller, E. K., & Rigotti, M. (2016). Why neurons mix: High dimensionality for higher cognition. *Current Opinion in Neurobiology*, *37*, 66–74. https://doi.org/10.1016/j.conb.2016.01.010

Gagliano, G., Monteverdi, A., Casali, S., Laforenza, U., Gandini Wheeler-Kingshott, C. A. M., D'Angelo, E., & Mapelli, L. (2022). Non-Linear Frequency Dependence of Neurovascular Coupling in the Cerebellar Cortex Implies Vasodilation–Vasoconstriction Competition. *Cells*, *11*(6), 1047. https://doi.org/10.3390/cells11061047

Gallego, J. A., Perich, M. G., Chowdhury, R. H., Solla, S. A., & Miller, L. E. (2020). Long-term stability of cortical population dynamics underlying consistent behavior. *Nature Neuroscience*, *23*(2), 260–270. https://doi.org/10.1038/s41593-019-0555-4

Gallego, J. A., Perich, M. G., Miller, L. E., & Solla, S. A. (2017). Neural Manifolds for the Control of Movement. *Neuron*, *94*(5), 978–984. https://doi.org/10.1016/j.neuron.2017.05.025

Gallego, J. A., Perich, M. G., Naufel, S. N., Ethier, C., Solla, S. A., & Miller, L. E. (2018). Cortical population activity within a preserved neural manifold underlies multiple motor behaviors. *Nature Communications*, *9*(1), 4233. https://doi.org/10.1038/s41467-018-06560-z

Ganis, G., & Kievit, R. (2015). A New Set of Three-Dimensional Shapes for Investigating Mental Rotation Processes: Validation Data and Stimulus Set. *Journal of Open Psychology Data*, *3*(e3). https://doi.org/10.5334/jopd.ai

Gao, Z., Davis, C., Thomas, A. M., Economo, M. N., Abrego, A. M., Svoboda, K., De Zeeuw, C. I., & Li, N. (2018). A cortico-cerebellar loop for motor planning. *Nature*, *563*(7729), 113–116. https://doi.org/10.1038/s41586-018-0633-x

Garrett, D. D., Kovacevic, N., McIntosh, A. R., & Grady, C. L. (2011). The Importance of Being Variable. *The Journal of Neuroscience*, *31*(12), 4496–4503. https://doi.org/10.1523/JNEUROSCI.5641-10.2011

Gellersen, H. M., Guo, C. C., O'Callaghan, C., Tan, R. H., Sami, S., & Hornberger, M. (2017). Cerebellar atrophy in neurodegeneration—A meta-analysis. *Journal of Neurology, Neurosurgery & Psychiatry*, *88*(9), 780–788. https://doi.org/10.1136/jnnp-2017-315607

Gilbert, P. F. C., & Thach, W. T. (1977). Purkinje cell activity during motor learning. *Brain Research*, *128*(2), 309–328. https://doi.org/10.1016/0006-8993(77)90997-0

Glasser, M. F., Sotiropoulos, S. N., Wilson, J. A., Coalson, T. S., Fischl, B., Andersson, J. L., Xu, J., Jbabdi, S., Webster, M., Polimeni, J. R., Van Essen, D. C., & Jenkinson, M. (2013). The minimal preprocessing pipelines for the Human Connectome Project. *NeuroImage*, *80*, 105–124. https://doi.org/10.1016/j.neuroimage.2013.04.127

Glickstein, M. (2000). How are visual areas of the brain connected to motor areas for the sensory guidance of movement? *Trends in Neurosciences*.

Glickstein, M., Cohen, J. L., Dixon, B., Gibson, A., Hollins, M., Labossiere, E., & Robinson, F. (1980). Corticopontine Visual Projections in Macaque Monkeys. *The Journal of Comparative Neurology*.

Glickstein, M., & Doron, K. (2008). Cerebellum: Connections and Functions. *Cerebellum*.

Glover, G. H. (1999). Deconvolution of Impulse Response in Event-Related BOLD fMRI. *NeuroImage*, *9*(4), 416–429. https://doi.org/10.1006/nimg.1998.0419

Gozzi, A., Stuefer, A., Alvino, F. G., Bedin, V., Cover, C., Kang, C., Galbusera, A., Gil, R., Gini, S., De Guzman, E., Desrosiers-Grégoire, G., Gutierrez-Barragan, D., Mandino, F., Mariani, J.-C., Micotti, E., Reimann, H., Pagani, M., Pepe, C., Sastre-Yagüe, D., … Zhang, N. (2025). Charting the path in rodent functional neuroimaging. *Imaging Neuroscience*, *3*, IMAG.a.12. https://doi.org/10.1162/IMAG.a.12

Grady, C. L., & Garrett, D. D. (2014). Understanding variability in the BOLD signal and why it matters for aging. *Brain Imaging and Behavior*, *8*(2), 274–283. https://doi.org/10.1007/s11682-013-9253-0

Grady, C. L., Rieck, J. R., Baracchini, G., & DeSouza, B. (2023). Relation of resting brain signal variability to cognitive and socioemotional measures in an adult lifespan sample. *Social Cognitive and Affective Neuroscience*, *18*(1), nsad044. https://doi.org/10.1093/scan/nsad044

Graybiel, A. M., & Grafton, S. T. (2015). The Striatum: Where Skills and Habits Meet. *Cold Spring Harbor Perspectives in Biology*, *7*(8), a021691. https://doi.org/10.1101/cshperspect.a021691

Guell, X. (2021). Functional Gradients of the Cerebellum: A Review of Practical Applications. *The Cerebellum*. https://doi.org/10.1007/s12311-021-01342-8

Guell, X., & Schmahmann, J. (2020). Cerebellar Functional Anatomy: A Didactic Summary Based on Human fMRI Evidence. *The Cerebellum*, *19*(1), 1–5. https://doi.org/10.1007/s12311-019-01083-9

Guell, X., Schmahmann, J. D., Gabrieli, J. D., & Ghosh, S. S. (2018). Functional gradients of the cerebellum. *eLife*, *7*, e36652. https://doi.org/10.7554/eLife.36652

Hartigan, J. A., & Wong, M. A. (1979). Algorithm AS 136: A K-Means Clustering Algorithm. *Journal of the Royal Statistical Society. Series C (Applied Statistics)*, *28*(1), 100–108. https://doi.org/10.2307/2346830

Hautzel, H., Mottaghy, F. M., Specht, K., Müller, H.-W., & Krause, B. J. (2009). Evidence of a modality-dependent role of the cerebellum in working memory? An fMRI study comparing

verbal and abstract n-back tasks. *NeuroImage*, *47*(4), 2073–2082. https://doi.org/10.1016/j.neuroimage.2009.06.005

Hayter, A. L., Langdon, D. W., & Ramnani, N. (2007). Cerebellar contributions to working memory. *NeuroImage*, *36*(3), 943–954. https://doi.org/10.1016/j.neuroimage.2007.03.011

Heath, R. G., & Harper, J. W. (1974). Ascending projections of the cerebellar fastigial nucleus to the hippocampus, amygdala, and other temporal lobe sites: Evoked potential and histological studies in monkeys and cats. *Experimental Neurology*, *45*(2), 268–287. https://doi.org/10.1016/0014-4886(74)90118-6

Heitz, R. P. (2014). The speed-accuracy tradeoff: History, physiology, methodology, and behavior. *Frontiers in Neuroscience*, *8*. https://doi.org/10.3389/fnins.2014.00150

Henz, D., & Schöllhorn, W. I. (2016). Differential Training Facilitates Early Consolidation in Motor Learning. *Frontiers in Behavioral Neuroscience*, *10*. https://doi.org/10.3389/fnbeh.2016.00199

Hikosaka, O., Nakamura, K., Sakai, K., & Nakahara, H. (2002). Central mechanisms of motor skill learning. *Current Opinion in Neurobiology*, *12*(2), 217–222. https://doi.org/10.1016/S0959-4388(02)00307-0

Hocker, D., Constantinople, C. M., & Savin, C. (2025). Compositional pretraining improves computational efficiency and matches animal behaviour on complex tasks. *Nature Machine Intelligence*, *7*(5), 689–702. https://doi.org/10.1038/s42256-025-01029-3

I. Schollhorn, W. (2012). The Nonlinear Nature of Learning—A Differential Learning Approach. *The Open Sports Sciences Journal*, *5*(1), 100–112. https://doi.org/10.2174/1875399X01205010100

Iadecola, C., Li, J., Xu, S., & Yang, G. (1996). Neural mechanisms of blood flow regulation during synaptic activity in cerebellar cortex. *Journal of Neurophysiology*, *75*(2), 940–950. https://doi.org/10.1152/jn.1996.75.2.940

Imamizu, H., & Kawato, M. (2009). Brain mechanisms for predictive control by switching internal models: Implications for higher-order cognitive functions. *Psychological Research Psychologische Forschung*, *73*(4), 527–544. https://doi.org/10.1007/s00426-009-0235-1

Imamizu, H., Kuroda, T., Miyauchi, S., Yoshioka, T., & Kawato, M. (2003). Modular organization of internal models of tools in the human cerebellum. *Proceedings of the National Academy of Sciences*, *100*(9), 5461–5466. https://doi.org/10.1073/pnas.0835746100

Imamizu, H., Miyauchi, S., Tamada, T., Sasaki, Y., Takino, R., & Kawato, M. (2000a). *Human cerebellar activity reflecting an acquired internal model of a new tool*. *403*, 4.

Imamizu, H., Miyauchi, S., Tamada, T., Sasaki, Y., Takino, R., & Kawato, M. (2000b). *Human cerebellar activity reflecting an acquired internal model of a new tool*. *403*.

Israely, S., Ninou, H., Rajchert, O., Elmaleh, L., Harel, R., Mawase, F., Kadmon, J., & Prut, Y. (2025). Cerebellar output shapes cortical preparatory activity during motor adaptation. *Nature Communications*, *16*(1), 2574. https://doi.org/10.1038/s41467-025-57832-4

Ito, M. (2002). Historical Review of the Significance of the Cerebellum and the Role of Purkinje Cells in Motor Learning. *Annals of the New York Academy of Sciences*, *978*(1), 273–288. https://doi.org/10.1111/j.1749-6632.2002.tb07574.x

Ito, M. (2008). Control of mental activities by internal models in the cerebellum. *Nature Reviews Neuroscience*, *9*(4), 304–313. https://doi.org/10.1038/nrn2332

Ito, T., Klinger, T., Schultz, D. H., Murray, J. D., Cole, M. W., & Rigotti, M. (2022). *Compositional generalization through abstract representations in human and artificial neural networks*. Conference on Neural Information Processing (NeurIPS).

Ito, T., Kulkarni, K. R., Schultz, D. H., Mill, R. D., Chen, R. H., Solomyak, L. I., & Cole, M. W. (2017). Cognitive task information is transferred between brain regions via resting-state network topology. *Nature Communications*, *8*(1), 1027. https://doi.org/10.1038/s41467-017-01000-w

Ito, T., Yang, G. R., Laurent, P., Schultz, D. H., & Cole, M. W. (2022). Constructing neural network models from brain data reveals representational transformations linked to adaptive behavior. *Nature Communications*, *13*(1), 673. https://doi.org/10.1038/s41467-022-28323-7

Johnston, W. J., & Fusi, S. (2023). Abstract representations emerge naturally in neural networks trained to perform multiple tasks. *Nature Communications*, *14*(1), 1040. https://doi.org/10.1038/s41467-023-36583-0

Kang, S., Jun, S., Baek, S. J., Park, H., Yamamoto, Y., & Tanaka-Yamamoto, K. (2021). Recent Advances in the Understanding of Specific Efferent Pathways Emerging From the Cerebellum. *Frontiers in Neuroanatomy*, *15*. https://doi.org/10.3389/fnana.2021.759948

Karnath, H.-O. (2001). New insights into the functions of the superior temporal cortex. *Nature Reviews Neuroscience*, *2*(8), 568–576. https://doi.org/10.1038/35086057

Kawai, R., Markman, T., Poddar, R., Ko, R., Fantana, A. L., Dhawale, A. K., Kampff, A. R., & Ölveczky, B. P. (2015). Motor Cortex Is Required for Learning but Not for Executing a Motor Skill. *Neuron*, *86*(3), 800–812. https://doi.org/10.1016/j.neuron.2015.03.024

Kawato, M., Ohmae, S., Hoang, H., & Sanger, T. (2021). 50 Years Since the Marr, Ito, and Albus Models of the Cerebellum. *Neuroscience*, *462*, 151–174. https://doi.org/10.1016/j.neuroscience.2020.06.019

Kelly, A. M. C., & Garavan, H. (2005). Human Functional Neuroimaging of Brain Changes Associated with Practice. *Cerebral Cortex*, *15*(8), 1089–1102. https://doi.org/10.1093/cercor/bhi005

Kelly, R. M., & Strick, P. L. (2003). Cerebellar Loops with Motor Cortex and Prefrontal Cortex of a Nonhuman Primate. *The Journal of Neuroscience*, *23*(23), 8432–8444. https://doi.org/10.1523/JNEUROSCI.23-23-08432.2003

Khilkevich, A., Zambrano, J., Richards, M.-M., & Mauk, M. D. (2018). Cerebellar implementation of movement sequences through feedback. *eLife*, *7*, e37443. https://doi.org/10.7554/eLife.37443

Kikumoto, A., Bhandari, A., Shibata, K., & Badre, D. (2024). A transient high-dimensional geometry affords stable conjunctive subspaces for efficient action selection. *Nature Communications*, *15*(1), 8513. https://doi.org/10.1038/s41467-024-52777-6

King, L., King, M., Zhen, Z., Ivry, R. B., & Weiner, K. S. (2025). Transcriptomic gradients of the human cerebellum. *Imaging Neuroscience*, *3*, imag_a_00494. https://doi.org/10.1162/imag_a_00494

King, M., Hernandez-Castillo, C. R., Poldrack, R. A., Ivry, R. B., & Diedrichsen, J. (2019). Functional boundaries in the human cerebellum revealed by a multi-domain task battery. *Nature Neuroscience*, *22*(8), 1371–1378. https://doi.org/10.1038/s41593-019-0436-x

Kobak, D., Brendel, W., Constantinidis, C., Feierstein, C. E., Kepecs, A., Mainen, Z. F., Qi, X.-L., Romo, R., Uchida, N., & Machens, C. K. (2016). Demixed principal component analysis of neural population data. *eLife*, *5*, e10989. https://doi.org/10.7554/eLife.10989

Kostadinov, D., & Häusser, M. (2022). Reward signals in the cerebellum: Origins, targets, and functional implications. *Neuron*, S0896627322001805. https://doi.org/10.1016/j.neuron.2022.02.015

Koziol, L. F., Budding, D., Andreasen, N., D'Arrigo, S., Bulgheroni, S., Imamizu, H., Ito, M., Manto, M., Marvel, C., Parker, K., Pezzulo, G., Ramnani, N., Riva, D., Schmahmann, J., Vandervert, L., & Yamazaki, T. (2014). Consensus Paper: The Cerebellum's Role in Movement and Cognition. *The Cerebellum*, *13*(1), 151–177. https://doi.org/10.1007/s12311-013-0511-x

Krakauer, J. W. (2009). Motor Learning and Consolidation: The Case of Visuomotor Rotation. In D. Sternad (Ed.), *Progress in Motor Control* (Vol. 629, pp. 405–421). Springer US. https://doi.org/10.1007/978-0-387-77064-2_21

Krakauer, J. W., Ghilardi, M.-F., Mentis, M., Barnes, A., Veytsman, M., Eidelberg, D., & Ghez, C. (2004). Differential Cortical and Subcortical Activations in Learning Rotations and Gains for Reaching: A PET Study. *Journal of Neurophysiology*, *91*(2), 924–933. https://doi.org/10.1152/jn.00675.2003

Krakauer, J. W., & Mazzoni, P. (2011). Human sensorimotor learning: Adaptation, skill, and beyond. *Current Opinion in Neurobiology*, *21*(4), 636–644. https://doi.org/10.1016/j.conb.2011.06.012

Krishnan, A., Williams, L. J., McIntosh, A. R., & Abdi, H. (2011). Partial Least Squares (PLS) methods for neuroimaging: A tutorial and review. *NeuroImage*, *56*(2), 455–475. https://doi.org/10.1016/j.neuroimage.2010.07.034

Kübler, A., Dixon, V., & Garavan, H. (2006). Automaticity and Reestablishment of Executive Control—An fMRI Study. *Journal of Cognitive Neuroscience*, *18*(8), 1331–1342. https://doi.org/10.1162/jocn.2006.18.8.1331

Kurth-Nelson, Z., Behrens, T., Wayne, G., Miller, K., Luettgau, L., Dolan, R., Liu, Y., & Schwartenbeck, P. (2023). Replay and compositional computation. *Neuron*, *111*(4), 454–469. https://doi.org/10.1016/j.neuron.2022.12.028

Lanciego, J. L., Luquin, N., & Obeso, J. A. (2012). Functional Neuroanatomy of the Basal Ganglia. *Cold Spring Harbor Perspectives in Medicine*, *2*(12), a009621–a009621. https://doi.org/10.1101/cshperspect.a009621

Lande, K. J. (2024). Compositionality in perception: A framework. *WIREs Cognitive Science*, e1691. https://doi.org/10.1002/wcs.1691

Leiner, H. C., Leiner, A. L., & Dow, R. S. (1986). Does the Cerebellum Contribute to Mental Skills? *Behavioural Neuroscience*, *100*(4), 443–454.

Lewis, S. J. G., Cools, R., Robbins, T. W., Dove, A., Barker, R. A., & Owen, A. M. (2003). Using executive heterogeneity to explore the nature of working memory deficits in Parkinson's disease. *Neuropsychologia*, *41*(6), 645–654. https://doi.org/10.1016/S0028-3932(02)00257-9

Liesefeld, H. R., Fu, X., & Zimmer, H. D. (2015). Fast and careless or careful and slow? Apparent holistic processing in mental rotation is explained by speed-accuracy trade-offs. *Journal of Experimental Psychology: Learning, Memory, and Cognition*, *41*(4), 1140–1151. https://doi.org/10.1037/xlm0000081

Liesefeld, H. R., & Janczyk, M. (2019). Combining speed and accuracy to control for speed-accuracy trade-offs(?). *Behavior Research Methods*, *51*(1), 40–60. https://doi.org/10.3758/s13428-018-1076-x

Livne, T., Kim, D., Metcalf, N. V., Zhang, L., Pini, L., Shulman, G. L., & Corbetta, M. (2022). Spontaneous activity patterns in human motor cortex replay evoked activity patterns for hand movements. *Scientific Reports*, *12*(1), 16867. https://doi.org/10.1038/s41598-022-20866-5

Logan, G. D. (1988). Toward an Instance Theory of Automatization. *Psychological Review*, *95*(4), 492–527.

Logothetis, N. K. (2003). The Underpinnings of the BOLD Functional Magnetic Resonance Imaging Signal. *The Journal of Neuroscience*, *23*(10), 3963–3971. https://doi.org/10.1523/JNEUROSCI.23-10-03963.2003

Logothetis, N. K., Pauls, J., Augath, M., Trinath, T., & Oeltermann, A. (2001). *Neurophysiological investigation of the basis of the fMRI signal*. *412*, 8.

Luis, E. O., Arrondo, G., Vidorreta, M., Martínez, M., Loayza, F., Fernández-Seara, M. A., & Pastor, M. A. (2015). Successful Working Memory Processes and Cerebellum in an Elderly Sample: A Neuropsychological and fMRI Study. *PLOS ONE*, *10*(7), e0131536. https://doi.org/10.1371/journal.pone.0131536

Mackinnon, M. J., Song, S., Chao, T.-H. H., Hsu, L.-M., Albert, S. T., Ma, Y., Shnitko, T., Wang, T.-W. W., Nonneman, R. J., Freeman, C. D., Ozarkar, S. S., Emir, U. E., Shen, M. D., Philpot, B. D., Hantman, A. W., Lee, S.-H., Chang, W.-T., & Shih, Y.-Y. I. (2025). *SORDINO for Silent, Sensitive, Specific, and Artifact-Resisting fMRI in awake behaving mice*. https://doi.org/10.1101/2025.03.10.642406

Magielse, N., Manoli, A., Eickhoff, S. B., Fox, P. T., Saberi, A., & Valk, S. L. (2024). *Bias-accounting meta-analyses overcome cerebellar neglect to refine the cerebellar behavioral topography*. https://doi.org/10.1101/2024.10.31.621398

Magielse, N., Toro, R., Steigauf, V., Abbaspour, M., Eickhoff, S. B., Heuer, K., & Valk, S. L. (2023). Phylogenetic comparative analysis of the cerebello-cerebral system in 34 species highlights primate-general expansion of cerebellar crura I-II. *Communications Biology*, *6*(1188). https://doi.org/10.1038/s42003-023-05553-z

Mandino, F., Cerri, D. H., Garin, C. M., Straathof, M., Van Tilborg, G. A. F., Chakravarty, M. M., Dhenain, M., Dijkhuizen, R. M., Gozzi, A., Hess, A., Keilholz, S. D., Lerch, J. P., Shih, Y.-Y. I., & Grandjean, J. (2020). Animal Functional Magnetic Resonance Imaging: Trends and Path Toward Standardization. *Frontiers in Neuroinformatics*, *13*, 78. https://doi.org/10.3389/fninf.2019.00078

Manktelow, A. E., Menon, D. K., Sahakian, B. J., & Stamatakis, E. A. (2017). Working Memory after Traumatic Brain Injury: The Neural Basis of Improved Performance with Methylphenidate. *Frontiers in Behavioral Neuroscience*, *11*(58). https://doi.org/10.3389/fnbeh.2017.00058

Mante, V., Sussillo, D., Shenoy, K. V., & Newsome, W. T. (2013). Context-dependent computation by recurrent dynamics in prefrontal cortex. *Nature*, *503*(7474), 78–84. https://doi.org/10.1038/nature12742

Manto, M. U. (2008). The Cerebellum, Cerebellar Disorders, and Cerebellar Research—Two Centuries of Discoveries. *The Cerebellum*, *7*(4), 505–516. https://doi.org/10.1007/s12311-008-0063-7

Manto, M. U., Gruol, D. L., Schmahmann, J. D., Koibuchi, N., & Sillitoe, R. V. (Eds.). (2022). *Handbook of the Cerebellum and Cerebellar Disorders*. Springer International Publishing. https://doi.org/10.1007/978-3-030-23810-0

Mapelli, L., Gagliano, G., Soda, T., Laforenza, U., Moccia, F., & D'Angelo, E. U. (2017). Granular Layer Neurons Control Cerebellar Neurovascular Coupling Through an NMDA Receptor/NO-Dependent System. *The Journal of Neuroscience*, *37*(5), 1340–1351. https://doi.org/10.1523/JNEUROSCI.2025-16.2016

Margulies, D. S., Ghosh, S. S., Goulas, A., Falkiewicz, M., Huntenburg, J. M., Langs, G., Bezgin, G., Eickhoff, S. B., Castellanos, F. X., Petrides, M., Jefferies, E., & Smallwood, J. (2016). Situating the default-mode network along a principal gradient of macroscale cortical organization. *Proceedings of the National Academy of Sciences*, *113*(44), 12574–12579. https://doi.org/10.1073/pnas.1608282113

Markello, R. D., Hansen, J. Y., Liu, Z.-Q., Bazinet, V., Shafiei, G., Suárez, L. E., Blostein, N., Seidlitz, J., Baillet, S., Satterthwaite, T. D., Chakravarty, M. M., Raznahan, A., & Misic, B. (2022). neuromaps: Structural and functional interpretation of brain maps. *Nature Methods*. https://doi.org/10.1038/s41592-022-01625-w

Masse, N. Y., Yang, G. R., Song, H. F., Wang, X.-J., & Freedman, D. J. (2019). Circuit mechanisms for the maintenance and manipulation of information in working memory. *Nature Neuroscience*, *22*(7), 1159–1167. https://doi.org/10.1038/s41593-019-0414-3

Mathiesen, C., Caesar, K., Akgören, N., & Lauritzen, M. (1998). Modification of activity-dependent increases of cerebral blood flow by excitatory synaptic activity and spikes in rat cerebellar cortex. *The Journal of Physiology*, *512*(2), 555–566. https://doi.org/10.1111/j.1469-7793.1998.555be.x

Mazzoni, P., & Krakauer, J. W. (2006). An Implicit Plan Overrides an Explicit Strategy during Visuomotor Adaptation. *The Journal of Neuroscience*, *26*(14), 3642–3645. https://doi.org/10.1523/JNEUROSCI.5317-05.2006

McDougle, S. D., Ivry, R. B., & Taylor, J. A. (2016). Taking Aim at the Cognitive Side of Learning in Sensorimotor Adaptation Tasks. *Trends in Cognitive Sciences*, *20*(7), 535–544. https://doi.org/10.1016/j.tics.2016.05.002

McDougle, S. D., Tsay, J. S., Pitt, B., King, M., Saban, W., Taylor, J. A., & Ivry, R. B. (2022). Continuous manipulation of mental representations is compromised in cerebellar degeneration. *Brain*, *145*, 4246–4263.

McIntosh, A. R., Chau, W. K., & Protzner, A. B. (2004). Spatiotemporal analysis of event-related fMRI data using partial least squares. *NeuroImage*, *23*(2), 764–775. https://doi.org/10.1016/j.neuroimage.2004.05.018

McIntosh, A. R., & Lobaugh, N. J. (2004). Partial least squares analysis of neuroimaging data: Applications and advances. *NeuroImage*, *23*, S250–S263. https://doi.org/10.1016/j.neuroimage.2004.07.020

Meirhaeghe, N., Riehle, A., & Brochier, T. (2023). Parallel movement planning is achieved via an optimal preparatory state in motor cortex. *Cell Reports*, *42*(2). https://doi.org/10.1016/j.celrep.2023.112136

Mesulam, M. (1998). From sensation to cognition. *Brain*, *121*(6), 1013–1052. https://doi.org/10.1093/brain/121.6.1013

Middleton, F. A., & Strick, P. L. (1994). Anatomical Evidence for Cerebellar and Basal Ganglia Involvement in Higher Cognitive Function. *Science*, *266*(5184), 458–461. https://doi.org/10.1126/science.7939688

Milardi, D., Quartarone, A., Bramanti, A., Anastasi, G., Bertino, S., Basile, G. A., Buonasera, P., Pilone, G., Celeste, G., Rizzo, G., Bruschetta, D., & Cacciola, A. (2019). The Cortico-Basal Ganglia-Cerebellar Network: Past, Present and Future Perspectives. *Frontiers in Systems Neuroscience*, *13*, 61. https://doi.org/10.3389/fnsys.2019.00061

Mill, R. D., & Cole, M. W. (2025). *Dynamically shifting from compositional to conjunctive brain representations supports cognitive task learning*. https://doi.org/10.1101/2023.06.27.546751

Montgomery, J., & Bodznick, D. (2016). *Evolution of the Cerebellar Sense of Self*. Oxford University Press. https://doi.org/10.1093/acprof:oso/9780198758860.001.0001

Morton, S. M., & Bastian, A. J. (2006). Cerebellar Contributions to Locomotor Adaptations during Splitbelt Treadmill Walking. *The Journal of Neuroscience*, *26*(36), 9107–9116. https://doi.org/10.1523/JNEUROSCI.2622-06.2006

Müller, E. J., Munn, B., Mohr, H., Ruge, H., & Shine, J. M. (2021). Brain state kinematics and the trajectory of task performance improvement. *NeuroImage*, *243*, 118510. https://doi.org/10.1016/j.neuroimage.2021.118510

Müller, E. J., Palesi, F., Hou, K. Y., Tan, J., Close, T., Gandini Wheeler-Kingschott, C. A. M., D'Angelo, E., Calamante, F., & Shine, J. M. (2023). Parallel processing relies on a distributed, low-dimensional cortico-cerebellar architecture. *Network Neuroscience*, 1–20. https://doi.org/10.1162/netn_a_00308

Munn, B. R., Müller, E. J., Wainstein, G., & Shine, J. M. (2021). The ascending arousal system shapes neural dynamics to mediate awareness of cognitive states. *Nature Communications*, *12*(6016). https://doi.org/10.1038/s41467-021-26268-x

Muscinelli, S. P., Wagner, M. J., & Litwin-Kumar, A. (2023). Optimal routing to cerebellum-like structures. *Nature Neuroscience*, *26*(9), 1630–1641. https://doi.org/10.1038/s41593-023-01403-7

Nambu, A. (2008). Seven problems on the basal ganglia. *Current Opinion in Neurobiology*, *18*(6), 595–604. https://doi.org/10.1016/j.conb.2008.11.001

Nashef, A., Cohen, O., Perlmutter, S. I., & Prut, Y. (2022). A cerebellar origin of feedforward inhibition to the motor cortex in non-human primates. *Cell Reports*, *39*(6), 110803. https://doi.org/10.1016/j.celrep.2022.110803

Nashef, A., Rapp, H., Nawrot, M. P., & Prut, Y. (2018). Area-specific processing of cerebellar-thalamo-cortical information in primates. *Biological Cybernetics*, *112*(1–2), 141–152. https://doi.org/10.1007/s00422-017-0738-6

Nau, M., Schmid, A. C., Kaplan, S. M., Baker, C. I., & Kravitz, D. J. (2024). Centering cognitive neuroscience on task demands and generalization. *Nature Neuroscience*. https://doi.org/10.1038/s41593-024-01711-6

Nettekoven, C., Zhi, D., Shahshahani, L., Pinho, A. L., Saadon-Grosman, N., Buckner, R. L., & Diedrichsen, J. (2024). A hierarchical atlas of the human cerebellum for functional precision mapping. *Nature Communications*, *15*(1), 8376. https://doi.org/10.1038/s41467-024-52371-w

Nguyen, L. H., & Holmes, S. (2019). Ten quick tips for effective dimensionality reduction. *PLOS Computational Biology*, *15*(6), e1006907. https://doi.org/10.1371/journal.pcbi.1006907

Nozari, N., & Martin, R. C. (2024). Is working memory domain-general or domain-specific? *Trends in Cognitive Sciences*, S1364661324001645. https://doi.org/10.1016/j.tics.2024.06.006

Nyberg, L., & Eriksson, J. (2016). Working Memory: Maintenance, Updating, and the Realization of Intentions. *Cold Spring Harbor Perspectives in Biology*, *8*(2), a021816. https://doi.org/10.1101/cshperspect.a021816

Oberhuber, M., Jones, ʻŌiwi Parker, Hope, T. M. H., Prejawa, S., Seghier, M. L., Green, D. W., & Price, C. J. (2013). Functionally distinct contributions of the anterior and posterior putamen during sublexical and lexical reading. *Frontiers in Human Neuroscience*, *7*. https://doi.org/10.3389/fnhum.2013.00787

O'Callaghan, C., Hornberger, M., Balsters, J. H., Halliday, G. M., Lewis, S. J. G., & Shine, J. M. (2016). Cerebellar atrophy in Parkinson's disease and its implication for network connectivity. *Brain*, *139*(3), 845–855. https://doi.org/10.1093/brain/awv399

Oldfield, R. C. (1971). The assessment and analysis of handedness: The Edinburgh inventory. *Neuropsychologia*, *9*(1), 97–113. https://doi.org/10.1016/0028-3932(71)90067-4

O'Reilly, R. C., & Frank, M. J. (2006). Making Working Memory Work: A Computational Model of Learning in the Prefrontal Cortex and Basal Ganglia. *Neural Computation*, *18*(2), 283–328. https://doi.org/10.1162/089976606775093909

Pang, J. C., Aquino, K. M., Oldehinkel, M., Robinson, P. A., Fulcher, B. D., Breakspear, M., & Fornito, A. (2023). Geometric constraints on human brain function. *Nature*. https://doi.org/10.1038/s41586-023-06098-1

Park, J., Holmes, C. D., & Snyder, L. H. (2025). *Compositional architecture: Orthogonal neural codes for task context and spatial memory in prefrontal cortex*. https://doi.org/10.1101/2025.02.25.640211

Park, S. (1992). Schizophrenics Show Spatial Working Memory Deficits. *Archives of General Psychiatry*, *49*(12), 975. https://doi.org/10.1001/archpsyc.1992.01820120063009

Pemberton, J., Chadderton, P., & Costa, R. P. (2022). *Cerebellar-driven cortical dynamics enable task acquisition, switching and consolidation* [Preprint]. Neuroscience. https://doi.org/10.1101/2022.11.14.516257

Pemberton, J., Chadderton, P., & Costa, R. P. (2024). Cerebellar-driven cortical dynamics can enable task acquisition, switching and consolidation. *Nature Communications*, *15*(1), 10913. https://doi.org/10.1038/s41467-024-55315-6

Perich, M. G., Gallego, J. A., & Miller, L. E. (2018). A NEURAL POPULATION MECHANISM FOR RAPID LEARNING. *Neuron*, *100*(4), 964-976.e7. https://doi.org/10.1016/j.neuron.2018.09.030

Perich, M. G., & Miller, L. E. (2017). Altered tuning in primary motor cortex does not account for behavioral adaptation during force field learning. *Experimental Brain Research*, *235*(9), 2689–2704. https://doi.org/10.1007/s00221-017-4997-1

Pickut, B. (1999). Validation of the cerebellum as a reference region for SPECT quantification in patients suffering from dementia of the Alzheimer type. *Psychiatry Research: Neuroimaging*, *90*(2), 103–112. https://doi.org/10.1016/S0925-4927(99)00004-9

Poldrack, R. A. (2005). The Neural Correlates of Motor Skill Automaticity. *Journal of Neuroscience*, *25*(22), 5356–5364. https://doi.org/10.1523/JNEUROSCI.3880-04.2005

Poldrack, R. A. (2012). The future of fMRI in cognitive neuroscience. *NeuroImage*, *62*(2), 1216–1220. https://doi.org/10.1016/j.neuroimage.2011.08.007

Posani, L., Wang, S., Muscinelli, S., Paninski, L., & Fusi, S. (2025). *Rarely categorical, always high-dimensional: How the neural code changes along the cortical hierarchy*. https://doi.org/10.1101/2024.11.15.623878

Power, J. D., Mitra, A., Laumann, T. O., Snyder, A. Z., Schlaggar, B. L., & Petersen, S. E. (2014). Methods to detect, characterize, and remove motion artifact in resting state fMRI. *NeuroImage*, *84*, 320–341. https://doi.org/10.1016/j.neuroimage.2013.08.048

Prati, J. M., Pontes-Silva, A., & Gianlorenço, A. C. L. (2024). The cerebellum and its connections to other brain structures involved in motor and non-motor functions: A comprehensive review. *Behavioural Brain Research*, *465*, 114933. https://doi.org/10.1016/j.bbr.2024.114933

Prut, Y., Perlmutter, S. I., & Fetz, E. E. (2001). Chapter 17 Distributed processing in the motor system: Spinal cord perspective. In *Progress in Brain Research* (Vol. 130, pp. 267–278). Elsevier. https://doi.org/10.1016/S0079-6123(01)30018-3

Raichle, M. E. (2015). The Brain's Default Mode Network. *Annual Review of Neuroscience*, *38*(1), 433–447. https://doi.org/10.1146/annurev-neuro-071013-014030

Rakic, P. (2009). Evolution of the neocortex: A perspective from developmental biology. *Nature Reviews Neuroscience*, *10*(10), 724–735. https://doi.org/10.1038/nrn2719

Ramnani, N. (2012). Frontal Lobe and Posterior Parietal Contributions to the Cortico-cerebellar System. *The Cerebellum*, *11*(2), 366–383. https://doi.org/10.1007/s12311-011-0272-3

Ramnani, N. (2014). Automatic and Controlled Processing in the Corticocerebellar System. In *Progress in Brain Research* (Vol. 210, pp. 255–285). Elsevier. https://doi.org/10.1016/B978-0-444-63356-9.00010-8

Ramnani, N., Behrens, T. E. J., Johansen-Berg, H., Richter, M. C., Pinsk, M. A., Andersson, J. L. R., Rudebeck, P., Ciccarelli, O., Richter, W., Thompson, A. J., Gross, C. G., Robson, M. D., Kastner, S., & Matthews, P. M. (2006). The Evolution of Prefrontal Inputs to the Cortico-pontine System: Diffusion Imaging Evidence from Macaque Monkeys and Humans. *Cerebral Cortex*, *16*(6), 811–818. https://doi.org/10.1093/cercor/bhj024

Ramnani, N., & Miall, R. C. (2004). A system in the human brain for predicting the actions of others. *Nature Neuroscience*, *7*(1), 85–90. https://doi.org/10.1038/nn1168

Ravizza, S. M., McCormick, C. A., Schlerf, J. E., Justus, T., Ivry, R. B., & Fiez, J. A. (2006). Cerebellar damage produces selective deficits in verbal working memory. *Brain*, *129*(2), 306–320. https://doi.org/10.1093/brain/awh685

Reeber, S. L., Otis, T. S., & Sillitoe, R. V. (2013). New roles for the cerebellum in health and disease. *Frontiers in Systems Neuroscience*, *7*. https://doi.org/10.3389/fnsys.2013.00083

Reverberi, C., Görgen, K., & Haynes, J.-D. (2012). Compositionality of Rule Representations in Human Prefrontal Cortex. *Cerebral Cortex*, *22*(6), 1237–1246. https://doi.org/10.1093/cercor/bhr200

Rigotti, M., Barak, O., Warden, M. R., Wang, X.-J., Daw, N. D., Miller, E. K., & Fusi, S. (2013). The importance of mixed selectivity in complex cognitive tasks. *Nature*, *497*(7451), 585–590. https://doi.org/10.1038/nature12160

Rotondo, A. P., Raman, D. V., & O'Leary, T. (2022). *How cerebellar architecture facilitates rapid online learning* [Preprint]. Neuroscience. https://doi.org/10.1101/2022.10.20.512268

Rubinov, M., & Sporns, O. (2010). Complex network measures of brain connectivity: Uses and interpretations. *NeuroImage*, *52*(3), 1059–1069. https://doi.org/10.1016/j.neuroimage.2009.10.003

Salo, T., Yarkoni, T., Nichols, T., Poline, J.-B., Bilgel, M., Bottenhorn, K., Jarecka, D., Kent, J., Kimbler, A., Nielson, D., Oudyk, K., Peraza, J., Pérez, A., Reeders, P., Yanes, J., & Laird, A. (2022). NiMARE: Neuroimaging Meta-Analysis Research Environment. *NeuroLibre Reproducible Preprint Server*, *1*(1), 7. https://doi.org/10.55458/neurolibre.00007

Samuels, S. J., & Flor, R. F. (1997). THE IMPORTANCE OF AUTOMATICITY FOR DEVELOPING EXPERTISE IN READING. *Reading & Writing Quarterly*, *13*(2), 107–121. https://doi.org/10.1080/1057356970130202

Santos, S., Coutinho, D., Gonçalves, B., Schöllhorn, W., Sampaio, J., & Leite, N. (2018). Differential Learning as a Key Training Approach to Improve Creative and Tactical Behavior in Soccer. *Research Quarterly for Exercise and Sport*, *89*(1), 11–24. https://doi.org/10.1080/02701367.2017.1412063

Schaefer, A., Kong, R., Gordon, E. M., Laumann, T. O., Zuo, X.-N., Holmes, A. J., Eickhoff, S. B., & Yeo, B. T. T. (2018). Local-Global Parcellation of the Human Cerebral Cortex from Intrinsic Functional Connectivity MRI. *Cerebral Cortex*, *28*(9), 3095–3114. https://doi.org/10.1093/cercor/bhx179

Schmahmann, J. D., & Pandya, D. N. (1997). Anatomic Organization of the Basilar Pontine Projections from Prefrontal Cortices in Rhesus Monkey. *The Journal of Neuroscience*, *17*(1), 438–458. https://doi.org/10.1523/JNEUROSCI.17-01-00438.1997

Schneider, W., Eschman, A., & Zuccolotto, A. (2007). *E-Prime 2 User Guide*. Psychology Software Tools, Inc.

Schöllhorn, W. I., Beckmann, H., Michelbrink, M., Sechelmann, M., Trockel, M., & Davids, K. (2006). *Does noise provide a basis for the unification of motor learning theories?*

Scholz, V. H., Flaherty, A. W., Kraft, E., Keltner, J. R., Kwong, K. K., Chen, Y. I., Rosen, B. R., & Jenkins, B. G. (2000). Laterality, somatotopy and reproducibility of the basal ganglia and motor cortex during motor tasks. *Brain Research*.

Schwartenbeck, P., Baram, A., Liu, Y., Mark, S., Muller, T., Dolan, R., Botvinick, M., Kurth-Nelson, Z., & Behrens, T. (2023). Generative replay underlies compositional inference in the hippocampal-prefrontal circuit. *Cell*, *186*(22), 4885-4897.e14. https://doi.org/10.1016/j.cell.2023.09.004

Sendhilnathan, N., Bostan, A. C., Strick, P. L., & Goldberg, M. E. (2024). A cerebro-cerebellar network for learning visuomotor associations. *Nature Communications*, *15*(1), 2519. https://doi.org/10.1038/s41467-024-46281-0

Shahshahani, L., King, M., Nettekoven, C., Ivry, R. B., & Diedrichsen, J. (2024). Selective recruitment of the cerebellum evidenced by task-dependent gating of inputs. *eLife*, *13*, RP96386. https://doi.org/10.7554/eLife.96386

Shine, J. M. (2021). The thalamus integrates the macrosystems of the brain to facilitate complex, adaptive brain network dynamics. *Progress in Neurobiology*, *199*, 101951. https://doi.org/10.1016/j.pneurobio.2020.101951

Shine, J. M. (2022). Adaptively navigating affordance landscapes: How interactions between the superior colliculus and thalamus coordinate complex, adaptive behaviour. *Neuroscience & Biobehavioral Reviews*, *143*, 104921. https://doi.org/10.1016/j.neubiorev.2022.104921

Shine, J. M., Breakspear, M., Bell, P. T., Ehgoetz Martens, K. A., Shine, R., Koyejo, O., Sporns, O., & Poldrack, R. A. (2019). Human cognition involves the dynamic integration of neural activity

and neuromodulatory systems. *Nature Neuroscience*, *22*(2), 289–296. https://doi.org/10.1038/s41593-018-0312-0

Shine, J. M., & Shine, R. (2014). Delegation to automaticity: The driving force for cognitive evolution? *Frontiers in Neuroscience*, *8*(90). https://doi.org/10.3389/fnins.2014.00090

Shinn, M., Hu, A., Turner, L., Noble, S., Preller, K. H., Ji, J. L., Moujaes, F., Achard, S., Scheinost, D., Constable, R. T., Krystal, J. H., Vollenweider, F. X., Lee, D., Anticevic, A., Bullmore, E. T., & Murray, J. D. (2023). Functional brain networks reflect spatial and temporal autocorrelation. *Nature Neuroscience*. https://doi.org/10.1038/s41593-023-01299-3

Sinha, P., Kjelgaard, M. M., Gandhi, T. K., Tsourides, K., Cardinaux, A. L., Pantazis, D., Diamond, S. P., & Held, R. M. (2014). Autism as a disorder of prediction. *Proceedings of the National Academy of Sciences*, *111*(42), 15220–15225. https://doi.org/10.1073/pnas.1416797111

Smith, S. M. (2012). The future of FMRI connectivity. *NeuroImage*, *62*(2), 1257–1266. https://doi.org/10.1016/j.neuroimage.2012.01.022

Spreng, R. N., & Grady, C. L. (2010). Patterns of Brain Activity Supporting Autobiographical Memory, Prospection, and Theory of Mind, and Their Relationship to the Default Mode Network. *Journal of Cognitive Neuroscience*, *22*(6), 1112–1123. https://doi.org/10.1162/jocn.2009.21282

Standage, D. I., Areshenkoff, C. N., Gale, D. J., Nashed, J. Y., Flanagan, J. R., & Gallivan, J. P. (2023). Whole-brain dynamics of human sensorimotor adaptation. *Cerebral Cortex*, *33*(8), 4761–4778. https://doi.org/10.1093/cercor/bhac378

Stein, H. (2021). Why Does the Neocortex Need the Cerebellum for Working Memory? *The Journal of Neuroscience*, *41*(30), 6368–6370. https://doi.org/10.1523/JNEUROSCI.0701-21.2021

Streng, M. L. (2023). The bidirectional relationship between the cerebellum and seizure networks: A double-edged sword. *Current Opinion in Behavioral Sciences*, *54*, 101327. https://doi.org/10.1016/j.cobeha.2023.101327

Streng, M. L., Kottke, B. W., Wasserman, E. M., Zecker, L., Luong, L., Kodandaramaiah, S., Ebner, T. J., & Krook-Magnuson, E. (2024). Early and widespread cerebellar engagement during

hippocampal seizures and interictal discharges. *Neurobiology of Disease*. https://doi.org/10.1101/2024.05.14.593969

Streng, M. L., Popa, L. S., & Ebner, T. J. (2018). Complex Spike Wars: A New Hope. *The Cerebellum*, *17*(6), 735–746. https://doi.org/10.1007/s12311-018-0960-3

Striemer, C. L., Enns, J. T., & Whitwell, R. L. (2019). Visuomotor adaptation in the absence of input from early visual cortex. *Cortex*, *115*, 201–215. https://doi.org/10.1016/j.cortex.2019.01.022

Sussillo, D., & Barak, O. (2013). Opening the Black Box: Low-Dimensional Dynamics in High-Dimensional Recurrent Neural Networks. *Neural Computation*, *25*(3), 626–649. https://doi.org/10.1162/NECO_a_00409

Taatgen, N. A. (2013). The nature and transfer of cognitive skills. *Psychological Review*, *120*(3), 439–471. https://doi.org/10.1037/a0033138

Tafazoli, S., Bouchacourt, F. M., Ardalan, A., Markov, N. T., Uchimura, M., Mattar, M. G., Daw, N. D., & Buschman, T. J. (2024). *Building compositional tasks with shared neural subspaces*. https://doi.org/10.1101/2024.01.31.578263

Tan, J. B., Müller, E., Zahorodnii, A., & Shine, J. M. (2024). The engagement of the cerebellum and basal ganglia enhances expertise in a sensorimotor adaptation task. *Imaging Neuroscience*, *2*, 1–20. https://doi.org/10.1162/imag_a_00271

Taylor, J. A., & Ivry, R. B. (2011). Flexible Cognitive Strategies during Motor Learning. *PLoS Computational Biology*, *7*(3), e1001096. https://doi.org/10.1371/journal.pcbi.1001096

Teich, A. F., & Qian, N. (2003). Learning and Adaptation in a Recurrent Model of V1 Orientation Selectivity. *Journal of Neurophysiology*, *89*(4), 2086–2100. https://doi.org/10.1152/jn.00970.2002

Thomsen, K., Piilgaard, H., Gjedde, A., Bonvento, G., & Lauritzen, M. (2009). Principal Cell Spiking, Postsynaptic Excitation, and Oxygen Consumption in the Rat Cerebellar Cortex. *Journal of Neurophysiology*, *102*(3), 1503–1512. https://doi.org/10.1152/jn.00289.2009

Tian, Y., Margulies, D. S., Breakspear, M., & Zalesky, A. (2020). Topographic organization of the human subcortex unveiled with functional connectivity gradients. *Nature Neuroscience*, *23*(11), 1421–1432. https://doi.org/10.1038/s41593-020-00711-6

Todorov, D. I., Capps, R. A., Barnett, W. H., Latash, E. M., Kim, T., Hamade, K. C., Markin, S. N., Rybak, I. A., & Molkov, Y. I. (2019). The interplay between cerebellum and basal ganglia in motor adaptation: A modeling study. *PLOS ONE*, *14*(4), e0214926. https://doi.org/10.1371/journal.pone.0214926

Tomlinson, S. P., Davis, N. J., Morgan, H. M., & Bracewell, R. M. (2014). Cerebellar Contributions to Verbal Working Memory. *The Cerebellum*, *13*(3), 354–361. https://doi.org/10.1007/s12311-013-0542-3

Tomov, M. S., Tsividis, P. A., Pouncy, T., Tenenbaum, J. B., & Gershman, S. J. (2023). The neural architecture of theory-based reinforcement learning. *Neuron*, *111*(8), 1331-1344.e8. https://doi.org/10.1016/j.neuron.2023.01.023

Toner, J., Montero, B. G., & Moran, A. (2015). The Perils of Automaticity. *Review of General Psychology*, *19*(4), 431–442. https://doi.org/10.1037/gpr0000054

Tsay, J. S., Kim, H., Haith, A. M., & Ivry, R. B. (2022). Understanding implicit sensorimotor adaptation as a process of proprioceptive re-alignment. *eLife*, *11*, e76639. https://doi.org/10.7554/eLife.76639

Tseng, Y., Diedrichsen, J., Krakauer, J. W., Shadmehr, R., & Bastian, A. J. (2007). Sensory Prediction Errors Drive Cerebellum-Dependent Adaptation of Reaching. *Journal of Neurophysiology*, *98*(1), 54–62. https://doi.org/10.1152/jn.00266.2007

Tye, K. M., Miller, E. K., Taschbach, F. H., Benna, M. K., Rigotti, M., & Fusi, S. (2024). Mixed selectivity: Cellular computations for complexity. *Neuron*, *112*(14), 2289–2303. https://doi.org/10.1016/j.neuron.2024.04.017

Tzvi, E., Koeth, F., Karabanov, A. N., Siebner, H. R., & Krämer, U. M. (2020). Cerebellar – Premotor cortex interactions underlying visuomotor adaptation. *NeuroImage*, *220*, 117142. https://doi.org/10.1016/j.neuroimage.2020.117142

Tzvi, E., Loens, S., & Donchin, O. (2022). Mini-review: The Role of the Cerebellum in Visuomotor Adaptation. *The Cerebellum*, *21*(2), 306–313. https://doi.org/10.1007/s12311-021-01281-4

Van Der Zwaag, W., Tse, D. H. Y., Poser, B. A., & Priovoulos, N. (2025). Cerebellar imaging for neuroscience at 9.4 T. *Magnetic Resonance in Medicine*, mrm.30596. https://doi.org/10.1002/mrm.30596

Vandervert, L. R., Schimpf, P. H., & Liu, H. (2007). How Working Memory and the Cerebellum Collaborate to Produce Creativity and Innovation. *Creativity Research Journal*, *19*(1), 1–18. https://doi.org/10.1080/10400410709336873

Vijayraghavan, S., Wang, M., Birnbaum, S. G., Williams, G. V., & Arnsten, A. F. T. (2007). Inverted-U dopamine D1 receptor actions on prefrontal neurons engaged in working memory. *Nature Neuroscience*, *10*(3), 376–384. https://doi.org/10.1038/nn1846

Viñas-Guasch, N., & Wu, Y. J. (2017). The role of the putamen in language: A meta-analytic connectivity modeling study. *Brain Structure and Function*, *222*(9), 3991–4004. https://doi.org/10.1007/s00429-017-1450-y

Vinh, N. X., & Epps, J. (2009). A Novel Approach for Automatic Number of Clusters Detection in Microarray Data Based on Consensus Clustering. *2009 Ninth IEEE International Conference on Bioinformatics and BioEngineering*, 84–91. https://doi.org/10.1109/BIBE.2009.19

Vinh, N. X., Epps, J., & Bailey, J. (2009). *Information Theoretic Measures for Clusterings Comparison: Is a Correction for Chance Necessary?* https://doi.org/10.1145/1553374.1553511

Vinh, N. X., Epps, J., & Bailey, J. (2010). Information Theoretic Measures for Clusterings Comparison: Variants, Properties, Normalization and Correction for Chance. *Journal of Machine Learning Research*, *11*(95), 2837–2854.

Wager, T. D., & Smith, E. E. (2003). Neuroimaging studies of working memory: *Cognitive, Affective, & Behavioral Neuroscience*, *3*(4), 255–274. https://doi.org/10.3758/CABN.3.4.255

Wagner, M. J., Kim, T. H., Kadmon, J., Nguyen, N. D., Ganguli, S., Schnitzer, M. J., & Luo, L. (2019). Shared Cortex-Cerebellum Dynamics in the Execution and Learning of a Motor Task. *Cell*, *177*(3), 669-682.e24. https://doi.org/10.1016/j.cell.2019.02.019

Wang, B. (2025). Ignoring the cerebellum is hindering progress in neuroscience. *Trends in Cognitive Sciences*, *29*(4), 13.

Wang, Y., Yin, X., Zhang, Z., Li, J., Zhao, W., & Guo, Z. V. (2021). A cortico-basal ganglia-thalamo-cortical channel underlying short-term memory. *Neuron*, *109*(21), 3486-3499.e7. https://doi.org/10.1016/j.neuron.2021.08.002

Williams, L. J., Abdi, H., French, R., & Orange, J. B. (2010). A Tutorial on Multiblock Discriminant Correspondence Analysis (MUDICA): A New Method for Analyzing Discourse Data From Clinical Populations. *Journal of Speech, Language, and Hearing Research*, *53*(5), 1372–1393. https://doi.org/10.1044/1092-4388(2010/08-0141)

Wilson, C. J. (2013). Active decorrelation in the basal ganglia. *Neuroscience*, *250*, 467–482. https://doi.org/10.1016/j.neuroscience.2013.07.032

Wolff, S. B. E., Ko, R., & Ölveczky, B. P. (2022). Distinct roles for motor cortical and thalamic inputs to striatum during motor skill learning and execution. *Science Advances*, *8*(8), eabk0231. https://doi.org/10.1126/sciadv.abk0231

Wolpert, D. M., Diedrichsen, J., & Flanagan, J. R. (2011). Principles of sensorimotor learning. *Nature Reviews Neuroscience*, *12*(12), 739–751. https://doi.org/10.1038/nrn3112

Wolpert, D. M., Doya, K., & Kawato, M. (2003). A unifying computational framework for motor control and social interaction. *Philosophical Transactions of the Royal Society of London. Series B: Biological Sciences*, *358*(1431), 593–602. https://doi.org/10.1098/rstb.2002.1238

Wolpert, D. M., & Flanagan, J. R. (2001). Motor prediction. *Current Biology*, *11*(18), R729–R732. https://doi.org/10.1016/S0960-9822(01)00432-8

Wolpert, D. M., & Kawato, M. (1998). Multiple paired forward and inverse models for motor control. *Neural Networks*, *11*(7–8), 1317–1329. https://doi.org/10.1016/S0893-6080(98)00066-5

Wolpert, D. M., Miall, R. C., & Kawato, M. (1998). Internal models in the cerebellum. *Trends in Cognitive Sciences*, *2*(9), 338–347. https://doi.org/10.1016/S1364-6613(98)01221-2

World Medical Association Declaration of Helsinki: Ethical Principles for Medical Research Involving Human Subjects. (2013). *JAMA*, *310*(20), 2191. https://doi.org/10.1001/jama.2013.281053

Wu, C. M., Meder, B., & Schulz, E. (2024). *Unifying Principles of Generalization: Past, Present, and Future*.

Xue, A., Kong, R., Yang, Q., Eldaief, M. C., Angeli, P. A., DiNicola, L. M., Braga, R. M., Buckner, R. L., & Yeo, B. T. T. (2021). The detailed organization of the human cerebellum estimated by intrinsic functional connectivity within the individual. *Journal of Neurophysiology*, *125*(2), 358–384. https://doi.org/10.1152/jn.00561.2020

Yang, G. R., Joglekar, M. R., Song, H. F., Newsome, W. T., & Wang, X.-J. (2019). Task representations in neural networks trained to perform many cognitive tasks. *Nature Neuroscience*, *22*(2), 297–306. https://doi.org/10.1038/s41593-018-0310-2

Yang, J. (2015). The influence of motor expertise on the brain activity of motor task performance: A meta-analysis of functional magnetic resonance imaging studies. *Cognitive, Affective, & Behavioral Neuroscience*, *15*(2), 381–394. https://doi.org/10.3758/s13415-014-0329-0

Yarkoni, T., Poldrack, R. A., Nichols, T. E., Van Essen, D. C., & Wager, T. D. (2011). Large-scale automated synthesis of human functional neuroimaging data. *Nature Methods*, *8*(8), 665–670. https://doi.org/10.1038/nmeth.1635

Yeo, T. B. T., Krienen, F. M., Sepulcre, J., Sabuncu, M. R., Lashkari, D., Hollinshead, M., Roffman, J. L., Smoller, J. W., Zöllei, L., Polimeni, J. R., Fischl, B., Liu, H., & Buckner, R. L. (2011). The organization of the human cerebral cortex estimated by intrinsic functional connectivity. *Journal of Neurophysiology*, *106*(3), 1125–1165. https://doi.org/10.1152/jn.00338.2011

Yin, H. H., & Knowlton, B. J. (2006). The role of the basal ganglia in habit formation. *Nature Reviews Neuroscience*, *7*(6), 464–476. https://doi.org/10.1038/nrn1919

Zagon, I. S., McLaughlin, P. J., & Smith, S. (1977). Neural populations in the human cerebellum: Estimations from isolated cell nuclei. *Brain Research*, *127*(2), 279–282. https://doi.org/10.1016/0006-8993(77)90541-8

Zhi, D., Shahshahani, L., Nettekoven, C., Pinho, A. L., Bzdok, D., & Diedrichsen, J. (2025). A hierarchical Bayesian brain parcellation framework for fusion of functional imaging datasets. *Imaging Neuroscience*, *3*, imag_a_00408. https://doi.org/10.1162/imag_a_00408

Zhu, J., Hasanbegović, H., Liu, L. D., Gao, Z., & Li, N. (2023). Activity map of a cortico-cerebellar loop underlying motor planning. *Nature Neuroscience*. https://doi.org/10.1038/s41593-023-01453-x

Zinger, N., Harel, R., Gabler, S., Israel, Z., & Prut, Y. (2013). Functional Organization of Information Flow in the Corticospinal Pathway. *The Journal of Neuroscience*, *33*(3), 1190–1197. https://doi.org/10.1523/JNEUROSCI.2403-12.2013

Appendices

Appendix I: Supplementary Material for Chapter 2

Cerebellar and Subcortical Contributions to Working Memory Manipulation

1. fMRIprep preprocessing

Anatomical data preprocessing

A total of 2 T1-weighted (T1w) images were found within the input BIDS dataset. All of them were corrected for intensity non-uniformity (INU) with `N4BiasFieldCorrection` [@n4], distributed with ANTs 2.3.1 [@ants, RRID:SCR_004757]. The T1w-reference was then skull-stripped with a *Nipype* implementation of the `antsBrainExtraction.sh` workflow (from ANTs), using OASIS30ANTs as target template. Brain tissue segmentation of cerebrospinal fluid (CSF), white-matter (WM) and gray-matter (GM) was performed on the brain-extracted T1w using `fast` [FSL 6.0.3:b862cdd5, RRID:SCR_002823, @fsl_fast]. An anatomical T1w-reference map was computed after registration of 2 T1w images (after INU-correction) using `mri_robust_template` [FreeSurfer 7.1.1, @fs_template]. Volume-based spatial normalization to two standard spaces (MNI152NLin6Asym, MNI152NLin2009cAsym) was performed through nonlinear registration with `antsRegistration` (ANTs 2.3.1), using brain-extracted versions of both T1w reference and the T1w template. The following templates were were selected for spatial normalization and accessed with *TemplateFlow* [23.0.0, @templateflow]: *FSL's MNI ICBM 152 non-linear 6th Generation Asymmetric Average Brain Stereotaxic Registration Model* [@mni152nlin6asym, RRID:SCR_002823; TemplateFlow ID: MNI152NLin6Asym], *ICBM 152 Nonlinear Asymmetrical template version 2009c* [@mni152nlin2009casym, RRID:SCR_008796; TemplateFlow ID: MNI152NLin2009cAsym].

Functional data preprocessing

For each of the 16 BOLD runs found per subject (across all tasks and sessions), the following preprocessing was performed. First, a reference volume and its skull-stripped version were generated using a custom methodology of *fMRIPrep*. Head-motion parameters with respect to the BOLD reference (transformation matrices, and six corresponding rotation and translation parameters) are estimated before any spatiotemporal filtering using `mcflirt` [FSL 6.0.3:b862cdd5, @mcflirt]. BOLD runs were slice-time corrected to 0.459s (0.5 of slice acquisition range 0s-0.917s) using `3dTshift` from AFNI 20170202 [@afni, RRID:SCR_005927].

The BOLD time-series (including slice-timing correction when applied) were resampled onto their original, native space by applying the transforms to correct for head-motion. These resampled BOLD time-series will be referred to as *preprocessed BOLD in original space*, or just *preprocessed BOLD*. The BOLD reference was then co-registered to the T1w reference using `mri_coreg` (FreeSurfer) followed by `flirt` [FSL 6.0.3:b862cdd5, @flirt] with the boundary-based registration [@bbr] cost-function. Co-registration was configured with six degrees of freedom. Several confounding time-series were calculated based on the *preprocessed BOLD*: framewise displacement (FD), DVARS and three region-wise global signals. FD was computed using two formulations following Power (absolute sum of relative motions, @power_fd_dvars) and Jenkinson (relative root mean square displacement between affines, @mcflirt). FD and DVARS are calculated for each functional run, both using their implementations in *Nipype* [following the definitions by @power_fd_dvars]. The three global signals are extracted within the CSF, the WM, and the whole-brain masks. Additionally, a set of physiological regressors were extracted to allow for component-based noise correction [*CompCor*, @compcor]. Principal components are estimated after high-pass filtering the *preprocessed BOLD* time-series (using a discrete cosine filter with 128s cut-off) for the two *CompCor* variants: temporal (tCompCor) and anatomical (aCompCor). tCompCor components are then calculated from the top 2% variable voxels within the brain mask. For aCompCor, three probabilistic masks (CSF, WM and combined CSF+WM) are generated in anatomical space. The implementation differs from that of Behzadi et al. in that instead of eroding the masks by 2 pixels on BOLD space, a mask of pixels that likely contain a volume fraction of GM is subtracted from the aCompCor masks. This mask is obtained by thresholding the corresponding partial volume map at 0.05, and it ensures components are not extracted from voxels containing a minimal fraction of GM. Finally, these masks are resampled into BOLD space and binarized by thresholding at 0.99 (as in the original implementation). Components are also calculated separately within the WM and CSF masks. For each CompCor decomposition, the *k* components with the largest singular values are retained, such that the retained components' time series are sufficient to explain 50 percent of variance across the nuisance mask (CSF, WM, combined, or temporal). The remaining components are dropped from consideration. The head-motion estimates calculated in the correction step were also placed within the corresponding confounds file. The confound time series derived from head motion estimates and global signals were expanded with the inclusion of temporal derivatives and quadratic terms for each [@confounds_satterthwaite_2013]. Frames that exceeded a threshold of 0.5 mm FD or 1.5

standardized DVARS were annotated as motion outliers. Additional nuisance timeseries are calculated by means of principal components analysis of the signal found within a thin band (*crown*) of voxels around the edge of the brain, as proposed by [@patriat_improved_2017].

The BOLD time-series were resampled into standard space, generating a *preprocessed BOLD run in MNI152NLin6Asym space*. First, a reference volume and its skull-stripped version were generated using a custom methodology of *fMRIPrep*. All resamplings can be performed with *a single interpolation step* by composing all the pertinent transformations (i.e. head-motion transform matrices, susceptibility distortion correction when available, and co-registrations to anatomical and output spaces). Gridded (volumetric) resamplings were performed using `antsApplyTransforms` (ANTs), configured with Lanczos interpolation to minimize the smoothing effects of other kernels [@lanczos]. Non-gridded (surface) resamplings were performed using `mri_vol2surf (FreeSurfer).

Many internal operations of *fMRIPrep* use *Nilearn* 0.10.0 [@nilearn, RRID:SCR_001362], mostly within the functional processing workflow. For more details of the pipeline, see [the section corresponding to workflows in *fMRIPrep*'s documentation] (https://fmriprep.readthedocs.io/en/latest/workflows.html "FMRIPrep's documentation").

2. LDA training and performance evaluation

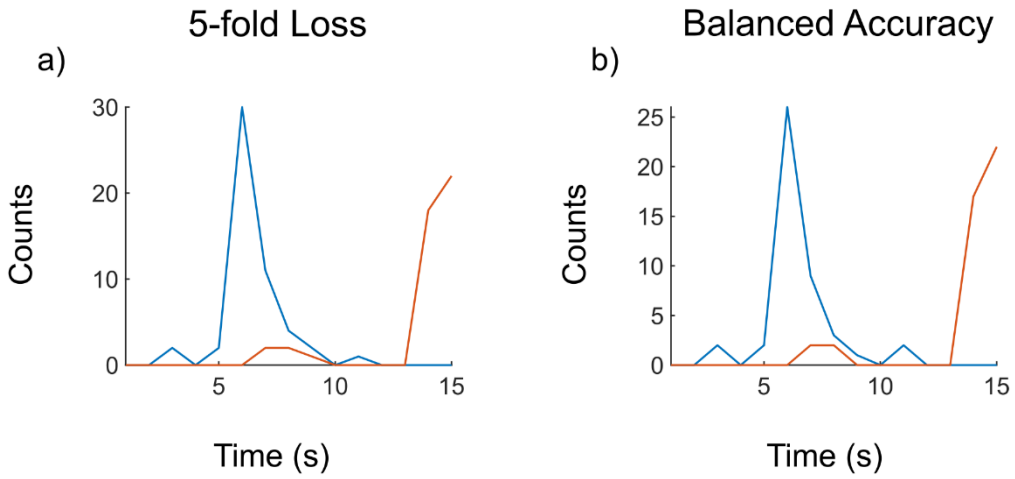

Fig. S1.

Performance measures of LDA classifiers across time and with varying number of principal components. a) Number of times that each timepoint had the least loss. **b)** Number of times that each timepoint had the highest balanced accuracy.

3. Replication of LDA results in Schaefer 1000

Similar to the LDA training with the Schaefer 400 atlas, the timepoints which best separated the conditions were t = 6 (Easy vs. Hard), and t = 15 (Hard-Correct vs. Hard-Incorrect) (Figure 6). For these two separations, the minimum number of principal components (PC) in order to reach maximal balanced accuracy was 5 and 12 respectively. Following dimensionality reduction guidelines and choosing up to the first PC with added explained variance <1% (PC 12). The first 12 PCs explained ~ 36% variance of the data.

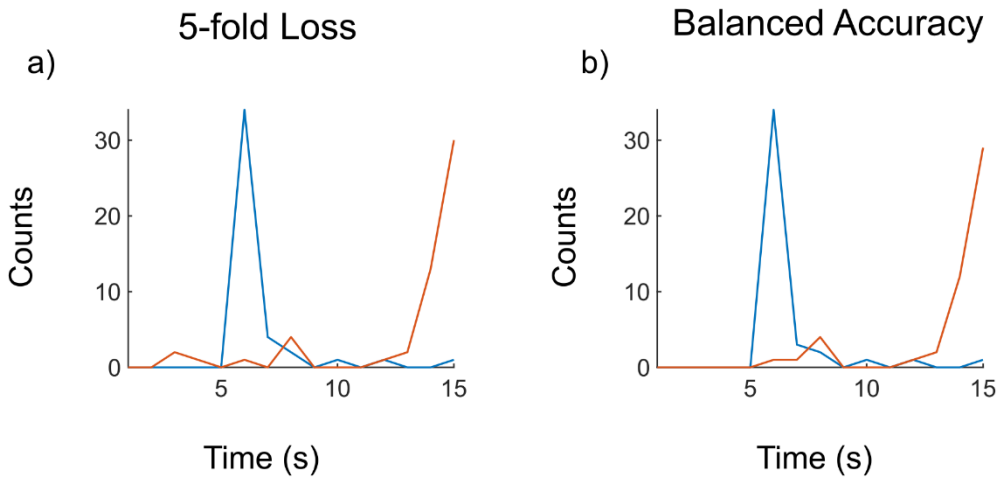

Fig. S2.

Performance measures of LDA classifiers across time and with varying number of principal components for finer parcellation. a) Number of times that each timepoint had the least loss. **b)** Number of times that each timepoint had the highest balanced accuracy.

4. Supplementary data 1. Atlas labels for brain regions comparing Easy-Correct vs. Hard-Correct

ROI Name	X	Y	Z
17Networks_LH_VisCent_ExStr_1	-36	-62	-17
17Networks_LH_VisCent_ExStr_2	-23	-73	-10
17Networks_LH_VisCent_ExStr_6	-41	-87	-3
17Networks_LH_VisCent_ExStr_7	-46	-73	6
17Networks_LH_VisCent_ExStr_9	-39	-84	14
17Networks_LH_VisCent_ExStr_10	-11	-97	17
17Networks_LH_VisCent_ExStr_11	-25	-85	21
17Networks_LH_VisPeri_ExStrInf_1	-24	-55	-8
17Networks_LH_VisPeri_ExStrInf_2	-12	-62	-5
17Networks_LH_VisPeri_ExStrInf_3	-7	-76	-6
17Networks_LH_VisPeri_ExStrInf_4	-13	-43	-5
17Networks_LH_VisPeri_ExStrInf_5	-14	-57	1
17Networks_LH_VisPeri_StriCal_1	-5	-88	2
17Networks_LH_VisPeri_StriCal_2	-7	-74	9
17Networks_LH_VisPeri_ExStrSup_1	-19	-65	7
17Networks_LH_VisPeri_ExStrSup_2	-3	-84	24
17Networks_LH_VisPeri_ExStrSup_3	-12	-71	20
17Networks_LH_VisPeri_ExStrSup_4	-16	-89	33
17Networks_LH_VisPeri_ExStrSup_5	-12	-81	36
17Networks_LH_SomMotA_1	-8	-15	47
17Networks_LH_SomMotA_4	-48	-29	58
17Networks_LH_SomMotA_5	-39	-25	53
17Networks_LH_SomMotA_6	-9	-38	54
17Networks_LH_SomMotA_7	-4	-25	56
17Networks_LH_SomMotA_8	-4	-9	59
17Networks_LH_SomMotA_11	-30	-38	65
17Networks_LH_SomMotA_12	-23	-11	65
17Networks_LH_SomMotA_19	-12	-27	73
17Networks_LH_SomMotB_Ins_1	-36	-24	10
17Networks_LH_SomMotB_S2_2	-36	-26	19
17Networks_LH_DorsAttnA_TempOcc_4	-45	-70	-8
17Networks_LH_DorsAttnA_ParOcc_1	-48	-65	15
17Networks_LH_DorsAttnA_ParOcc_2	-32	-84	27
17Networks_LH_DorsAttnA_SPL_1	-26	-70	31
17Networks_LH_DorsAttnA_SPL_2	-21	-79	45
17Networks_LH_DorsAttnA_SPL_3	-23	-65	46
17Networks_LH_DorsAttnA_SPL_4	-29	-58	50

17Networks_LH_DorsAttnA_SPL_5	-36	-52	56
17Networks_LH_DorsAttnA_SPL_6	-15	-71	57
17Networks_LH_DorsAttnA_SPL_7	-29	-61	62
17Networks_LH_DorsAttnB_PostC_2	-55	-20	41
17Networks_LH_DorsAttnB_PostC_3	-55	-32	45
17Networks_LH_DorsAttnB_PostC_4	-46	-29	44
17Networks_LH_DorsAttnB_PostC_5	-39	-37	49
17Networks_LH_DorsAttnB_PostC_6	-30	-46	63
17Networks_LH_DorsAttnB_PostC_8	-20	-57	66
17Networks_LH_DorsAttnB_FEF_2	-25	-1	55
17Networks_LH_DorsAttnB_FEF_3	-30	-8	52
17Networks_LH_DorsAttnB_PrCv_1	-50	3	38
17Networks_LH_SalVentAttnA_Ins_3	-33	19	8
17Networks_LH_SalVentAttnA_FrMed_2	-5	9	48
17Networks_LH_SalVentAttnB_PFCl_1	-38	49	11
17Networks_LH_SalVentAttnB_Ins_1	-34	16	-8
17Networks_LH_SalVentAttnB_Ins_2	-33	25	-1
17Networks_LH_LimbicB_OFC_3	-10	47	-21
17Networks_LH_LimbicB_OFC_4	-4	23	-19
17Networks_LH_LimbicB_OFC_5	-15	65	-8
17Networks_LH_ContA_IPS_4	-45	-41	47
17Networks_LH_ContA_IPS_5	-33	-46	41
17Networks_LH_ContA_PFCd_1	-21	5	65
17Networks_LH_ContA_PFCl_1	-49	6	26
17Networks_LH_ContA_Cingm_1	-3	5	29
17Networks_LH_ContB_IPL_1	-49	-60	47
17Networks_LH_ContB_IPL_3	-42	-52	49
17Networks_LH_ContB_PFCd_1	-30	14	57
17Networks_LH_ContB_PFClv_1	-42	49	-6
17Networks_LH_ContB_PFCmp_1	-4	28	47
17Networks_LH_ContC_pCun_2	-9	-77	45
17Networks_LH_DefaultA_IPL_1	-47	-64	31
17Networks_LH_DefaultA_PFCd_1	-25	28	43
17Networks_LH_DefaultA_PFCd_2	-18	36	48
17Networks_LH_DefaultA_PFCd_3	-22	20	52
17Networks_LH_DefaultA_pCunPCC_1	-4	-53	20
17Networks_LH_DefaultA_pCunPCC_2	-5	-60	30
17Networks_LH_DefaultA_pCunPCC_3	-7	-44	32
17Networks_LH_DefaultA_PFCm_1	-5	55	-10
17Networks_LH_DefaultA_PFCm_2	-6	35	-9
17Networks_LH_DefaultA_PFCm_3	-6	59	7

17Networks_LH_DefaultA_PFCm_4	-6	45	6
17Networks_LH_DefaultA_PFCm_6	-5	34	21
17Networks_LH_DefaultB_Temp_1	-44	13	-34
17Networks_LH_DefaultB_Temp_2	-54	-2	-30
17Networks_LH_DefaultB_Temp_4	-57	-9	-14
17Networks_LH_DefaultB_Temp_6	-52	-22	-6
17Networks_LH_DefaultB_IPL_1	-45	-58	21
17Networks_LH_DefaultB_PFCd_1	-4	51	28
17Networks_LH_DefaultB_PFCd_2	-14	58	31
17Networks_LH_DefaultB_PFCd_4	-8	43	51
17Networks_LH_DefaultB_PFCd_5	-13	24	61
17Networks_LH_DefaultB_PFCd_6	-6	10	65
17Networks_LH_DefaultB_PFCl_1	-41	19	48
17Networks_LH_DefaultB_PFCv_1	-36	22	-16
17Networks_LH_DefaultB_PFCv_3	-46	32	-10
17Networks_LH_DefaultB_PFCv_5	-53	19	11
17Networks_LH_DefaultC_IPL_1	-40	-79	30
17Networks_LH_DefaultC_Rsp_1	-13	-49	4
17Networks_LH_DefaultC_Rsp_2	-8	-52	9
17Networks_LH_DefaultC_Rsp_3	-13	-61	19
17Networks_LH_DefaultC_PHC_3	-18	-37	-12
17Networks_RH_VisCent_ExStr_1	36	-53	-17
17Networks_RH_VisCent_ExStr_2	37	-73	-16
17Networks_RH_VisCent_ExStr_3	23	-74	-11
17Networks_RH_VisCent_Striate_1	8	-92	-2
17Networks_RH_VisCent_ExStr_7	35	-89	2
17Networks_RH_VisCent_ExStr_9	43	-79	10
17Networks_RH_VisCent_ExStr_10	13	-94	19
17Networks_RH_VisCent_ExStr_11	27	-87	21
17Networks_RH_VisPeri_ExStrInf_1	26	-52	-9
17Networks_RH_VisPeri_ExStrInf_2	18	-36	-12
17Networks_RH_VisPeri_ExStrInf_3	9	-72	-5
17Networks_RH_VisPeri_ExStrInf_4	13	-58	-3
17Networks_RH_VisPeri_ExStrInf_5	18	-45	-3
17Networks_RH_VisPeri_StriCal_1	9	-74	9
17Networks_RH_VisPeri_StriCal_2	22	-59	6
17Networks_RH_VisPeri_ExStrSup_1	16	-66	19
17Networks_RH_VisPeri_ExStrSup_2	5	-80	24
17Networks_RH_VisPeri_ExStrSup_3	14	-78	34
17Networks_RH_VisPeri_ExStrSup_4	16	-87	36
17Networks_RH_SomMotA_1	54	-17	40

17Networks_RH_SomMotA_11	4	-25	58
17Networks_RH_SomMotB_Cent_1	61	6	30
17Networks_RH_DorsAttnA_TempOcc_1	34	-37	-23
17Networks_RH_DorsAttnA_TempOcc_3	50	-64	-9
17Networks_RH_DorsAttnA_ParOcc_1	48	-66	4
17Networks_RH_DorsAttnA_ParOcc_3	36	-79	24
17Networks_RH_DorsAttnA_SPL_1	29	-78	37
17Networks_RH_DorsAttnA_SPL_2	32	-66	35
17Networks_RH_DorsAttnA_SPL_3	19	-79	50
17Networks_RH_DorsAttnA_SPL_4	31	-64	53
17Networks_RH_DorsAttnA_SPL_5	21	-69	53
17Networks_RH_DorsAttnA_SPL_6	34	-50	54
17Networks_RH_DorsAttnA_SPL_7	27	-58	61
17Networks_RH_DorsAttnA_SPL_8	14	-64	65
17Networks_RH_DorsAttnB_TempOcc_1	59	-55	-2
17Networks_RH_DorsAttnB_PostC_1	61	-14	30
17Networks_RH_DorsAttnB_PostC_2	57	-23	44
17Networks_RH_DorsAttnB_PostC_3	44	-37	50
17Networks_RH_DorsAttnB_PostC_4	45	-28	42
17Networks_RH_DorsAttnB_PostC_5	35	-36	51
17Networks_RH_DorsAttnB_PostC_6	7	-54	59
17Networks_RH_DorsAttnB_FEF_2	27	-3	52
17Networks_RH_DorsAttnB_FEF_3	25	-3	64
17Networks_RH_SalVentAttnA_PrC_1	51	3	41
17Networks_RH_SalVentAttnA_FrOper_3	54	12	12
17Networks_RH_SalVentAttnA_FrMed_2	6	11	58
17Networks_RH_SalVentAttnB_Ins_1	34	21	-8
17Networks_RH_SalVentAttnB_Ins_2	37	23	5
17Networks_RH_SalVentAttnB_PFCmp_1	8	35	25
17Networks_RH_LimbicB_OFC_1	13	24	-21
17Networks_RH_LimbicB_OFC_2	23	22	-21
17Networks_RH_LimbicB_OFC_3	8	47	-23
17Networks_RH_LimbicB_OFC_4	20	43	-18
17Networks_RH_LimbicB_OFC_5	5	22	-21
17Networks_RH_LimbicB_OFC_6	9	63	-14
17Networks_RH_ContA_IPS_2	54	-33	51
17Networks_RH_ContA_IPS_3	47	-44	46
17Networks_RH_ContA_IPS_4	36	-44	45
17Networks_RH_ContA_PFCl_1	50	30	18
17Networks_RH_ContA_PFCl_2	48	18	23
17Networks_RH_ContA_PFCl_3	47	29	28

17Networks_RH_ContA_PFCl_4	49	8	25
17Networks_RH_ContA_PFCl_5	39	11	34
17Networks_RH_ContA_Cingm_1	5	1	30
17Networks_RH_ContB_PFClv_3	42	51	-6
17Networks_RH_ContB_PFCmp_1	5	28	48
17Networks_RH_DefaultA_pCunPCC_1	6	-52	23
17Networks_RH_DefaultA_PFCm_1	5	41	-11
17Networks_RH_DefaultA_PFCm_2	9	67	1
17Networks_RH_DefaultA_PFCm_3	7	42	4
17Networks_RH_DefaultA_PFCm_4	7	54	13
17Networks_RH_DefaultA_PFCm_6	6	25	18
17Networks_RH_DefaultB_PFCd_3	5	44	40
17Networks_RH_DefaultB_PFCd_4	14	39	52
17Networks_RH_DefaultB_PFCv_1	35	23	-18
17Networks_RH_DefaultC_IPL_1	48	-64	22
17Networks_RH_DefaultC_IPL_2	45	-75	31
17Networks_RH_DefaultC_Rsp_1	14	-46	4
17Networks_RH_DefaultC_Rsp_2	12	-55	15
17Networks_RH_DefaultC_PHC_2	31	-31	-18
HIP-head-m1-rh	20	-12	22
THA-VAip-rh	8	-14	4
THA-VAia-rh	6	-6	2
HIP-head-l-rh	30	-14	-20
HIP-body-rh	30	-28	-10
THA-VPm-rh	10	-24	2
PUT-VA-rh	22	12	-6
PUT-DA-rh	26	6	2
PUT-VP-rh	30	-12	0
PUT-DP-rh	28	-2	6
CAU-VA-rh	10	12	4
CAU-DA-rh	16	18	8
CAU-body-rh	14	6	16
CAU-tail-rh	16	-2	20
NAc-shell-rh	12	10	-6
NAc-core-rh	14	18	-2
pGP-rh	24	-8	-2
aGP-rh	18	0	-2
HIP-head-m1-lh	-18	-12	-22
THA-VAip-lh	-6	-14	4
THA-VAia-lh	-4	-6	2
HIP-body-lh	-28	-28	-10

THA-VPm-lh	-8	-24	2
THA-VPl-lh	-16	-22	4
THA-DAl-lh	-14	-20	12
PUT-VA-lh	-20	12	-6
PUT-DA-lh	-24	6	2
PUT-VP-lh	-28	-12	0
PUT-DP-lh	-26	-2	6
CAU-VA-lh	-8	12	4
CAU-DA-lh	-14	18	8
CAU-body-lh	-12	6	16
CAU-tail-lh	-14	-2	20
NAc-shell-lh	-10	10	-6
NAc-core-lh	-12	18	-2
pGP-lh	-22	-8	-2
aGP-lh	-16	0	-2
Left_I_IV	-4	-50	-11
Right_I_IV	4	-50	-11
Right_V	18	-50	-19
Left_VI	-30	-50	-27
Vermis_VI	0	-65	-27
Right_VI	30	-50	-27
Vermis_CrusII	0	-76	-35
Vermis_VIIb	0	-68	-32
Left_IX	-5	-51	-55
Vermis_IX	0	-55	-35
Left_X	-22	-35	-43
Vermis_X	0	-47	-37

5. Supplementary data 2. Atlas labels for brain regions comparing hard-correct vs. hard-incorrect

ROI Name	X	Y	Z
17Networks_LH_VisPeri_ExStrInf_2	-12	-62	-5
17Networks_LH_VisPeri_ExStrInf_4	-13	-43	-5
17Networks_LH_VisPeri_ExStrInf_5	-14	-57	1
17Networks_LH_VisPeri_StriCal_2	-7	-74	9
17Networks_LH_VisPeri_ExStrSup_1	-19	-65	7
17Networks_LH_VisPeri_ExStrSup_2	-3	-84	24
17Networks_LH_VisPeri_ExStrSup_3	-12	-71	20
17Networks_LH_VisPeri_ExStrSup_5	-12	-81	36
17Networks_LH_SomMotA_8	-4	-9	59
17Networks_LH_SomMotA_12	-23	-11	65
17Networks_LH_SomMotA_16	-14	-11	73
17Networks_LH_SomMotB_Cent_4	-51	-7	43
17Networks_LH_DorsAttnA_TempOcc_1	-45	-42	-21
17Networks_LH_DorsAttnA_TempOcc_2	-33	-42	-21
17Networks_LH_DorsAttnA_TempOcc_3	-49	-56	-15
17Networks_LH_DorsAttnA_ParOcc_1	-48	-65	15
17Networks_LH_DorsAttnA_ParOcc_2	-32	-84	27
17Networks_LH_DorsAttnA_SPL_1	-26	-70	31
17Networks_LH_DorsAttnA_SPL_2	-21	-79	45
17Networks_LH_DorsAttnA_SPL_3	-23	-65	46
17Networks_LH_DorsAttnA_SPL_4	-29	-58	50
17Networks_LH_DorsAttnA_SPL_5	-36	-52	56
17Networks_LH_DorsAttnA_SPL_6	-15	-71	57
17Networks_LH_DorsAttnA_SPL_7	-29	-61	62
17Networks_LH_DorsAttnB_PostC_1	-61	-23	33
17Networks_LH_DorsAttnB_PostC_3	-55	-32	45
17Networks_LH_DorsAttnB_PostC_5	-39	-37	49
17Networks_LH_DorsAttnB_PostC_6	-30	-46	63
17Networks_LH_DorsAttnB_PostC_7	-7	-59	63
17Networks_LH_DorsAttnB_PostC_8	-20	-57	66
17Networks_LH_DorsAttnB_PostC_9	-13	-50	72
17Networks_LH_DorsAttnB_FEF_1	-40	-3	51
17Networks_LH_DorsAttnB_FEF_2	-25	-1	55
17Networks_LH_DorsAttnB_FEF_3	-30	-8	52
17Networks_LH_DorsAttnB_PrCv_1	-50	3	38
17Networks_LH_SalVentAttnA_ParOper_2	-58	-44	27
17Networks_LH_SalVentAttnA_ParOper_3	-61	-36	33

17Networks_LH_SalVentAttnA_Ins_2	-40	-15	-2
17Networks_LH_SalVentAttnA_Ins_3	-33	19	8
17Networks_LH_SalVentAttnA_FrOper_2	-52	9	13
17Networks_LH_SalVentAttnA_ParMed_1	-11	-27	41
17Networks_LH_SalVentAttnA_ParMed_2	-13	-41	47
17Networks_LH_SalVentAttnA_ParMed_3	-6	-49	57
17Networks_LH_SalVentAttnA_FrMed_1	-7	0	41
17Networks_LH_SalVentAttnA_FrMed_2	-5	9	48
17Networks_LH_SalVentAttnA_FrMed_3	-8	-3	71
17Networks_LH_SalVentAttnB_PFCl_2	-29	43	30
17Networks_LH_SalVentAttnB_PFCl_3	-36	32	38
17Networks_LH_SalVentAttnB_Ins_1	-34	16	-8
17Networks_LH_SalVentAttnB_Ins_2	-33	25	-1
17Networks_LH_SalVentAttnB_Ins_3	-43	12	2
17Networks_LH_SalVentAttnB_OFC_1	-27	49	-14
17Networks_LH_SalVentAttnB_PFCmp_1	-6	22	31
17Networks_LH_LimbicB_OFC_2	-24	23	-20
17Networks_LH_LimbicB_OFC_3	-10	47	-21
17Networks_LH_LimbicA_TempPole_1	-37	-5	-42
17Networks_LH_LimbicA_TempPole_3	-26	-9	-33
17Networks_LH_LimbicA_TempPole_5	-40	-21	-27
17Networks_LH_LimbicA_TempPole_6	-32	12	-29
17Networks_LH_ContA_Temp_1	-55	-62	-1
17Networks_LH_ContA_IPS_1	-29	-74	42
17Networks_LH_ContA_IPS_2	-58	-42	45
17Networks_LH_ContA_IPS_3	-35	-62	48
17Networks_LH_ContA_IPS_4	-45	-41	47
17Networks_LH_ContA_IPS_5	-33	-46	41
17Networks_LH_ContA_PFCd_1	-21	5	65
17Networks_LH_ContA_PFClv_1	-48	35	10
17Networks_LH_ContA_PFClv_2	-42	38	22
17Networks_LH_ContA_PFCl_1	-49	6	26
17Networks_LH_ContA_PFCl_2	-45	20	27
17Networks_LH_ContA_PFCl_3	-39	7	34
17Networks_LH_ContA_Cingm_1	-3	5	29
17Networks_LH_ContB_Temp_2	-60	-49	-10
17Networks_LH_ContB_IPL_2	-53	-50	45
17Networks_LH_ContB_PFCd_1	-30	14	57
17Networks_LH_ContB_PFClv_2	-28	58	-1
17Networks_LH_ContB_PFClv_3	-28	57	13
17Networks_LH_ContB_PFCmp_1	-4	28	47

17Networks_LH_ContC_pCun_1	-10	-70	32
17Networks_LH_ContC_pCun_2	-9	-77	45
17Networks_LH_ContC_pCun_3	-5	-64	52
17Networks_LH_ContC_Cingp_1	-6	-41	24
17Networks_LH_ContC_Cingp_2	-4	-22	29
17Networks_LH_DefaultA_PFCd_1	-25	28	43
17Networks_LH_DefaultA_PFCd_3	-22	20	52
17Networks_LH_DefaultA_pCunPCC_2	-5	-60	30
17Networks_LH_DefaultA_pCunPCC_4	-4	-34	38
17Networks_LH_DefaultA_pCunPCC_6	-3	-68	41
17Networks_LH_DefaultA_pCunPCC_7	-7	-51	43
17Networks_LH_DefaultA_PFCm_2	-6	35	-9
17Networks_LH_DefaultA_PFCm_4	-6	45	6
17Networks_LH_DefaultA_PFCm_6	-5	34	21
17Networks_LH_DefaultB_Temp_1	-44	13	-34
17Networks_LH_DefaultB_Temp_2	-54	-2	-30
17Networks_LH_DefaultB_Temp_4	-57	-9	-14
17Networks_LH_DefaultB_Temp_5	-61	-35	-3
17Networks_LH_DefaultB_Temp_6	-52	-22	-6
17Networks_LH_DefaultB_IPL_1	-45	-58	21
17Networks_LH_DefaultB_IPL_2	-57	-55	30
17Networks_LH_DefaultB_PFCd_3	-22	51	31
17Networks_LH_DefaultB_PFCd_6	-6	10	65
17Networks_LH_DefaultB_PFCl_1	-41	19	48
17Networks_LH_DefaultB_PFCl_2	-42	7	48
17Networks_LH_DefaultB_PFCv_1	-36	22	-16
17Networks_LH_DefaultB_PFCv_2	-36	37	-13
17Networks_LH_DefaultB_PFCv_3	-46	32	-10
17Networks_LH_DefaultB_PFCv_4	-48	28	0
17Networks_LH_DefaultB_PFCv_5	-53	19	11
17Networks_LH_DefaultC_IPL_1	-40	-79	30
17Networks_LH_DefaultC_Rsp_1	-13	-49	4
17Networks_LH_DefaultC_Rsp_2	-8	-52	9
17Networks_LH_DefaultC_Rsp_3	-13	-61	19
17Networks_LH_DefaultC_PHC_2	-30	-33	-18
17Networks_LH_TempPar_1	-53	6	-11
17Networks_LH_TempPar_2	-61	-13	-3
17Networks_LH_TempPar_3	-62	-32	5
17Networks_LH_TempPar_4	-52	-43	5
17Networks_LH_TempPar_5	-57	-54	10
17Networks_LH_TempPar_6	-59	-49	16

17Networks_RH_VisPeri_ExStrInf_4	13	-58	-3
17Networks_RH_VisPeri_ExStrInf_5	18	-45	-3
17Networks_RH_VisPeri_StriCal_1	9	-74	9
17Networks_RH_VisPeri_StriCal_2	22	-59	6
17Networks_RH_VisPeri_ExStrSup_1	16	-66	19
17Networks_RH_VisPeri_ExStrSup_2	5	-80	24
17Networks_RH_VisPeri_ExStrSup_3	14	-78	34
17Networks_RH_SomMotA_1	54	-17	40
17Networks_RH_SomMotA_5	7	-10	51
17Networks_RH_SomMotA_6	43	-21	54
17Networks_RH_SomMotA_7	37	-20	64
17Networks_RH_SomMotA_8	32	-34	63
17Networks_RH_SomMotA_9	31	-41	64
17Networks_RH_SomMotA_12	29	-11	65
17Networks_RH_SomMotA_17	17	-6	69
17Networks_RH_SomMotB_Ins_1	39	-19	5
17Networks_RH_SomMotB_S2_4	41	-29	18
17Networks_RH_SomMotB_S2_7	49	-21	19
17Networks_RH_DorsAttnA_ParOcc_2	54	-56	12
17Networks_RH_DorsAttnA_SPL_3	19	-79	50
17Networks_RH_DorsAttnA_SPL_5	21	-69	53
17Networks_RH_DorsAttnA_SPL_7	27	-58	61
17Networks_RH_DorsAttnA_SPL_8	14	-64	65
17Networks_RH_DorsAttnB_PostC_4	45	-28	42
17Networks_RH_DorsAttnB_PostC_5	35	-36	51
17Networks_RH_DorsAttnB_PostC_6	7	-54	59
17Networks_RH_DorsAttnB_PostC_7	24	-50	68
17Networks_RH_DorsAttnB_PostC_8	16	-47	74
17Networks_RH_DorsAttnB_FEF_2	27	-3	52
17Networks_RH_DorsAttnB_FEF_3	25	-3	64
17Networks_RH_SalVentAttnA_ParOper_2	60	-22	22
17Networks_RH_SalVentAttnA_ParOper_3	63	-26	38
17Networks_RH_SalVentAttnA_Ins_1	40	5	-15
17Networks_RH_SalVentAttnA_Ins_3	40	-10	-4
17Networks_RH_SalVentAttnA_FrMed_1	7	2	43
17Networks_RH_SalVentAttnA_ParMed_1	11	-17	41
17Networks_RH_SalVentAttnA_ParMed_2	12	-34	43
17Networks_RH_SalVentAttnA_FrMed_2	6	11	58
17Networks_RH_SalVentAttnA_ParMed_3	10	-43	53
17Networks_RH_SalVentAttnA_ParMed_4	11	-32	50
17Networks_RH_SalVentAttnA_FrMed_3	7	-2	67

17Networks_RH_SalVentAttnA_FrMed_4	16	7	69
17Networks_RH_SalVentAttnB_IPL_1	62	-37	37
17Networks_RH_SalVentAttnB_Ins_1	34	21	-8
17Networks_RH_SalVentAttnB_Ins_2	37	23	5
17Networks_RH_SalVentAttnB_PFCmp_2	7	19	35
17Networks_RH_LimbicB_OFC_2	23	22	-21
17Networks_RH_LimbicA_TempPole_2	49	-7	-39
17Networks_RH_LimbicA_TempPole_3	37	17	-38
17Networks_RH_LimbicA_TempPole_4	39	-15	-31
17Networks_RH_LimbicA_TempPole_5	29	12	-30
17Networks_RH_ContA_PFCd_1	24	10	58
17Networks_RH_ContA_PFCl_5	39	11	34
17Networks_RH_ContA_Cingm_1	5	1	30
17Networks_RH_ContB_IPL_1	55	-45	33
17Networks_RH_ContB_PFCld_1	39	33	38
17Networks_RH_ContB_PFCmp_1	5	28	48
17Networks_RH_ContC_pCun_1	17	-63	28
17Networks_RH_ContC_pCun_2	13	-71	39
17Networks_RH_ContC_pCun_3	5	-64	44
17Networks_RH_ContC_pCun_4	7	-50	45
17Networks_RH_ContC_pCun_5	8	-71	53
17Networks_RH_ContC_Cingp_1	7	-44	20
17Networks_RH_ContC_Cingp_2	6	-26	28
17Networks_RH_DefaultB_AntTemp_1	49	9	-33
17Networks_RH_DefaultB_PFCv_1	35	23	-18
17Networks_RH_DefaultB_PFCv_2	48	32	-8
17Networks_RH_DefaultB_PFCv_3	54	24	6
17Networks_RH_DefaultC_IPL_2	45	-75	31
17Networks_RH_DefaultC_Rsp_1	14	-46	4
17Networks_RH_DefaultC_Rsp_2	12	-55	15
17Networks_RH_TempPar_1	47	16	-20
17Networks_RH_TempPar_3	49	-20	-8
17Networks_RH_TempPar_5	50	-33	2
17Networks_RH_TempPar_6	59	-46	7
17Networks_RH_TempPar_7	51	-41	13
17Networks_RH_TempPar_9	55	-46	19
17Networks_RH_TempPar_10	62	-40	22
HIP-head-l-rh	30	-14	-20
PUT-VA-rh	22	12	-6
PUT-DA-rh	26	6	2
CAU-VA-rh	10	12	4

CAU-DA-rh	16	18	8
CAU-body-rh	14	6	16
NAc-shell-rh	12	10	-6
NAc-core-rh	14	18	-2
HIP-head-m1-lh	-18	-12	-22
HIP-head-m2-lh	-20	-18	-16
HIP-head-l-lh	-28	-14	-20
HIP-body-lh	-28	-28	-10
HIP-tail-lh	-22	-38	-2
THA-VAs-lh	-8	-10	12
THA-DAm-lh	-8	-24	12
PUT-VA-lh	-20	12	-6
PUT-DA-lh	-24	6	2
CAU-VA-lh	-8	12	4
CAU-DA-lh	-14	18	8
CAU-body-lh	-12	6	16
CAU-tail-lh	-14	-2	20
lAMY-lh	-26	-2	-22
NAc-shell-lh	-10	10	-6
NAc-core-lh	-12	18	-2
Left_VI	-30	-50	-27
Vermis_VI	0	-65	-27
Right_VI	30	-50	-27
Right_CrusI	-45	-65	-32
Right_CrusII	39	-65	-47
Right_VIIb	33	-65	-53
Right_IX	5	-51	-55
Right_X	22	-35	-43

6. Supplementary data 3. Atlas labels for brain regions important for both comparisons

ROI Name	X	Y	Z
17Networks_LH_VisPeri_ExStrInf_2	-12	-62	-5
17Networks_LH_VisPeri_ExStrInf_4	-13	-43	-5
17Networks_LH_VisPeri_ExStrInf_5	-14	-57	1
17Networks_LH_VisPeri_StriCal_2	-7	-74	9
17Networks_LH_VisPeri_ExStrSup_1	-19	-65	7
17Networks_LH_VisPeri_ExStrSup_2	-3	-84	24
17Networks_LH_VisPeri_ExStrSup_3	-12	-71	20
17Networks_LH_VisPeri_ExStrSup_5	-12	-81	36
17Networks_LH_SomMotA_8	-4	-9	59
17Networks_LH_SomMotA_12	-23	-11	65
17Networks_LH_DorsAttnA_ParOcc_1	-48	-65	15
17Networks_LH_DorsAttnA_ParOcc_2	-32	-84	27
17Networks_LH_DorsAttnA_SPL_1	-26	-70	31
17Networks_LH_DorsAttnA_SPL_2	-21	-79	45
17Networks_LH_DorsAttnA_SPL_3	-23	-65	46
17Networks_LH_DorsAttnA_SPL_4	-29	-58	50
17Networks_LH_DorsAttnA_SPL_5	-36	-52	56
17Networks_LH_DorsAttnA_SPL_6	-15	-71	57
17Networks_LH_DorsAttnA_SPL_7	-29	-61	62
17Networks_LH_DorsAttnB_PostC_3	-55	-32	45
17Networks_LH_DorsAttnB_PostC_5	-39	-37	49
17Networks_LH_DorsAttnB_PostC_6	-30	-46	63
17Networks_LH_DorsAttnB_PostC_8	-20	-57	66
17Networks_LH_DorsAttnB_FEF_2	-25	-1	55
17Networks_LH_DorsAttnB_FEF_3	-30	-8	52
17Networks_LH_DorsAttnB_PrCv_1	-50	3	38
17Networks_LH_SalVentAttnA_Ins_3	-33	19	8
17Networks_LH_SalVentAttnA_FrMed_2	-5	9	48
17Networks_LH_SalVentAttnB_Ins_1	-34	16	-8
17Networks_LH_SalVentAttnB_Ins_2	-33	25	-1
17Networks_LH_LimbicB_OFC_3	-10	47	-21
17Networks_LH_ContA_IPS_4	-45	-41	47
17Networks_LH_ContA_IPS_5	-33	-46	41
17Networks_LH_ContA_PFCd_1	-21	5	65
17Networks_LH_ContA_PFCl_1	-49	6	26
17Networks_LH_ContA_Cingm_1	-3	5	29
17Networks_LH_ContB_PFCd_1	-30	14	57
17Networks_LH_ContB_PFCmp_1	-4	28	47

17Networks_LH_ContC_pCun_2	-9	-77	45
17Networks_LH_DefaultA_PFCd_1	-25	28	43
17Networks_LH_DefaultA_PFCd_3	-22	20	52
17Networks_LH_DefaultA_pCunPCC_2	-5	-60	30
17Networks_LH_DefaultA_PFCm_2	-6	35	-9
17Networks_LH_DefaultA_PFCm_4	-6	45	6
17Networks_LH_DefaultA_PFCm_6	-5	34	21
17Networks_LH_DefaultB_Temp_1	-44	13	-34
17Networks_LH_DefaultB_Temp_2	-54	-2	-30
17Networks_LH_DefaultB_Temp_4	-57	-9	-14
17Networks_LH_DefaultB_Temp_6	-52	-22	-6
17Networks_LH_DefaultB_IPL_1	-45	-58	21
17Networks_LH_DefaultB_PFCd_6	-6	10	65
17Networks_LH_DefaultB_PFCl_1	-41	19	48
17Networks_LH_DefaultB_PFCv_1	-36	22	-16
17Networks_LH_DefaultB_PFCv_3	-46	32	-10
17Networks_LH_DefaultB_PFCv_5	-53	19	11
17Networks_LH_DefaultC_IPL_1	-40	-79	30
17Networks_LH_DefaultC_Rsp_1	-13	-49	4
17Networks_LH_DefaultC_Rsp_2	-8	-52	9
17Networks_LH_DefaultC_Rsp_3	-13	-61	19
17Networks_RH_VisPeri_ExStrInf_4	13	-58	-3
17Networks_RH_VisPeri_ExStrInf_5	18	-45	-3
17Networks_RH_VisPeri_StriCal_1	9	-74	9
17Networks_RH_VisPeri_StriCal_2	22	-59	6
17Networks_RH_VisPeri_ExStrSup_1	16	-66	19
17Networks_RH_VisPeri_ExStrSup_2	5	-80	24
17Networks_RH_VisPeri_ExStrSup_3	14	-78	34
17Networks_RH_SomMotA_1	54	-17	40
17Networks_RH_DorsAttnA_SPL_3	19	-79	50
17Networks_RH_DorsAttnA_SPL_5	21	-69	53
17Networks_RH_DorsAttnA_SPL_7	27	-58	61
17Networks_RH_DorsAttnA_SPL_8	14	-64	65
17Networks_RH_DorsAttnB_PostC_4	45	-28	42
17Networks_RH_DorsAttnB_PostC_5	35	-36	51
17Networks_RH_DorsAttnB_PostC_6	7	-54	59
17Networks_RH_DorsAttnB_FEF_2	27	-3	52
17Networks_RH_DorsAttnB_FEF_3	25	-3	64
17Networks_RH_SalVentAttnA_FrMed_2	6	11	58
17Networks_RH_SalVentAttnB_Ins_1	34	21	-8
17Networks_RH_SalVentAttnB_Ins_2	37	23	5

17Networks_RH_LimbicB_OFC_2	23	22	-21
17Networks_RH_ContA_PFCl_5	39	11	34
17Networks_RH_ContA_Cingm_1	5	1	30
17Networks_RH_ContB_PFCmp_1	5	28	48
17Networks_RH_DefaultB_PFCv_1	35	23	-18
17Networks_RH_DefaultC_IPL_2	45	-75	31
17Networks_RH_DefaultC_Rsp_1	14	-46	4
17Networks_RH_DefaultC_Rsp_2	12	-55	15
HIP-head-l-rh	30	-14	-20
PUT-VA-rh	22	12	-6
PUT-DA-rh	26	6	2
CAU-VA-rh	10	12	4
CAU-DA-rh	16	18	8
CAU-body-rh	14	6	16
NAc-shell-rh	12	10	-6
NAc-core-rh	14	18	-2
HIP-head-m1-lh	-18	-12	-22
HIP-body-lh	-28	-28	-10
PUT-VA-lh	-20	12	-6
PUT-DA-lh	-24	6	2
CAU-VA-lh	-8	12	4
CAU-DA-lh	-14	18	8
CAU-body-lh	-12	6	16
CAU-tail-lh	-14	-2	20
NAc-shell-lh	-10	10	-6
NAc-core-lh	-12	18	-2
Left_VI	-30	-50	-27
Vermis_VI	0	-65	-27
Right_VI	30	-50	-27

7. Brain maps for other quadrants

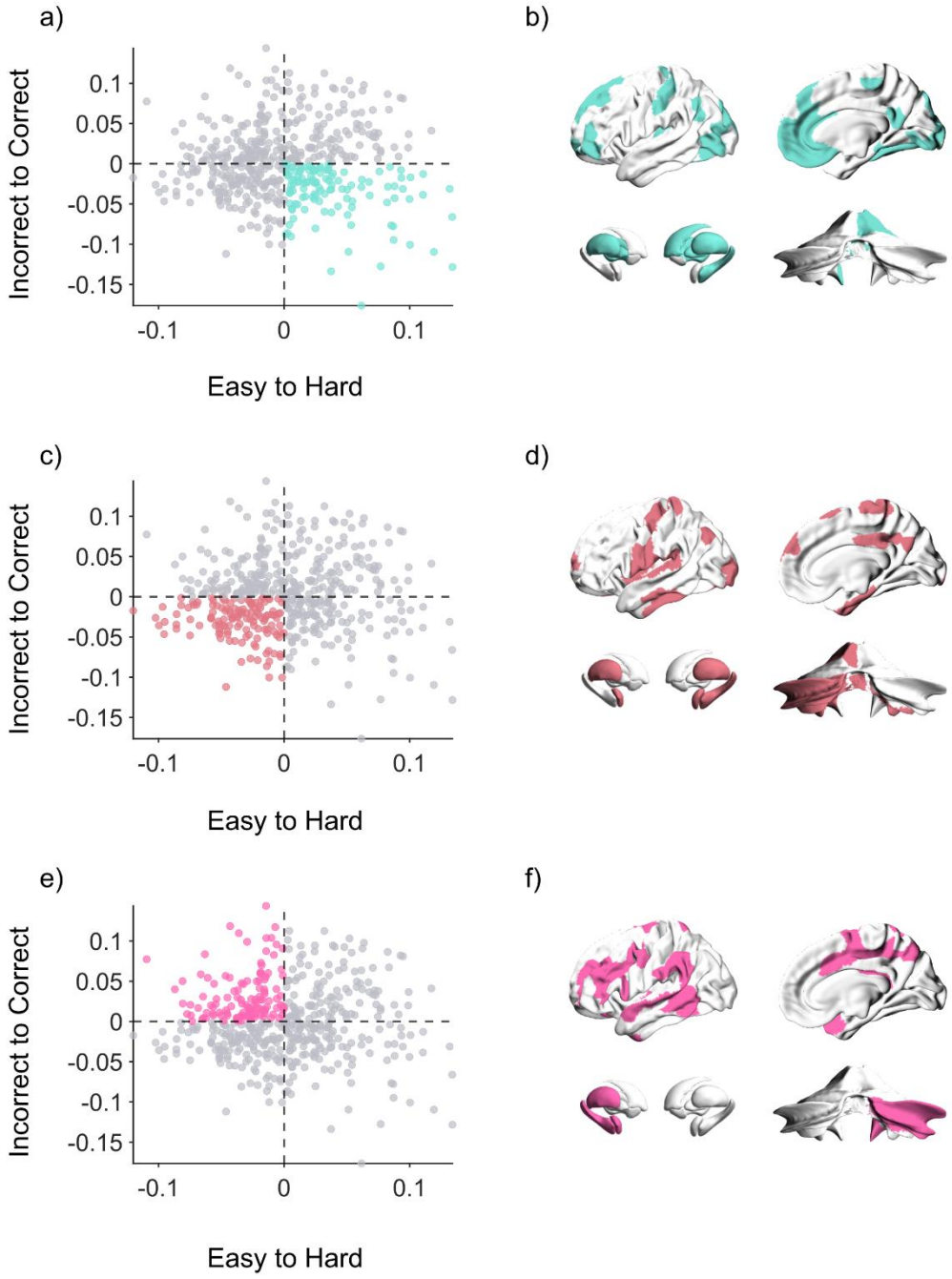

Fig. S3.

Brain maps for other quadrants. a, b) Quadrant 2: regions related to Hard-Incorrect trials. **c, d)** Quadrant 3: regions related to Easy-Incorrect trials. **e, f)** Quadrant 4: regions related to Easy-Correct trials.

8. Cross-correlation of Medium vs. Hard trials

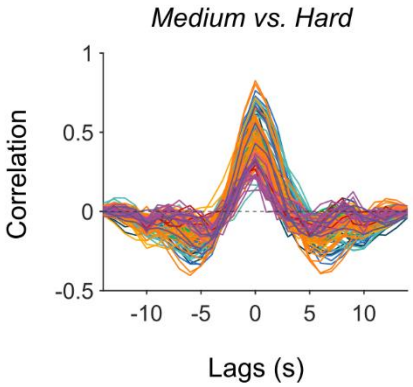

Fig. S4

Cross-correlation of Medium vs. Hard trials. Each line is a brain region. Lines are colored by their allocation to the 7-Yeo cortical networks, cerebellum, and subcortex.

Appendix II: Supplementary Material for Chapter 3

Cerebellar engagement enhances expertise in a sensorimotor adaptation task

1. fMRI preprocessing

2. fMRI scan timing

3. Table of correlation coefficients for significant regions in BIS GLM

4. Schaefer 1000 analysis

1. fMRI preprocessing

Anatomical data preprocessing

A total of 2 T1-weighted (T1w) images were found within the input BIDS dataset. All of them were corrected for intensity non-uniformity (INU) with `N4BiasFieldCorrection` [@n4], distributed with ANTs 2.3.1 [@ants, RRID:SCR_004757]. The T1w-reference was then skull-stripped with a *Nipype* implementation of the `antsBrainExtraction.sh` workflow (from ANTs), using OASIS30ANTs as target template. Brain tissue segmentation of cerebrospinal fluid (CSF), white-matter (WM) and gray-matter (GM) was performed on the brain-extracted T1w using `fast` [FSL 6.0.3:b862cdd5, RRID:SCR_002823, @fsl_fast]. A T1w-reference map was computed after registration of 2 T1w images (after INU-correction) using `mri_robust_template` [FreeSurfer 7.1.1, @fs_template]. Volume-based spatial normalization to one standard space (MNI152NLin2009cAsym) was performed through nonlinear registration with `antsRegistration` (ANTs 2.3.1), using brain-extracted versions of both T1w reference and the T1w template. The following template was selected for spatial normalization: *ICBM 152 Nonlinear Asymmetrical template version 2009c* [@mni152nlin2009casym, RRID:SCR_008796; TemplateFlow ID: NI152NLin2009cAsym].

Functional data preprocessing

For each of the 2 BOLD runs found per subject (across all tasks and sessions), the following preprocessing was performed. First, a reference volume and its skull-stripped version were generated using a custom methodology of *fMRIPrep*. Head-motion parameters with respect to the BOLD reference (transformation matrices, and six corresponding rotation and translation parameters) are estimated before any spatiotemporal filtering using `mcflirt` [FSL 6.0.3:b862cdd5, @mcflirt]. BOLD runs were slice-time corrected to 0.975s (0.5 of slice acquisition range 0s-1.95s) using `3dTshift` from AFNI 20170202 [@afni, RRID:SCR_005927].

The BOLD time-series (including slice-timing correction when applied) were resampled onto their original, native space by applying the transforms to correct for head-motion. These resampled BOLD time-series will be referred to as *preprocessed BOLD in original space*, or just *preprocessed BOLD*. The BOLD reference was then co-registered to the T1w reference using `mri_coreg` (FreeSurfer) followed by `flirt` [FSL 6.0.3:b862cdd5, @flirt] with the

boundary-based registration [@bbr] cost-function. Co-registration was configured with six degrees of freedom.

Several confounding time-series were calculated based on the *preprocessed BOLD*: framewise displacement (FD), DVARS and three region-wise global signals. FD was computed using two formulations following Power (absolute sum of relative motions, @power_fd_dvars) and Jenkinson (relative root mean square displacement between affines, @mcflirt). FD and DVARS are calculated for each functional run, both using their implementations in *Nipype* [following the definitions by @power_fd_dvars]. The three global signals are extracted within the CSF, the WM, and the whole-brain masks. Additionally, a set of physiological regressors were extracted to allow for component-based noise correction [*CompCor*, @compcor]. Principal components are estimated after high-pass filtering the *preprocessed BOLD* time-series (using a discrete cosine filter with 128s cut-off) for the two *CompCor* variants: temporal (tCompCor) and anatomical (aCompCor). tCompCor components are then calculated from the top 2% variable voxels within the brain mask. For aCompCor, three probabilistic masks (CSF, WM and combined CSF+WM) are generated in anatomical space. The implementation differs from that of Behzadi et al. in that instead of eroding the masks by 2 pixels on BOLD space, the aCompCor masks are subtracted a mask of pixels that likely contain a volume fraction of GM. This mask is obtained by thresholding the corresponding partial volume map at 0.05, and it ensures components are not extracted from voxels containing a minimal fraction of GM. Finally, these masks are resampled into BOLD space and binarized by thresholding at 0.99 (as in the original implementation). Components are also calculated separately within the WM and CSF masks. For each CompCor decomposition, the *k* components with the largest singular values are retained, such that the retained components' time series are sufficient to explain 50 percent of variance across the nuisance mask (CSF, WM, combined, or temporal). The remaining components are dropped from consideration. The head-motion estimates calculated in the correction step were also placed within the corresponding confounds file. The confound time series derived from head motion estimates and global signals were expanded with the inclusion of temporal derivatives and quadratic terms for each [@confounds_satterthwaite_2013]. Frames that exceeded a threshold of 0.5 mm FD or 1.5 standardised DVARS were annotated as motion outliers.

The BOLD time-series were resampled into standard space, generating a *preprocessed BOLD run in MNI152NLin2009cAsym space*. First, a reference volume and its skull-stripped version were generated using a custom methodology of *fMRIPrep*. All resamplings can be

performed with *a single interpolation step* by composing all the pertinent transformations (i.e. head-motion transform matrices, susceptibility distortion correction when available, and co-registrations to anatomical and output spaces). Gridded (volumetric) resamplings were performed using `antsApplyTransforms` (ANTs), configured with Lanczos interpolation to minimize the smoothing effects of other kernels [@lanczos]. Non-gridded (surface) resamplings were performed using `mri_vol2surf` (FreeSurfer).

Many internal operations of *fMRIPrep* use *Nilearn* 0.9.1 [@nilearn, RID:SCR_001362], mostly within the functional processing workflow. For more details of the pipeline, see [the section corresponding to workflows in *fMRIPrep*'s documentation](https://fmriprep.readthedocs.io/en/latest/workflows.html "FMRIPrep's documentation").

2. fMRI scan timing

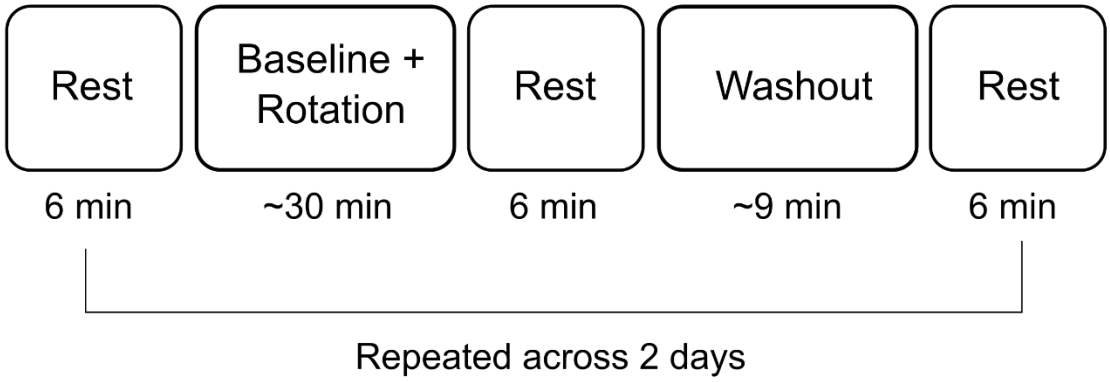

Figure 7 Breakdown of fMRI scan timing. fMRI scanning was spread across two days. Each day participants underwent three 6 min resting state scans prior to, in-between, and after the task scans. The first task scan was ~30 min consisting of the Baseline and Rotation conditions. The second task scan was ~9 min and consisted of the Washout condition. The total scanning time each day was 75 min including setup time.

3. Table of correlation coefficients for significant regions in BIS GLM

ROI Name	MNI Coordinates			GLM Coefficient
	X	Y	Z	
17Networks_LH_VisCent_ExStr_5	-24	-97	-12	0.05462
17Networks_LH_VisPeri_ExStrInf_5	-14	-57	1	-0.0255
17Networks_LH_VisPeri_ExStrSup_1	-19	-65	7	-0.0265
17Networks_LH_SomMotA_1	-8	-15	47	-0.0639
17Networks_LH_SomMotA_3	-49	-17	54	-0.0913
17Networks_LH_SomMotA_4	-48	-29	58	-0.1062
17Networks_LH_SomMotA_5	-39	-25	53	-0.1118
17Networks_LH_SomMotA_8	-4	-9	59	-0.0552
17Networks_LH_SomMotA_9	-36	-19	65	-0.1091
17Networks_LH_SomMotA_10	-32	-29	63	-0.1062
17Networks_LH_SomMotA_11	-30	-38	65	-0.064
17Networks_LH_SomMotA_12	-23	-11	65	-0.0819
17Networks_LH_SomMotA_13	-19	-24	67	-0.0404
17Networks_LH_SomMotA_16	-14	-11	73	-0.0498
17Networks_LH_SomMotA_19	-12	-27	73	-0.0348
17Networks_LH_SomMotB_Ins_1	-36	-24	10	-0.0271
17Networks_LH_SomMotB_S2_2	-36	-26	19	-0.0436
17Networks_LH_SomMotB_S2_3	-49	-13	14	-0.0258
17Networks_LH_SomMotB_S2_5	-48	-24	18	-0.06
17Networks_LH_DorsAttnA_ParOcc_1	-48	-65	15	-0.0331
17Networks_LH_DorsAttnA_SPL_3	-23	-65	46	-0.029
17Networks_LH_DorsAttnA_SPL_4	-29	-58	50	-0.0255
17Networks_LH_DorsAttnA_SPL_5	-36	-52	56	-0.0364
17Networks_LH_DorsAttnA_SPL_6	-15	-71	57	-0.0363
17Networks_LH_DorsAttnA_SPL_7	-29	-61	62	-0.0409
17Networks_LH_DorsAttnB_PostC_1	-61	-23	33	-0.0347
17Networks_LH_DorsAttnB_PostC_2	-55	-20	41	-0.0824
17Networks_LH_DorsAttnB_PostC_3	-55	-32	45	-0.0433

17Networks_LH_DorsAttnB_PostC_4	-46	-29	44	-0.0732
17Networks_LH_DorsAttnB_PostC_5	-39	-37	49	-0.0921
17Networks_LH_DorsAttnB_PostC_6	-30	-46	63	-0.0725
17Networks_LH_DorsAttnB_PostC_7	-7	-59	63	-0.0546
17Networks_LH_DorsAttnB_PostC_8	-20	-57	66	-0.0508
17Networks_LH_DorsAttnB_PostC_9	-13	-50	72	-0.0238
17Networks_LH_DorsAttnB_FEF_2	-25	-1	55	-0.0617
17Networks_LH_DorsAttnB_FEF_3	-30	-8	52	-0.0797
17Networks_LH_DorsAttnB_PrCv_1	-50	3	38	-0.0346
17Networks_LH_SalVentAttnA_ParOper_1	-55	-32	22	-0.0272
17Networks_LH_SalVentAttnA_ParOper_3	-61	-36	33	-0.0369
17Networks_LH_SalVentAttnA_Ins_1	-39	2	-4	-0.0268
17Networks_LH_SalVentAttnA_Ins_2	-40	-15	-2	-0.0287
17Networks_LH_SalVentAttnA_Ins_3	-33	19	8	-0.0537
17Networks_LH_SalVentAttnA_FrOper_2	-52	9	13	-0.0282
17Networks_LH_SalVentAttnA_ParMed_3	-6	-49	57	-0.0437
17Networks_LH_SalVentAttnA_FrMed_1	-7	0	41	-0.0404
17Networks_LH_SalVentAttnA_FrMed_2	-5	9	48	-0.0649
17Networks_LH_SalVentAttnB_PFCl_2	-29	43	30	-0.0292
17Networks_LH_SalVentAttnB_PFCl_3	-36	32	38	-0.0321
17Networks_LH_SalVentAttnB_Ins_2	-33	25	-1	-0.0593
17Networks_LH_SalVentAttnB_Ins_3	-43	12	2	-0.0328
17Networks_LH_SalVentAttnB_PFCmp_1	-6	22	31	-0.03
17Networks_LH_LimbicA_TempPole_4	-54	-21	-31	-0.0266
17Networks_LH_LimbicA_TempPole_6	-32	12	-29	-0.0276
17Networks_LH_LimbicA_TempPole_7	-44	5	-17	-0.0279
17Networks_LH_ContA_IPS_4	-45	-41	47	-0.0537
17Networks_LH_ContA_IPS_5	-33	-46	41	-0.045
17Networks_LH_ContA_PFCd_1	-21	5	65	-0.0515
17Networks_LH_ContA_PFClv_2	-42	38	22	-0.0256
17Networks_LH_ContA_PFCl_1	-49	6	26	-0.0325
17Networks_LH_ContA_PFCl_2	-45	20	27	-0.0295

17Networks_LH_ContA_PFCl_3	-39	7	34	-0.0467
17Networks_LH_ContB_IPL_3	-42	-52	49	-0.0378
17Networks_LH_ContB_PFCd_1	-30	14	57	-0.0232
17Networks_LH_ContB_PFCmp_1	-4	28	47	-0.0508
17Networks_LH_ContC_pCun_3	-5	-64	52	-0.044
17Networks_LH_DefaultA_PFCd_2	-18	36	48	0.03881
17Networks_LH_DefaultA_pCunPCC_3	-7	-44	32	0.02499
17Networks_LH_DefaultA_pCunPCC_5	-3	-15	37	0.03063
17Networks_LH_DefaultA_PFCm_3	-6	59	7	0.03513
17Networks_LH_DefaultB_Temp_2	-54	-2	-30	-0.0247
17Networks_LH_DefaultB_PFCd_6	-6	10	65	-0.0281
17Networks_LH_DefaultB_PFCv_1	-36	22	-16	-0.0269
17Networks_LH_DefaultC_IPL_1	-40	-79	30	-0.0304
17Networks_RH_VisCent_ExStr_5	42	-84	-12	0.03368
17Networks_RH_VisCent_ExStr_6	25	-97	-10	0.06323
17Networks_RH_VisCent_ExStr_7	35	-89	2	0.07488
17Networks_RH_VisCent_ExStr_8	24	-99	7	0.04861
17Networks_RH_VisPeri_ExStrInf_4	13	-58	-3	-0.0256
17Networks_RH_VisPeri_ExStrInf_5	18	-45	-3	-0.0315
17Networks_RH_VisPeri_StriCal_2	22	-59	6	-0.0341
17Networks_RH_VisPeri_ExStrSup_4	16	-87	36	0.03028
17Networks_RH_SomMotA_1	54	-17	40	-0.0808
17Networks_RH_SomMotA_4	49	-26	56	-0.0303
17Networks_RH_SomMotA_5	7	-10	51	-0.0327
17Networks_RH_SomMotA_7	37	-20	64	-0.0329
17Networks_RH_SomMotA_12	29	-11	65	-0.077
17Networks_RH_SomMotA_17	17	-6	69	-0.0345
17Networks_RH_SomMotA_19	17	-18	73	-0.0317
17Networks_RH_SomMotB_S2_7	49	-21	19	-0.0301
17Networks_RH_SomMotB_Cent_1	61	6	30	-0.0334
17Networks_RH_DorsAttnA_SPL_5	21	-69	53	-0.0338
17Networks_RH_DorsAttnA_SPL_6	34	-50	54	-0.0367

17Networks_RH_DorsAttnA_SPL_7	27	-58	61	-0.0313
17Networks_RH_DorsAttnA_SPL_8	14	-64	65	-0.0366
17Networks_RH_DorsAttnB_PostC_1	61	-14	30	-0.0476
17Networks_RH_DorsAttnB_PostC_2	57	-23	44	-0.0446
17Networks_RH_DorsAttnB_PostC_3	44	-37	50	-0.0529
17Networks_RH_DorsAttnB_PostC_4	45	-28	42	-0.0575
17Networks_RH_DorsAttnB_PostC_5	35	-36	51	-0.0624
17Networks_RH_DorsAttnB_PostC_6	7	-54	59	-0.0502
17Networks_RH_DorsAttnB_PostC_7	24	-50	68	-0.0421
17Networks_RH_DorsAttnB_PostC_8	16	-47	74	-0.0241
17Networks_RH_DorsAttnB_FEF_2	27	-3	52	-0.0692
17Networks_RH_DorsAttnB_FEF_3	25	-3	64	-0.056
17Networks_RH_SalVentAttnA_ParOper_3	63	-26	38	-0.0293
17Networks_RH_SalVentAttnA_FrOper_3	54	12	12	-0.0295
17Networks_RH_SalVentAttnA_FrMed_1	7	2	43	-0.0434
17Networks_RH_SalVentAttnA_FrMed_2	6	11	58	-0.0678
17Networks_RH_SalVentAttnA_ParMed_3	10	-43	53	-0.0335
17Networks_RH_SalVentAttnA_FrMed_3	7	-2	67	-0.0344
17Networks_RH_SalVentAttnA_FrMed_4	16	7	69	-0.0548
17Networks_RH_SalVentAttnB_IPL_1	62	-37	37	-0.0313
17Networks_RH_SalVentAttnB_PFCl_2	25	54	25	-0.0278
17Networks_RH_SalVentAttnB_PFCl_3	33	45	28	-0.0388
17Networks_RH_SalVentAttnB_Ins_2	37	23	5	-0.0445
17Networks_RH_SalVentAttnB_PFCmp_1	8	35	25	-0.0248
17Networks_RH_SalVentAttnB_PFCmp_2	7	19	35	-0.0555
17Networks_RH_LimbicB_OFC_2	23	22	-21	-0.0199
17Networks_RH_ContA_IPS_2	54	-33	51	-0.0342
17Networks_RH_ContA_IPS_3	47	-44	46	-0.0332
17Networks_RH_ContA_IPS_4	36	-44	45	-0.0426
17Networks_RH_ContA_PFCd_1	24	10	58	-0.0545
17Networks_RH_ContA_PFCl_3	47	29	28	-0.035
17Networks_RH_ContA_PFCl_4	49	8	25	-0.038

17Networks_RH_ContA_PFCl_5	39	11	34	-0.0274
17Networks_RH_ContB_PFCld_1	39	33	38	-0.0337
17Networks_RH_ContB_PFCld_2	45	19	44	-0.0322
17Networks_RH_ContB_PFCld_3	43	7	51	-0.0218
17Networks_RH_ContB_PFCld_4	34	15	56	-0.029
17Networks_RH_ContB_PFCmp_1	5	28	48	-0.0533
17Networks_RH_ContC_pCun_1	17	-63	28	-0.0296
17Networks_RH_ContC_pCun_3	5	-64	44	-0.0282
17Networks_RH_ContC_pCun_5	8	-71	53	-0.037
17Networks_RH_DefaultA_pCunPCC_2	5	-63	31	0.02473
17Networks_RH_DefaultA_pCunPCC_5	10	-53	35	0.01765
17Networks_RH_DefaultA_PFCm_3	7	42	4	0.02618
17Networks_RH_DefaultB_PFCv_2	48	32	-8	-0.0277
17Networks_RH_DefaultC_IPL_1	48	-64	22	-0.0306
17Networks_RH_DefaultC_IPL_2	45	-75	31	-0.0433
Right_V	18	-50	-19	-0.0476
Right_CrusI	-45	-65	-32	0.0254
Right_IX	5	-51	-55	-0.0279
Right_X	22	-35	-43	-0.0215
PUT-VA-rh	22	12	-6	0.05165
PUT-DA-rh	26	6	2	0.03852
PUT-VP-rh	30	-12	0	0.03365
PUT-DP-rh	28	-2	6	0.0307
PUT-DA-lh	-24	6	2	0.03217
CAU-tail-lh	-14	-2	20	-0.0263
aGP-lh	-16	0	-2	-0.0221

4. Schaefer 1000 analysis

The general linear model results conducted with the Voltron-400 atlas was replicated with using the Voltron-1000 atlas. The main difference between the two atlas' is the use of 1000 Schaefer cortical nodes, instead of 400 Schaefer cortical nodes. The rest of the regions of the interests (basal ganglia, cerebellum) remain the same.

Improved performance is driven by basal ganglia and cerebellar engagement

The peak BOLD response for each region across all trials was fit to BIS in a general linear model. A one-sample test was used to create a thresholded group map (Figure 7A, $p < 0.05$). Regions that increased in BOLD with better performance included the right Crus I of the cerebellum, right putamen, and sparse activation across the medial cerebral cortex including regions such as the medial prefrontal cortex and cingulate cortex. Regions that were associated with worse performance included bilaterally the primary motor, parietal, extrastriate cortices, as well as the right frontal lobe.

Balanced Integration Score (BIS) retains insights from Response Time (RT) and Response Error (RE) in granular parcellations

The BIS group map was compared to group maps fitted with response time (RT) and response error (RE). From Pearson's correlations, the BIS map was significantly similar to both the RT and RE brain maps (Figure 7B, 7C; $r = 0.75$, $p = 0$; $r = 0.73$, $p = 0$, respectively). To compare whether there were differences between task conditions, the BIS scores and BOLD responses were divided into four conditions (baseline, early rotation, late rotation, and washout). All conditions were similar to each other, and the strongest correlation was between the baseline and late rotation (Figure 7D; $r = 0.63$, $p = 0$).

Expertise brain maps were robust to individual effects

After dividing the dataset in half and fitting each group to their BIS scores in two separate GLMs, the average beta coefficients were compared between the two groups. The beta coefficients between the two groups were strongly correlated (Figure 7E; $r = 0.62$, $p = 0$), providing evidence that the current results were not driven by individual subjects.

All cerebral cortical correlations were corrected for spatial autocorrelation using spin-permutation tests, and all comparisons remained significantly different ($p_{spin} = 0$).

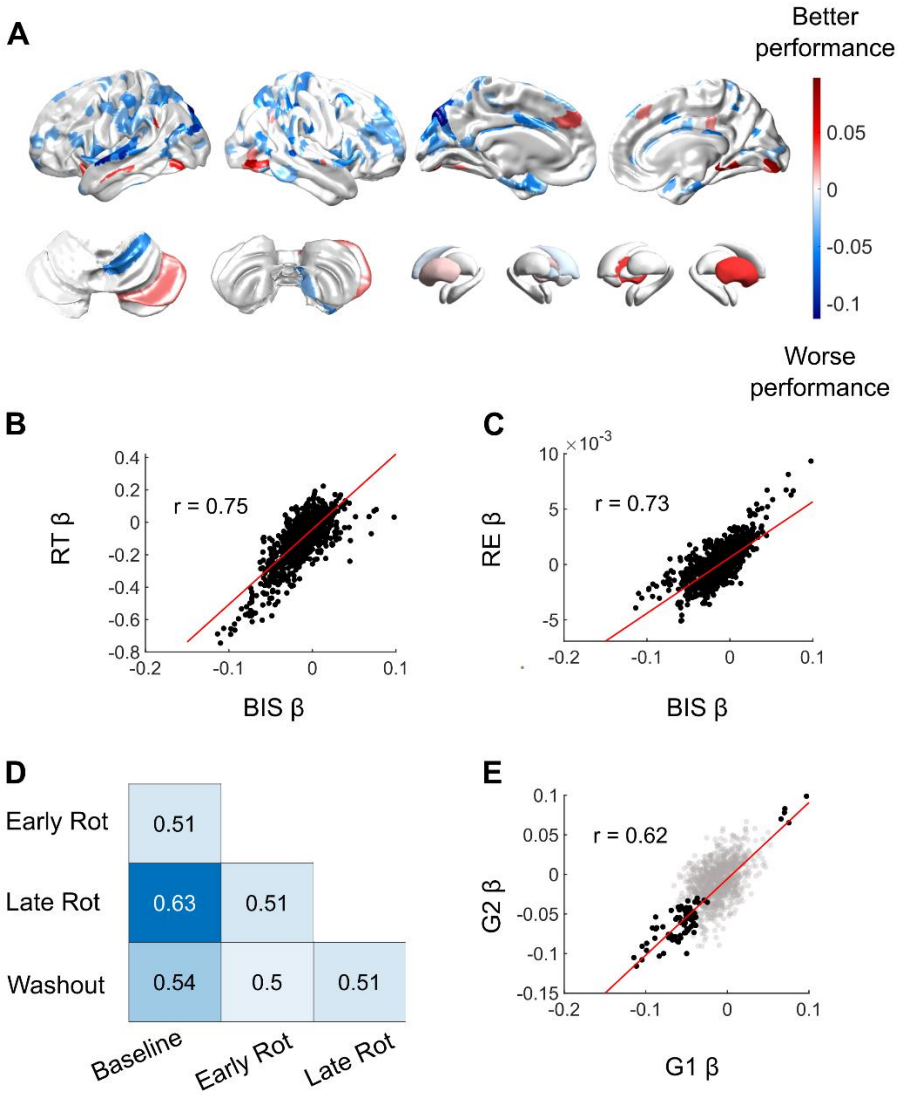

Figure 8 Summary of general linear modelling in the Voltron-1000 parcellation. A. Thresholded brain maps of beta coefficients comparing BIS against peak BOLD response across all trials. B. Comparison of BIS beta coefficients against response time (RT) beta coefficients. C. Comparison of BIS beta coefficients against response error (RE) beta coefficients. D. Comparison of beta coefficients for each condition. E. The dataset was divided into two groups (n = 12, n = 11). Comparison of group 1 BIS beta coefficients against group 2 BIS beta coefficients.

References

Abraham, Alexandre, *et al.* (2014) "Machine Learning for Neuroimaging with Scikit-Learn." Frontiers in Neuroinformatics 8. https://doi.org/10.3389/fninf.2014.00014.

Avants, B.B., C.L. Epstein, M. Grossman, and J.C. Gee (2008) "Symmetric Diffeomorphic Image Registration with Cross-Correlation: Evaluating Automated Labeling of Elderly and Neurodegenerative Brain." Medical Image Analysis 12 (1): 26–41. https://doi.org/10.1016/j.media.2007.06.004.

Behzadi, Yashar, Khaled Restom, Joy Liau, and Thomas T. Liu. (2007) "A Component Based Noise Correction Method (CompCor) for BOLD and Perfusion Based fMRI." *NeuroImage* 37 (1): 90–101. https://doi.org/10.1016/j.neuroimage.2007.04.042.

Esteban, Oscar, *et al.* (2018) "FMRIPrep." *Software*. Zenodo. https://doi.org/10.5281/zenodo.852659.

Esteban, Oscar, *et al.* (2018) "fMRIPrep: A Robust Preprocessing Pipeline for Functional MRI." *Nature Methods*. https://doi.org/10.1038/s41592-018-0235-4.

Evans, AC, *et al.* (2012) "Brain Templates and Atlases." *NeuroImage* 62 (2): 911–22. https://doi.org/10.1016/j.neuroimage.2012.01.024.

Fonov, VS, *et al.* (2009) "Unbiased Nonlinear Average Age-Appropriate Brain Templates from Birth to Adulthood." *NeuroImage* 47, Supplement 1: S102. https://doi.org/10.1016/S1053-8119(09)70884-5.

Gorgolewski, K., *et al.* (2011) "Nipype: A Flexible, Lightweight and Extensible Neuroimaging Data Processing Framework in Python." *Frontiers in Neuroinformatics* 5: 13. https://doi.org/10.3389/fninf.2011.00013.

Gorgolewski, Krzysztof J. *et al*. (2018) "Nipype." *Software*. Zenodo. https://doi.org/10.5281/zenodo.596855.

Greve, Douglas N, and Bruce Fischl (2009) "Accurate and Robust Brain Image Alignment Using Boundary-Based Registration." *NeuroImage* 48 (1): 63–72. https://doi.org/10.1016/j.neuroimage.2009.06.060.

Jenkinson, Mark, *et al.* (2002) "Improved Optimization for the Robust and Accurate Linear Registration and Motion Correction of Brain Images." *NeuroImage* 17 (2): 825–41. https://doi.org/10.1006/nimg.2002.1132.

Jenkinson, Mark, and Stephen Smith (2001) "A Global Optimisation Method for Robust Affine Registration of Brain Images." *Medical Image Analysis* 5 (2): 143–56. https://doi.org/10.1016/S1361-8415(01)00036-6.

Lanczos, C. (1964) "Evaluation of Noisy Data." *Journal of the Society for Industrial and Applied Mathematics Series B Numerical Analysis* 1 (1): 76–85. https://doi.org/10.1137/0701007.

Power, Jonathan D. *et al.* (2014) "Methods to Detect, Characterize, and Remove Motion Artifact in Resting State fMRI." *NeuroImage* 84 (Supplement C): 320–41. https://doi.org/10.1016/j.neuroimage.2013.08.048.

Pruim, Raimon H. R. *et al.* (2015) "ICA-AROMA: A Robust ICA-Based Strategy for Removing Motion Artifacts from fMRI Data." *NeuroImage* 112 (Supplement C): 267–77. https://doi.org/10.1016/j.neuroimage.2015.02.064.

Satterthwaite, T.D. *et al.* (2013) 'An improved framework for confound regression and filtering for control of motion artifact in the preprocessing of resting-state functional connectivity data', *NeuroImage*, 64, pp. 240–256. Available at: https://doi.org/10.1016/j.neuroimage.2012.08.052.

Thomas Yeo, B.T. *et al.* (2011) 'The organization of the human cerebral cortex estimated by intrinsic functional connectivity', *Journal of Neurophysiology*, 106(3), pp. 1125–1165. Available at: https://doi.org/10.1152/jn.00338.2011.

Tustison, N. J. *et al.* (2010) "N4ITK: Improved N3 Bias Correction." *IEEE Transactions on Medical Imaging* 29 (6): 1310–20. https://doi.org/10.1109/TMI.2010.2046908.

Zhang, Y., M. Brady, and S. Smith, (2001) "Segmentation of Brain MR Images Through a Hidden Markov Random Field Model and the Expectation-Maximization Algorithm." *IEEE Transactions on Medical Imaging* 20 (1): 45–57. https://doi.org/10.1109/42.906424.

Appendix III: Supplementary Material for Chapter 4

Compositional Recombination relies on a Distributed Cortico-Cerebellar Network

1. fMRIprep preprocessing

Anatomical data preprocessing

A total of 1 T1-weighted (T1w) images were found within the input BIDS dataset. The T1-weighted (T1w) image was corrected for intensity non-uniformity (INU) with `N4BiasFieldCorrection` [@n4], distributed with ANTs 2.3.1 [@ants, RRID:SCR_004757], and used as T1w-reference throughout the workflow. The T1w-reference was then skull-stripped with a *Nipype* implementation of the `antsBrainExtraction.sh` workflow (from ANTs), using OASIS30ANTs as target template.

Brain tissue segmentation of cerebrospinal fluid (CSF), white-matter (WM) and gray-matter (GM) was performed on the brain-extracted T1w using `fast` [FSL 6.0.3:b862cdd5, RRID:SCR_002823, @fsl_fast]. Volume-based spatial normalization to two standard spaces (MNI152NLin6Asym, MNI152NLin2009cAsym) was performed through nonlinear registration with `antsRegistration` (ANTs 2.3.1), using brain-extracted versions of both T1w reference and the T1w template. The following templates were were selected for spatial normalization and accessed with *TemplateFlow* [23.0.0, @templateflow]: *FSL's MNI ICBM 152 non-linear 6th Generation Asymmetric Average Brain Stereotaxic Registration Model* [@mni152nlin6asym, RRID:SCR_002823; TemplateFlow ID: MNI152NLin6Asym], *ICBM 152 Nonlinear Asymmetrical template version 2009c* [@mni152nlin2009casym, RRID:SCR_008796; TemplateFlow ID: MNI152NLin2009cAsym].

Functional data preprocessing

For each of the 8 BOLD runs found per subject (across all tasks and sessions), the following preprocessing was performed. First, a reference volume and its skull-stripped version were generated by aligning and averaging 1 single-band references (SBRefs). Head-motion parameters with respect to the BOLD reference (transformation matrices, and six corresponding rotation and translation parameters) are estimated before any spatiotemporal filtering using `mcflirt` [FSL 6.0.3:b862cdd5, @mcflirt]. The BOLD time-series (including slice-timing correction when applied) were resampled onto their original, native space by applying the transforms to correct for head-motion. These resampled BOLD time-series will be referred to as *preprocessed BOLD in original space*, or just *preprocessed BOLD*. The

BOLD reference was then co-registered to the T1w reference using `mri_coreg` (FreeSurfer) followed by `flirt` [FSL 6.0.3:b862cdd5, @flirt] with the boundary-based registration [@bbr] cost-function.

Co-registration was configured with six degrees of freedom. First, a reference volume and its skull-stripped version were generated using a custom methodology of *fMRIPrep*. Several confounding time-series were calculated based on the *preprocessed BOLD*: framewise displacement (FD), DVARS and three region-wise global signals. FD was computed using two formulations following Power (absolute sum of relative motions, @power_fd_dvars) and Jenkinson (relative root mean square displacement between affines, @mcflirt). FD and DVARS are calculated for each functional run, both using their implementations in *Nipype* [following the definitions by @power_fd_dvars]. The three global signals are extracted within the CSF, the WM, and the whole-brain masks. Additionally, a set of physiological regressors were extracted to allow for component-based noise correction [*CompCor*, @compcor]. Principal components are estimated after high-pass filtering the *preprocessed BOLD* time-series (using a discrete cosine filter with 128s cut-off) for the two *CompCor* variants: temporal (tCompCor) and anatomical (aCompCor). tCompCor components are then calculated from the top 2% variable voxels within the brain mask. For aCompCor, three probabilistic masks (CSF, WM and combined CSF+WM) are generated in anatomical space. The implementation differs from that of Behzadi et al. in that instead of eroding the masks by 2 pixels on BOLD space, a mask of pixels that likely contain a volume fraction of GM is subtracted from the aCompCor masks. This mask is obtained by thresholding the corresponding partial volume map at 0.05, and it ensures components are not extracted from voxels containing a minimal fraction of GM.

Finally, these masks are resampled into BOLD space and binarized by thresholding at 0.99 (as in the original implementation). Components are also calculated separately within the WM and CSF masks. For each CompCor decomposition, the *k* components with the largest singular values are retained, such that the retained components' time series are sufficient to explain 50 percent of variance across the nuisance mask (CSF, WM, combined, or temporal). The remaining components are dropped from consideration. The head-motion estimates calculated in the correction step were also placed within the corresponding confounds file. The confound time series derived from head motion estimates and global signals were expanded with the inclusion of temporal derivatives and quadratic terms for each [@confounds_satterthwaite_2013]. Frames that exceeded a threshold of 0.5 mm FD or 1.5

standardized DVARS were annotated as motion outliers. Additional nuisance timeseries are calculated by means of principal components analysis of the signal found within a thin band (*crown*) of voxels around the edge of the brain, as proposed by [@patriat_improved_2017].

The BOLD time-series were resampled into several standard spaces, correspondingly generating the following *spatially-normalized, preprocessed BOLD runs*: MNI152NLin6Asym, MNI152NLin2009cAsym. First, a reference volume and its skull-stripped version were generated using a custom methodology of *fMRIPrep*. All resamplings can be performed with *a single interpolation step* by composing all the pertinent transformations (i.e. head-motion transform matrices, susceptibility distortion correction when available, and co-registrations to anatomical and output spaces). Gridded (volumetric) resamplings were performed using `antsApplyTransforms` (ANTs), configured with Lanczos interpolation to minimize the smoothing effects of other kernels [@lanczos]. Non-gridded (surface) resamplings were performed using `mri_vol2surf` (FreeSurfer).

Many internal operations of *fMRIPrep* use *Nilearn* 0.10.0 [@nilearn, RRID:SCR_001362], mostly within the functional processing workflow. For more details of the pipeline, see [the section corresponding to workflows in *fMRIPrep*'s documentation](https://fmriprep.readthedocs.io/en/latest/workflows.html "FMRIPrep's documentation").

2. Partial Least Squares analyses on Instruction period time series

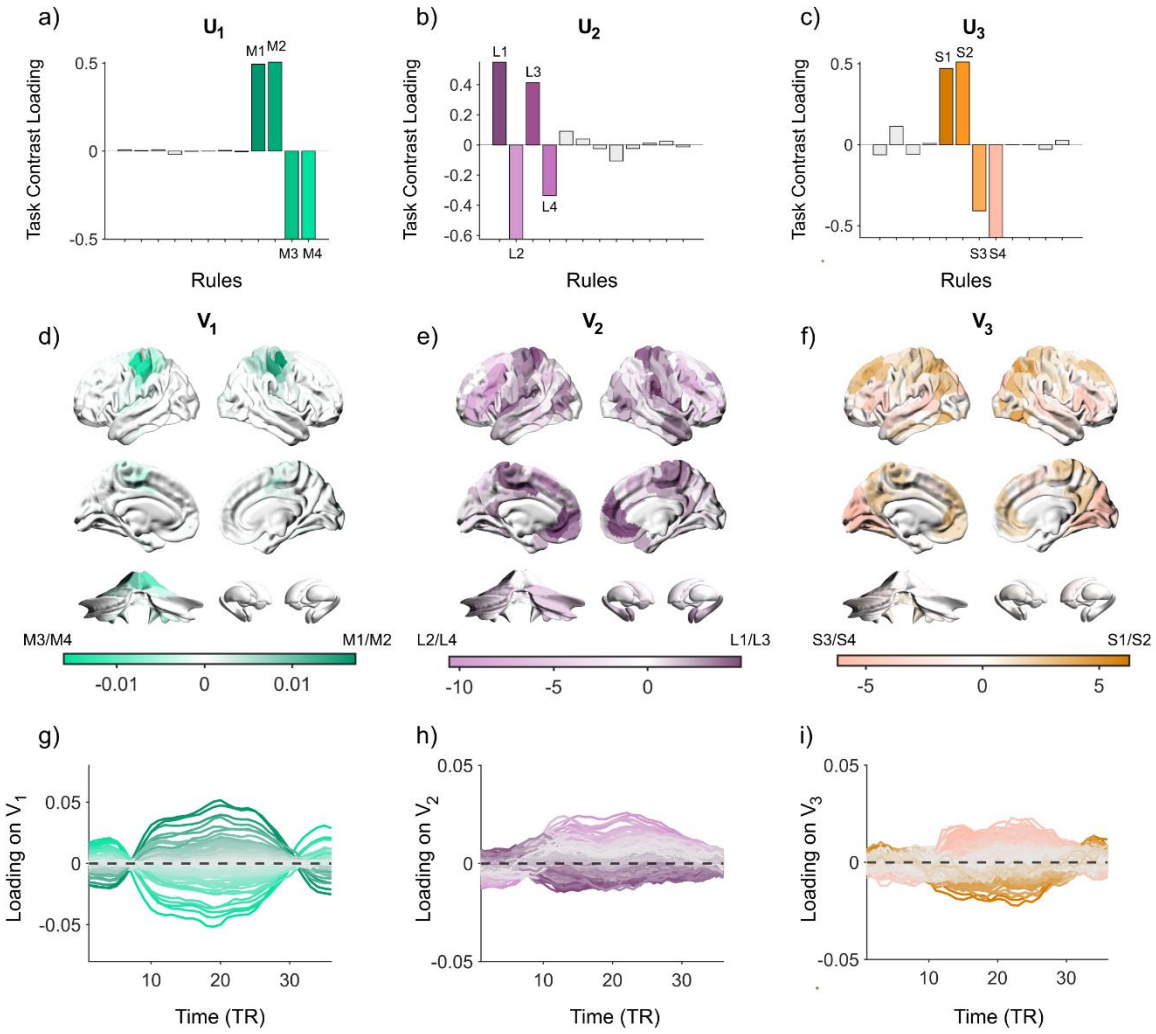

Figure S1. Partial Least Squares Analysis on Instruction period time series. a-c) Bar plot of the first 3 LVs of Task Contrast scores in PLS space. d-f) Brain visualisation of first 3 LVs of average brain activity in PLS space. g-i) Loadings of brain activity across time in PLS space. Each line denotes an individual region's dynamics across time.

3. Delta Functional Connectivity Matrices

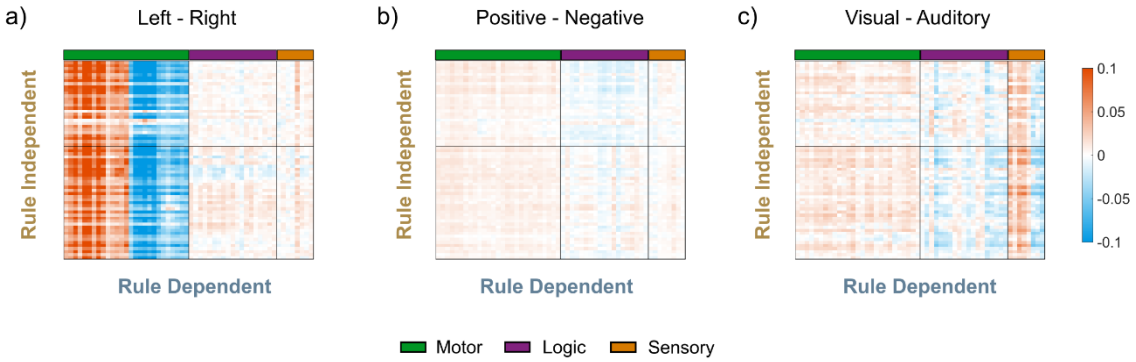

Figure S2. Average difference in functional connectivity between rule dependent and rule independent regions for each domain. a) Motor domain: left hand – right hand. b) Logic domain: positive – negative. c) Sensory domain: visual – auditory. Rule dependent regions (columns) were assigned to specific domains (green = motor, purple = logic, orange = sensory) based off their strongest loading on the PLS axes.

4. Table 1. Labels for Component brain regions

ROI Name	X	Y	Z
17Networks_LH_SomMotA_1	-8	-15	47
17Networks_LH_SomMotA_3	-49	-17	54
17Networks_LH_SomMotA_4	-48	-29	58
17Networks_LH_SomMotA_5	-39	-25	53
17Networks_LH_SomMotA_9	-36	-19	65
17Networks_LH_SomMotA_10	-32	-29	63
17Networks_LH_SomMotA_11	-30	-38	65
17Networks_LH_SomMotA_12	-23	-11	65
17Networks_LH_DorsAttnA_SPL_1	-26	-70	31
17Networks_LH_DorsAttnB_PostC_2	-55	-20	41
17Networks_LH_DorsAttnB_PostC_4	-46	-29	44
17Networks_LH_DorsAttnB_PostC_5	-39	-37	49
17Networks_LH_DorsAttnB_PostC_6	-30	-46	63
17Networks_LH_SalVentAttnA_FrOper_2	-52	9	13
17Networks_LH_SalVentAttnB_PFCl_1	-38	49	11
17Networks_LH_SalVentAttnB_Ins_2	-33	25	-1
17Networks_LH_ContA_IPS_1	-29	-74	42
17Networks_LH_ContA_IPS_3	-35	-62	48
17Networks_LH_ContA_PFClv_1	-48	35	10
17Networks_LH_ContA_PFClv_2	-42	38	22
17Networks_LH_ContA_PFCl_2	-45	20	27
17Networks_LH_ContA_PFCl_3	-39	7	34
17Networks_LH_ContB_IPL_3	-42	-52	49
17Networks_LH_ContB_PFCd_1	-30	14	57
17Networks_LH_ContB_PFClv_1	-42	49	-6
17Networks_LH_ContB_PFCmp_1	-4	28	47
17Networks_LH_DefaultB_PFCd_6	-6	10	65
17Networks_LH_DefaultB_PFCl_1	-41	19	48
17Networks_LH_DefaultB_PFCl_2	-42	7	48
17Networks_LH_DefaultB_PFCv_4	-48	28	0
17Networks_LH_DefaultB_PFCv_5	-53	19	11
17Networks_RH_SomMotA_1	54	-17	40
17Networks_RH_SomMotA_2	52	-13	49
17Networks_RH_SomMotA_4	49	-26	56

17Networks_RH_SomMotA_5	7	-10	51
17Networks_RH_SomMotA_6	43	-21	54
17Networks_RH_SomMotA_7	37	-20	64
17Networks_RH_SomMotA_9	31	-41	64
17Networks_RH_SomMotA_10	34	-27	61
17Networks_RH_SomMotA_12	29	-11	65
17Networks_RH_DorsAttnA_TempOcc_3	50	-64	-9
17Networks_RH_DorsAttnA_SPL_2	32	-66	35
17Networks_RH_DorsAttnA_SPL_6	34	-50	54
17Networks_RH_DorsAttnB_PostC_3	44	-37	50
17Networks_RH_DorsAttnB_PostC_4	45	-28	42
17Networks_RH_DorsAttnB_PostC_5	35	-36	51
17Networks_RH_DorsAttnB_PostC_7	24	-50	68
17Networks_RH_SalVentAttnB_Ins_2	37	23	5
17Networks_RH_ContA_PFCl_2	48	18	23
17Networks_RH_ContA_PFCl_3	47	29	28
17Networks_RH_ContB_PFCmp_1	5	28	48
17Networks_RH_DefaultB_PFCv_3	54	24	6
Left_V	-18	-50	-19
Right_V	18	-50	-19

5. Table 2. Labels for Recombination brain regions

ROI Name	X	Y	Z
17Networks_LH_SomMotB_Aud_1	-50	-9	0
17Networks_LH_SomMotB_Aud_2	-56	-22	8
17Networks_LH_SomMotB_Ins_1	-36	-24	10
17Networks_LH_SomMotB_Aud_3	-59	-37	16
17Networks_LH_SomMotB_Aud_4	-41	-35	14
17Networks_LH_DorsAttnA_SPL_4	-29	-58	50
17Networks_LH_DorsAttnB_PostC_3	-55	-32	45
17Networks_LH_DorsAttnB_FEF_1	-40	-3	51
17Networks_LH_DorsAttnB_FEF_2	-25	-1	55
17Networks_LH_DorsAttnB_FEF_3	-30	-8	52
17Networks_LH_DorsAttnB_PrCv_1	-50	3	38
17Networks_LH_SalVentAttnA_ParOper_1	-55	-32	22
17Networks_LH_SalVentAttnA_ParOper_2	-58	-44	27
17Networks_LH_SalVentAttnA_Ins_3	-33	19	8
17Networks_LH_SalVentAttnA_FrMed_2	-5	9	48
17Networks_LH_ContA_IPS_2	-58	-42	45
17Networks_LH_ContA_IPS_4	-45	-41	47
17Networks_LH_ContA_IPS_5	-33	-46	41
17Networks_LH_ContA_PFCl_1	-49	6	26
17Networks_LH_TempPar_3	-62	-32	5
17Networks_LH_TempPar_4	-52	-43	5
17Networks_LH_TempPar_6	-59	-49	16
17Networks_RH_SomMotB_Aud_1	53	3	-6
17Networks_RH_SomMotB_Aud_2	53	-14	6
17Networks_RH_SomMotB_Ins_1	39	-19	5
17Networks_RH_SomMotB_Aud_3	60	-24	11
17Networks_RH_SomMotB_S2_4	41	-29	18
17Networks_RH_DorsAttnB_FEF_1	39	-3	53
17Networks_RH_SalVentAttnA_PrC_1	51	3	41
17Networks_RH_SalVentAttnA_FrOper_3	54	12	12
17Networks_RH_SalVentAttnA_FrMed_2	6	11	58
17Networks_RH_SalVentAttnA_FrMed_3	7	-2	67
17Networks_RH_SalVentAttnA_FrMed_4	16	7	69
17Networks_RH_SalVentAttnB_PFCl_1	42	46	14
17Networks_RH_ContA_IPS_2	54	-33	51
17Networks_RH_ContA_IPS_3	47	-44	46
17Networks_RH_ContA_IPS_4	36	-44	45

17Networks_RH_ContA_PFCl_4	49	8	25
17Networks_RH_ContA_PFCl_5	39	11	34
17Networks_RH_ContB_IPL_3	56	-41	48
17Networks_RH_ContB_IPL_4	41	-55	48
17Networks_RH_ContB_PFCld_1	39	33	38
17Networks_RH_ContB_PFCld_2	45	19	44
17Networks_RH_ContB_PFCld_3	43	7	51
17Networks_RH_TempPar_6	59	-46	7
17Networks_RH_TempPar_8	65	-34	11
Left_VI	-30	-50	-27
Right_VI	30	-50	-27
Left_VIIb	-33	-65	-53
Right_VIIb	33	-65	-53
Right_VIIIa	20	-65	-53

Appendix IV: Parallel processing relies on a distributed, low-dimensional cortico-cerebellar architecture

Published as: Müller, E. J., Palesi, F., Hou, K. Y., **Tan, J.**, Close, T., Gandini Wheeler-Kingschott, C. A. M., D'Angelo, E., Calamante, F., & Shine, J. M. (2023). Parallel processing relies on a distributed, low-dimensional cortico-cerebellar architecture. *Network Neuroscience*, 1–20. https://doi.org/10.1162/netn_a_00308

Authors

Eli J. Müller[1,2], Fulvia Palesi[4,5], Kevin Y. Hou[1,2], Joshua Tan[2], Thomas Close[6,7,8], Claudia A.M. Gandini Wheeler-Kingschott[3,4,5], Egidio D'Angelo[4,5], Fernando Calamante[2,6,7] and James M. Shine[1,2,*]

Affiliations

1 Complex Systems Research Group, The University of Sydney, Sydney, NSW, Australia
2 Brain and Mind Centre, The University of Sydney, Sydney, NSW, Australia
3 NMR Research Unit, Queen Square Multiple Sclerosis Centre, Faculty of Brain Sciences, UCL Queen Square Institute of Neurology, UCL, London, UK
4 Department of Brain and Behavioral Sciences, University of Pavia, Pavia, Italy
5 Brain Connectivity Research Center, IRCCS Mondino Foundation, Pavia, Italy
6 School of Biomedical Engineering, The University of Sydney, Sydney, NSW, Australia
7 Sydney Imaging, The University of Sydney, Sydney, NSW, Australia
8 National Imaging Facility, Sydney, NSW, Australia
* Corresponding author: mac.shine@sydney.edu.au

Abstract

A characteristic feature of human cognition is our ability to 'multi-task' – performing two or more tasks in parallel – particularly when one task is well-learned. How the brain supports this capacity remains poorly understood. Most past studies have focussed on identifying the areas of the brain – typically the dorsolateral prefrontal cortex – that are required to navigate information processing bottlenecks. In contrast, we take a systems neuroscience approach to test the hypothesis that the capacity to conduct effective parallel processing relies on a distributed architecture that interconnects the cerebral cortex with the cerebellum. The latter structure contains over half of the neurons in the adult human brain, and is well-suited to support the fast, effective, dynamic sequences required to perform tasks relatively automatically. By delegating stereotyped within-task computations to the cerebellum, the cerebral cortex can be freed up to focus on the more challenging aspects of performing the tasks in parallel. To test this hypothesis, we analysed task-based fMRI data from 50 participants who performed a task in which they either balanced an avatar on a screen ('Balance'), performed serial-7 subtractions ('Calculation') or performed both in parallel ('Dual-Task'). Using a set of approaches that include dimensionality reduction, structure-function coupling and time-varying functional connectivity, we provide robust evidence in support of our hypothesis. We conclude that distributed interactions between the cerebral cortex and cerebellum are crucially involved in parallel processing in the human brain.

Introduction

How do distributed whole-brain neural activity patterns give rise to human cognitive function? This question lies at the heart of modern psychology and neuroscience but, despite decades of neuroimaging experiments, we still do not have a clear answer. One reason is that conventional neuroimaging methods applied to data from cognitive tasks typically represent the brain as a static snapshot of independent parts or at best, 'functionally connected' pairs of brain regions[1]. Another important issue is that neuroimaging experiments are usually designed to identify regions that are most selectively associated with a specific task, but are less well-suited to distinguishing the presence of multiple concurrent cognitive constructs within the same task[2]. For these reasons, many leading theories in cognitive neuroscience have relied on relatively static descriptions of the 'key brain regions involved' in a particular task.

In contrast to this view, there is evidence to suggest that the neural implementation of cognitive function in humans is far more dynamic and integrative[3]. In solving real world problems, we rarely isolate a specific cognitive capacity, such as focussed attention or resistance to distraction, but instead combine multiple cognitive constructs together in order to solve challenges in real-time[4]. Consider an experienced driver navigating heavy highway traffic in the pouring rain – the driver must remain focussed on the road, ensure the windshield wipers are on, regularly check their blind spots and also keep the pedals depressed at the appropriate level. This view of cognitive function in the real world is crucially dependent on the parallel processing of multiple distinct challenges, however for the reasons outlined above, we still lack a satisfying description of how the human brain is capable of supporting parallel processing.

To facilitate complex coordinated behavioural responses underpinned by similarly complex spatiotemporal activity patterns, the brain may first learn to execute at least one of the computations automatically (i.e., without paying close, conscious attention to the completion of the task). To achieve this, the system must be capable of responding to specific contexts with a high degree of spatial and temporal precision[5]. Secondly, the responses must be relatively error-free and reliable. Finally, the system must be able to be triggered in the presence of a specific stimulus or context without the need for deliberate attention. Without making the responses to different computational burdens relatively stereotyped in this fashion, performing two (or more) computations in parallel would require the prioritisation of one of the computations, likely to the detriment of the other task(s). In addition, any two tasks learned by the same network could potentially run into structural interference[6], particularly if the networks required to complete the overlapping tasks use similar cortical regions.

Crucially, the architecture of the cerebellum is ideally suited to fulfil each of the features required for automatic processing, both in the sensorimotor and cognitive domains[7–10]. First, the cerebellum is organized in parallel modules with different cerebrocortical regions[8]. In direct contrast to the basal ganglia, the internal circuitry of the cerebellar cortex consists of sparse,

distributed connectivity patterns that likely support dimensionality expansion[11], rather than reduction (as is the case for the basal ganglia[12,13]). In addition, the glutamatergic outputs of the cerebellum through the deep cerebellar nuclei innervate 'core' thalamic nuclei[14], which project to the granular layers of the frontal cortex[15] in a much more precise manner than the 'matrix' thalamic nuclei. There is also evidence that cerebellar circuits can condition on their own outputs, and hence learn to execute specific sequences of effects based on triggering context signals[16]. Anatomically, the cerebellum is bidirectionally interconnected with multiple cerebrocortical areas, with major tracts connecting the dentate nucleus to the frontal and prefrontal cerebral cortex, along with other associative areas[17,18]. Functionally, the cerebellum plays a critical role in shaping complex functional network dynamics[19], as evidenced by its role in both resting state[20,21] and task-related neuroimaging studies[7,22–24]. Based on these architectural features and relationships with complex, dynamic neuroimaging patterns, we hypothesized that connections between the cerebellar cortex and cerebellum are crucial for the facilitation of parallel processing. Using a set of approaches that include dimensionality reduction, structure-function coupling and time-varying functional connectivity, we provide robust evidence in support of our hypothesis.

Results

To test this hypothesis, we reanalysed an existing fMRI dataset[25] consisting of 50 healthy individuals who performed a challenging 'Dual-task' in a 3T MRI scanner with their feet resting on a force-plate (Fig. 1A), and their vision oriented towards a 2-dimensional avatar that tilted forwards and backwards. There were three distinct trial types: during Balance blocks (Fig. 1B; blue), participants had to stabilize the slow fluctuations of the avatar using forward and backwards movements on the force-plate; during Calculation blocks (Fig. 1C; red), subjects had to track between 3-4 audible beeps, and then subtract that number, multiplied by 7, from a cue number presented prior to the trial; and during Dual-task blocks (Fig. 1D; purple), subjects performed both trials simultaneously.

Brain state signatures during dual-task performance

First, we compared the BOLD patterns associated with the performance of the three different tasks blocks. Specifically, we created a difference map between the average group-level β parameters estimated from 400 cortical and 28 cerebellar regions of interest for the Balance and Calculation trials (Δ). By comparing this difference map to the β map from the Dual-task trials – $r(\Delta,\beta_{DT})$ – we could determine whether performing the two tasks in tandem led to a brain map that was more or less like one or the other single tasks – a positive correlation with this map (λ_1) was suggestive of the Dual-task reflecting the more challenging Calculation task; a negative correlation with the less challenging Balance task; and a null correlation with the

notion of optimally splitting activity between the two (or a pattern orthogonal to the two single tasks). Consistent with the second option, we found that the low-dimensional signature of Dual-task performance was more similar to the Calculation β map than the Balance β map ($r = 0.192 \pm 0.05$, $p = 6.5x10^{-5}$; Fig. 1F), suggesting that during the Dual-task trials, the cerebral cortex and cerebellum configured their activity to ensure the effective completion of the Calculation trials.

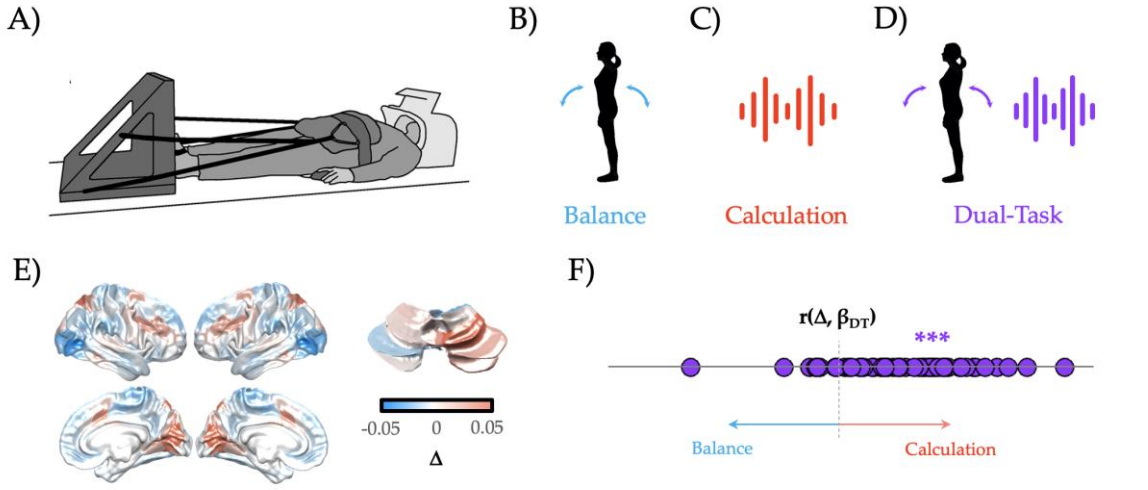

Figure 1 – Low-dimensional balance between Integration and Segregation during Dual-task performance. A) participants lay supine in an MRI scanner, with their legs controlling a force-plate; B) Balance trials (blue) involved a dynamically moving avatar that the participant had to match; C) Calculation trials involved listening to a series of beeps, and then subtracting the multiple of 7 times the number of beeps from a cue number (red); D) Dual-task trials required performing both tasks, simultaneously (purple); E) The Calculation trials recruited increased BOLD in frontoparietal and visual cortices, along with right superior cerebellum, whereas Balance trials were associated with increased BOLD in lateral visual cortex, medial motor cortex and parietal operculum; F) the Dual-task β map across all 50 subjects was more similar to the Calculation β map (i.e., positive correlation with λ_1) than the Balance β map (i.e., inverse correlation with λ_1). *** - $p < 0.001$.

Despite the brain states during Dual-task trials having more in common with the Calculation than the Balance trials, close examination of the RMS error of the Balance portion of the Dual-task trials suggests that subjects were performing the task as well as than when they performed the Balance trial on its own (Kolmogorov-Smirnov test: $p = 0.358$). So how was the brain configured on these Dual-task trials in order to mediate this stability? Based on previous empirical[23] and theoretical[8,26,27] work, we hypothesized that the distributed architecture integrating the cerebral cortex and cerebellum should be important for mediating this putative parallel processing performance. One straight-forward prediction is that balancing multiple tasks at the same time should recruit more regions of the cerebellum, and hence that cerebellar blood flow should be more strongly associated with Dual-Task performance than either the Balance or Calculation task alone. We found evidence to confirm this hypothesis – namely, a

greater proportion of cerebellar regions were associated with a positive mean β value in Dual-Task as compared to Balance and/or Calculation trials (67.3% vs. 35.7% and 39.3%, respectively; χ^2 (2, N = 50) = 249.6, $p < 1.0x10^{-4}$).

Unique patterns of cortico-cerebellar functional connectivity during dual-task performance

Given that the Dual-Task trials were more similar to Calculation trials than Balance trials (Fig. 1F), how was the brain capable of supporting multiple tasks at the same time? We hypothesized that Balance, Calculation and Dual-task trials should have unique patterns of cortico-cerebellar functional connectivity that could allow the brain to support multiple channels of communication within the same system. To test this hypothesis, we calculated the time-varying functional connectivity between all cortical and cerebellar parcels using the Multiplication of Temporal Derivatives approach (window = 20 TRs[28]) and then contrasted the three trial types with one another. We observed robust differences between the three trial types (Fig. 2). For instance, Calculation trials (when compared to Balance trials) were associated with wide-spread cortico-cerebellar connectivity between lobule V and the majority of cortical networks, as well as more targeted connections between VIIIa/IX and primary sensorimotor networks (Fig. 2A). In contrast, Balance trials (when compared to Calculation trials) showed predominant increases in intermediate cerebellar lobules (e.g., Crus I and II) with higher-order cortical networks. In contrast, Dual-task trials were associated with heightened frontoparietal connections with intermediate cerebellar lobules, particularly Crus I and VIIIa, when compared to both Balance (Fig. 2B) and Calculation trials (Fig. 2C).

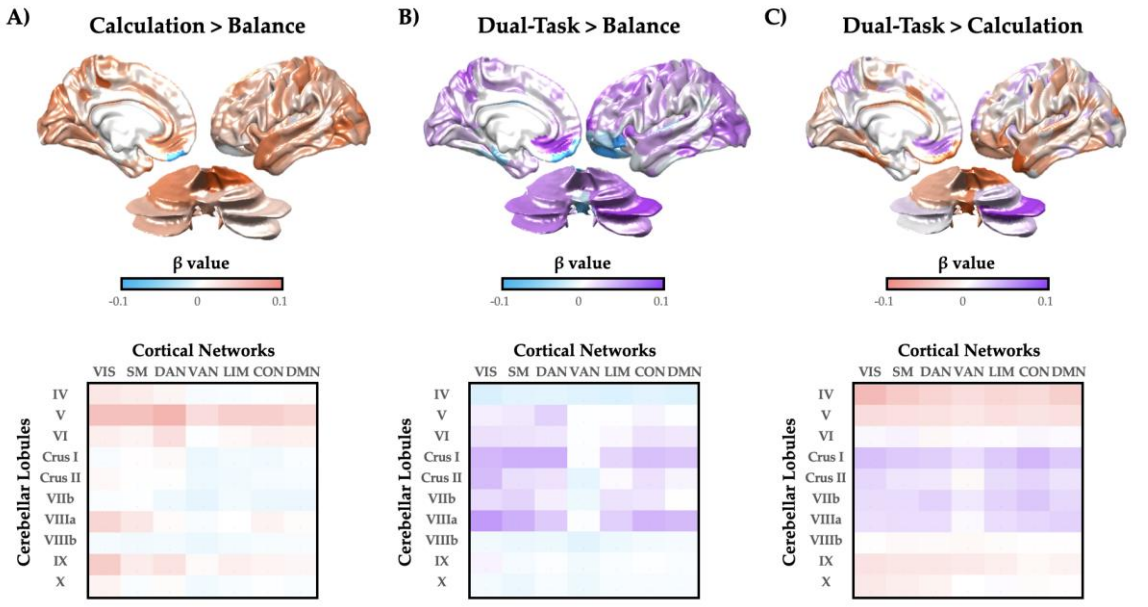

Figure 2 – Cortico-cerebellar task-based functional connectivity. A) patterns of task-based cortico-cerebellar functional connectivity during Calculation (red) when compared to Balance (blue) trials – upper: mean task-based connectivity strength for cerebral cortex and cerebellum; lower: mean task-based connectivity strength collapsed

into 7 Yeo networks (columns) and 10 average lobules (rows); B) similar maps for Dual-task (purple) versus Balance; C) similar maps for Dual-task versus Calculation. Note: results were consistent for left and right hemispheres. Key: VIS – visual; SM – somatomotor; DAN – dorsal attention network; VAN – ventral attention network; LIM – limbic network; CON – control network; DMN – default mode network.

Having confirmed a robust relationship between the cerebral cortex and cerebellum during Dual-task performance, we next asked whether cortico-cerebellar functional connectivity patterns differentiated between correct and error Dual-task trials. To test this hypothesis, we fit a General Linear Model to each Dual-task trial, independently, for each cortico-cerebellar time-varying connectivity score. We then split Dual-task trials into correct (accurate calculation and small RMS error [< 50% of population distribution]) and incorrect (inaccurate calculation, large RMS error [>50%] or both) trials and compared (using a set of independent-samples T-tests) the task-based functional connectivity between cortical and cerebellar parcels as a function of effective Dual-task performance. We conducted a permutation test (5,000 iterations) to determine the likelihood of each edge being distinct between the two groups by chance. To summarize these results, we computed the mean significant β-value for the functional connectivity between each cerebellar lobule (averaged across hemispheres, and ignoring the connections of the vermis; from the cerebellar SUIT atlas[29]) and each of 7 pre-identified cortical networks (the Yeo 7 parcellation from the 400-region Schaefer atlas[30]; Fig 3). We found a robust increase in task-based functional connectivity between the ventral attention network (VAN) and lobules Crus II, VIIb, VIIIa and VI (Fig. 3), as well as more distributed connections between lobule X and multiple cortical sub-networks. In contrast, Crus I was relatively functionally disconnected from all cortical networks (except VAN) during effective dual-task performance, which is consistent with known patterns of cerebellar lesion-related cognitive impairments[31].

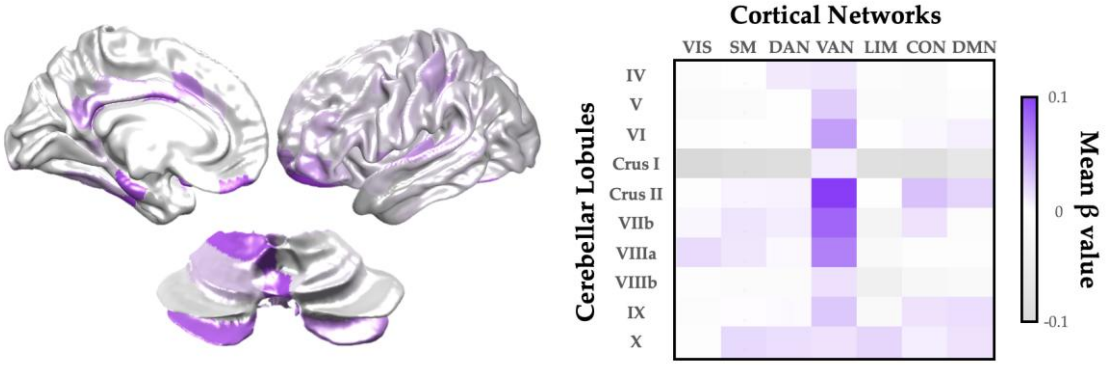

Figure 3 – Increased cortico-cerebellar task-based functional connectivity associated with successful Dual-Task performance. Left: Key cortical and cerebellar regions with heightened task-based functional connectivity during Dual-task trials with correct vs. incorrect answers. Right: Mean significant β-value (cortical sub-network [Yeo 7 atlas] vs. cerebellar lobule [SUIT atlas]) associated with task-based functional connectivity values for correct vs. incorrect Dual-Task performance ($p < 0.001$; random permutation test). Key: VIS – visual; SM – somatomotor; DAN – dorsal attention network; VAN – ventral attention network; LIM – limbic network; CON – control network; DMN – default mode network.

Dual-task performance balances network integration and segregation

One way in which the distributed cortico-cerebellar architecture could facilitate effective parallel processing is by striking an effective balance between integration and segregation[32–34]. In previous work, we have used a combination of time-varying functional connectivity and a topological measure that quantifies network-level integration – the Participation Coefficient (PC)[35] – to demonstrate that the systems-level network structure of functional connectivity changes during task performance, with cognitively challenging tasks requiring higher integration than relatively simple tasks[35]. From this, we predicted that the Balance task should be relatively segregated (i.e., low PC), the Calculation task should be relatively integrated (i.e., high PC) and the Dual-task trials should strike a balance between the two extremes (i.e., intermediate PC). Using our standard time-varying analysis (see Methods), we observed robust evidence for our predictions (Fig. 4; $F_{2,147} = 3.41$; $p = 0.036$). In addition, although the Dual-task topological pattern was positively correlated with the average of Balance and Calculation ($r = 0.464$; $p < 0.001$), it was not a direct super-position of the two maps, suggesting topological reconfiguration during the different task states. Together, these results confirm that parallel processing in the brain is supported by a topological balance between integration and segregation.

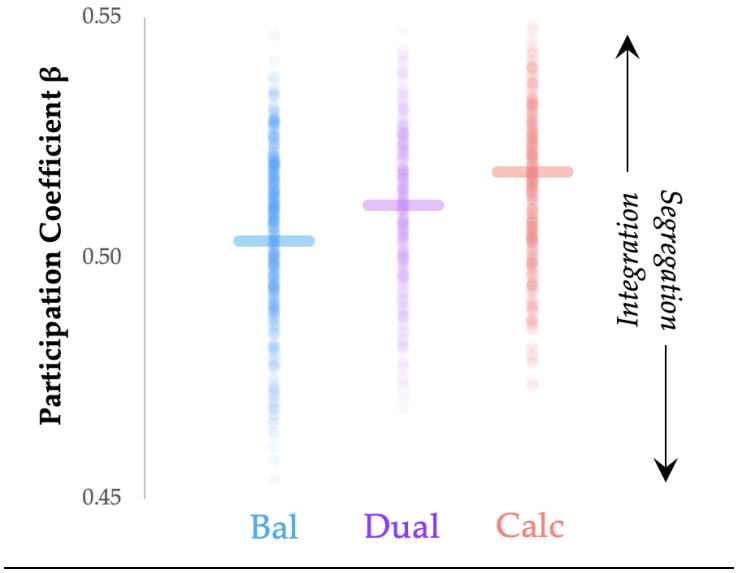

Figure 4 – Parallel processing balances integration and segregation. Balance trials were associated with relative Segregation (low PC; blue), Calculation trials with relative Integration (high PC; red) and Dual-task trials with a balance between Integration and Segregation (intermediate PC; purple) – $F_{2,147} = 3.41$; $p = 0.036$. Thick lines represent the median value for each group.

Cortico-cerebellar activity flow mapping

The input and output streams of cerebral cortex and cerebellum interact via distinct white matter pathways. Importantly, while the structural connections between these two structures are reciprocal, they are imbalanced[17,18] – different pathways exist from the cerebral cortex to the cerebellum than from the cerebellum to the cerebral cortex. Specifically, thick-tufted layer V pyramidal neurons in the deep layers of the cerebral cortex send projections to the mossy fibre pathway of the cerebellum (via the pontine nuclei), thus forming the Cortico-Ponto-Cerebellar (CPC) tract (Fig. 5A). In contrast, the cerebral cortex receives feedback from the cerebellum via the deep cerebellar nuclei, which project via the 'Core' nuclei of the thalamus – i.e., the Cerebello-Thalamo-Cortical (CTC) tract (Fig. 5B). Plastic changes between the mossy fibre pathway and the Purkinje cells of the cerebellar cortex are proposed to act as a major site for the refinement of automatized behaviour[10,26,27,36] and hence, the capacity to perform multiple tasks simultaneously. From our observations that the timeseries of the cerebral cortex and cerebellum were highly coordinated during Dual-task behaviour, we hypothesized that the specific patterns of BOLD activity in both the cortex and cerebellum should be related to the intersection between prior BOLD activity in the cerebellum (via the CTC) and cerebral cortex (via the CPC).

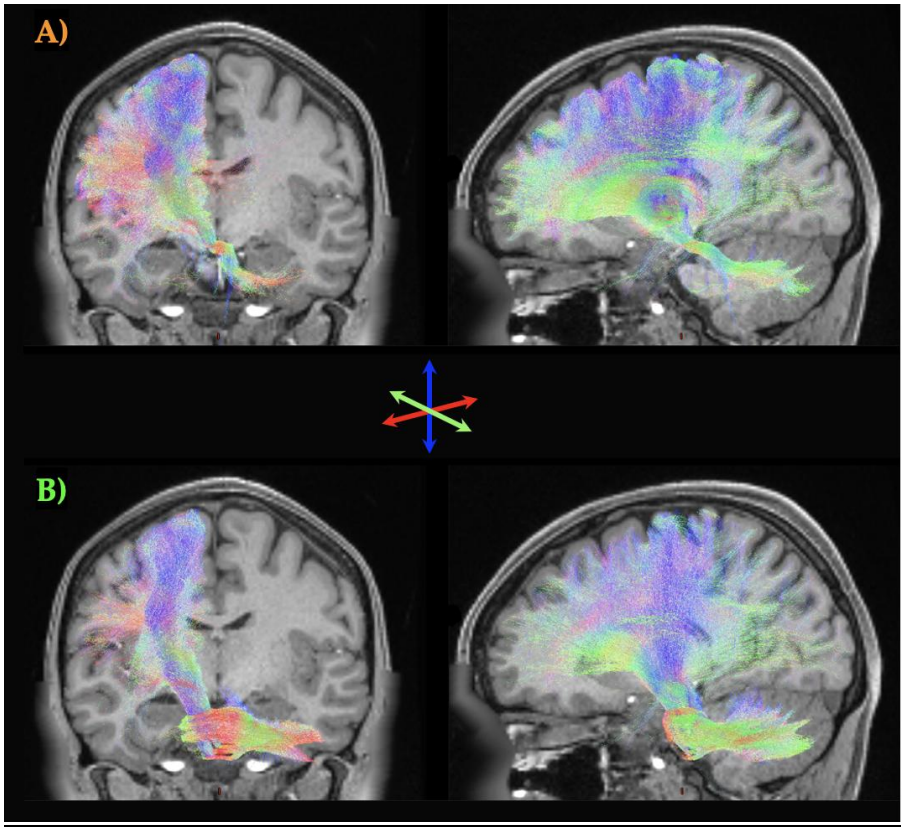

Figure 5 – White matter streamlines interconnecting the cerebellum and the cerebral cortex. A) the Cortico-Ponto-Cerebellar (CPC) tract sends projections from the cortex via the pontine nuclei into the mossy fibres of the cerebellum; B) the Cerebello-Thalamo-Cortical (CTC) –B) tract derives from the deep cerebellar nuclei, which project back via the core thalamic nuclei to the cerebral cortex. Tracts created using *mrtrix* were projected onto a T1-weighted structural image from individual 100307 from the Human Connectome Project (de-faced to preserve

autonomy). The colours of each tract represent the primary direction of each tract: blue = inferior-superior; red = left-right; green = anterior-posterior.

To test this hypothesis, we adapted the activity flow mapping approach[37] to incorporate the structural connectivity between the cortex and cerebellum. Specifically, we extracted $9x10^7$ structural connectivity weights for both the contralateral CPC (Fig. 6A; orange) and CTC (Fig. 6B; green) tracts[17] from a single healthy 26-30yo female (ID#: 100307) from the Human Connectome Project (a single subject connectome was chosen so as to retain precision in the parcel-to-parcel connectivity estimates for both CPC and CTC – note however that maps were highly similar to those previously extracted from 28 healthy participants from the HCP[17]). While both tracts are over-expressed in the frontal cortices, there were relatively more CPC projections from the parietal lobes and more CTC projections that innervate the frontal cortex, which is consistent with known anatomical projection patterns[8,26,38,39]. A parsimonious interpretation of these data is that the frontal cortex benefits from the information provided to the cerebellum by posterior cortices that process potential opportunities for action (also known as affordances[40]).

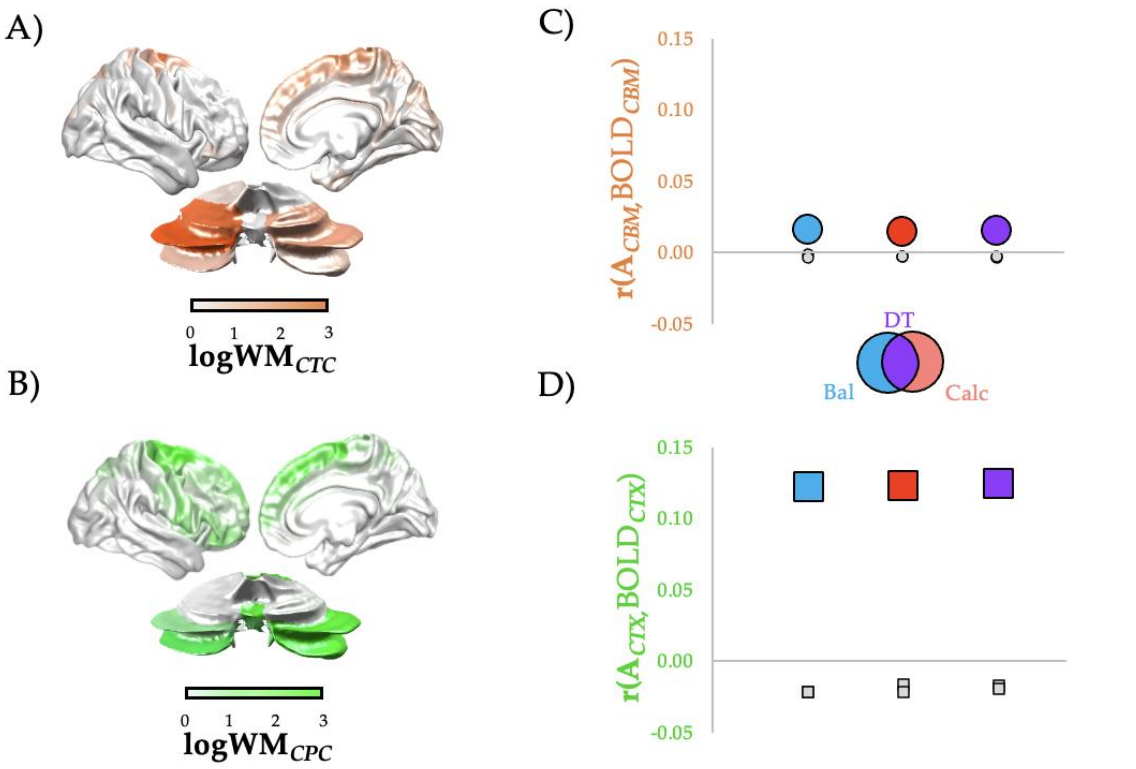

Figure 6 – Cortico-cerebellar Structure-Function Mapping across Trial types. C) normalized (in $\log_{10}$ of white matter connectivity) map of projections from the cerebral cortex to cerebellum via CPC (orange); D) normalized (in $\log_{10}$ of white matter connectivity) map of projections from cerebellum to the cerebellar cortex via CTC (green); E) activity flow mapping[37] between cerebellar BOLD patterns predicted from CPC tract in Balance (Bal; blue), Calculation (Calc; orange) and Dual-Task (DT; purple) trials (circles) – see Methods for details; F)

the same for cortical BOLD patterns predicted from the CTC tract (squares). All activity flow map correlations were greater than permuted null levels.

If cortico-cerebellar communication is required for effective Dual-task performance, then blood flow within either the cerebral cortex or cerebellum during Dual-task trials should be predictive of subsequent blood flow (assuming sufficient delay) within the cortical (or cerebellar) regions to which they are connected by white matter projections. To create an estimate of what these predicted BOLD responses should be, we created two template maps – one for predicted cerebellar activity (estimated cerebellar activity: $A_{CTX} = W_{CBM} \,.\, CPC$) and one for predicted cortical activity (estimated cortical activity: $A_{CBM} = W_{CTX} \,.\, CTC$) – by multiplying the cortico-cerebellar structural connectivity matrices with the pre-processed BOLD pattern observed during the three different trial types. We then correlated these prediction vectors with the actual BOLD patterns in the respective regions. If the observed patterns of activity were similar, we can conclude that BOLD activity patterns were intimately related to the reciprocal structural connections between the cerebral cortex and cerebellum.

Across all three trial types, both cortico-cerebellar (via CPC; Fig. 6C, circles) and cerebello-cortical (via CTC; Fig. 6D, squares) activity flow patterns were significantly greater for actual *vs.* randomly-shuffled data (all $p < 0.05$), suggesting that functional activity was coordinated by connections both from the cerebral cortex to the cerebellum (i.e., CPC) and vice versa (i.e., CTC) across all tasks. Interestingly, despite the consistent positive relationships, cerebello-cortical connections (i.e., CTC) were more robustly able to predict subsequent cortical patterns than cortico-cerebellar connections (i.e., CPC), suggesting that the feedback from the cerebellum to the cerebral cortex was more crucial for task performance. Finally, we found that the match between A_{CTX}/A_{CBM} and the raw data was greater in correct versus incorrect Dual-task trials for both cerebral cortex ($T = 2.397$, $p = 0.017$) and cerebellum ($T = 2.049$, $p = 0.041$), further confirming the importance of cortico-cerebellar interaction for parallel processing.

Discussion

In this study, we used systems-level neuroimaging analysis to demonstrate that robust interactions between the cerebral cortex and cerebellum are associated with effective Dual-task performance. We hypothesized that, through distributed white matter pathways that interconnect these major cortical systems, the brain can differentiate different task contexts so as to effectively maintain the performance of two computational tasks in parallel. To test this hypothesis, we analysed BOLD data from the cerebral cortex and cerebellum, and in doing so demonstrated that Dual-Task performance recruited heightened cerebellar activity (Fig. 1) and functional connectivity between the cerebral cortex and cerebellum (Figs. 2 and 3) that was linked to the balance between integration and segregation (Fig. 4) and related to the structural connections between the cerebellum and cerebral cortex (Figs. 5 and 6). Together, these results

highlight the importance of systems-level interactions in the manifestation of complex cognitive capacities.

Our results clearly demonstrate that models that incorporate the cerebellum and its massive, high-dimensional architecture provide a more parsimonious account for how the brain can balance the challenges inherent with parallel processing[8,23,26,41]. The distributed circuits that interconnect the cerebral cortex and cerebellum are optimally set-up to fulfil this capacity. Specifically, the major output of the cerebral cortex – layer V PT-type pyramidal neurons – provides the primary afferent input to the cerebellar cortex (i.e., granule cells), by way of the pontine nuclei[8,26,42]. Following a massive dimensionality expansion that has been argued to facilitate pattern separation[11], the outputs of the cerebellum (the deep cerebellar nuclei) send large glutamatergic projections to the ventral tier of the thalamus[39], wherein they innervate the cerebral cortex. The thalamic targets of the cerebellum then go on to drive activity in the cerebral cortex, typically in a high-frequency, precise fashion[43] that we have argued to form the basis of relatively automatic modes of behaviour[26,27]. Here, we extend these functional neuroanatomical principles to incorporate the completion of challenging, dual tasks, thus augmenting and reinforcing conclusions from previous functional neuroimaging work on dual-task performance[23,34,41]. We anticipate that similar patterns will be observed in future experiments that interrogate different types of dual tasks, particularly those in which one (or both) of the tasks is capable of relative automaticity. Whether such automaticity benefits extend to purely perceptual tasks, such as the attentional blink[44], is an interesting open question for future work.

The topological signature of functional networks estimated from BOLD data have previously been linked to effective performance on cognitive tasks. For instance, an integrated brain has been linked to the completion of a range of complex tasks, such as those that probe working memory[35,45,46], logical reasoning[47] and attentional tracking[48,49]. In contrast, a relatively segregated functional network has been linked to relative sensorimotor automaticity[32,33], as well as to attentional vigilance[50]. Our results are consistent with the spectrum implied by these previous results – the Balance task, which presumably tapped into relatively well-learned behaviours, was associated with a segregated functional network; and the Calculation task, which likely required more focussed, flexible attention, was associated with a relatively integrated network. Interestingly, although the Dual-task trials were arguably more challenging than the Calculation trials on their own, the topology of the network actually demonstrated a balance between integration and segregation, suggesting that performing tasks in parallel requires an ability to avoid topological extremes, perhaps so as to maximise information processing capabilities[51]. In addition, there are theoretical reasons to believe that the finite nature of biological networks may imbue specific limits on the number of possible tasks that can be run in parallel, although we expect that the high-dimensional architecture of the cerebellum[11] will likely boost this capacity, particularly as a function of experience[26,27]. Precisely which systems in the brain help to control this balance remains an open question,

however there is intriguing results to suggest that the neuromodulatory system may play a crucial role in this process[26,52,53].

Systems-level neuroimaging analysis provides an integrated perspective of cognitive capacities[33], however BOLD dynamics are necessarily indirect – i.e., they don't measure neural activity directly, but rather filtered through the low-dimensional lens of perfusion[54,55]. While BOLD signal remains a robust measurement for neural signalling[56,57], it only reveals a part of how the brain functions. This is particularly true for the cerebellar cortex, whose complex, convoluted anatomy[8,58] and idiosyncratic firing properties[16,59,60] render simple, linear readouts of neural activity from BOLD problematic. Specifically, there is evidence to suggest that BOLD measurements in the cerebellar cortex predominantly track activity in the mossy fibre pathway (via the CPC)[61,62], whereas outputs from the Purkinje cells (via the CTC) are more difficult to characterize with BOLD signalling[63,64]. While this does suggest caution with respect to the interpretation of our results, it makes the presence of robust cerebello-cortical activity flow mapping via the CTC (Fig. 6D) all the more fascinating of a result, as it suggests that the fate of the Purkinje cells is relatively sealed by the specific pattern of mossy fibre inputs that they received, although we anticipate that this mapping is likely augmented by the process of learning – i.e., it should be less profound when facing highly novel task contexts. Irrespective, we hope that by consolidating analysis from multiple neuroimaging techniques that we have provided a robust illustration of changes to cortico-cerebellar circuits during a parallel processing task.

The capacity to perform tasks in parallel clearly scales positively with experience. In the future, it will be fascinating to examine the interactions between the cerebral cortex and cerebellum as individuals learn to perform individual tasks to relative automaticity. There is robust empirical previous work linking cerebellar output with highly-overtrained behaviours in rodents[65]. Similar arguments have been made when analysing automaticity in the performance of challenging cognitive tasks[23]. Interestingly, there is also evidence suggesting that, over the course of learning a simple sensorimotor task, the brain shifts from a relatively integrated to a segregated architecture[32,33]. This suggests a novel prediction: the extent to which a particular task has been well-learned will lead to relative segregation of the topological network signature of the brain, which in turn will make the task easier to automatise, and hence to combine successfully with other, more challenging dual tasks.

A key factor that was not well-controlled in this study was cognitive load, which is well-known to play an important role in our capacity to perform multiple tasks in parallel[66–68]. Simply put, it's much easier to perform two tasks simultaneously if (at least) one of the tasks is either highly automatic, or is sufficiently easy that its performance requires little-to-no focussed attention[69]. In these cases, the simpler or more automatic task can be performed with minimal awareness, freeing up higher-cognitive systems to aid in the completion of the second, harder/more-challenging task. In our study, the Balance task was presumed to be easier than the Calculation

task, as participants were expected to have been unlikely to have practiced the subtraction of the digit “7” from random large numbers, whereas balance is something many of us perform so much as to take it for granted. In future studies, it will be important to attempt to stack together multiple tasks that are difficult to perform in the same manner, such as comprehending an auditory stream while performing a calculation on concurrent visual input. Although we anticipate that both the cerebellum and cerebral cortex would be engaged in such a task, it is less likely that effective performance would be as crucially dependent on their interaction, as the mechanism we propose invokes the cerebellar-mediated anticipation of expected consequences as a means for freeing-up higher cognitive resources[10,26,27]. It is not currently clear whether these anticipatory processes are as important in the more deliberate, flexible stages of cognitive processing that would be required to complete two more deliberate cognitive tasks simultaneously.

Conclusions

Here, we have demonstrated that dynamic interactions between the cerebral cortex and cerebellum are critically related to the performance of a challenging dual-task. Future research is required to determine whether similar principals are related to parallel processing of other simultaneous cognitive and perceptual challenges, as well as across distinct spatiotemporal scales.

Methods

Experimental setup

The functional data from this study arose from a re-analysis of a previously published dataset[25] – here, we will include the minimal information required to interpret the results, and point the interested reader to the original study for full details. 50 healthy female participants (mean age = 49+-20 years)[25] lay supine in the MRI scanner with their feet against a custom-made force platform attached to the MRI bed (Fig 1A; sample frequency of 100 Hz), with the position of the force platform was adjusted to subject height. To minimize excessive head movement, participants were pulled towards the force platform using thick elastic ropes attached to a hip belt[25]. A four-button device was placed underneath the right hand for the calculation task. The tasks were projected onto a white screen placed at the head of the scanner. Participants could see the screen via a mirror attached to the head coil.

During the Balance task, an avatar in the shape of a woman was displayed on the screen. The avatar swayed forward and backward. Participants were instructed to try to keep the avatar in the upright position by increasing or decreasing the level of plantar flexion force measured by the load cell. As in normal standing, increasing the plantar flexion force led to a backward sway (and *v.v.*). At the start of every balance condition, participants were given two seconds to bring the avatar in the upright position. After these two seconds, a disturbance signal was added, causing the avatar to sway forward and backward. To keep the avatar upright, participants had to counteract these disturbances. The disturbance signal was made by combining fifteen sinusoidal signals with random phases and with frequency characteristics based on an average frequency spectrum of centre of pressure movement during upright standing (0.025–1 Hz), measured in ten young and ten old adults. The maximum amplitude of the disturbance was ±30°. The error for each Balance trial was created by calculating the sum of the Root Mean Squared error between the optimal balanced avatar (i.e., 90^0) and the position of the actual avatar. Trials were subsequently median split to identify ‘good’ and ‘bad’ balance trials.

The Calculation task consisted of serial subtractions with increments of seven – at the beginning of each trial, a number between 50 and 100 was projected on the screen for two seconds, after which a plus sign was displayed on the screen and a beep was generated every 3 to 4 seconds through an MRI compatible headphone (MR confon Optime 1, Magdeburg, Germany), with a total of four beeps per trial. Participants were instructed to subtract the number ‘7’ with every beep. At the end of each trial, four answer possibilities were displayed on the screen: one indicating the correct answer, two erroneous answers, and the option that none of the other answers is correct. Participants indicated which answer they thought was correct by pressing the corresponding button of the four-button device.

During the Dual-task condition, subjects performed the Balance and Calculation tasks simultaneously. The distribution of RMS errors in the Balance trials and Dual-task trials were compared using a Kolmogorov-Smirnov test.

An fMRI block-design was used to alternate between the three conditions: Balance, Calculation, and Dual-task. Every participant performed twelve blocks, each block including one trial of each condition (thus three trials), with the order of the conditions randomized, both across blocks and between subjects. At the end of every block a 15-second rest period was given in which the participants fixated their gaze on a plus sign.

MRI acquisition and pre-processing

Brain imaging was performed on a 3-T SIEMENS Magnetom Skyra System (Siemens, Erlangen, Germany) with a 20-channel head/neck coil. For functional scans, a T2*-weighted multiband gradient echo-planar imaging (EPI) sequence was used (TR = 700 msec, TE = 30 msec, flip angle = 55°, 48 axial slices, slice thickness = 3 mm, no gap, in-plane resolution 3x3 mm)[70]. After the functional scanning session, a high-resolution magnetization prepared rapid acquisition gradient echo (MPRAGE) T1-weighted sequence (TR = 2,100 msec, TE = 4.6 msec, TI = 900 msec, flip angle = 8°, 192 contiguous slices, voxel resolution 1 mm^3, FOV = 256x256x192 mm, iPAT factor of 2) was obtained in sagittal orientation. These anatomical scans were used to co-register the functional runs using SPM 12. The anatomical scan was segmented using the SPM tissue probability maps. The functional data were pre-processed as part of a different study[25]. For each subject, inter-scan movement was corrected by realigning and unwarping the data, with the first scan as a reference. All functional scans were then co-registered to the anatomical scan and normalized to the Montreal Neurological Institute (MNI) template brain via the forward deformations revealed by the structural segmentation. Movement in the scanner was assessed by calculating framewise displacement (FD) from the derivatives of the six rigid-body realignment parameters estimated during standard volume realignment, as well as the root mean square change in BOLD signal from volume to volume (DVARS). Across the cohort, head motion was found to be minimal (group mean FD = 0.183 ± 0.08mm; group mean DVARS = 0.811 ± 0.13), in large part due to the fact that participants were pulled towards the force platform using thick elastic ropes attached to a hip belt .

Temporal artifacts were identified in each dataset by calculating framewise displacement (FD) from the derivatives of the six rigid-body realignment parameters estimated during standard volume realignment [71], as well as the root mean square change in BOLD signal from volume to volume (DVARS). Frames associated with FD > 0.25 mm or DVARS > 2.5% were identified; however, as no participants were identified with greater than 10% of the resting time points exceeding these values, no trials were excluded from further analysis.

Brain parcellation

Following pre-processing, the mean time series was extracted from 400 pre-defined cortical parcels using the Schaefer atlas[30] and 28 pre-defined cerebellar parcels from the SUIT atlas[29] (cerebellar nuclei were not included). The mean BOLD signal intensity from each region was extracted and then used for subsequent analyses.

General linear model and principal component analysis

A general linear model was fit to pre-processed, parcellated BOLD data with separate terms modelling each trial type (i.e., Balance, Calculation and Dual-task). The event time series used to analyse the task included a convolution with a canonical haemodynamic response function. The proportion of cerebellar regions associated with positive cerebellar β-values was compared across Balance, Calculation and Dual-task trials using a χ^2 test with degrees of freedom = (rows – 1) x (columns – 1) = (3-1) x (2-1) = 2.

The average β-value for the Balance and Calculation trials were demeaned and analysed with a Principal Component Analysis. The coefficient of the leading principal component was correlated with the mean β map from the Balance and Calculation trials to demonstrate its utility as a linear decoder between Balance and Calculation. The dot-product between the Dual-task β map for each subject and the leading principal component was calculated, and then subjected to a 1-sample t-test to determine whether the loading was more similar to Calculation (positive loadings) or Balance (negative loadings).

Time-varying functional connectivity

We used the multiplication of temporal derivatives (MTD) approach[28] to calculate time-resolved dynamic functional connectivity between the selected ROIs; code is freely available at https://github.com/macshine/coupling/) with a window size of 20 TRs (results were stable for window sizes of 10-50 TR). For each node, *n*, with time points, *t*, a vector of *t-1* temporal derivatives was calculated and normalized (temporal derivatives divided by the standard deviation of temporal derivatives, σ). Then, we created a matrix of functional coupling between the i^{th} and j^{th} nodes for each time point, by multiplying the temporal derivatives of each pair of nodes across each time point.

$$\mathrm{MTD}_{ijt} = \frac{1}{w}\sum_{t}^{t+w}\frac{(dt_{it} \times dt_{jt})}{(\sigma_{dt_i} \times \sigma_{dt_j})} \qquad [1]$$

where *dt* is the first temporal derivative of the i^{th} and j^{th} time-series, and σ standard deviation of the temporal derivative, w is the window length of the simple moving average[28]. The MTD values for the cortico-cerebellar system (i.e., 400 x 28 = 11,200 edges) were entered into a similar General Linear Model to the cortico-cerebellar BOLD values, with a permutation test (5,000 iterations) used to test for statistical significance.

Modularity maximization

The Louvain modularity algorithm from the Brain Connectivity Toolbox (BCT[72]; http://www.brain-connectivity-toolbox.net) was used on the neural network edge weights to estimate community structure. The Louvain algorithm iteratively maximizes the modularity statistic, *Q*, for different community assignments until the maximum possible score of *Q* has been obtained (see Equation 2). The modularity of a given network is therefore a quantification of the extent to which the network may be subdivided into communities with stronger within-module than between-module connections.

$$Q_T = \frac{1}{v^+}\sum_{ij}\left(w_{ij}^+ - e_{ij}^+\right)\delta_{M_iM_j} - \frac{1}{v^+ + v^-}\sum_{ij}\left(w_{ij}^- - e_{ij}^-\right)\delta_{M_iM_j} \qquad [2]$$

where *v* is the total weight of the network (sum of all negative and positive connections), w_{ij} is the weighted and signed connection between regions *i* and *j*, e_{ij} is the strength of a connection divided by the total weight of the network, and δ_{MiMj} is set to 1 when regions are in the same community and 0 otherwise. '+' and '–' super-scripts denote all positive and negative connections, respectively.

For each epoch, we assessed the community assignment for each region 500 times and a consensus partition was identified using a fine-tuning algorithm (BCT). We calculated all graph theoretical measures on un-thresholded, weighted and signed connectivity matrices[72]. The stability of the γ parameter was estimated by iteratively calculating the modularity across a range of γ values (0.5-2.5; mean Pearson's r = 0.859 +-0.01) on the time-averaged connectivity matrix for each subject – across iterations and subjects, a γ value of 1.0 was found to be the least variable, and hence was used for the resultant topological analyses.

Participation Coefficient

The participation coefficient, *PC*, quantifies the extent to which a region connects across all modules (i.e., between-module strength) and has previously been used to successfully characterize hubs within brain networks[7,35]. The PC for each region was calculated within each temporal window using Equation 3, where k_{isT} is the strength of the positive connections of region *i* to regions in module *s* at time *T*, and k_{iT} is the sum of strengths of all positive connections of region *i* at time *T*. Negative connections were discarded prior to calculation. The participation coefficient of a region is therefore close to 1 if its connections are uniformly distributed among all the modules and 0 if all of its links are within its own module.

$$PC = 1 - \sum_{s=1}^{n_M} \left(\frac{\kappa_{isT}}{\kappa_{iT}}\right)^2 \quad [3]$$

The participation coefficient for each parcel was compared across Balance, Calculation and Dual-task trials using paired t-tests (FDR $q = 0.05$).

Diffusion MRI Analysis

Data were selected from a single, 26-30yo female subject from the HCP (code#: 100307). The minimally processed HCP diffusion dataset (which included correction for motion, susceptibility distortions, gradient non-linearity and eddy currents) were subject to additional image processing, which multi-shell multi-tissue constrained spherical deconvolution to generate the fibre orientation distribution (FOD) in each voxel[73–75]. These steps were implemented in accordance with previous work[76] and were performed using the *MRtrix* software package (http://www.mrtrix.org[77,78]).

The T1-weighted images were used to generate a so-called 'five-tissue-type' (5TT) image[79] using FSL[80]; the 5TT image classifies the voxel into one of 5 tissue types: cortical grey matter, sub-cortical grey matter, white matter, cerebrospinal fluid, and '5th type' (e.g., pathology). The FOD data and the 5TT image were used to generate 120 million streamlines using the anatomically constrained tractography (ACT) framework[79], using dynamic and the 2nd-order Integration over Fibre Orientation Distributions (iFOD2)[77] probabilistic fibre-tracking algorithm, using default MRtrix parameters, with the exception of FOD cutoff 0.06, maximum length 250 mm, step size 1 mm, and backtrack specified. This set of streamlines is referred to as the *whole-brain-tractogram* thereafter.

Specifically, we calculated from a highly curated tractography rendering of the cerebro-cerebellar loop, after thresholding the streamlines to eliminate possible spurious tracts. An average tract obtained from 5-10-28 subjects, thresholded to represent the group, may lose the finer details of the connectome that are key when using a ~400 region grey matter parcellation

atlas as in this work. On the other hand, the connectome from the union of the tracts, if not thresholded, would inflate this finer connectivity (if thresholded, these connections would be downweighted). The impact of averaging individual subject streamlines on the actual connectome has to be demonstrated in a separate study as the high variability of the streamlines is likely to correspond to a fairly stable connectome.

The cerebello-thalamo-cortical (CTC) and cortico-ponto-cerebellar (CPC) tracts were extracted from the *whole-brain-tractogram* by using contralateral cerebral and cerebellar cortices, cerebellar peduncles, contralateral red nuclei, and thalami as regions of interest (see [17,18] for more details). To define the strength of the cerebellar connectivity with each of brain parcel, the $\log_{10}$ of the number of streamlines was used to weight the CTC and CPC tracts[81,82]. To ensure that the single-subject connectome was representative of the group-level parcellation, we calculated the DICE coefficient between the mean map of both the CTC and CPC tracts (L and R) of a further 27 subjects in MNI space (including only those voxels that were common to at least 70% of subjects – i.e., less than the 90,000,000 streamlines used for the individual connectome) – the DICE was 0.7, suggesting strong correspondence between our single subject (who preserved the fine-scale nature of the connectome) and the group-template.

Cortico-cerebellar activity flow mapping

To determine whether cortico-cerebellar interactions could transform cortical or cerebellar task-evoked activity into respective cerebello-cortical task activity, we modified the activity flow mapping procedure[37] to incorporate estimates of cortico-cerebellar (CPC) and cerebello-cortical (CTC) structural connectivity. Specifically, for each trial type, block and subject, we calculated:

$$\mathrm{A_{CTX}} = \mathrm{W_{CBM}^{t}} \cdot \mathrm{CPC} \quad [4]$$

$$\mathrm{A_{CBM}} = \mathrm{W_{CTX}^{t}} \cdot \mathrm{CTC} \quad [5]$$

where $\mathrm{W_t}$ is the evoked response estimate for every cortical (W_{CTX}) or cerebellar (W_{CBM}) parcel, CPC and CTC are the structural connectivity matrices described above, and $\mathrm{A_{CTX}}$ and $\mathrm{A_{CBM}}$ are the predicted activity pattern for each subgroup. For each trial type, block and subject, the predicted cortical and cerebellar activity patterns were then empirically compared to the observed activity patterns using Pearson correlations. A series of t-tests were used to

compare the Pearson's correlation loadings, with the non-matching predictions (e.g., using the cortical BOLD for Balance trials to predict cerebellar BOLD for Calculation trials) used a simple null model that contained all the same spectral features but spatiotemporal sequences that did not match the data. Finally, we created separate null distributions following a random permutation[83] of both CPC and CTC, separately (each with 5,000 iterations).

Supplementary Figures

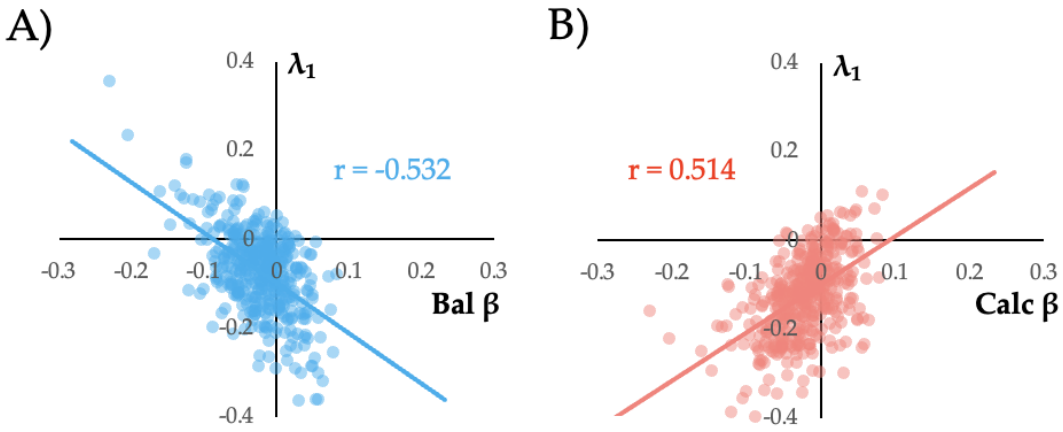

Figure S1 – Correlation between Balance and Calculation maps and leading principal component. A) Loadings of the principal eigenvector (λ_1) in both cerebral cortex (left) and cerebellum (right); F) scatter between mean Balance β map and λ_1 ($r = -0.532$; $p_{SPIN} = 0.002$); G) scatter plot between the mean Calculation β map and λ_1 ($r = 0.514$; $p_{SPIN} < 0.0001$).

Acknowledgements

Data were provided by the Human Connectome Project, WU-Minn Consortium (PI: David Van Essen and Kamil Ugurbil; 1U54MH091657) funded by the 16 NIH Institutes and Centers that support the NIH Blueprint for Neuroscience Research; and by the McDonnell Center for Systems Neuroscience, Washington University.

JMS was supported by the National Health and Medical Research Council (GNT1193857). FC was supported by the National Health and Medical Research Council (GNT1117724) and the Australian Research Council (DP170101815). ED, CGW-K and FP received funding from H2020 Research and Innovation Action Grants Human Brain Project (#945539, SGA3). ED also received funding from the MNL Project “Local Neuronal Microcircuits” of the Centro Fermi (Rome, Italy). CGW-K receives funding from the MS Society (#77), Wings for Life (#169111), Horizon2020 (Human Brain Project), UCL-UCLH Biomedical Research Center (London, UK) BRC (#BRC704/CAP/CGW), MRC (#MR/S026088/1), Ataxia UK. CGWK is a shareholder in Queen Square Analytics Ltd. CGW-K is also a shareholder in Queen Square Analytics. TC was supported by the National Imaging Facility, a National Collaborative Research Infrastructure Strategy (NCRIS) capability.

References and Notes

1. John, Y. J. *et al.* It's about time: Linking dynamical systems with human neuroimaging to understand the brain. *Network Neuroscience* 1–20 (2022) doi:10.1162/netn_a_00230.
2. Poldrack, R. A. The future of fMRI in cognitive neuroscience. *NeuroImage* **62**, 1216–1220 (2012).
3. Eisenreich, B. R., Akaishi, R. & Hayden, B. Y. Control without Controllers: Toward a Distributed Neuroscience of Executive Control. *Journal of Cognitive Neuroscience* **29**, 1684–1698 (2017).
4. Poldrack, R. A. *et al.* The Cognitive Atlas: Toward a Knowledge Foundation for Cognitive Neuroscience. *Frontiers in neuroinformatics* **5**, 17 (2011).
5. Schmitz, T. W. & Duncan, J. Normalization and the Cholinergic Microcircuit: A Unified Basis for Attention. *Trends in Cognitive Sciences* **22**, 422–437 (2018).
6. Petri, G. *et al.* Topological limits to the parallel processing capability of network architectures. *Nat. Phys.* (2021) doi:10.1038/s41567-021-01170-x.
7. Shine, J. M. *et al.* Human cognition involves the dynamic integration of neural activity and neuromodulatory systems. *Nat Neurosci* **22**, 289–296 (2019).
8. D'Angelo, E. & Casali, S. Seeking a unified framework for cerebellar function and dysfunction: from circuit operations to cognition. *Front. Neural Circuits* **6**, (2013).
9. D'Angelo, E. The cerebellum gets social. *Science* **363**, 229–229 (2019).
10. Ramnani, N. Automatic and Controlled Processing in the Corticocerebellar System. in *Cerebellar Learning* 255–285 (Elsevier, 2014).
11. Cayco-Gajic, N. A. & Silver, R. A. Re-evaluating Circuit Mechanisms Underlying Pattern Separation. *Neuron* **101**, 584–602 (2019).

12. Bar-Gad, I., Morris, G. & Bergman, H. Information processing, dimensionality reduction and reinforcement learning in the basal ganglia. *Progress in Neurobiology* **71**, 439–473 (2003).

13. Wilson, C. J. Active decorrelation in the basal ganglia. *Neuroscience* **250**, 467–482 (2013).

14. Kuramoto, E. *et al.* Two types of thalamocortical projections from the motor thalamic nuclei of the rat: a single neuron-tracing study using viral vectors. *Cerebral cortex (New York, N.Y. : 1991)* **19**, 2065–2077 (2009).

15. Preuss, T. M. & Wise, S. P. Evolution of prefrontal cortex. *Neuropsychopharmacol.* **47**, 3–19 (2022).

16. Khilkevich, A., Zambrano, J., Richards, M.-M. & Mauk, M. D. Cerebellar implementation of movement sequences through feedback. *Elife* **7**, e06262 (2018).

17. Palesi, F. *et al.* Contralateral cortico-ponto-cerebellar pathways reconstruction in humans in vivo: implications for reciprocal cerebro-cerebellar structural connectivity in motor and non-motor areas. *Sci Rep* **7**, 12841 (2017).

18. Palesi, F. *et al.* Contralateral cerebello-thalamo-cortical pathways with prominent involvement of associative areas in humans in vivo. *Brain Struct Funct* **220**, 3369–3384 (2015).

19. Palesi, F. *et al.* The Importance of Cerebellar Connectivity on Simulated Brain Dynamics. *Front. Cell. Neurosci.* **14**, 240 (2020).

20. Castellazzi, G. *et al.* A comprehensive assessment of resting state networks: bidirectional modification of functional integrity in cerebro-cerebellar networks in dementia. *Front. Neurosci.* **8**, (2014).

21. Castellazzi, G. *et al.* Prominent Changes in Cerebro-Cerebellar Functional Connectivity During Continuous Cognitive Processing. *Front. Cell. Neurosci.* **12**, 331 (2018).

22. Casiraghi, L. *et al.* I See Your Effort: Force-Related BOLD Effects in an Extended Action Execution–Observation Network Involving the Cerebellum. *Cerebral Cortex* **29**, 1351–1368 (2019).

23. Balsters, J. H. & Ramnani, N. Cerebellar plasticity and the automation of first-order rules. *The Journal of neuroscience : the official journal of the Society for Neuroscience* **31**, 2305–2312 (2011).

24. Alahmadi, A. A. S. *et al.* Complex motor task associated with non-linear BOLD responses in cerebro-cortical areas and cerebellum. *Brain Struct Funct* **221**, 2443–2458 (2016).

25. Papegaaij, S. *et al.* Neural correlates of motor-cognitive dual-tasking in young and old adults. *PLoS ONE* **12**, e0189025 (2017).

26. Shine, J. M. The thalamus integrates the macrosystems of the brain to facilitate complex, adaptive brain network dynamics. *Progress in Neurobiology* 101951 (2020) doi:10.1016/j.pneurobio.2020.101951.

27. Shine, J. M. & Shine, R. Delegation to automaticity: the driving force for cognitive evolution? *Frontiers in Neuroscience* **8**, (2014).

28. Shine, J. M. *et al.* Estimation of dynamic functional connectivity using Multiplication of Temporal Derivatives. *NeuroImage* **122**, 399–407 (2015).

29. Diedrichsen, J. A spatially unbiased atlas template of the human cerebellum. *NeuroImage* **33**, 127–138 (2006).

30. Schaefer, A. *et al.* Local-Global Parcellation of the Human Cerebral Cortex from Intrinsic Functional Connectivity MRI. *Cerebral cortex (New York, N.Y. : 1991)* **28**, 3095–3114 (2018).

31. Ilg, W. *et al.* Effects of cerebellar lesions on working memory interacting with motor tasks of different complexities. *Journal of Neurophysiology* **110**, 2337–2349 (2013).

32. Mohr, H. *et al.* Integration and segregation of large-scale brain networks during short-term task automatization. *Nature communications* **7**, 13217 (2016).

33. Bassett, D. S., Yang, M., Wymbs, N. F. & Grafton, S. T. Learning-induced autonomy of sensorimotor systems. *Nature Neuroscience* **18**, 744–751 (2015).

34. Shine, J. M. & Poldrack, R. A. Principles of dynamic network reconfiguration across diverse brain states. *NeuroImage* **180**, 396–405 (2017).

35. Shine, J. M. *et al.* The Dynamics of Functional Brain Networks: Integrated Network States during Cognitive Task Performance. *Neuron* **92**, 544–554 (2016).

36. D'Angelo, E. *et al.* Distributed Circuit Plasticity: New Clues for the Cerebellar Mechanisms of Learning. *Cerebellum* **15**, 139–151 (2016).

37. Cole, M. W., Ito, T., Bassett, D. S. & Schultz, D. H. Activity flow over resting-state networks shapes cognitive task activations. *Nature Neuroscience* (2016).

38. Ramnani, N. The primate cortico-cerebellar system: anatomy and function. *Nature Reviews Neuroscience* **7**, 511–522 (2006).

39. Prevosto, V. & Sommer, M. A. Cognitive control of movement via the cerebellar-recipient thalamus. *Frontiers in systems neuroscience* **7**, 56 (2013).

40. Pezzulo, G. & Cisek, P. Navigating the Affordance Landscape: Feedback Control as a Process Model of Behavior and Cognition. *Trends in Cognitive Sciences* **20**, 414–424 (2016).

41. Wu, T., Liu, J., Hallett, M., Zheng, Z. & Chan, P. Cerebellum and integration of neural networks in dual-task processing. *NeuroImage* **65**, 466–475 (2013).

42. Kratochwil, C. F., Maheshwari, U. & Rijli, F. M. The Long Journey of Pontine Nuclei Neurons: From Rhombic Lip to Cortico-Ponto-Cerebellar Circuitry. *Frontiers in neural circuits* **11**, 33 (2017).

43. Nashef, A., Cohen, O., Perlmutter, S. I. & Prut, Y. A cerebellar origin of feedforward inhibition to the motor cortex in non-human primates. *Cell Reports* **39**, 110803 (2022).

44. Sergent, C. & Dehaene, S. Is consciousness a gradual phenomenon? Evidence for an all-or-none bifurcation during the attentional blink. *Psychological science* (2004).

45. Cruzat, J. *et al.* The dynamics of human cognition: Increasing global integration coupled with decreasing segregation found using iEEG. *NeuroImage* **172**, 492–505 (2018).

46. Fransson, P., Schiffler, B. C. & Thompson, W. H. Brain network segregation and integration during an epoch-related working memory fMRI experiment. *NeuroImage* **178**, 147–161 (2018).

47. Hearne, L. J., Cocchi, L., Zalesky, A. & Mattingley, J. B. Reconfiguration of Brain Network Architectures between Resting-State and Complexity-Dependent Cognitive Reasoning. *The Journal of neuroscience : the official journal of the Society for Neuroscience* **37**, 8399–8411 (2017).

48. Mäki-Marttunen, V. Pupil-based States of Brain Integration across Cognitive States. *Neuroscience* **471**, 61–71 (2021).

49. Wainstein, G. *et al.* The ascending arousal system promotes optimal performance through mesoscale network integration in a visuospatial attentional task. *Network Neuroscience* **5**, 890–910 (2021).

50. Sadaghiani, S., Poline, J.-B., Kleinschmidt, A. & D'Esposito, M. Ongoing dynamics in large-scale functional connectivity predict perception. *Proceedings of the National Academy of Sciences of the United States of America* **112**, 8463–8468 (2015).

51. Sporns, O. Network attributes for segregation and integration in the human brain. *Current Opinion in Neurobiology* **23**, 162–171 (2013).

52. Shine, J. M. *et al.* Computational models link cellular mechanisms of neuromodulation to large-scale neural dynamics. *Nat Neurosci* **24**, 765–776 (2021).

53. Breton-Provencher, V., Drummond, G., Feng, J., Li, Y. & Sur, M. Spatiotemporal dynamics of norepinephrine during learned behavior. *Nature* **Ahead of Print**, (2022).

54. Pang, J. C., Robinson, P. A. & Aquino, K. M. Response-mode decomposition of spatio-temporal haemodynamics. *J. R. Soc. Interface.* **13**, 20160253 (2016).

55. Aquino, K. M., Robinson, P. A. & Drysdale, P. M. Spatiotemporal hemodynamic response functions derived from physiology. *J. Theor. Biol.* **347**, 118–136 (2014).

56. Attwell, D. & Iadecola, C. The neural basis of functional brain imaging signals. *Trends in Neurosciences* **25**, 621–625 (2002).

57. Moore, C. I. & Cao, R. The Hemo-Neural Hypothesis: On The Role of Blood Flow in Information Processing. *Journal of Neurophysiology* **99**, 2035–2047 (2008).

58. Caligiore, D. *et al.* Consensus Paper: Towards a Systems-Level View of Cerebellar Function: the Interplay Between Cerebellum, Basal Ganglia, and Cortex. *The Cerebellum* **16**, 203–229 (2016).

59. Person, A. L. & Raman, I. M. Purkinje neuron synchrony elicits time-locked spiking in the cerebellar nuclei. *Nature* **481**, 502–505 (2011).

60. Kostadinov, D., Beau, M., Pozo, M. B. & Häusser, M. Predictive and reactive reward signals conveyed by climbing fiber inputs to cerebellar Purkinje cells. *Nature Neuroscience* **2**, 338 (2019).

61. Caesar, K., Gold, L. & Lauritzen, M. Context sensitivity of activity-dependent increases in cerebral blood flow. *Proc. Natl. Acad. Sci. U.S.A.* **100**, 4239–4244 (2003).

62. Mathiesen, C., Caesar, K. & Lauritzen, M. Temporal coupling between neuronal activity and blood flow in rat cerebellar cortex as indicated by field potential analysis. *The Journal of Physiology* **523**, 235–246 (2000).

63. Diedrichsen, J., King, M., Hernandez-Castillo, C., Sereno, M. & Ivry, R. B. Universal Transform or Multiple Functionality? Understanding the Contribution of the Human Cerebellum across Task Domains. *Neuron* **102**, 918–928 (2019).

64. Thomsen, K., Piilgaard, H., Gjedde, A., Bonvento, G. & Lauritzen, M. Principal Cell Spiking, Postsynaptic Excitation, and Oxygen Consumption in the Rat Cerebellar Cortex. *Journal of Neurophysiology* **102**, 1503–1512 (2009).

65. Callu, D., Lopez, J. & El Massioui, N. Cerebellar deep nuclei involvement in cognitive adaptation and automaticity. *Learn. Mem.* **20**, 344–347 (2013).

66. Just, M. A. *et al.* Interdependence of Nonoverlapping Cortical Systems in Dual Cognitive Tasks. *NeuroImage* **14**, 417–426 (2001).

67. Michael, E. B., Keller, T. A., Carpenter, P. A. & Just, M. A. fMRI investigation of sentence comprehension by eye and by ear: Modality fingerprints on cognitive processes. *Hum. Brain Mapp.* **13**, 239–252 (2001).

68. Whelan, R. R. Neuroimaging of cognitive load in instructional multimedia. *Educational Research Review* **2**, 1–12 (2007).

69. Fischer, R. & Plessow, F. Efficient multitasking: parallel versus serial processing of multiple tasks. *Front. Psychol.* **6**, (2015).

70. Feinberg, D. A. *et al.* Multiplexed Echo Planar Imaging for Sub-Second Whole Brain FMRI and Fast Diffusion Imaging. *PLoS ONE* **5**, e15710 (2010).

71. Power, J. D. *et al.* Methods to detect, characterize, and remove motion artifact in resting state fMRI. *NeuroImage* **84**, 320–41 (2014).

72. Rubinov, M. & Sporns, O. Complex network measures of brain connectivity: Uses and interpretations. *NeuroImage* **52**, 1059–1069 (2010).

73. Jeurissen, B., Tournier, J.-D., Dhollander, T., Connelly, A. & Sijbers, J. Multi-tissue constrained spherical deconvolution for improved analysis of multi-shell diffusion MRI data. *NeuroImage* **103**, 411–426 (2014).

74. Tournier, J.-D., Calamante, F., Gadian, D. G. & Connelly, A. Direct estimation of the fiber orientation density function from diffusion-weighted MRI data using spherical deconvolution. *NeuroImage* **23**, 1176–1185 (2004).

75. Tournier, J.-D., Calamante, F. & Connelly, A. Robust determination of the fibre orientation distribution in diffusion MRI: Non-negativity constrained super-resolved spherical deconvolution. *NeuroImage* **35**, 1459–1472 (2007).

76. Civier, O., Smith, R. E., Yeh, C.-H., Connelly, A. & Calamante, F. Is removal of weak connections necessary for graph-theoretical analysis of dense weighted structural connectomes from diffusion MRI? *NeuroImage* **194**, 68–81 (2019).

77. Tournier, J.-D., Calamante, F. & Connelly, A. MRtrix: Diffusion tractography in crossing fiber regions. *Int. J. Imaging Syst. Technol.* **22**, 53–66 (2012).

78. Tournier, J.-D. *et al.* MRtrix3: A fast, flexible and open software framework for medical image processing and visualisation. *NeuroImage* **202**, 116137 (2019).

79. Smith, R. E., Tournier, J.-D., Calamante, F. & Connelly, A. Anatomically-constrained tractography: Improved diffusion MRI streamlines tractography through effective use of anatomical information. *NeuroImage* **62**, 1924–1938 (2012).

80. Smith, S. M. *et al.* Advances in functional and structural MR image analysis and implementation as FSL. *NeuroImage* **23**, S208–S219 (2004).

81. Palesi, F. *et al.* Motor and higher-order functions topography of the human dentate nuclei identified with tractography and clustering methods. *Hum Brain Mapp* **42**, 4348–4361 (2021).

82. Abos, A. *et al.* Differentiation of multiple system atrophy from Parkinson's disease by structural connectivity derived from probabilistic tractography. *Sci Rep* **9**, 16488 (2019).

83. Nichols, T. E. & Holmes, A. P. Nonparametric permutation tests for functional neuroimaging: a primer with examples. *Human Brain Mapping* **15**, 1–25 (2002).

Appendix V:

Abnormal Higher-Order Network Interactions in Parkinson's Disease Visual Hallucinations

Joshua B. Tan[1], Eli J. Müller[1,2], Isabella F. Orlando[1], Natasha L. Taylor[1], Daniel S. Margulies[3,4], Jennifer Szeto[1], Simon J.G. Lewis[1], James M. Shine[1,2], Claire O'Callaghan[1]

Author affiliations:

1 Brain and Mind Centre, School of Medical Sciences, Faculty of Medicine and Health, University of Sydney, Sydney, Australia
2 Centre for Complex Systems, School of Physics, University of Sydney, Sydney, Australia
3 Integrative Neuroscience and Cognition Center, Center National de la Recherche Scientifique (CNRS) and Université de Paris, Paris, France
4 Max Planck Research Group for Neuroanatomy and Connectivity, Max Planck Institute for Human Cognitive and Brain Sciences, Leipzig, Germany

Chapter 5 of this thesis is published as: Tan, J. B., Müller, E. J., Orlando, I. F., Taylor, N. L., Margulies, D. S., Szeto, J., Lewis, S. J. G., Shine, J. M., & O'Callaghan, C. (2023). Abnormal higher-order network interactions in Parkinson's disease visual hallucinations. *Brain.* https://doi.org/10.1093/brain/awad305

Abbreviations: 5-HT = 5-hydoxytryptamine; DAN = dorsal attention network; DDE = dopaminergic dose equivalent; DMN = default mode network; DST = Digit Span Test; fMRI = functional magnetic resonance imaging; FPC = frontoparietal control network; HADS = Hospital Anxiety and Depression Scale; LIM = limbic network; LM = Logical Memory; MDS-UPDRS = Movement Disorder Society-Sponsored Revision of the Unified Parkinson's Disease Rating Scale; MICE = Multivariate Imputation via Chained Equations; MMSE = Mini-Mental State Examination; MoCA = Montreal Cognitive Assessment; PCA = Principal Component Analysis; PD+VH = Parkinson's disease with visual hallucinations; PD-VH = Parkinson's disease without visual hallucinations; PsycH-Q = Psychosis and Hallucinations Questionnaire; SCOPA-PC = Scales for Outcomes in Parkinson's Disease - Psychiatric Complications; SOM = somatomotor network; TMT = Trail Making Test; t-SNE = t-distributed Stochastic Neighbour Embedding; VAN = ventral attention network; VIS = visual network.

Abstract

Visual hallucinations in Parkinson's disease can be viewed from a systems-level perspective, whereby dysfunctional communication between brain networks responsible for perception predisposes a person to hallucinate. To this end, abnormal functional interactions between higher-order and primary sensory networks have been implicated in the pathophysiology of visual hallucinations in Parkinson's disease, however the precise signatures remain to be determined. Dimensionality reduction techniques offer a novel means for simplifying the interpretation of multidimensional brain imaging data, identifying hierarchical patterns in the data that are driven by both within- and between- functional network changes. Here, we applied two complementary non-linear dimensionality reduction techniques – diffusion-map embedding and t-distributed Stochastic Neighbour Embedding (t-SNE) – to resting state fMRI data, in order to characterise the altered functional hierarchy associated with susceptibility to visual hallucinations. Our study involved 77 people with Parkinson's disease (31 with hallucinations; 46 without hallucinations) and 19 age-matched healthy controls. In patients with visual hallucinations, we found compression of the unimodal-heteromodal gradient consistent with increased functional integration between sensory and higher order networks. This was mirrored in a traditional functional connectivity analysis, which showed increased connectivity between the visual and default-mode networks in the hallucinating group. Together, these results suggest a route by which higher-order regions may have excessive influence over earlier sensory processes, as proposed by theoretical models of hallucinations across disorders. By contrast, the t-SNE analysis identified distinct alterations in prefrontal regions, suggesting an additional layer of complexity in the functional brain network abnormalities implicated in hallucinations, which was not apparent in traditional functional connectivity analyses. Together, the results confirm abnormal brain organisation associated with the hallucinating phenotype in Parkinson's disease and highlight the utility of applying convergent dimensionality reduction techniques to investigate complex clinical symptoms. In addition, the patterns we describe in Parkinson's disease converge with those seen in other conditions, suggesting that reduced hierarchical differentiation across sensory-perceptual systems may be a common transdiagnostic vulnerability in neuropsychiatric disorders with perceptual disturbances.

Introduction

Veridical perception requires the ability to interact with and process a continuous stream of sensory information. These interactions rely on associations developed over time, whereby perceptual interpretations are informed by matching sensory inputs with statistics learned about features of the external environment (Collerton et al., 2005; Hardstone et al., 2021). In this framework, hallucinations are proposed to occur due to an imbalance between higher-order ("top-down") vs. sensory ("bottom-up") processes (C. D. Gilbert & Li, 2013; O'Callaghan, Kveraga, et al., 2017; Powers et al., 2016; Thomas et al., 2022). More concretely, hallucinations have been proposed to arise due to disruptions across networks involved in higher-order perceptual processing (i.e., attentional networks, the default mode network) and primary sensory networks (Powers et al., 2016; Shine et al., 2014). In clinical populations with visual hallucinations, including Parkinson's disease and Lewy body dementia, abnormal interactions within and between these networks have been consistently observed (O'Callaghan, Firbank, et al., 2021; Shine et al., 2014; Shine, Keogh, et al., 2015; Thomas et al., 2022). In this way, a systems-level perspective that focuses on dysfunctional patterns of communication between brain networks can provide insight into the neural signatures of visual hallucinations.

Tracking neural activity during hallucinatory episodes is notoriously difficult, but trait-level signatures of the tendency to hallucinate can be explored using structural imaging or resting state fMRI (Okuneye et al., 2020; Rollins et al., 2019; Spinosa et al., 2022). These approaches identify patterns of abnormal brain structure, activity or connectivity associated with the hallucinating phenotype, which are presumably implicated in hallucinatory events. For example, the network abnormalities observed during fMRI of hallucination-like events in Parkinson's disease overlaps with trait-level network abnormalities observed in the resting state (Shine, Keogh, et al., 2015; Shine, Muller, et al., 2015; Walpola et al., 2020). However, one challenge is that resting state fMRI patterns are inherently high-dimensional – i.e., the data has an extensive and unwieldy number of features – which poses issues for interpretability and reproducibility. A tractable way to handle this complexity is to apply dimensionality reduction techniques, which are algorithms that extract latent components from high-dimensional data while preserving relationships of the original data (Cunningham & Yu, 2014) and discarding more idiosyncratic features (Cunningham & Yu, 2014; Shine, Hearne, et al., 2019). This approach offers a means of summarising feature-rich data into components that can then be more meaningfully related to symptoms and behaviour.

One popular method for reducing dimensionality is diffusion map embedding – a non-linear dimensionality reduction technique, which projects high-dimensional data into an n-dimensional gradient space where n ≤ the number of data points (Coifman et al., 2005; Vos de Wael et al., 2020). In the case of resting-state fMRI, the resulting "map" of brain activity represents the global connectivity structure as a distribution of cortical nodes: nodes that share stronger connections are grouped closer together, whereas nodes that do not share connections are grouped further apart (Haak et al., 2018; Langs et al., 2015). Diffusion map embedding has been used to demonstrate a key organisational principle in healthy human brains that links "bottom-up", sensory (unimodal) regions with "top-down", higher-order (heteromodal) cortical areas along a primary gradient (Huntenburg et al., 2018; Margulies et al., 2016).

The unimodal-heteromodal gradient is widely replicated across studies and populations (Huntenburg et al., 2018; Margulies et al., 2016), and is sensitive to age-related changes (Bethlehem et al., 2020) and clinical conditions, including autism (Hong et al., 2019) and schizophrenia (Dong et al., 2021). Specifically, a reduced separation (i.e., a compression) along the gradient between sensory and higher-order regions is seen in neuropsychiatric patient groups relative to controls (Dong et al., 2021; Hong et al., 2019). In Parkinson's disease, this unimodal-heteromodal gradient has been shown to be compressed in patients with visual dysfunction (Zarkali et al., 2021). It follows that increased functional integration between previously well-separated sensory and higher-order regions (i.e., primary sensory and default mode regions) may reflect abnormal interactions between such regions. These changes could potentially disturb perceptual processes, allowing for an increased influence from higher-order regions over lower-level sensory processes – increasing the vulnerability to hallucinate. Taken together, changes in the hierarchical organisation of the unimodal-heteromodal gradient may serve as a transdiagnostic feature across neuropsychiatric disorders. In turn, alterations in this unimodal-heteromodal gradient organisation may be an underlying feature that helps explain the network disruptions observed in Parkinson's disease patients prone to visual hallucinations.

A pitfall of dimensionality reduction techniques is that they require simplifying assumptions, which can obscure interpretation of the underlying functional neuroanatomy. One solution is to use multiple approaches, each with their own strengths and weaknesses, to converge on a plausible interpretation of the data. In contrast to diffusion map embedding, t-distributed Stochastic Neighbour Embedding (t-SNE) (Böhm et al., 2021; Kobak & Berens, 2019) computes a similarity score between all data points in a high-dimensional space, and then maps

these similarities into a lower (typically 2-3) dimensional space. In this way, t-SNE allows for visual interrogation of network organisation (Arora et al., 2018; van der Maaten, 2013), while conserving the relationships between data points (Belkina et al., 2019; van der Maaten, 2013), albeit in a different way than diffusion-map embedding that is potentially more sensitive to non-linear reconfigurations in network architecture (i.e., t-SNE captures both local and global features, whereas diffusion map embedding only focuses on local features). Combining diffusion-map embedding and t-SNE thus has the potential to expose the higher-order organisation of resting-state networks and offer unique insights into the changes in network topology brought on by neurodegenerative disease processes.

Here, we combine diffusion map embedding and t-SNE to determine the low-dimensional signature of the tendency to hallucinate in individuals with Parkinson's disease. To do so, we analysed resting-state fMRI data from Parkinson's disease patients with visual hallucinations compared to those without, along with age-matched healthy controls. We hypothesised that patients with visual hallucinations would show compression in their unimodal-heteromodal gradient, and the extent of gradient compression would be associated with cognitive decline. We also predicted that compression in the gradient would be complemented by a decreased distance between subsets of the whole-brain network as detected through t-SNE analysis.

Materials and methods

Case Selection

A total of 96 individuals were recruited from the Parkinson's disease Research Clinic at the Brain and Mind Centre, University of Sydney, Australia, including 19 healthy controls and 77 people diagnosed with idiopathic Parkinson's disease. All Parkinson's disease patients satisfied the United Kingdom Parkinson's Disease Society Brain Bank criteria and did not meet criteria for dementia (Martinez-Martin et al., 2011). Parkinson's disease symptoms were assessed with the Movement Disorder Society-Sponsored Revision of the Unified Parkinson's Disease Rating Scale (MDS-UPDRS) (Goetz et al., 2008). Patients with visual hallucinations were identified from a positive response to question two of the MDS-UPDRS (i.e., "Over the past week have you seen, heard, smelled, or felt things that were not really there? If yes, examiner asks the patient or caregiver to elaborate and probes for information"). Individuals scoring ≥1 on this item, with a subsequent description consistent with visual hallucinatory phenomena, were

included in the hallucinating group. Thirty-one patients were identified as experiencing visual hallucinations and 46 did not experience visual hallucinations. All patients were tested on their regular dopamine medications and a dopaminergic dose equivalent (DDE) score was calculated (mg dopamine/per day) (C. L. Tomlinson et al., 2010). Psychiatric symptoms were screened using the Scales for Outcomes in Parkinson's Disease - Psychiatric Complications (SCOPA-PC) (Visser et al., 2007), and as part of a related study a subset of 47 patients (20 with hallucinations, 27 without) underwent the Psychosis and Hallucinations Questionnaire (PsycH-Q) (Shine, Mills, et al., 2015).

Neuropsychological and behavioural assessments

Global cognition was assessed via the Mini-Mental State Examination (MMSE) (Folstein, 1983) and Montreal Cognitive Assessment (MoCA) (Nasreddine et al., 2005). The Trail Making Test parts A and B (TMT-A, TMT-B) measured psychomotor speed and attentional set shifting capacity (TMT-B minus TMT-A) (Bowie & Harvey, 2006). Working memory maintenance and manipulation was assessed using the Digit Span Test (Wechsler, 1977), consisting of two parts: digit spans forwards and backwards, which were summed to create a digit span total score (Digit Span Total; DST). Memory was assessed via the percentage of a short story correctly recalled after 30 minutes (Logical Memory retention: LM Retention) (Wechsler, 1977).

Statistical analysis

Demographic analyses were performed in R version 4.2.1 (2022). For missing scores in the cognitive dataset, data imputation was conducted using Multivariate Imputation via Chained Equations (MICE) from the 'mice' package (van Buuren, 2021). As the missing values all belonged to quantitative variables, predictive mean matching was used. A detailed breakdown of the distribution spread for missing scores is presented in the Supplementary Material. For all analyses, the group comparisons focused on the Parkinson's disease group as a whole versus controls (PD vs. controls) and within the Parkinson's group, hallucinators versus non-hallucinators (PD+VH vs. PD–VH). Group comparisons were conducted through non-parametric permutation testing (5000 permutations) which provide a control for family-wise error rate (Camargo et al., 2008; Nichols & Holmes, 2001).

MRI acquisition

All 96 individuals underwent magnetic resonance imaging (MRI) on a 3-Tesla MRI scanner (GE medical systems), generating T1-weighted structural images and resting-state blood-oxygenation level dependent (BOLD) functional scans (rsfMRI). Sagittal 3D T1w were acquired using a 256 × 256 matrix, 200 slices, slice thickness of 1 mm, echo time/repetition time = 2.7/7.2 ms. Functional images were acquired with repetition time = 3 s, echo time = 36 ms, flip angle = 90º, 32 axial slices covering the whole brain, field of view = 220 mm, slice thickness of 3 mm, raw voxel size = 3.9 mm × 3.9 mm × 4 mm, and 140 repetition times (scanning duration of 7 min). Individuals were instructed to lie awake with their eyes open.

MRI preprocessing

Scans were converted into the Brain Imaging Data Structure (Gorgolewski et al., 2016) format using the dicm2nii (Li, 2022) and dicm2niix (Li et al., 2016) toolboxes. Preprocessing was completed using *fMRIPrep* 20.2.3 (Esteban et al., 2019), a standard pipeline that incorporates toolboxes from the gold-standard preprocessing software in the field. *fMRIPrep* involves the basic preprocessing steps (coregistration, normalisation, unwarping, noise component extraction, segmentation, skullstripping etc.) and produces a report for quality checking at each step. See Supplementary Material for a full description of each step.

Denoising

The confounds timeseries data extracted from *fMRIprep* were passed through *fmridenoise* (Finc et al., 2019) specifying eight physiological signals to be regressed (mean physiological signals from white matter and cerebrospinal fluid, and their quadratic terms (Satterthwaite et al., 2013)), with high-pass and low-pass band filters set at 0.01 and 0.1 respectively.

Gradient connectivity analysis

Mean BOLD signal time-series data were extracted from the rsfMRI data for 400 cortical regions from the Schaefer atlas - a robust parcellation that reveals meaningful neurobiological features, with parcels that share relatively homogenous functional connectivity patterns, thus making them well suited to dimensionality reduction techniques (Schaefer et al., 2018). The time-series data was z-scored, using MATLAB scripts adapted from the fieldtrip toolbox (Oostenveld et al., 2011). A functional connectivity matrix was calculated for each individual using Pearson correlation values, producing a 400 × 400 matrix that represented cortical-

cortical functional connectivity. These 400 cortical regions were assigned to 7 resting state networks (Yeo et al., 2011), allowing for comparisons between the cortical regions and large-scale cortical networks (Schaefer et al., 2018).

Gradient analysis was performed using the *Brainspace* toolbox and custom MATLAB scripts (Vos de Wael et al., 2020). First, a population average connectivity matrix was calculated using the extracted timeseries data from all the individual 400 × 400 connectivity matrices. The average matrix was thresholded, with the top 10% of measurements per row retained and all remaining measurements zeroed. An affinity matrix was then computed using the normalised angle method – this reflected the similarity of connectivity profiles between each pair of regions. Then, diffusion map embedding was used to simplify the high-dimensional nature of the data into lower dimensions, allowing for components to be generated in descending order from highest to lowest variance explained. The density of sampling points was controlled through the parameter $\alpha = 0.5$, following recommendations from previous studies, retaining global relations between the data points in the embedded space (Langs et al., 2015; Vos de Wael et al., 2020).

Gradient components were calculated for each individual using the same parameters as the group-level average gradient. Individual gradients were then aligned to the group-level gradient using Procrustes alignment (Langs et al., 2015), allowing for more accurate comparisons across individuals. The first and second gradients which explained most variance in the data (14% and 12%, respectively) were extracted and compared against the presumed network hierarchy as a comparison against the principal gradient described by Margulies and colleagues (Margulies et al., 2016; Mesulam, 1998; Zarkali et al., 2021).

Comparison of unimodal-heteromodal gradient with behavioural data

To determine whether changes in the gradient score were associated with cognitive performance, for each individual we calculated the average gradient score for each network in the Yeo 7-network atlas (Yeo et al., 2011). We focused on networks significantly different between the three groups in our cohort (i.e., visual, ventral attentional, and frontoparietal control) and correlated those network gradient scores with clinical scores that were significantly different between the patient groups (i.e., TMT-B and HADS).

t-Stochastic Neighbour Embedding (t-SNE) analysis

The t-SNE algorithm in MATLAB (*Tsne: T-Distributed Stochastic Neighbor Embedding*, 2016) was used to construct 3-dimensional embeddings of each individual functional connectivity matrix. Before running the data through the t-SNE algorithm, the data underwent a principal component analysis (PCA) initialisation step in which the top 3 components were selected (Kobak & Linderman, 2021). This resulted in a 400 × 3 matrix where each of the 400 cortical regions was described by x-y-z coordinates. The algorithm was run for 1,000 iterations using the Barnes-Hut algorithm which performs an approximate optimisation. The distance metric was set to "Euclidean"; perplexity = 90; learning rate = 500; exaggeration = 50 for the first 99 optimisations to facilitate cluster formation (Belkina et al., 2019). For specific details regarding the choice of parameter values refer to the Supplementary Materials. A t-SNE map was generated for each individual using the parameters specified above. For each individual t-SNE map, the Euclidean distance was calculated between each pair of cortical regions generating a "distance map" that described how far each region was from every other region (400 × 400 matrix).

Comparing functional connectivity and t-SNE analysis

To compare functional connectivity maps between the groups, we ran non-parametric permutation tests for each pairwise correlation value. This analysis was carried out twice: firstly, to compare edge differences between healthy individuals and Parkinson's disease patients (control vs. PD), and secondly to compare edge differences between patients with and without visual hallucinations (PD+VH vs. PD-VH**;** Figure 1). To isolate edge differences uniquely associated with visual hallucinations, we looked for non-overlapping significant edges between the two comparisons (subtracting PD+VH vs. PD-VH comparison from the control vs. PD comparison, Figure 1C). Edges with values of -1 were unique to the PD+VH vs. PD-VH comparison and visualised on the cortical surface. The same analysis was conducted on the t-SNE distance maps. Non-parametric tests were run for each correlation value (5,000 permutations; Figure 1) (Nichols & Holmes, 2001), comparing control vs. PD, and PD-VH vs. PD+VH. The PD-VH matrix was subtracted from the PD+VH matrix (Figure 1B minus Figure 1A) isolating edge differences unique to the PD-VH vs. PD+VH comparison (Figure 1C).

As a by-product of the above analysis, we noticed that group differences in the t-SNE distance maps appeared distinct from the group differences observed in the functional connectivity

matrices. To determine whether the t-SNE distance maps did in fact describe distinct patterns, we ran eigendecomposition on both the functional connectivity and t-SNE binary matrices (Figure 1A and Figure 1B). Eigenvectors describe core patterns that underlie the high-dimensional comparison matrix with the first eigenvector describing a principal pattern of group differences and explaining the most variance of the data. The first eigenvector of the t-SNE binary matrices was compared with the corresponding first eigenvector of the correlation binary matrices through spin permutation testing (5000 permutations) to determine whether there was a common underlying pattern found in both the t-SNE and correlation matrices.

Comparing t-SNE results with the unimodal-heteromodal gradient

To determine whether the binary matrices described different patterns to those observed in the unimodal-to-heteromodal gradients, we averaged both binary matrices of the PD-VH vs. PD+VH comparison across regions. This resulted in a vector for each binary matrix that described the proportion of edges that were different between groups. We then compared the edge vectors with the change in average gradient score across regions between Parkinson's disease patients with and without visual hallucinations with spin permutation tests (5000 permutations).

Given that the parcellation method can influence results (Arslan et al., 2018), we replicated the functional connectivity and t-SNE analysis using 200 cortical nodes from the Schaefer-200 atlas (Schaefer et al., 2018) (see Supplementary Materials for these results).

Data availability

All data and code required to reproduce the statistical analyses and figures are publicly available (https://github.com/ShineLabUSYD/PD_Hallucinations).

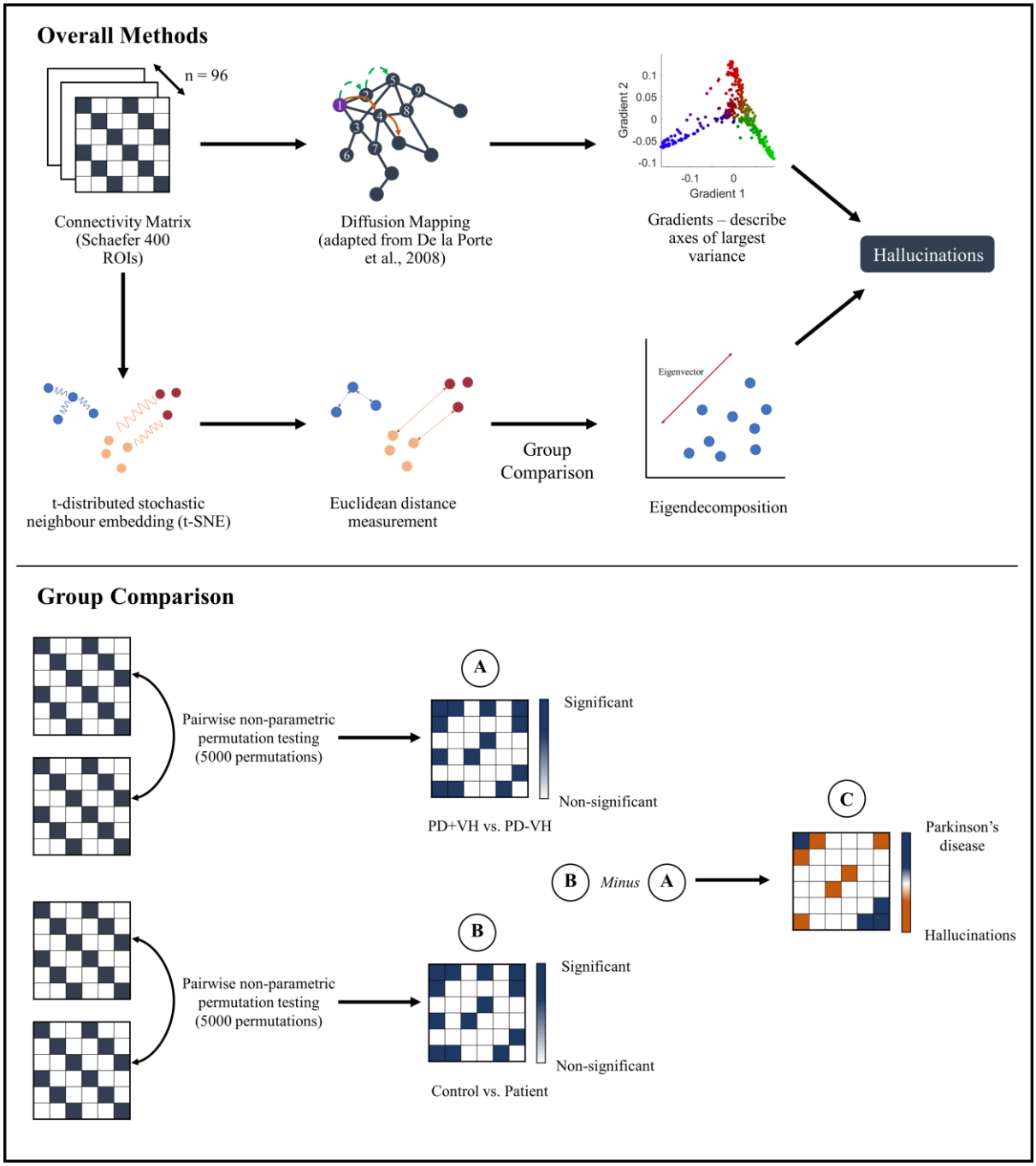

Figure 1 Summary of analyses conducted (top panel) and finding differences unique to hallucinations (bottom panel). A gradient map was constructed for each subject (n = 96) and group differences were analysed. A t-SNE map was also constructed for each subject (n = 96). Pairwise non-parametric permutation testing was used to find significant edge connections. Resulting in a binary matrix for each group comparison (A = PD+VH vs. PD-VH; B = Control vs. Patient) where 1 = significant, 0 = non-significant. Subtracting A from B results in matric C which differentiates between differences associated with hallucinations and other differences caused by Parkinson's disease (motor and cognitive). Eigenvectors summarising the key differences between groups were compared against each other. PD+VH = Parkinson's disease with visual hallucinations. PD-VH = Parkinson's disease without visual hallucinations.

Results

Demographic and clinical data

Demographic and clinical data was compared between patients and healthy controls, and within patients to compare hallucinators vs. non-hallucinators (Table 1). Sex ratio differed between the controls and overall patient group (t = 5.717, p = 0.017), but was equivalent in the hallucinating vs. non-hallucinating group (t = 0.589, p = 0.443). All the groups were matched for age and years of education, as well as for scores on the Montreal Cognitive Assessment, Logical Memory retention, and Trail-Making B-A score (p > 0.05). Performance in the Parkinson's disease group was reduced relative to controls on some cognitive assessments, including the Mini-Mental State Examination (t = 2.962, p = 0.015), the Digit Span Task (t = 2.271, p = 0.033), and Part A of the Trail-Making test (t = 2.731, p = 0.016). The within-Parkinson's groups were matched for daily dopamine dose (DDE), disease duration, motor assessments (UPDRS-III, UPDRS-IV), Hoehn and Yahr scale, and the SCOPA-PC (p > 0.05). However, patients with visual hallucinations performed worse than non-hallucinating patients in Part B of the Trail-Making test (t = 2.305, p = 0.022), they reported a higher burden of daily motor problems (UDPRS-II; t = -3.836, p < 0.001), and they endorsed more severe mood symptoms on the Hospital Anxiety and Depression Scale (t = -2.636, p = 0.011). There was a significant difference in total PsycH-Q scores, as patients with hallucinations had a higher burden of symptoms (t = 2.8081, p = 0.007). For a detailed breakdown of PsycH-Q subscales, refer to the Supplementary Materials.

Table 1 Summary of statistical differences between group demographics

	PD – VH (n = 46)			**PD + VH (n = 31)**			**PD – VH vs PD + VH**
	n	Mean	SD	n	Mean	SD	p-value
Gender (Male:Female)	36:10			21:10			0.443
Age		65.5	9.41		66.8	6.08	0.444
Years of Education		14.6	2.95		13.7	3.38	0.234
MMSE		28.7	1.71		28.4	2.06	0.483
MoCA		27.1	2.95		26.5	2.95	0.326
Digit Span		10.9	2.84		11.5	2.91	0.404
LM Retention		11.6	2.88		11.5	3.25	0.930
TMT A z-score		0.251	0.823		-0.289	1.35	0.053
TMT B z-score		0.133	0.851		-0.591	1.61	**0.022**
TMT B-A z-score		-0.111	0.84		-0.213	1.17	0.195
HADS		6.13	4.77		10	7.17	**0.011**
UPDRS							
Section II		8.26	6.41		15	8.25	**0.0004**
Section III		25.7	14.5		30.7	14.5	0.143
Section IV		0.804	1.87		1.65	2.99	0.172
Hoehn and Yahr		1.93	0.574		2.15	0.503	0.096
SCOPA-PC		1.89	2.20		2.97	2.69	0.072
DDE		620	396		706	520	0.4511
PsycH-Q (20 PD+VH, 27 PD-VH)		6.07	5.69		13.2	10.3	**0.007**
Disease Duration (Years)		5	4.5		6	3.5	0.2953

PD-VH = Parkinson's disease without visual hallucinations. PD+VH = Parkinson's disease with visual hallucinations. MMSE = Mini-Mental State Examination total score. MoCA = Montreal Cognitive Assessment total score. SCOPA-PC = Scales for Outcomes in Parkinson's disease - Psychiatric Complications total score. LM Retention = Logical Memory Retention score. TMT A, TMT B are the z-scored trail-making test results. TMT B-A is the difference between TMT B and A and has been z-scored. HADS = Hospital and Anxiety Depression Scale total score. UPDRS = Unified Parkinson's Disease Rating Scale. Hoehn and Yahr total score. PsycH-Q = Psychosis and Hallucinations Questionnaire**.** Sex comparisons were conducted using chi-square tests. All the continuous variables underwent pairwise comparisons with non-parametric permutation testing of the mean score. Significant p-values are in bold ($p < 0.05$). Section I of the UPDRS questionnaire as part of the questionnaire (Q2) was used to separate the patients into PD+VH and PD-VH groups. For comparisons and summary statistics of control participants, refer to Supplementary Material.

Functional connectivity nuisance variables

The Parkinson's disease group as a whole had more head movements during scanning compared to controls, as indicated by higher framewise displacement (t = -3.486, p < 0.001), however there was no difference between patients with and without visual hallucinations (t = -1.414, p = 0.157). There was no significant correlation between participants' head movement and average gradient score (r = 0.053, p = 0.607).

Gradient connectivity analysis

The first gradient explained 14% of the variance and was anchored by the visual cortex at the lower end and the primary motor cortex at the upper end (Figure 2A). This gradient differed from the well-established unimodal-heteromodal gradient identified by Margulies and colleagues (Margulies et al., 2016) and it was not significantly correlated with the presumed brain network hierarchical organisation (r = 0.07, p = 0.16; Figure 2B) (Margulies et al., 2016). However, the second gradient, which explained 12% variance, did demonstrate a unimodal-heteromodal axis (Figure 2C) and was significantly correlated with network hierarchy organisation (r = 0.75; p < 0.05; Figure 2D). Therefore, we used the second gradient for our subsequent analyses concerned with unimodal-heteromodal organisation principles.

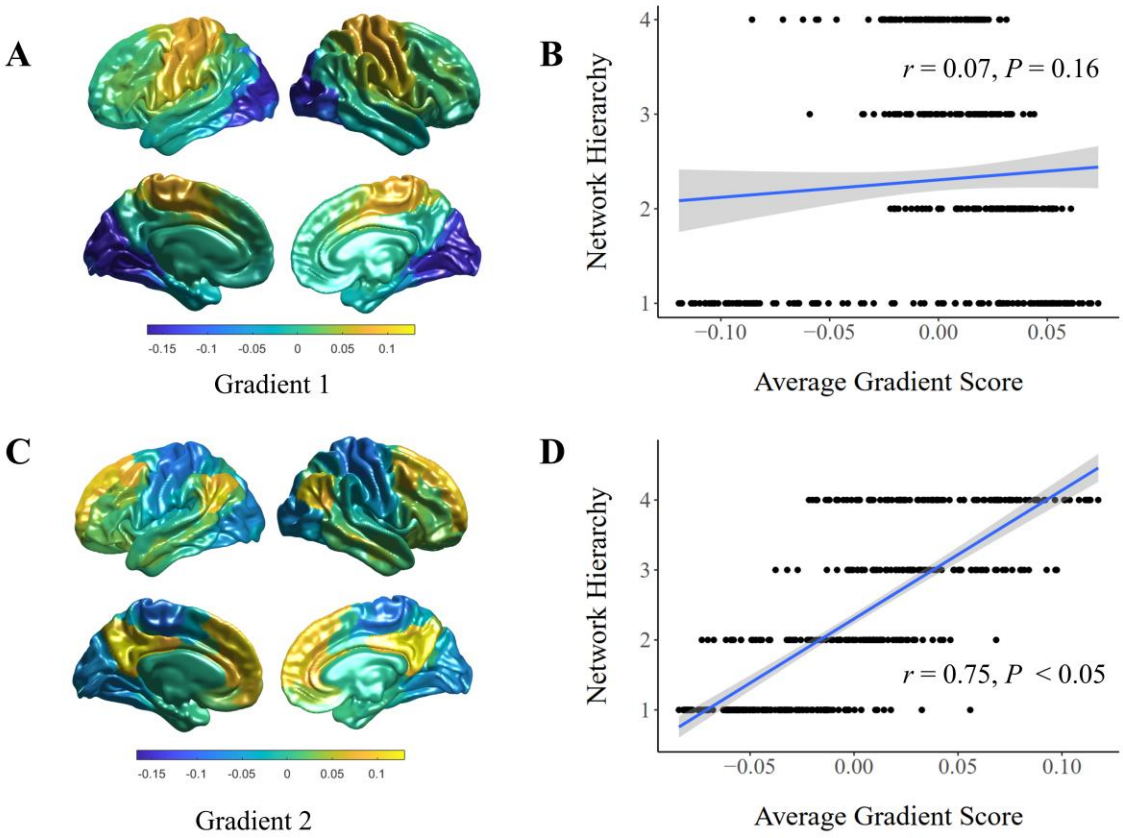

Figure 2 Comparison of gradients with network hierarchy organisation. **(A)** Population average of the first gradient that explains the most variance (14%). **(B)** First gradient score assigned to Yeo's 7-network atlas and organised into proposed network hierarchy (1 = visual, somatomotor; 2 = dorsal attention, salience ventral attention; 3 = limbic, frontoparietal control; 4 = default mode network). **(C)** Population average of the second gradient that explains 12% variance. **(D)** Second gradient score assigned to Yeo's 7-network atlas and organised into proposed network hierarchy.

Assessing the average gradient score distributions for each group (Figure 3A), all distributions were slightly right-skewed (*skewness* > 0), and they were also light-tailed – i.e., distribution of points were closer to the mean (*kurtosis* < 0). Distribution shape in the patient groups differed from controls (D = 0.057, p_{fdr} < 0.05), but was not significantly different between the hallucinating and non-hallucinating patient groups (D = 0.015, p_{fdr} = 0.06).

Group comparisons of gradient scores at the regional and network levels

Permutation testing was conducted at both the regional (n = 400) and network (n = 7) levels, comparing differences between Parkinson's disease patients against controls, and differences

between the Parkinson's disease groups. These results are shown in Figure 3B. Prominent differences between the patients and controls were observed in regions of the primary motor cortex ($p < 0.05$); differences were also found in regions from the extra-striate visual cortex and laterally in the temporal lobe ($p < 0.05$). Regions significantly different for patients with visual hallucinations consisted of regions near the temporoparietal junction ($p < 0.05$). For all these regions, the gradient score was higher in the disease groups. For a detailed breakdown of individual regions and p-values refer to the Supplementary Materials.

By assigning each of the 400 regions to the 7-network atlas (Yeo et al., 2011), we observed group differences at the network level (Figure 3C). Comparing controls and Parkinson's disease patients, the average gradient score significantly increased in patients for the visual and somatomotor networks ($p < 0.05$, *mean difference* = 0.007 and 0.008, respectively). In contrast, there were significant decreases in patients' gradient scores for the ventral attentional and frontoparietal control networks ($p < 0.05$, *mean difference* = -0.005 and -0.009, respectively). In Parkinson's disease patients with versus without visual hallucinations, significant gradient score differences were observed in the visual, ventral attention and frontoparietal control networks ($p < 0.05$). Patients with visual hallucinations had higher gradient scores in the visual network (*mean difference* = 0.003), and lower gradient scores in the ventral attention (*mean difference* = -0.005) and frontoparietal control networks (*mean difference* = -0.003). Overall, these results demonstrated reduced functional separation between sensory and higher-order networks along the unimodal-heteromodal axis in patients with visual hallucinations.

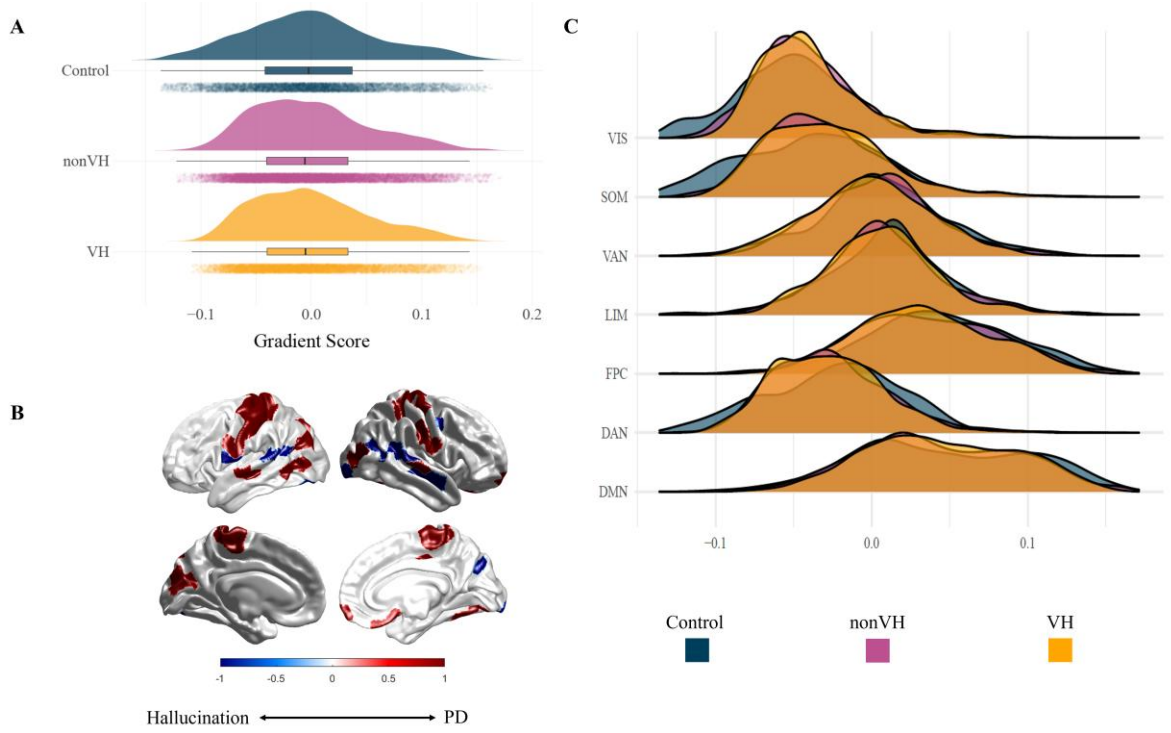

Figure 3 Group comparisons of gradient scores. (A) Distribution of average gradients score for each group. **(B)** Regions significantly different between groups. Values greater than 0 (red) refer to regions unique to Parkinson's disease patients. Values less than 0 (blue) were regions unique to Parkinson's disease patients with visual hallucinations. **(C)** Gradient score distributions across networks for each group**.** VIS = visual, SOM = somatomotor, VAN = ventral attention, LIM = limbic, FPC = frontoparietal control, DAN = dorsal attention, DMN = default mode network.

Relationship between average network gradient score, TMT-B and PsycH-Q

Average gradient scores of the visual, ventral attention, and frontoparietal control networks were compared against clinical scores that differed significantly between the groups. The ventral attention network average gradient score was significantly correlated to performance in the TMT-B (r = 0.210, p = 0.040) consistent with worse performance on the task being associated with gradient scores shifted towards the sensory regions. However, this result did not survive false discovery rate correction ($p_{fdr} > 0.05$). No other comparisons between these clinical measures and network gradient scores were significant ($p > 0.05$).

Group differences in functional connectivity

Functional connectivity comparisons between the Parkinson's disease and control groups showed increases within the somatomotor network and in edges connecting the somatomotor network with the visual, dorsal attention and default mode networks ($p < 0.05$). Specifically,

these were edges between the primary motor cortex to the extra-striate cortex, parietal lobe, and regions of the temporoparietal junction. There was also a significant increase in edges connecting regions of the somatomotor network with dorsal and lateral regions of the prefrontal cortex ($p < 0.05$). Comparing Parkinson's disease patients with and without visual hallucinations revealed a distinct pattern of increased connectivity in edges between the visual and default mode networks ($p < 0.05$). These included regions in the temporal lobe, temporoparietal junction, extra-striate cortex. There was also a secondary pattern involving edges between the primary motor cortex, superior parietal lobe and the frontal lobe ($p < 0.05$).

To focus on differences that might relate specifically to visual hallucinations, we looked at the edges that differed between patients with and without hallucinations but did not differ when comparing the patient group as a whole with controls. These edges were also unique to the correlation matrix and were not significantly different in the Euclidean matrix from the t-SNE results. Overall, edges between the visual and default mode networks, specifically regions of the extra-striate cortex, temporal, parietal, and frontal lobes were unique to Parkinson's disease patients with visual hallucinations (Figure 5A). For a detailed list of regions and coordinates refer to Supplementary Materials.

Group differences in t-SNE distance analysis

Figure 4 shows the t-SNE embedding from each group. Between Parkinson's disease and healthy controls, a significant increase in Euclidean distance was found in the t-SNE analysis for the limbic, ventral attention, and executive (frontoparietal control, default mode) networks ($p < 0.05$). Specifically, these regions were from the inferior parietal lobule, medial regions of the motor cortex, ventral and lateral prefrontal cortex, and the inferior and superior regions of the temporal lobe. These reconfigurations included somatomotor regions that have been assigned to the visual network of the Yeo 7-network atlas. There was also an increase in distance between the extra-striate cortex and the rest of the visual network ($p < 0.05$).

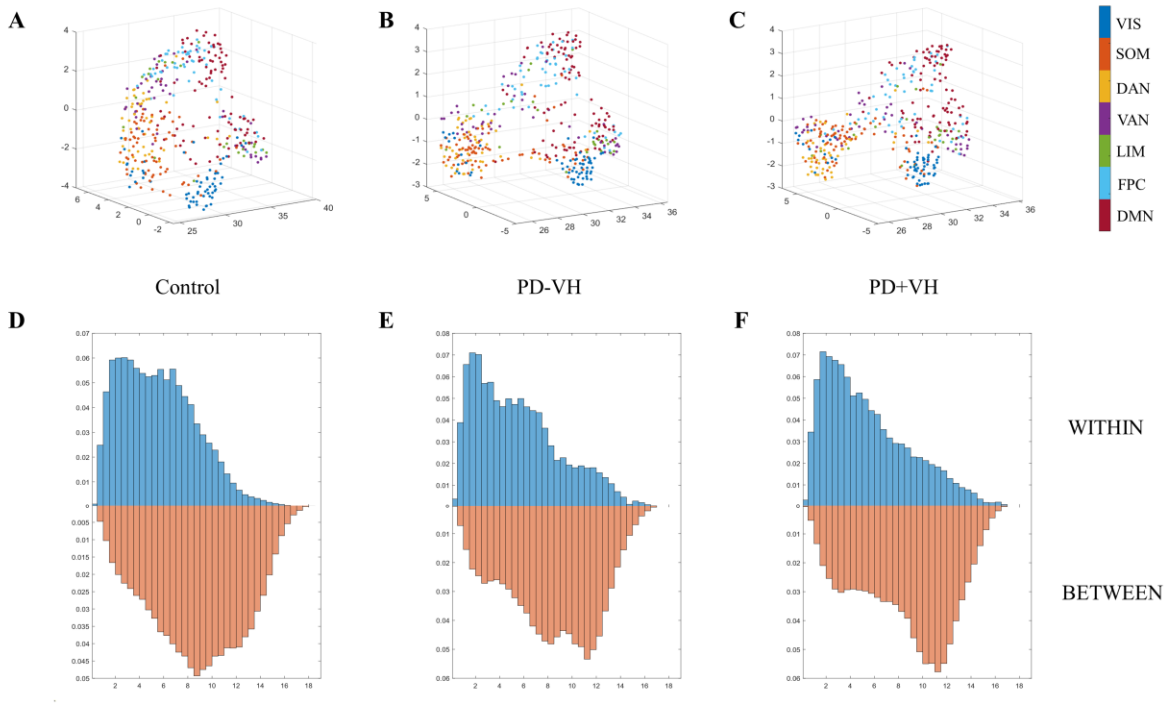

Figure 4 t-SNE plots of 400 Schaefer regions. (A) t-SNE plot of control group average functional connectivity. **(B)** t-SNE plot of PD-VH average functional connectivity. **(C)** t-SNE plot of PD+VH average functional connectivity. Plots A-C are coloured by Yeo 7-network atlas (VIS = visual, SOM = somatomotor, DAN = dorsal attention, VAN = ventral attention, LIM = limbic, FPC = frontoparietal control, DMN = default mode network). (D-F) Density histograms of the Euclidean distance within vs. between networks for each t-SNE plot.

Narrowing the focus to differences between patients with and without visual hallucinations, we found increased Euclidean distances from the visual network to the superior and inferior regions of the parietal cortex, lateral and ventral regions of the prefrontal cortex, and the posterior cingulate ($p < 0.05$). There was also a significant increase in distance between regions of the lateral motor cortex and temporal occipital cortex to regions of the frontoparietal control and default mode networks ($p < 0.05$). Significant increases in distance in the superior temporal lobe and the temporal pole of the right hemisphere were also evident ($p < 0.05$).

From the t-SNE results, we isolated differences that were unique to patients with visual hallucinations. Patients with visual hallucinations had an increased Euclidean distance between regions from the dorsal and ventral prefrontal cortex, lateral motor cortex, inferior parietal cortex, temporal occipital cortex, and posterior cingulate. The unilateral increased distances found in the right temporal pole and superior temporal cortex were also attributed to patients with visual hallucinations only (Figure 5B). Overall, the t-SNE results showed that brain

regions were situated further apart (less compressed) in patients with visual hallucinations. For a detailed list of the regions and coordinates refer to Supplementary Materials.

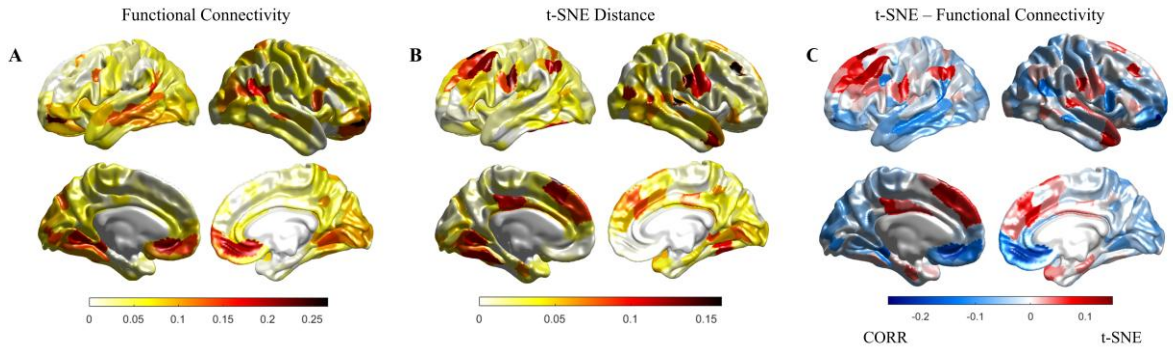

Figure 5 Proportion of edges that defined patients with hallucinations from the other two groups. (A) Proportion of edges that were different in functional connectivity. **(B)** Proportion of edges that were different in Euclidean distance. **(C)** Proportion of edges that are different in Euclidean distance compared to functional connectivity. Regions coloured in red have more differences in Euclidean distance, and regions coloured in blue have more differences in functional connectivity.

Relationship between functional connectivity and t-SNE distances

Group differences observed by analysing the correlation matrix were not always replicated in the t-SNE Euclidean distance matrix. For instance, comparing the correlation and t-SNE differences for the control vs. Parkinson's disease groups showed that increased functional connectivity in the primary motor cortex was mirrored by increased Euclidean distance in the t-SNE analysis. However, this contradicts our intuition of the relationship between functional connectivity and Euclidean distance: an *increase* in functional connectivity should equate to a *decrease* in Euclidean distance. Using this intuition as a guide, we could investigate the latent network signatures. In doing so, we noticed that the prominent between-group differences in standard functional connectivity between the visual and somatomotor networks were not upheld by the t-SNE analysis. Specifically, the increased Euclidean distance between the somatomotor network and higher order networks we observed on the t-SNE plots were not as prominent in the correlation matrix, suggesting that passing the functional data through the unique filter of the t-SNE was sufficient to expose specific differences in network-level organisation that were not detectable through standard functional connectivity analyses.

Given the difference in interpretation associated with the functional connectivity and t-SNE matrices, we compared the two directly – i.e., finding the eigenvectors of the correlation and t-SNE Euclidean distance matrices through eigendecomposition and calculating the Pearson's correlation between them. This can be interpreted as capturing latent components of the original low-dimensional embedding: the first eigenvector that explains the most variance of the data describes a pattern that differentiates the Parkinson's disease group from controls. In the first eigenvector for functional connectivity, the main differences between the controls vs. Parkinson's disease were in regions of the occipital lobe, temporal and frontal pole, motor cortex and anterior cingulate (Figure 6A). For the first eigenvector for Euclidean distance, main differences were observed in the prefrontal cortex, inferior temporal cortex and temporal parietal junction laterally, both posterior and anterior cingulate cortex medially, primary motor cortex, extra-striate cortex, and regions of the superior temporal cortex (Figure 6C). We then established whether these patterns were equivalent by conducting spin permutation tests with the Pearson's correlation between the two eigenvectors. There was no significant correlation between the two eigenvectors (p_{spin} = 0.3345), confirming that the correlation and Euclidean distance matrices highlight distinct differences between the control and Parkinson's disease groups.

Comparing patients with and without visual hallucinations, there were no edge differences that overlapped between the correlation and Euclidean distance matrices. Similar to the previous comparison, we can confirm that these matrices describe different patterns by calculating the Pearson's correlation between the eigenvector for each matrix. For the correlation eigenvector, main differences were found in the temporal lobe, extending to the temporoparietal junction, the primary visual cortex, the medial extrastriate cortex and parts of the parietal cortex (Figure 6B). For the Euclidean distance eigenvector, the main differences were in the prefrontal cortex, inferior parietal cortex, lateral motor cortex and regions of the extrastriate cortex (Figure 6D). There was no significant correlation between the two eigenvectors (p_{spin} = 0.3258), confirming that the correlation and Euclidean distance matrices differentiated between patients with and without visual hallucinations in distinct ways. In summary, the functional connectivity correlation matrices revealed increased connectivity between primary visual and temporal regions, whereas the t-SNE matrices showed increased Euclidean distances between the prefrontal, motor and extrastriate cortex.

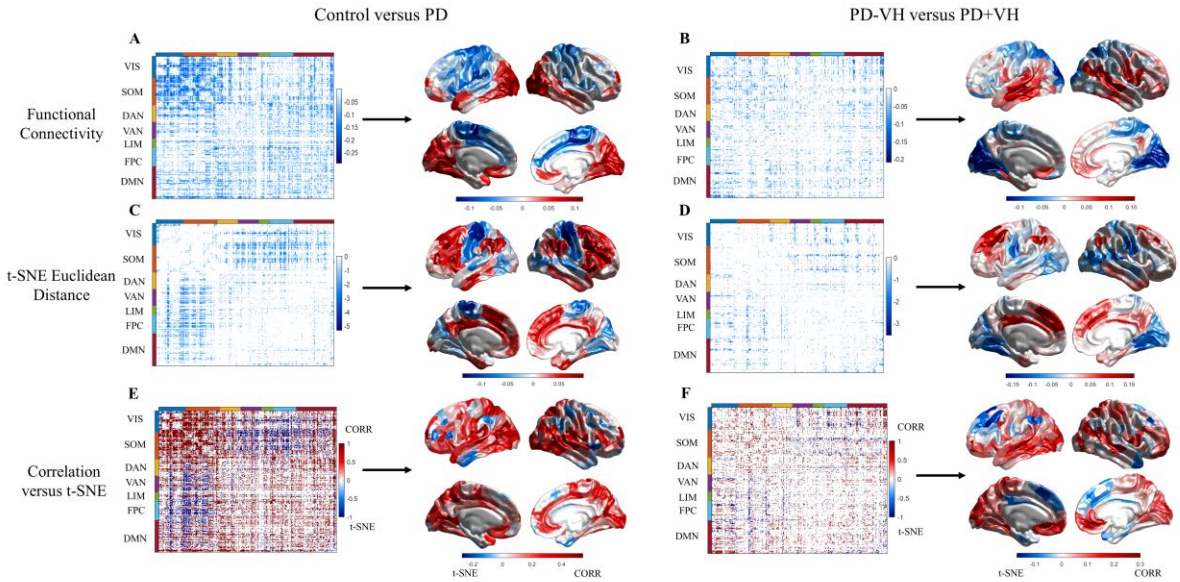

Figure 6 Functional connectivity (FC) and t-SNE analysis for Control vs Parkinson's disease. Left column **(A, C, E)** refers to Control vs. PD comparisons. Right column **(B, D, F)** refers to PD-VH vs. PD+VH comparisons. The first row **(A, B)** were group differences in FC. Matrices were coloured by group differences (Control - PD; PD-VH - PD+VH respectively), with values less than 0 indicating higher FC between regions in PD and PD+VH respectively. The first eigenvector of each matrix was visualised on the cortical surface. The second row **(C, D)** refers to group differences in Euclidean distance between t-SNE maps. Matrices were coloured by group differences (Control - PD; PD-VH - PD+VH respectively), with values less than 0 indicating greater Euclidean distance between regions in PD and PD+VH respectively. The first eigenvector of each matrix was visualised on the cortical surface. The third row **(E, F)** refers to differences between the FC and t-SNE results. Matrices were coloured by group differences, with 1 indicating a difference observed from FC analysis, -1 indicating a difference observed from t-SNE analysis, and 0 indicating a difference observed in either both or none of the analyses. The average difference between analyses across regions was visualised on the cortical surface such that *values* > 0 indicate differences more common in FC analysis, and *values* < 0 indicate differences more common in t-SNE analysis. VIS = visual, SOM = somatomotor, DAN = dorsal attention, VAN = ventral attention, LIM = limbic, FPC = frontoparietal control, DMN = default mode network.

Relationship between t-SNE distances and the unimodal-heteromodal gradient

Group differences found in the correlation and t-SNE analyses were compared against differences observed in the unimodal-heteromodal gradients. We did this in two steps: 1) by identifying the proportion of edges that were significantly different between groups for each region in the correlation and Euclidean distance matrices; and 2) we then compared whether the number of edges that were different between the groups shared a significant correlation with the change in gradient scores between patients with and without visual hallucinations. Spin permutation tests confirmed a weak correlation between the proportion of edges in the

Euclidean matrix and the change in gradient score (r = -0.100, p_{spin} = 0.0654). For the proportion of edges in the correlation matrix, there was a significant correlation with the change in gradient scores (r = -0.324, p_{spin} < 0.001). Therefore, the correlation matrix differences aligned more with differences in gradient scores compared to the t-SNE results, further confirming that the t-SNE analysis revealed unique signatures from patients with visual hallucinations that are not found when directly interrogating the raw functional correlation matrix.

Discussion

Here we combined insights across functional connectivity, cortical gradients and t-SNE distance mapping, to demonstrate the altered network hierarchy in Parkinson's disease visual hallucinations. In patients with hallucinations, gradients analysis revealed increased functional integration (i.e., compression) between sensory and higher order networks. This was mirrored by results from the correlation matrices, which showed increased connectivity between the visual and default-mode networks in the hallucinating group. However, when projecting into the t-SNE space, new reconfigurations that defined hallucinating patients were revealed. The hallucinating group was characterised by increased Euclidean distances in edges connecting regions of the visual network to the frontoparietal control and default mode networks, as well as edges within the default mode network. Furthermore, group differences observed in the t-SNE space were only weakly correlated with differences in the unimodal-heteromodal functional gradient, compared to the strong correspondence between the correlation matrix and gradient results. Together, our results confirm altered network hierarchy in Parkinson's disease hallucinations across multiple dimensionality reduction techniques. Furthermore, our novel application of t-SNE distance analysis may provide new insights into the neural signatures of visual hallucinations – exposing non-linear, network-level reconfigurations not typically identifiable in traditional functional connectivity and gradient analyses.

Compression of the unimodal-heteromodal gradient may disrupt perceptual processing and contribute to hallucination vulnerability. Separation between functional regions in the gradient context has been linked to spatial separation along the cortex, with long-range connections between unimodal and heteromodal regions serving as one of the foundations for information processing (Oligschläger et al., 2017; Y. Wang, Royer, et al., 2021). In Parkinson's disease with

visual hallucinations, there was increased functional integration between sensory and higher order networks, as gradient scores for regions from the visual, attentional, and frontoparietal control networks shifted closer together. Decreased separation along the gradient implies increased similarity in connectivity profiles and increased integration between regions. Indeed, we observed higher functional connectivity between the visual network and regions of the ventral attention, frontoparietal control, and default mode networks in patients with visual hallucinations. This is consistent with previous work showing increased coupling between sensory and higher-order networks in Parkinson's disease and other neuropsychiatric disorders that involve perceptual disturbances (Butler et al., 2012; Martínez et al., 2020; Shine, Muller, et al., 2015; Walpola et al., 2020). Increased connectivity between higher-order and sensory regions, and compression of the unimodal-heteromodal gradient, are routes that may permit excessive influence over earlier perceptual processes – consistent with the proposal that abnormal modulation from top-down regions over the visual system increases susceptibility to visual hallucinations (Barnes et al., 2003; Collerton et al., 2005; Lenka et al., 2015; O'Callaghan, Hall, et al., 2017; Shine, Keogh, et al., 2015; Zarkali et al., 2019).

Compression of the unimodal-heteromodal gradient is not unique to Parkinson's disease and may be a transdiagnostic feature in disorders with perceptual disturbances. Previous studies in other neuropsychiatric disorders, including autism spectrum disorder and schizophrenia, also showed compression of the unimodal-heteromodal gradient (Dong et al., 2021; Hong et al., 2019). Both studies observed an association between changes in the gradient and measures of disease severity (Dong et al., 2021; Hong et al., 2019). Similarly, in Parkinson's disease, the extent of visual impairment has been related to the amount of compression in the unimodal-heteromodal gradient (Zarkali et al., 2021). We observed an association between gradient scores and measures of attentional set-shifting – consistent with poorer attention associated with a lower (more compressed) gradient score. While these are not direct clinical measures of hallucination severity, attentional problems are prominent features of the hallucinating phenotype (Gallagher et al., 2011; Montagnese et al., 2022) and may predict the development of visual hallucinations (Muller et al., 2017). Taken together, compression of the unimodal-heteromodal gradient has been observed across neuropsychiatric disorders, varying with clinical measures of disease severity, and may be a predisposing trait for hallucinations in Parkinson's disease.

Between the groups, there was increased functional differentiation between sensory and higher-order networks in the t-SNE space. The distance between regions in the t-SNE plot are based on the similarity of their functional connectivity profiles (van der Maaten, 2013), with regions functionally similar to each other placed closer together in t-SNE space. From this intuition, regions that share increased functional connectivity should be mirrored by decreased Euclidean distance (and *vice versa*). However, we observed certain regions with relatively strong functional correlations in hallucinating patients were increasingly separated in t-SNE space. Regional pairs that demonstrate this pattern may have strong correlations but retain the ability for relatively segregated processing, based on the highly non-linear patterns stored within the rest of the network. Importantly, most regional pairs we observed with this pattern were in the prefrontal cortex, which serves an important role in "top-down" perceptual processing (Miller & Cohen, 2001; Spreng et al., 2010), possibly via its initial rapid processing of ambiguous information via magnocellular pathways (Bar, 2004; Kveraga et al., 2007). Abnormalities in the prefrontal cortex reduce cognitive flexibility and impair performance in tasks that involve distractions or ambiguous information (Miller & Cohen, 2001). Increased distance between the prefrontal cortex and sensory regions suggests reduced interactions and functional coupling between these regions, possibly decreasing the reliance on the prefrontal cortex for information processing, and impairing the ability to process ambiguous information. These results demonstrate that the t-SNE analysis captures a unique facet of hallucination susceptibility, which is complementary to the functional gradients results and not typically identified in correlation matrix analyses.

All of the results for group differences in functional connectivity and t-SNE were replicated under an alternate parcellation scheme (Schaefer-200). We further replicated the distinctive patterns that emerged when comparing between the functional connectivity and t-SNE, with only one exception where the 200-parcellation scheme identified a significant relationship between the t-SNE spatial pattern and the unimodal-heteromodal gradient that was not evident under the 400- parcellation scheme. While this minor difference does not change the overall interpretation of the paper, it emphasises the importance of comparing results under different parcellation schemes.

Our sample of patients with visual hallucinations displayed relatively preserved cognition, with the exception of deficits on an attentional task (Trail-making test). Cognitive impairment is one of the major concomitant features with visual hallucinations in Parkinson's disease. And

indeed, in our cohort we found that impaired performance on the Trail-making test Part B was related to more compressed gradient scores in the ventral attention network. This contrasted with a lack of relationship between hallucination severity scores (i.e., PsycH-Q) and gradient scores – although it should be noted that we only had the PsycH-Q in a subset of patients, which may have impacted our ability to detect an effect. Future work applying these approaches in patients with more advanced cognitive impairment will inform whether the changes identified via gradients and t-SNE approaches bear stronger links with the progression of cognitive decline and/or hallucination severity. Given the inextricable link between hallucinations and other cognitive abilities – especially perception and attention abilities – we suggest that our results speak to a hallucinations phenotype, whereby this symptom is seen in the context of other perceptual-attentional deficits.

The current study focused on neuroimaging analyses of patients at rest, however previous studies measuring hallucination-like events in Parkinson's disease have converged on similar brain regions, suggesting these regions are functionally relevant to the hallucination state (Shine, Keogh, et al., 2015). Perception is influenced by past experiences, reconciling incoming sensory information with known statistics about the external world – allowing us to predict and interpret incoming information, even in ambiguous situations (Collerton et al., 2005; Hardstone et al., 2021). From resting state analyses, we observed reconfigurations in network organisation that could disrupt how our perceptual system processes internal and external information. Compression of the unimodal-heteromodal gradient suggests that in patients susceptible to visual hallucinations, there is potential for increased influence from top-down processes to override sensory information**.** The t-SNE analysis highlights increased differentiation between the prefrontal cortex and sensory regions, which may result in a decreased reliance on the prefrontal cortex for processing ambiguous information. Taken together, when patients vulnerable to hallucinations encounter environments with minimal sensory information, they may be unable to process the ambiguous information appropriately and increase their dependence on internal associations, resulting in misleading predictions of their surrounding environment and the formation of hallucinations (Hardstone et al., 2021; Zarkali et al., 2019).

Treatment of visual hallucinations and psychosis in Parkinson's disease is challenging, and dimensionality reduction techniques may provide a novel objective for medicinal drugs (ffytche et al., 2017). The standard dopaminergic medication has minimal benefits on

hallucinations, and in many cases will exacerbate them (Chaudhuri & Schapira, 2009; Iarkov et al., 2020). However, treatment with classic antipsychotic medications can have adverse secondary effects, including worsened motor symptoms (O'Brien et al., 2020; Powell et al., 2020). A newer medication for Parkinson's disease psychosis is the selective serotonin inverse agonist pimavanserin, which acts primarily at the 5-HT_{2A} receptor (ffytche et al., 2017; Meltzer et al., 2010). This drug, which effectively antagonises the 5-HT_{2A} receptor, improves psychosis symptoms without the unintended motor side effects (Meltzer et al., 2010; O'Brien et al., 2020). Single-dose studies in healthy people using pro-serotonergic drugs (acting primarily at 5-HT_{2A}) reveal a compression of the principal gradient induced by drugs that agonise 5-HT_{2A} (Girn et al., 2022). It could be speculated that pimavaserin may promote a recovery of separation within the principal gradient, consistent with a role for 5-HT_{2A} activity in modulating the degree of feedback and information transfer in the brain (Shine et al., 2022). This opens the possibility of gradient analysis being a useful means to reveal insights into visual hallucinations beyond traditional functional connectivity measures, which may be particularly relevant to measuring the impact of serotonergic drugs – consistent with the broader goal of establishing neuroimaging signatures that can advance personalised drug treatment in Parkinson's disease (O'Callaghan, Hezemans, et al., 2021).

This study revealed reconfigurations in network interactions for Parkinson's disease patients susceptible to visual hallucinations. Compression of the unimodal-heteromodal gradient was associated with cognitive performance and may be a useful measurement for understanding the extent of abnormal interactions between top-down and bottom-up processing. Furthermore, this study demonstrated that projecting functional connectivity into the t-SNE space provides an alternate perspective to hallucinations in Parkinson's disease that is overlooked in traditional functional connectivity analyses. With continued advancements in imaging methods and increased diversity in neuropsychiatric data, dimensionality reduction techniques are a lens through which the neural signatures of hallucinations, across modalities and disorders, might be reconciled.

Funding

S.J.G.L, J.M.S. and C.O. were supported by NHMRC fellowships (1195830; 1193857; 2016866, respectively).

Competing interests

The authors report no competing interests.

Supplementary material

Supplementary material is available at *Brain* online.

Supplementary Material

Abnormal higher-order network interactions in Parkinson's disease visual hallucinations

1. Extra demographic details

Table 2 Demographic missing values

Variable	**Number of missing values**		
	Control	PD-VH	PD+VH
MMSE	1	2	1
MoCA	3	7	4
Digit Span	0	1	0
LM Retention	0	1	1
TMT A z-score	0	1	1
TMT B z-score	0	1	1
HADS	1	4	0
Hoehn and Yahr	NA	0	1
SCOPA-PC	9	4	1

PD-VH = Parkinson's disease without visual hallucinations. PD+VH = Parkinson's disease with visual hallucinations. MMSE = Mini-Mental State Examination total score. MoCA = Montreal Cognitive Assessment total score. LM Retention = Logical Memory Retention. TMT A, TMT B are the z-scored trail-making test results. BDI = Beck's Depression Inventory total score. HADS = Hospital and Anxiety Depression Scale total score. SCOPA-PC = Scale for Outcomes in Parkinson's disease - Psychiatric Complications total score. The Hoehn and Yahr assessment was only given to Pakrinson's disease patients.

Table 3 Breakdown of PsycH-Q

	PD+VH (*n* = 20)	
	Mean	**SD**
Visual Misperceptions	3.3	5.13
Sensory Misperceptions	0.85	1.66
Disordered Thought	0.2	0.523
Attentional Dysfunction	6.45	4.88
Sleep Impairment	2.45	1.73
Hallucinations & Psychosis	4.35	6.13
Hallucinations Phenotype	8.9	5.65
PsycH-Q Total	13.2	10.3

PD+VH = Parkinson's disease with visual hallucinations. Hallucinations & Psychosis = combined score of visual, sensory misperceptions and disordered thought. Hallucinations Phenotype = combined score of attentional dysfunction and sleep impairment. PsycH-Q Total is combined score of the 5 subscales (visual, sensory misperceptions, disordered thought, attentional dysfunction, and sleep impairment).

2. fMRI preprocessing

Anatomical data preprocessing

The T1-weighted (T1w) image was corrected for intensity non-uniformity (INU) with N4BiasFieldCorrection (Tustison et al. 2010), distributed with ANTs 2.3.3 (Avants et al. 2008, RRID:SCR_004757), and used as T1w-reference throughout the workflow. The T1w-reference was then skull-stripped with a Nipype implementation of the antsBrainExtraction.sh workflow (from ANTs), using OASIS30ANTs as target template. Brain tissue segmentation of cerebrospinal fluid (CSF), white-matter (WM) and gray-matter (GM) was performed on the brain-extracted T1w using fast (FSL 5.0.9, RRID:SCR_002823, Zhang, Brady, and Smith 2001). Volume-based spatial normalization to two standard spaces (MNI152NLin2009cAsym, MNI152NLin6Asym) was performed through nonlinear registration with antsRegistration (ANTs 2.3.3), using brain-extracted versions of both T1w reference and the T1w template. The following templates were selected for spatial normalization: ICBM 152 Nonlinear Asymmetrical template version 2009c [Fonov et al. (2009), RRID:SCR_008796; TemplateFlow ID: MNI152NLin2009cAsym], FSL's MNI ICBM 152 non-linear 6th Generation Asymmetric Average Brain Stereotaxic Registration Model [Evans et al. (2012), RRID:SCR_002823; TemplateFlow ID: MNI152NLin6Asym].

Functional data preprocessing

First, a reference volume and its skull-stripped version were generated using a custom methodology of fMRIPrep. Susceptibility distortion correction (SDC) was omitted. The BOLD reference was then co-registered to the T1w reference using flirt (FSL 5.0.9, Jenkinson and Smith 2001) with the boundary-based registration (Greve and Fischl 2009) cost-function. Co-registration was configured with nine degrees of freedom to account for distortions remaining in the BOLD reference. Head-motion parameters with respect to the BOLD reference (transformation matrices, and six corresponding rotation and translation parameters) are estimated before any spatiotemporal filtering using mcflirt (FSL 5.0.9, Jenkinson et al. 2002). The BOLD time-series (including slice-timing correction when applied) were resampled onto their original, native space by applying the transforms to correct for head-motion. These resampled BOLD time-series will be referred to as preprocessed BOLD in original space, or just preprocessed BOLD.

The BOLD time-series were resampled into standard space, generating a preprocessed BOLD run in MNI152NLin2009cAsym space. First, a reference volume and its skull-stripped version

were generated using a custom methodology of fMRIPrep. Automatic removal of motion artifacts using independent component analysis (ICA-AROMA, Pruim et al. 2015) was performed on the preprocessed BOLD on MNI space time-series after removal of non-steady state volumes and spatial smoothing with an isotropic, Gaussian kernel of 6mm FWHM (full-width half-maximum). Corresponding "non-aggresively" denoised runs were produced after such smoothing. Additionally, the "aggressive" noise-regressors were collected and placed in the corresponding confounds file.

Several confounding time-series were calculated based on the preprocessed BOLD: framewise displacement (FD), DVARS and three region-wise global signals. FD was computed using two formulations following Power (absolute sum of relative motions, Power et al. (2014)) and Jenkinson (relative root mean square displacement between affines, Jenkinson et al. (2002)). FD and DVARS are calculated for each functional run, both using their implementations in Nipype (following the definitions by Power et al. 2014). The three global signals are extracted within the CSF, the WM, and the whole-brain masks. Additionally, a set of physiological regressors were extracted to allow for component-based noise correction (CompCor, Behzadi et al. 2007). Principal components are estimated after high-pass filtering the preprocessed BOLD time-series (using a discrete cosine filter with 128s cut-off) for the two CompCor variants: temporal (tCompCor) and anatomical (aCompCor). tCompCor components are then calculated from the top 2% variable voxels within the brain mask. For aCompCor, three probabilistic masks (CSF, WM and combined CSF+WM) are generated in anatomical space. The implementation differs from that of Behzadi et al. in that instead of eroding the masks by 2 pixels on BOLD space, the aCompCor masks are subtracted a mask of pixels that likely contain a volume fraction of GM. This mask is obtained by thresholding the corresponding partial volume map at 0.05, and it ensures components are not extracted from voxels containing a minimal fraction of GM.

Finally, these masks are resampled into BOLD space and binarized by thresholding at 0.99 (as in the original implementation). Components are also calculated separately within the WM and CSF masks. For each CompCor decomposition, the k components with the largest singular values are retained, such that the retained components' time series are sufficient to explain 50 percent of variance across the nuisance mask (CSF, WM, combined, or temporal). The remaining components are dropped from consideration. The head-motion estimates calculated in the correction step were also placed within the corresponding confounds file. The confound

time series derived from head motion estimates and global signals were expanded with the inclusion of temporal derivatives and quadratic terms for each (Satterthwaite et al. 2013). Frames that exceeded a threshold of 0.5 mm FD or 1.5 standardised DVARS were annotated as motion outliers. All resamplings can be performed with a single interpolation step by composing all the pertinent transformations (i.e., head-motion transform matrices, susceptibility distortion correction when available, and co-registrations to anatomical and output spaces). Gridded (volumetric) resamplings were performed using antsApplyTransforms (ANTs), configured with Lanczos interpolation to minimize the smoothing effects of other kernels (Lanczos 1964). Non-gridded (surface) resamplings were performed using mri_vol2surf (FreeSurfer).

Many internal operations of fMRIPrep use Nilearn 0.6.2 (Abraham et al. 2014, RRID:SCR_001362), mostly within the functional processing workflow. For more details of the pipeline, see the section corresponding to workflows in fMRIPrep's documentation.

3. Rationale for using t-SNE

Functional connectivity is the correlation between fMRI timeseries for different regions of the brain. Regions that activate at similar timings will have higher correlations between them, and regions with dissimilar activity timing will have lower correlations. t-Stochastic Neighbour Embedding (t-SNE), can take functional connectivity as an input and calculate a simplified similarity score of functional connectivity in lower dimensions (2-3), prioritising relationships between regions in the original space. The following similarity score can be visualised in a coordinate space such that regions sharing similar connectivity profiles are placed closer together and regions with dissimilar connectivity profiles are more distant from each other. As each region can be described by a set of coordinates (x, y, z), we can calculate the Euclidean distance between regions as a proxy of functional connectivity in the t-SNE embedding space. Regions with similar connectivity profiles will have *smaller* distances between each other and regions with dissimilar connectivity profiles will have *greater* distances between each other.

In MATLAB, the t-SNE algorithm (tsne, Copyright 2016-2019 The MathWorks, Inc.) can be employed with the following parameters for adjustment:

***Algorithm (Barneshut, exact*)**: Barnes-Hut approximation is an alternative algorithm for t-SNE developed to improve memory efficiency, making t-SNE calculations practical for large datasets. The alternative option ('exact') optimises the Kullback-Leibler divergence of

distributions between the original and embedded space. The Kullback-Leibler divergence considers how different the distribution of one probability distribution is different from another when calculating the similarity scores.

Distance: Specifies which distance metric is used to separate data points.

Embedding dimensions: Number of dimensions for data visualisation (2 or 3).

PCA Initialisation: Reducing the dimensions of the original data through Principal Component Analysis (PCA) and selecting the number of components to include in the t-SNE algorithm. PCA initialisation provides consistency to t-SNE output (Kobak and Linderman, 2021) and also increases computation efficiency by reducing the dimensions. Appropriate number of components was decided by running False Nearest Neighbours (FNN) and choosing the smallest number of components that resulted in <0.1% false neighbours.

Perplexity: Approximates how many local neighbours should be assigned to each point. Changing perplexity affects how many surrounding points should be considered neighbouring to a datapoint. Setting large values of perplexity would encourage denser clusters, while smaller values would result in distributed sparse clusters.

Learning Rate: The effect of learning on the optimisation process. Lower learning rates decrease the influence of learning during earlier optimisation processes. Higher learning rates retain learning even in later optimisation processes.

Exaggeration: Cluster size. Changing exaggeration affects the size of the clusters as well as the space between clusters. The t-SNE algorithm uses exaggeration in the first 99 optimisation iterations to facilitate cluster formation (Belkina *et al.*, 2019).

4. t-SNE Simulations and verification

To find t-SNE plots that represent the functional connectivity data in a meaningful way, we ran the t-SNE algorithm on a 7T fMRI data of healthy controls (n = 59). The algorithm was run across 11 iterations of perplexity (1-100), learning rate (1-1000), and exaggeration (1-100) each for a total of 1331 iterations. As t-SNE randomly generates the starting coordinates, a specific seed was set for consistency and reproducible results. The Euclidean distance was calculated between each region (n = 400) and every other region resulting in a region by region (400 x 400) Euclidean distance map for each t-SNE plot. As mentioned previously, the Euclidean distance is a measurement of functional similarity between regions where regions that are

different have a larger distance between them, and regions that are similar have smaller distances between them.

Yeo Network Ratio: As a measurement of how well the t-SNE output represents established networks from resting-state fMRI, we created a ratio that compares connections within and between networks from the Yeo 7-network atlas (Yeo *et al.*, 2011). An average *within* network score was computed by averaging the Euclidean distance for edges connecting regions within the same network (i.e., visual region to visual region). An average *between* networks score was computed by averaging the Euclidean distance for edges connecting regions from different networks (i.e., visual region to somatomotor region). These scores were combined into a ratio by dividing the average within network score by the average between network score (Equation 1). Ratio scores greater than 1 occur when the Euclidean distance *within* networks is greater than the distance *between* networks, suggesting less distinct networks. For our analyses we preferred lower ratios that indicated more distinct networks.

$$Yeo\ Network\ Ratio = \frac{mean\ ED\ within\ networks}{mean\ ED\ between\ networks} \qquad (1)$$

ED = Euclidean distance

Networks = Yeo 7-network atlas

Low- to High-dimension distance correlation: To check whether the t-SNE outputs were a faithful representation of the original embedding, we calculated the Pearson's correlation between each region in the t-SNE distance map, with the corresponding region from the distance map in the original embedding. The distance map in the original embedding (400 x 400) was produced by calculating the Euclidean distance for each region to every other region. The Pearson's correlation between the two maps was calculated for each region resulting in a correlation coefficient for each region (n = 400). The average correlation was used to summarise how well a t-SNE map represented the original embedding, where higher correlations indicated a more faithful representation.

K-means clustering and adjusted mutual information (AMI): To identify the range of values for each parameter that produces an 'ideal' t-SNE representation of the data, we applied k-means clustering on the correlation scores. K-means clustering aims to create clusters while minimising within-cluster variances (Hartigan, 1975). K-means clustering was applied for a range of possible k clusters (2-20) with 100 iterations for each number of k clusters. To identify numbers of clusters that were consistent, the Adjusted Mutual Information (AMI) (Vinh and Epps, 2009; Vinh, Epps and Bailey, 2009, 2010) was calculated between iterations of k clusters. The average AMI for each k cluster was visualised. For the correlation scores, specifying k = 5 clusters resulted in the most consistent results. Each of the five clusters were visualised and interpreted and the cluster with the highest correlation score and the lowest Yeo Network Ratio was chosen as the 'ideal' t-SNE plot. From these results, the chosen cluster included t-SNE plots (n = 27) with correlation scores >= 0.83 and a Yeo Network Ratio score <= 0.54.

Comparing 'ideal' t-SNE plots to other plots: A quality check of whether the cluster chosen was different to the other clusters is to compare the similarity of the distance maps within the chosen cluster and between the chosen cluster and distance maps outside the cluster (Böhm, Berens and Kobak, 2021). From our chosen cluster, we randomly sampled five t-SNE plots and correlated their t-SNE maps between each other (5 per plot). We also randomly sampled five t-SNE plots from outside the chosen cluster and correlated each t-SNE plot from our chosen cluster with each of the plots outside of the cluster (5 per plot). The average correlations for each plot were visualised, and permutation testing was conducted comparing correlations within a cluster against correlations between clusters (5000 permutations). Indeed, the correlations within the cluster were significantly higher than the correlations with plots between clusters ($p < 0.05$).

Final t-SNE plots

From the parameter sweep and cluster analysis, the chosen cluster was dependent on a high perplexity (80-100) and was insensitive to changes in learning rate and exaggeration. For further t-SNE analysis conducted in the Parkinson's disease dataset, the following values were set for each parameter:

- Algorithm = barneshut
- Distance = Euclidean

- NumDimensions = 3
- NumPCAComponents = 3
- Perplexity = 90
- LearnRate = 500
- Exaggeration = 50

Limitations

The t-SNE cluster identified from our analyses was specific to our question and the analysis pipeline we had in place. By no means is this cluster the ‘correct’ global representation of brain functional connectivity. We advise that before conducting t-SNE analyses in a dataset, one first follows our steps in designing a stringent criterion to test the t-SNE plots against before deciding on a set of parameter values to use. Furthermore, as the t-SNE algorithm does not project plots onto the exact same starting positions, in order to compare t-SNE plots directly we recommend aligning individual t-SNE plots to the population average (see procrustes, Copyright 1993-2009 The MathWorks, Inc.).

5. Schaefer 200 Analysis

The results from the main functional connectivity and t-SNE analysis are replicated below using the same analysis pipeline applied to the Schaefer-200 parcellation scheme. Between the Schaefer-200 and Schaefer-400 parcellations, the comparison between functional connectivity and t-SNE spatial patterns were qualitatively similar. When comparing the functional connectivity and t-SNE patterns against changes in the unimodal-heteromodal gradient both spatial patterns were significantly correlated with the gradient in the Schaefer-200 parcellation, whereas in the Schaefer-400 parcellation, only the functional connectivity spatial pattern shared a significant correlation with changes in the unimodal-heteromodal gradient.

Group differences in functional connectivity

Functional connectivity comparisons between the Parkinson's disease patients and control group revealed increased functional connectivity bilaterally between the somatomotor network and regions from the visual, dorsal attention, default mode network ($p < 0.05$). Specifically between the primary motor cortex and regions from the extra-striate cortex, parietal lobule, and temporoparietal junction. Comparing patients with and without visual hallucinations revealed increased functional connectivity between regions from the extra-striate cortex to regions of the parietal lobule, prefrontal cortex, temporal lobe, and temporoparietal junction ($p < 0.05$).

Focusing on differences that were unique to Parkinson's disease patients with visual hallucinations, revealed that edges from the extra-striate, primary motor, dorsolateral prefrontal, and frontal lobe were unique to patients with visual hallucinations.

Group differences in t-SNE distance analysis

Between Parkinson's disease patients and the control group, there was increased distance between regions. Specifically in regions such as the primary and lateral motor cortex, dorsolateral prefrontal cortex, superior temporal lobe, and extra-striate cortex ($p < 0.05$). Between patients with and without visual hallucinations there was increased distance between regions from the frontal lobe, dorsolateral prefrontal cortex, temporal lobe, and laterally in the primary motor cortex and posterior cingulate ($p < 0.05$).

Focusing on differences unique to Parkinson's disease patients with visual hallucinations revealed edges from the dorsolateral prefrontal, primary visual, extra-striate, primary motor cortices, and temporal lobe as unique to patients with visual hallucinations.

Relationship between functional connectivity, t-SNE distances, and unimodal-heteromodal gradient

In the Schaefer-200 parcellation, there was increased functional connectivity in edges that were significantly different between groups. From t-SNE analyses, there was increased Euclidean distance between regions that were significantly different between the groups. Therefore, results from the Schaefer-200 parcellation replicated the distinct relationship between functional connectivity and Euclidean distance originally found in the Schaefer-400 parcellation.

The functional connectivity and t-SNE binary matrices that described edges significantly different between groups were decomposed into their principal eigenvectors and compared using spin permutation tests. In both comparisons (control vs. Parkinsons' disease; VH vs. Non-VH), there was no significant correlation between the functional connectivity and t-SNE eigenvectors ($p_{spin} = 0.3365$; $p_{spin} = 0.3319$, respectively), reproducing the lack of relationship between functional connectivity and t-SNE seen in the Schaefer-400 parcellation.

We then compared whether the proportion of edges different between groups shared a significant correlation with changes in the gradient score. Both the t-SNE and functional connectivity results shared a significant correlation between proportion of significant edges and changes in the gradient score ($p_{spin} = 00246$; $p_{spin} = 0.0104$ respectively). These results were slightly different to the original Schaefer-400 results which found a significant correlation between functional connectivity and the changes in the unimodal-heteromodal gradient, but no significant correlation between the proportion of significant edges in t-SNE and gradient changes.

6. Table of p-values

The first table includes abbreviations and their full parcellation names. The tables after include the regions that were significantly different from the functional connectivity and t-SNE analyses.

Table 4 Full Parcel Names of Schaefer cortical node abbreviations.

Abbreviation	Full parcel Name
AntTemp	anterior temporal
Aud	auditory
Cent	central
Cinga	cingulate anterior
Cingm	mid-cingulate
Cingp	cingulate posterior
ExStr	extrastriate cortex
ExStrInf	extra-striate inferior
ExStrSup	extra-striate superior
FEF	frontal eye fields
FPole	frontal pole
FrMed	frontal medial
FrOper	frontal operculum
IFG	inferior frontal gyrus
Ins	insula
IPL	inferior parietal lobule
IPS	intraparietal sulcus
OFC	orbital frontal cortex
ParMed	parietal medial
ParOcc	parietal occipital
ParOper	parietal operculum
pCun	precuneus
pCunPCC	precuneus posterior cingulate cortex
PFCd	dorsal prefrontal cortex
PFCl	lateral prefrontal cortex
PFCld	lateral dorsal prefrontal cortex

PFClv	lateral ventral prefrontal cortex
PFCm	medial prefrontal cortex
PFCmp	medial posterior prefrontal cortex
PFCv	ventral prefrontal cortex
PHC	parahippocampal cortex
PostC	post central
PrC	precentral
PrCd	precentral dorsal
PrCv	precentral ventral
RSC	retrosplenial cortex
Rsp	retrosplenial
S2	S2
SPL	superior parietal lobule
ST	superior temporal
Striate	striate cortex
StriCal	striate calcarine
Temp	temporal
TempOcc	temporal occipital
TempPar	temporal parietal
TempPole	temporal pole

Table 5 Gradient results at the regional level comparing Parkinson's disease patients and controls.

ROI Name[a]	R	A	S	p_value
17Networks_LH_VisCent_Striate_1	-8	-98	-8	0.0212
17Networks_LH_VisCent_ExStr_7	-46	-74	6	0.0365
17Networks_LH_SomMotA_3	-48	-18	54	0.0438
17Networks_LH_SomMotA_4	-48	-30	58	0.0396
17Networks_LH_SomMotA_7	-4	-24	56	0.0200
17Networks_LH_SomMotA_9	-36	-20	64	0.0287
17Networks_LH_SomMotA_10	-32	-30	62	0.0134
17Networks_LH_SomMotA_11	-30	-38	66	0.0388

17Networks_LH_SomMotA_13	-20	-24	66	0.0182
17Networks_LH_SomMotA_14	-8	-42	70	0.0200
17Networks_LH_SomMotA_15	-4	-26	68	0.0038
17Networks_LH_SomMotA_17	-18	-32	68	0.0260
17Networks_LH_SomMotA_18	-18	-40	72	0.0271
17Networks_LH_SomMotA_19	-12	-26	74	0.0096
17Networks_LH_DorsAttnA_TempOcc_1	-44	-42	-22	0.0329
17Networks_LH_DorsAttnA_SPL_1	-26	-70	30	0.0368
17Networks_LH_DorsAttnA_SPL_2	-22	-78	44	0.0316
17Networks_LH_DorsAttnA_SPL_6	-14	-70	58	0.0114
17Networks_LH_SalVentAttnA_ParMed_1	-12	-28	42	0.0162
17Networks_LH_ContA_IPS_4	-44	-42	46	0.0028
17Networks_LH_ContA_IPS_5	-34	-46	40	0.0049
17Networks_LH_ContB_IPL_3	-42	-52	48	0.0101
17Networks_LH_ContB_PFClv_1	-42	48	-6	0.0309
17Networks_LH_ContC_Cingp_2	-4	-22	30	0.0230
17Networks_LH_DefaultA_pCunPCC_4	-4	-34	38	0.0360
17Networks_LH_DefaultB_Temp_6	-52	-22	-6	0.0317
17Networks_LH_TempPar_2	-60	-12	-2	0.0113
17Networks_RH_SomMotA_1	54	-16	40	0.0032
17Networks_RH_SomMotA_2	52	-12	50	0.0092
17Networks_RH_SomMotA_4	50	-26	56	0.0018
17Networks_RH_SomMotA_6	44	-22	54	0.002
17Networks_RH_SomMotA_7	38	-20	64	0.0184
17Networks_RH_SomMotA_8	32	-34	64	0.0015
17Networks_RH_SomMotA_9	30	-40	64	0.0037
17Networks_RH_SomMotA_10	34	-28	62	0.0032
17Networks_RH_SomMotA_11	4	-24	58	0.0294
17Networks_RH_SomMotA_13	10	-40	68	0.0031
17Networks_RH_SomMotA_15	22	-28	68	0.0085
17Networks_RH_SomMotA_16	22	-34	70	0.0382
17Networks_RH_SomMotA_19	16	-18	74	0.0483
17Networks_RH_SomMotB_Cent_3	52	-6	38	0.0431

17Networks_RH_DorsAttnA_SPL_4	30	-64	52	0.0256
17Networks_RH_DorsAttnB_PostC_2	58	-22	44	0.0297
17Networks_RH_SalVentAttnA_ParOper_1	58	-32	24	0.0076
17Networks_RH_SalVentAttnA_ParOper_3	62	-26	38	0.0192
17Networks_RH_SalVentAttnA_Ins_2	40	8	-2	0.0152
17Networks_RH_SalVentAttnA_Ins_4	40	-2	6	0.0352
17Networks_RH_SalVentAttnA_FrOper_2	48	4	4	0.0404
17Networks_RH_SalVentAttnB_PFClv_1	50	40	6	0.0382
17Networks_RH_LimbicB_OFC_5	4	22	-20	0.0196
17Networks_RH_ContA_IPS_3	46	-44	46	0.0065
17Networks_RH_ContA_PFCl_2	48	18	24	0.0283
17Networks_RH_ContA_PFCl_3	48	28	28	0.0464
17Networks_RH_ContB_IPL_3	56	-40	48	0.0342
17Networks_RH_ContB_IPL_4	42	-56	48	0.0418
17Networks_RH_ContB_PFCld_1	38	34	38	0.0457
17Networks_RH_ContC_pCun_1	16	-64	28	0.0497
17Networks_RH_DefaultA_PFCm_4	8	54	12	0.0290
17Networks_RH_TempPar_4	62	-18	0	0.0204

[a]Region labels follow the Schaefer-400 17-network 2mm parcellation labels.

Table 6 Gradient results at the regional level comparing PD+VH and PD-VH

ROI Name[a]	R	A	S	p_value
17Networks_LH_DorsAttnB_PostC_3	-54	-32	44	0.0223
17Networks_LH_SalVentAttnB_PFCmp_1	-6	22	32	0.0426
17Networks_LH_ContA_IPS_3	-34	-62	48	0.0225
17Networks_LH_ContC_Cingp_2	-4	-22	30	0.0458
17Networks_LH_DefaultB_IPL_1	-46	-58	20	0.0064
17Networks_RH_SomMotA_2	52	-12	50	0.0380
17Networks_RH_SomMotA_17	16	-6	70	0.0330
17Networks_RH_SomMotB_Aud_3	60	-24	10	0.0160
17Networks_RH_SomMotB_Cent_3	52	-6	38	0.0181
17Networks_RH_DorsAttnB_PostC_2	58	-22	44	0.0298

17Networks_RH_DorsAttnB_PostC_6	8	-54	60	0.0329
17Networks_RH_SalVentAttnA_PrC_1	52	4	40	0.0259
17Networks_RH_SalVentAttnA_ParMed_3	10	-44	54	0.0281
17Networks_RH_ContA_IPS_3	46	-44	46	0.0077
17Networks_RH_ContB_IPL_4	42	-56	48	0.0352
17Networks_RH_DefaultA_PFCd_1	26	34	38	0.0167
17Networks_RH_DefaultA_PFCm_1	6	42	-10	0.0054
17Networks_RH_DefaultC_IPL_1	48	-64	22	0.003
17Networks_RH_TempPar_3	48	-20	-8	0.0492
17Networks_RH_TempPar_8	64	-34	10	0.0490
17Networks_RH_TempPar_9	54	-46	20	0.0490

PD+VH = Parkinson's disease with visual hallucinations. PD-VH = Parkinson's disease without visual hallucinations.

[a]Region labels follow the Schaefer-400 17-network 2mm parcellation labels

7. List of regions with significant differences in edge connectivity

Table 7 Region labels and coordinates for regions that were different in functional connectivity due to hallucinations.

ROI Name	R	A	S
17Networks_LH_VisCent_ExStr_1	-36	-62	-16
17Networks_LH_VisCent_ExStr_2	-24	-72	-10
17Networks_LH_VisCent_ExStr_3	-36	-82	-16
17Networks_LH_VisCent_ExStr_6	-42	-86	-4
17Networks_LH_VisCent_Striate_1	-8	-98	-8
17Networks_LH_VisCent_ExStr_7	-46	-74	6
17Networks_LH_VisCent_ExStr_8	-24	-96	6
17Networks_LH_VisCent_ExStr_10	-10	-96	18
17Networks_LH_VisCent_ExStr_11	-26	-84	22
17Networks_LH_VisPeri_ExStrInf_1	-24	-54	-8
17Networks_LH_VisPeri_ExStrInf_2	-12	-62	-4
17Networks_LH_VisPeri_ExStrInf_3	-6	-76	-6
17Networks_LH_VisPeri_ExStrInf_4	-14	-44	-6
17Networks_LH_VisPeri_ExStrInf_5	-14	-56	2
17Networks_LH_VisPeri_StriCal_1	-4	-88	2
17Networks_LH_VisPeri_ExStrSup_2	-2	-84	24
17Networks_LH_VisPeri_ExStrSup_3	-12	-72	20
17Networks_LH_VisPeri_ExStrSup_4	-16	-88	34
17Networks_LH_VisPeri_ExStrSup_5	-12	-82	36
17Networks_LH_SomMotA_6	-8	-38	54
17Networks_LH_SomMotA_7	-4	-24	56
17Networks_LH_SomMotB_Aud_1	-50	-10	0
17Networks_LH_SomMotB_Aud_4	-40	-36	14
17Networks_LH_SomMotB_S2_4	-60	-2	10
17Networks_LH_SomMotB_Cent_2	-62	-10	32
17Networks_LH_DorsAttnA_TempOcc_1	-44	-42	-22
17Networks_LH_DorsAttnA_TempOcc_2	-32	-42	-20
17Networks_LH_DorsAttnA_TempOcc_3	-48	-56	-16
17Networks_LH_DorsAttnA_TempOcc_4	-46	-70	-8

17Networks_LH_DorsAttnA_ParOcc_2	-32	-84	26
17Networks_LH_DorsAttnA_SPL_1	-26	-70	30
17Networks_LH_DorsAttnA_SPL_4	-28	-58	50
17Networks_LH_DorsAttnA_SPL_5	-36	-52	56
17Networks_LH_DorsAttnA_SPL_6	-14	-70	58
17Networks_LH_DorsAttnB_PostC_5	-38	-38	50
17Networks_LH_DorsAttnB_FEF_2	-26	0	56
17Networks_LH_DorsAttnB_FEF_3	-30	-8	52
17Networks_LH_SalVentAttnA_ParOper_2	-58	-44	28
17Networks_LH_SalVentAttnA_Ins_1	-38	2	-4
17Networks_LH_SalVentAttnA_Ins_2	-40	-14	-2
17Networks_LH_SalVentAttnA_Ins_3	-32	18	8
17Networks_LH_SalVentAttnA_ParMed_3	-6	-48	56
17Networks_LH_SalVentAttnB_Ins_2	-32	24	0
17Networks_LH_SalVentAttnB_Ins_3	-44	12	2
17Networks_LH_SalVentAttnB_OFC_1	-26	50	-14
17Networks_LH_LimbicB_OFC_1	-12	24	-20
17Networks_LH_LimbicB_OFC_2	-24	22	-20
17Networks_LH_LimbicB_OFC_3	-10	48	-22
17Networks_LH_LimbicB_OFC_4	-4	24	-20
17Networks_LH_LimbicA_TempPole_1	-38	-6	-42
17Networks_LH_LimbicA_TempPole_5	-40	-22	-26
17Networks_LH_ContA_Temp_1	-56	-62	0
17Networks_LH_ContA_IPS_3	-34	-62	48
17Networks_LH_ContA_IPS_5	-34	-46	40
17Networks_LH_ContA_PFCl_3	-40	8	34
17Networks_LH_ContB_Temp_1	-60	-36	-18
17Networks_LH_ContB_Temp_2	-60	-48	-10
17Networks_LH_ContB_PFClv_1	-42	48	-6
17Networks_LH_ContB_PFClv_2	-28	58	0
17Networks_LH_ContC_pCun_1	-10	-70	32
17Networks_LH_ContC_pCun_2	-10	-78	46
17Networks_LH_ContC_Cingp_1	-6	-40	24

17Networks_LH_DefaultA_PFCd_1	-24	28	44
17Networks_LH_DefaultA_PFCd_3	-22	20	52
17Networks_LH_DefaultA_pCunPCC_1	-4	-54	20
17Networks_LH_DefaultA_pCunPCC_2	-6	-60	30
17Networks_LH_DefaultA_pCunPCC_5	-2	-16	38
17Networks_LH_DefaultA_PFCm_1	-4	56	-10
17Networks_LH_DefaultA_PFCm_2	-6	36	-8
17Networks_LH_DefaultA_PFCm_3	-6	60	6
17Networks_LH_DefaultA_PFCm_6	-6	34	20
17Networks_LH_DefaultB_Temp_1	-44	12	-34
17Networks_LH_DefaultB_Temp_3	-62	-18	-20
17Networks_LH_DefaultB_Temp_4	-56	-8	-14
17Networks_LH_DefaultB_Temp_5	-60	-34	-4
17Networks_LH_DefaultB_Temp_6	-52	-22	-6
17Networks_LH_DefaultB_IPL_2	-56	-54	30
17Networks_LH_DefaultB_PFCv_2	-36	36	-12
17Networks_LH_DefaultB_PFCv_3	-46	32	-10
17Networks_LH_DefaultB_PFCv_4	-48	28	0
17Networks_LH_DefaultC_Rsp_1	-14	-48	4
17Networks_LH_DefaultC_Rsp_2	-8	-52	10
17Networks_LH_DefaultC_PHC_2	-30	-32	-18
17Networks_LH_DefaultC_PHC_3	-18	-38	-12
17Networks_LH_TempPar_1	-52	6	-12
17Networks_LH_TempPar_4	-52	-44	4
17Networks_LH_TempPar_5	-58	-54	10
17Networks_LH_TempPar_6	-58	-48	16
17Networks_RH_VisCent_ExStr_1	36	-54	-18
17Networks_RH_VisCent_ExStr_3	24	-74	-10
17Networks_RH_VisCent_Striate_1	8	-92	-2
17Networks_RH_VisCent_ExStr_7	36	-88	2
17Networks_RH_VisCent_ExStr_9	44	-78	10
17Networks_RH_VisCent_ExStr_10	12	-94	18
17Networks_RH_VisCent_ExStr_11	28	-88	20

17Networks_RH_VisPeri_ExStrInf_1	26	-52	-8
17Networks_RH_VisPeri_ExStrInf_3	10	-72	-6
17Networks_RH_VisPeri_ExStrInf_4	14	-58	-4
17Networks_RH_VisPeri_ExStrInf_5	18	-44	-2
17Networks_RH_VisPeri_StriCal_1	10	-74	8
17Networks_RH_VisPeri_StriCal_2	22	-60	6
17Networks_RH_VisPeri_ExStrSup_2	4	-80	24
17Networks_RH_VisPeri_ExStrSup_3	14	-78	34
17Networks_RH_SomMotA_3	44	-10	48
17Networks_RH_SomMotA_4	50	-26	56
17Networks_RH_SomMotA_6	44	-22	54
17Networks_RH_SomMotA_7	38	-20	64
17Networks_RH_SomMotA_9	30	-40	64
17Networks_RH_SomMotA_10	34	-28	62
17Networks_RH_SomMotA_13	10	-40	68
17Networks_RH_SomMotB_Aud_3	60	-24	10
17Networks_RH_SomMotB_S2_3	42	-14	18
17Networks_RH_SomMotB_S2_5	50	-10	14
17Networks_RH_SomMotB_S2_6	60	0	10
17Networks_RH_SomMotB_S2_7	48	-22	18
17Networks_RH_SomMotB_Cent_2	60	-6	26
17Networks_RH_SomMotB_Cent_3	52	-6	38
17Networks_RH_DorsAttnA_TempOcc_2	50	-50	-18
17Networks_RH_DorsAttnA_ParOcc_1	48	-66	4
17Networks_RH_DorsAttnA_ParOcc_2	54	-56	12
17Networks_RH_DorsAttnA_ParOcc_3	36	-78	24
17Networks_RH_DorsAttnA_SPL_5	20	-68	52
17Networks_RH_DorsAttnA_SPL_7	26	-58	60
17Networks_RH_DorsAttnA_SPL_8	14	-64	64
17Networks_RH_DorsAttnB_PostC_1	62	-14	30
17Networks_RH_DorsAttnB_PostC_6	8	-54	60
17Networks_RH_DorsAttnB_PostC_7	24	-50	68
17Networks_RH_DorsAttnB_PostC_8	16	-46	74

17Networks_RH_SalVentAttnA_PrC_1	52	4	40
17Networks_RH_SalVentAttnA_Ins_1	40	6	-16
17Networks_RH_SalVentAttnA_Ins_3	40	-10	-4
17Networks_RH_SalVentAttnA_FrOper_3	54	12	12
17Networks_RH_SalVentAttnB_PFCl_1	42	46	14
17Networks_RH_SalVentAttnB_Ins_1	34	22	-8
17Networks_RH_LimbicB_OFC_3	8	46	-24
17Networks_RH_LimbicB_OFC_4	20	42	-18
17Networks_RH_LimbicB_OFC_5	4	22	-20
17Networks_RH_LimbicB_OFC_6	10	62	-14
17Networks_RH_ContA_IPS_2	54	-32	52
17Networks_RH_ContA_PFCd_1	24	10	58
17Networks_RH_ContA_PFCl_2	48	18	24
17Networks_RH_ContA_PFCl_3	48	28	28
17Networks_RH_ContA_PFCl_4	48	8	24
17Networks_RH_ContB_IPL_1	56	-46	32
17Networks_RH_ContB_PFClv_1	36	38	-14
17Networks_RH_ContB_PFClv_2	28	54	-14
17Networks_RH_ContB_PFClv_3	42	50	-6
17Networks_RH_ContB_PFClv_4	28	60	2
17Networks_RH_ContC_pCun_2	14	-72	40
17Networks_RH_ContC_Cingp_1	8	-44	20
17Networks_RH_DefaultA_IPL_1	54	-54	26
17Networks_RH_DefaultA_PFCd_1	26	34	38
17Networks_RH_DefaultA_pCunPCC_5	10	-52	36
17Networks_RH_DefaultA_PFCm_1	6	42	-10
17Networks_RH_DefaultA_PFCm_2	10	66	0
17Networks_RH_DefaultA_PFCm_3	8	42	4
17Networks_RH_DefaultB_Temp_1	64	-24	-8
17Networks_RH_DefaultB_PFCv_2	48	32	-8
17Networks_RH_DefaultC_IPL_1	48	-64	22
17Networks_RH_DefaultC_IPL_2	46	-76	30
17Networks_RH_DefaultC_Rsp_1	14	-46	4

17Networks_RH_DefaultC_Rsp_2	12	-56	16
17Networks_RH_TempPar_2	54	-4	-14
17Networks_RH_TempPar_3	48	-20	-8
17Networks_RH_TempPar_7	52	-40	12
17Networks_RH_TempPar_9	54	-46	20
17Networks_RH_TempPar_10	62	-40	22

Table 8 Region labels and coordinates for regions that were different in Euclidean distance due to hallucinations.

ROI Name	R	A	S
17Networks_LH_VisCent_ExStr_1	-36	-62	-16
17Networks_LH_VisCent_ExStr_2	-24	-72	-10
17Networks_LH_VisCent_ExStr_3	-36	-82	-16
17Networks_LH_VisCent_ExStr_4	-16	-86	-16
17Networks_LH_VisCent_ExStr_6	-42	-86	-4
17Networks_LH_VisCent_Striate_1	-8	-98	-8
17Networks_LH_VisCent_ExStr_7	-46	-74	6
17Networks_LH_VisPeri_ExStrInf_1	-24	-54	-8
17Networks_LH_VisPeri_ExStrInf_2	-12	-62	-4
17Networks_LH_VisPeri_ExStrInf_3	-6	-76	-6
17Networks_LH_VisPeri_ExStrInf_5	-14	-56	2
17Networks_LH_VisPeri_StriCal_2	-8	-74	10
17Networks_LH_VisPeri_ExStrSup_3	-12	-72	20
17Networks_LH_VisPeri_ExStrSup_5	-12	-82	36
17Networks_LH_SomMotA_13	-20	-24	66
17Networks_LH_SomMotB_Ins_1	-36	-24	10
17Networks_LH_SomMotB_S2_2	-36	-26	18
17Networks_LH_SomMotB_Aud_4	-40	-36	14
17Networks_LH_SomMotB_S2_5	-48	-24	18
17Networks_LH_SomMotB_Cent_1	-60	-2	24
17Networks_LH_SomMotB_Cent_2	-62	-10	32

17Networks_LH_SomMotB_Cent_3	-54	-8	30
17Networks_LH_SomMotB_Cent_5	-48	-16	40
17Networks_LH_DorsAttnA_TempOcc_1	-44	-42	-22
17Networks_LH_DorsAttnA_TempOcc_2	-32	-42	-20
17Networks_LH_DorsAttnA_TempOcc_3	-48	-56	-16
17Networks_LH_DorsAttnA_ParOcc_1	-48	-66	16
17Networks_LH_DorsAttnA_SPL_4	-28	-58	50
17Networks_LH_DorsAttnA_SPL_7	-28	-62	62
17Networks_LH_DorsAttnB_PostC_2	-54	-20	40
17Networks_LH_DorsAttnB_PostC_4	-46	-30	44
17Networks_LH_SalVentAttnB_PFCl_2	-28	44	30
17Networks_LH_SalVentAttnB_PFCl_3	-36	32	38
17Networks_LH_SalVentAttnB_PFCmp_1	-6	22	32
17Networks_LH_LimbicB_OFC_2	-24	22	-20
17Networks_LH_LimbicA_TempPole_3	-26	-10	-32
17Networks_LH_LimbicA_TempPole_5	-40	-22	-26
17Networks_LH_ContA_Temp_1	-56	-62	0
17Networks_LH_ContA_IPS_2	-58	-42	46
17Networks_LH_ContA_IPS_3	-34	-62	48
17Networks_LH_ContA_IPS_4	-44	-42	46
17Networks_LH_ContA_PFClv_2	-42	38	22
17Networks_LH_ContA_PFCl_1	-50	6	26
17Networks_LH_ContA_PFCl_2	-44	20	26
17Networks_LH_ContA_Cingm_1	-4	6	28
17Networks_LH_ContB_Temp_1	-60	-36	-18
17Networks_LH_ContB_IPL_1	-48	-60	46
17Networks_LH_ContB_IPL_2	-54	-50	44
17Networks_LH_ContB_IPL_3	-42	-52	48
17Networks_LH_ContB_PFCd_1	-30	14	58
17Networks_LH_ContB_PFCmp_1	-4	28	48
17Networks_LH_ContC_Cingp_1	-6	-40	24
17Networks_LH_ContC_Cingp_2	-4	-22	30
17Networks_LH_DefaultA_IPL_1	-48	-64	32

17Networks_LH_DefaultA_PFCd_1	-24	28	44
17Networks_LH_DefaultA_PFCd_2	-18	36	48
17Networks_LH_DefaultA_PFCd_3	-22	20	52
17Networks_LH_DefaultA_pCunPCC_3	-8	-44	32
17Networks_LH_DefaultA_pCunPCC_4	-4	-34	38
17Networks_LH_DefaultA_pCunPCC_5	-2	-16	38
17Networks_LH_DefaultA_PFCm_6	-6	34	20
17Networks_LH_DefaultB_IPL_1	-46	-58	20
17Networks_LH_DefaultB_PFCd_1	-4	52	28
17Networks_LH_DefaultB_PFCd_2	-14	58	30
17Networks_LH_DefaultB_PFCd_3	-22	50	32
17Networks_LH_DefaultB_PFCd_4	-8	42	52
17Networks_LH_DefaultB_PFCd_5	-12	24	60
17Networks_LH_DefaultB_PFCl_1	-40	20	48
17Networks_LH_DefaultB_PFCv_4	-48	28	0
17Networks_RH_VisCent_ExStr_1	36	-54	-18
17Networks_RH_VisCent_Striate_1	8	-92	-2
17Networks_RH_VisCent_ExStr_7	36	-88	2
17Networks_RH_VisCent_ExStr_9	44	-78	10
17Networks_RH_VisPeri_ExStrInf_1	26	-52	-8
17Networks_RH_VisPeri_ExStrInf_2	18	-36	-12
17Networks_RH_VisPeri_ExStrInf_3	10	-72	-6
17Networks_RH_VisPeri_ExStrInf_4	14	-58	-4
17Networks_RH_VisPeri_ExStrInf_5	18	-44	-2
17Networks_RH_VisPeri_StriCal_1	10	-74	8
17Networks_RH_VisPeri_ExStrSup_2	4	-80	24
17Networks_RH_VisPeri_ExStrSup_3	14	-78	34
17Networks_RH_SomMotA_1	54	-16	40
17Networks_RH_SomMotA_16	22	-34	70
17Networks_RH_SomMotB_Aud_1	52	4	-6
17Networks_RH_SomMotB_Aud_2	54	-14	6
17Networks_RH_SomMotB_Ins_1	40	-20	4
17Networks_RH_SomMotB_Aud_3	60	-24	10

17Networks_RH_SomMotB_S2_7	48	-22	18
17Networks_RH_SomMotB_Cent_1	60	6	30
17Networks_RH_SomMotB_Cent_2	60	-6	26
17Networks_RH_SomMotB_Cent_3	52	-6	38
17Networks_RH_DorsAttnA_TempOcc_2	50	-50	-18
17Networks_RH_DorsAttnA_TempOcc_3	50	-64	-10
17Networks_RH_DorsAttnA_ParOcc_1	48	-66	4
17Networks_RH_DorsAttnA_ParOcc_2	54	-56	12
17Networks_RH_DorsAttnA_ParOcc_3	36	-78	24
17Networks_RH_DorsAttnB_TempOcc_1	60	-54	-2
17Networks_RH_DorsAttnB_PostC_1	62	-14	30
17Networks_RH_DorsAttnB_PostC_2	58	-22	44
17Networks_RH_DorsAttnB_PostC_7	24	-50	68
17Networks_RH_DorsAttnB_PostC_8	16	-46	74
17Networks_RH_SalVentAttnA_ParOper_2	60	-22	22
17Networks_RH_SalVentAttnA_Ins_1	40	6	-16
17Networks_RH_SalVentAttnA_Ins_3	40	-10	-4
17Networks_RH_SalVentAttnB_PFCmp_1	8	34	24
17Networks_RH_SalVentAttnB_PFCmp_2	8	18	36
17Networks_RH_LimbicA_TempPole_3	36	18	-38
17Networks_RH_LimbicA_TempPole_4	40	-14	-32
17Networks_RH_ContA_PFCd_1	24	10	58
17Networks_RH_ContA_Cingm_1	4	2	30
17Networks_RH_ContB_Temp_2	64	-42	-10
17Networks_RH_ContC_pCun_4	8	-50	44
17Networks_RH_ContC_Cingp_1	8	-44	20
17Networks_RH_ContC_Cingp_2	6	-28	28
17Networks_RH_DefaultA_IPL_2	48	-64	42
17Networks_RH_DefaultA_PFCd_1	26	34	38
17Networks_RH_DefaultA_pCunPCC_2	4	-64	32
17Networks_RH_DefaultA_pCunPCC_3	6	-38	34
17Networks_RH_DefaultA_pCunPCC_4	4	-20	36
17Networks_RH_DefaultA_pCunPCC_5	10	-52	36

17Networks_RH_DefaultA_PFCm_4	8	54	12
17Networks_RH_DefaultB_Temp_2	64	-38	0
17Networks_RH_DefaultB_AntTemp_1	50	8	-32
17Networks_RH_DefaultB_PFCd_1	6	58	30
17Networks_RH_DefaultB_PFCd_3	4	44	40
17Networks_RH_DefaultB_PFCd_5	12	20	62
17Networks_RH_DefaultB_PFCv_2	48	32	-8
17Networks_RH_DefaultC_IPL_1	48	-64	22
17Networks_RH_DefaultC_PHC_1	22	-18	-28
17Networks_RH_TempPar_1	48	16	-20
17Networks_RH_TempPar_2	54	-4	-14
17Networks_RH_TempPar_3	48	-20	-8
17Networks_RH_TempPar_6	60	-46	6
17Networks_RH_TempPar_7	52	-40	12
17Networks_RH_TempPar_8	64	-34	10
17Networks_RH_TempPar_9	54	-46	20
17Networks_RH_TempPar_10	62	-40	22

References

Abraham, Alexandre, *et al.* (2014) "Machine Learning for Neuroimaging with Scikit Learn." Frontiers in Neuroinformatics 8. https://doi.org/10.3389/fninf.2014.00014.

Avants, B.B., C.L. Epstein, M. Grossman, and J.C. Gee (2008) "Symmetric Diffeomorphic Image Registration with Cross-Correlation: Evaluating Automated Labeling of Elderly and Neurodegenerative Brain." Medical Image Analysis 12 (1): 26–41. https://doi.org/10.1016/j.media.2007.06.004.

Behzadi, Yashar, Khaled Restom, Joy Liau, and Thomas T. Liu. (2007) "A Component Based Noise Correction Method (CompCor) for BOLD and Perfusion Based fMRI." *NeuroImage* 37 (1): 90–101. https://doi.org/10.1016/j.neuroimage.2007.04.042.

Belkina, A.C. *et al.* (2019) 'Automated optimized parameters for T-distributed stochastic neighbor embedding improve visualization and analysis of large datasets', *Nature Communications*, 10(1), p. 5415. Available at: https://doi.org/10.1038/s41467-019-13055-y.

Böhm, J.N., Berens, P. and Kobak, D. (2021) 'Attraction-Repulsion Spectrum in Neighbor Embeddings'. arXiv. Available at: http://arxiv.org/abs/2007.08902 (Accessed: 15 May 2022).

Esteban, Oscar, *et al.* (2018) "FMRIPrep." *Software*. Zenodo. https://doi.org/10.5281/zenodo.852659.

Esteban, Oscar, *et al.* (2018) "fMRIPrep: A Robust Preprocessing Pipeline for Functional MRI." *Nature Methods*. https://doi.org/10.1038/s41592-018-0235-4.

Evans, AC, *et al.* (2012) "Brain Templates and Atlases." *NeuroImage* 62 (2): 911–22. https://doi.org/10.1016/j.neuroimage.2012.01.024.

Fonov, VS, *et al.* (2009) "Unbiased Nonlinear Average Age-Appropriate Brain Templates from Birth to Adulthood." *NeuroImage* 47, Supplement 1: S102. https://doi.org/10.1016/S1053-8119(09)70884-5.

Gorgolewski, K., *et al.* (2011) "Nipype: A Flexible, Lightweight and Extensible Neuroimaging Data Processing Framework in Python." *Frontiers in Neuroinformatics* 5: 13. https://doi.org/10.3389/fninf.2011.00013.

Gorgolewski, Krzysztof J. *et al*. (2018) “Nipype.” *Software*. Zenodo. https://doi.org/10.5281/zenodo.596855.

Greve, Douglas N, and Bruce Fischl (2009) “Accurate and Robust Brain Image Alignment Using Boundary-Based Registration.” *NeuroImage* 48 (1): 63–72. https://doi.org/10.1016/j.neuroimage.2009.06.060.

Hartigan, J.A. (1975) *John A. Hartigan - Clustering Algorithms-John Wiley & Sons (1975).pdf*. John Wiley & Sons.

Jenkinson, Mark, *et al.* (2002) “Improved Optimization for the Robust and Accurate Linear Registration and Motion Correction of Brain Images.” *NeuroImage* 17 (2): 825–41. https://doi.org/10.1006/nimg.2002.1132.

Jenkinson, Mark, and Stephen Smith (2001) “A Global Optimisation Method for Robust Affine Registration of Brain Images.” *Medical Image Analysis* 5 (2): 143–56. https://doi.org/10.1016/S1361-8415(01)00036-6.

Kobak, D. and Linderman, G.C. (2021) ‘Initialization is critical for preserving global data structure in both t-SNE and UMAP’, *Nature Biotechnology*, 39(2), pp. 156–157. Available at: https://doi.org/10.1038/s41587-020-00809-z.

Lanczos, C. (1964) “Evaluation of Noisy Data.” *Journal of the Society for Industrial and Applied Mathematics Series B Numerical Analysis* 1 (1): 76–85. https://doi.org/10.1137/0701007.

Power, Jonathan D. *et al.* (2014) “Methods to Detect, Characterize, and Remove Motion Artifact in Resting State fMRI.” *NeuroImage* 84 (Supplement C): 320–41. https://doi.org/10.1016/j.neuroimage.2013.08.048.

Pruim, Raimon H. R. *et al.* (2015) “ICA-AROMA: A Robust ICA-Based Strategy for Removing Motion Artifacts from fMRI Data.” *NeuroImage* 112 (Supplement C): 267–77. https://doi.org/10.1016/j.neuroimage.2015.02.064.

Satterthwaite, T.D. *et al.* (2013) ‘An improved framework for confound regression and filtering for control of motion artifact in the preprocessing of resting-state functional connectivity data’, *NeuroImage*, 64, pp. 240–256. Available at: https://doi.org/10.1016/j.neuroimage.2012.08.052.

Thomas Yeo, B.T. *et al.* (2011) 'The organization of the human cerebral cortex estimated by intrinsic functional connectivity', *Journal of Neurophysiology*, 106(3), pp. 1125–1165. Available at: https://doi.org/10.1152/jn.00338.2011.

Tustison, N. J. *et al.* (2010) "N4ITK: Improved N3 Bias Correction." *IEEE Transactions on Medical Imaging* 29 (6): 1310–20. https://doi.org/10.1109/TMI.2010.2046908.

Vinh, N.X. and Epps, J. (2009) 'A Novel Approach for Automatic Number of Clusters Detection in Microarray Data Based on Consensus Clustering', in *2009 Ninth IEEE International Conference on Bioinformatics and BioEngineering*. *2009 Ninth IEEE International Conference on Bioinformatics and BioEngineering (BIBE)*, Taichung, Taiwan: IEEE, pp. 84–91. Available at: https://doi.org/10.1109/BIBE.2009.19.

Vinh, N.X., Epps, J. and Bailey, J. (2009) 'Information Theoretic Measures for Clusterings Comparison: Is a Correction for Chance Necessary?', p. 8.

Vinh, N.X., Epps, J. and Bailey, J. (2010) 'Information Theoretic Measures for Clusterings Comparison: Variants, Properties, Normalization and Correction for Chance', p. 18.

Zhang, Y., M. Brady, and S. Smith, (2001) "Segmentation of Brain MR Images Through a Hidden Markov Random Field Model and the Expectation-Maximization Algorithm." *IEEE Transactions on Medical Imaging* 20 (1): 45–57. https://doi.org/10.1109/42.906424.